
Design and Optimization of EMI Filters for Power Electronics Systems

Auslegung und Optimierung von EMV Filtern für Leistungselektronische Systeme

Zur Erlangung des akademischen Grades Doktor-Ingenieur (Dr.-Ing.)

Vorgelegte Dissertation von Illia Manushyn aus Charkiw

Tag der Einreichung: 27. August 2018

1. Gutachten: Prof. Dr.Ing. Gerd Griepentrog

2. Gutachten: Prof. Dr.Ing. Ralf Vick



TECHNISCHE
UNIVERSITÄT
DARMSTADT



Manushyn, Illia:

Design and Optimization of EMI Filters for Power Electronics Systems

Auslegung und Optimierung von EMV Filtern für Leistungselektronische Systeme

Darmstadt, Technische Universität Darmstadt,

Jahr der Veröffentlichung der Dissertation auf TUpriints: 2019

Tag der mündlichen Prüfung: 29.01.2019

Institut für Stromrichtertechnik und Antriebsregelung Fachbereich

Elektrotechnik und Informationstechnik Technische Universität Darmstadt

Darmstadt-D 17

Veröffentlicht unter CC BY-SA 4.0 International

Ehrenwörtliche Erklärung

Erklärung laut 9 §PromO

Ich versichere hiermit, dass ich die vorliegende Dissertation allein und nur unter Verwendung der angegebenen Literatur verfasst habe. Die Arbeit hat bisher noch nicht zu Prüfungszwecken gedient.

Darmstadt, den 27. August 2018

(Illia Manushyn)

Curriculum Vitae

Illia Manushyn

born September 9, 1987 in Kharkiv, Ukraine

Education

- 09/1994 - 09/2004 Primary and High School, Kharkiv, Ukraine
- 09/2004 - 09/2008 Bachelor degree in Electronics
Kharkiv National University of Radioelectronics. Thesis topic "Algorithms and programs of control devices for industrial devices using microcontrollers"
- 09/2008 - 07/2009 Master degree in Electronics
Kharkiv National University of Radioelectronics, Department of Automation and Computer Technology. Thesis topic "Methods and algorithms of microcontroller operation for peripheral units"
- 12/2013 - 08/2018 Doctor of Engineering degree in Power Electronics
Technical University of Darmstadt, Department of Power Electronics and Control of Drives. Thesis topic "Optimization of Grid Filters for Power Electronics Systems"

Experience

- 10/2006 - 07/2008 *Laboratory Engineer*
Kharkiv National University of Radioelectronics (microprocessor laboratory)
- 09/2008 - 11/2009 *Design Engineer*
Enterprise-group "Kharkov Electropanelboard works" production for middle voltage equipment for power systems
- 12/2009 - 08/2013 *Senior Design Engineer*
Corporation "Triol" (Variable frequency drives, equipment for oil extraction, telemetry systems)
- 11/2013 - 02/2017 *Research Assistant*
Technical University of Darmstadt, Department of Power Electronics and Control of Drives.
- as of 02/2017 *Electrical Drives and Power Electronics Expert*
Bosch GmbH, Power Train Solutions, Components development for vehicles electrification

Darmstadt, 27. August 2018

(Illia Manushyn)

Abstract

Modern power electronics develop very rapidly. The main direction for development nowadays is increasing power density. This can be achieved by utilizing higher switching frequencies. The last generation of SiC and GaN semiconductors can reach switching frequencies up to several MHz. At the same time the number of power electronics devices connected to the power grid has grown significantly during past decades and continues to increase. These two factors result in the high level of power grid pollution with electromagnetic interferences. In order to minimize the emission level, passive electromagnetic interference (EMI) filters are employed.

Within the frame of this thesis, issues related to design and improvement of EMI filters for three-phase power electronic converters are comprehensively studied. Detailed analyses of magnetic materials, filter components, mutual couplings, enhancement methods and filter topologies are presented. Insertion loss of EMI filters is analysed within a system under idealised conditions ($50\ \Omega$ reference impedance). Moreover the impact of the reference impedance used for EMI filter characterisation on insertion loss is investigated based on mathematical models.

Behavioural models of EMI filters with different complexity are developed. Diverse simulation approaches are used for profound understanding of the physical processes inherent in EMI filters. Exactness of the behavioural models is proven by measurements of built prototypes. The main insertion loss degradation mechanisms are derived from the developed models. The advantages and disadvantages of models based upon the network theory, S-functions and differential equations with the help of electronic design automation tools are shown.

Existing filter improvement methods are systematized and complemented. Novel improvement possibilities for conventional filters including parasitics compensation methods and mutual coupling minimization are developed. Different combinations of improvement methodologies are applied to reference EMI filters and tested. Multistage filters with enhanced topologies are proposed. Critical comparison of conventional and proposed filter topologies considering power density and costs is carried out. Obtained results demonstrate considerable advantages of enhanced EMI filter topologies over conventional ones.

Three phase power electronics systems are examined from the perspective of electromagnetic compatibility. Analysis of common and differential currents' contribution into the spectrum of a conventional drive system is carried out. EMI filters are tested together with different types of power electronic converters. Effects caused by variation of converter parameters on the emitted spectrum of disturbances are assessed from the EMI filter design point of view. It is determined that essentially all investigated parameters of a power electronics converter and a drive system except DC voltage fluctuation have feasible impact on the EMI spectrum. Thus EMC behaviour of the system can be adjusted by variation of these parameters. Semiconductor speed, motor stray capacitance and concept of protective earthing are determined as the most relevant system parameters influencing EMI filter design.

Kurzfassung

Die Entwicklung leistungselektronischer Systeme schreitet, getrieben durch globale Trends, wie Klimawandel und Digitalisierung, sehr schnell voran. Viele Anwendungen sind nur durch den Einsatz moderner leistungselektronischer Systeme überhaupt umsetzbar, was zu einem stetig steigenden Bedarf führt. Eines der Hauptziele, neben der Steigerung der Systemeffizienz, ist hierbei die Erhöhung der Leistungsdichte. Diese ist insbesondere zu erreichen durch höhere Schaltfrequenzen der verwendeten Halbleiterbauelemente. Gerade die neuste Generation von Halbleitern mit großem Bandabstand (SiC und GaN) ermöglicht den Betrieb mit Schaltfrequenzen bis in den Megahertz-Bereich.

Neben den Vorteilen, die moderne Systeme bieten, erwachsen aus den angewandten Technologien auch neue Herausforderungen. Gerade im Hinblick auf die Elektromagnetische Verträglichkeit (EMV) entstehen ungelöste Fragestellungen. Um bestehende Emissionsgrenzwerte einzuhalten und auf diese Weise den störungsfreien Betrieb anderer elektrischer oder elektronischer Systeme zu garantieren, kommt bei einer Mehrzahl der leistungselektronischen Systeme ein passiver EMV Filter zum Einsatz. Um den schnell schaltenden Halbleiterbauelementen Rechnung zu tragen, ist es notwendig, die Auslegung und den Entwurf der Filterschaltungen zu optimieren. Zu diesem Zweck untersucht die vorliegende Arbeit die unterschiedlichen magnetischen Materialien und Filterkomponenten. Weiterhin werden gegenseitige Verkopplungen innerhalb eines Filters analysiert, Methoden zur Verbesserung der Einfügungsdämpfung erarbeitet und Filtertopologie ausgewertet.

Es werden Verhaltensmodelle der EMV Filter mit unterschiedlicher Komplexität abgeleitet. Weiterhin kommen diverse Simulationsansätze zur Anwendung, um die physikalischen Prozesse zu verstehen und die Verhaltensmodelle schlussendlich anhand von Messungen zu validieren. Mittels der entwickelten Verhaltensmodelle werden negative Einflussfaktoren auf die Einfügungsdämpfung abgeleitet. Anhand der Netzwerktheorie, S-Funktionen und Differentialgleichungen werden die Vor- und Nachteile der Verhaltensmodelle von EMV Filtern verdeutlicht.

Bestehende Filterverbesserungsmethoden werden systematisiert und durch neuartige Verbesserungsoptionen ergänzt. Die entwickelten Erweiterungen umfassen Kompensationsverfahren parasitärer Komponenten und Vorschläge zur Minimierung von parasitären Kopplungen, welche die Einfügungsdämpfung des Filters negativ beeinflussen würden. Die Wirksamkeit der entwickelten Methoden für konventionelle Filterschaltungen wird anhand von Messungen nachgewiesen. Mehrstufige Filter mit erweiterten Topologien werden vorgeschlagen. Eine kritische Bewertung der Filterschaltungen erfolgt basierend auf der Leistungsdichte und den Kosten, wodurch erhebliche Vorteile der entwickelten Filterschaltungen deutlich werden.

Abschließend wird anhand eines dreiphasigen leistungselektronischen Antriebssystems die verursachte Störaussendung analysiert und die jeweiligen Beiträge von Gleich- und Gegentaktgrößen herausgestellt. Zu diesem Zweck werden verschiedene EMV Filter in Verbindung mit verschiedenen leistungselektronischen Schaltungen systematisch untersucht. Der Einfluss der Variation verschiedener Schaltungsparameter auf das Spektrum wird aus der Sichtweise der Filterschaltung ausgewertet. Es wird herausgestellt, dass alle Schaltungsparameter (außer der Spannungsschwankungen des Gleichspannungszwischenkreises) erheblichen Einfluss auf das erzeugte Spektrum haben. Auf diese Weise wird verdeutlicht, dass das EMV-Verhalten eines leistungselektronischen Systems erheblich durch die Veränderung einzelner Schaltungsparameter beeinflusst werden kann.

Contents

List of Figures	xiii
List of Tables	xv
Abbreviations and Symbols	xvii
1. Introduction	1
1.1. Power Electronics Converters	3
1.2. EMI Issues in Power Electronics	7
1.3. EMI Filters	15
1.4. Standards Overview	21
1.5. Objectives and Outline of the Thesis	23
2. EMI filter components	27
2.1. Soft magnetic materials	27
2.1.1. Ferrites	32
2.1.2. Amorphous Alloys	33
2.1.3. Nanocrystalline Alloys	34
2.1.4. Powder Materials	36
2.2. Inductive Components	37
2.2.1. Common Mode Chokes	40
2.3. Capacitors	42
2.4. Mutual Couplings	43
3. Modelling and Design Methods for EMI Filters	45
3.1. Design of EMI Filters Based on a Simplified Analytical Model	46
3.1.1. Analytical Model Validation	59
3.1.2. Impact of Load and Source Impedances on Insertion Loss	61
3.2. SPICE Based EMI Filter Design Assisted with FEM Modelling	63
3.2.1. Novel Behavioural Model of CMC	65
3.2.2. Mutual Coupling Determination	74
3.3. Combined FEM Simulation in CST Microwave Studio	79
3.3.1. Model Preparation	80
3.3.2. Simulation and Post-Processing	82
3.3.3. Validation	85

4. Parasitics Management in Three-Phase EMI Filters	89
4.1. Parasitics Compensation of The Filter Components	89
4.1.1. Compensation of EPC	91
4.1.2. Compensation of ESL	96
4.2. Minimisation of Mutual Couplings	104
5. Design of High Performance EMI Filters	113
5.1. Filter Structure Analysis and Advanced Topologies	113
5.1.1. Multistage or Ladder Filters	117
5.1.2. Ladder Filters with High Frequency Stages	121
5.2. Impact of Magnetic Material on EMI Filter Performance	127
5.3. Summary of EMI Filter Improvement Methods	131
6. Consideration of EMI Filters Within a Power Electronics System	135
6.1. Influence of AIC Parameters on the Emitted EMI Spectrum	135
6.1.1. PWM Frequency	137
6.1.2. Dead Time	138
6.1.3. DC Voltage Level	140
6.1.4. Load Current	141
6.1.5. Connection of Protective Earthing Conductor	142
6.1.6. Line Inductor	146
6.1.7. Damping Capabilities of Grid Side EMI Filters	147
6.2. Investigation of the Motor and Inverter Parameters Focused on the EMI	150
6.2.1. Motor Stray Capacitance	150
6.2.2. PWM Frequency	151
6.2.3. Load Current	152
6.2.4. Switching Speed of Semiconductors	153
6.2.5. Protective Earthing Conductor Impact	155
6.2.6. Damping Capabilities of DC Side EMI Filters	156
7. Conclusions	159
7.1. Summary	159
7.2. General Conclusions	159
7.3. Future Research	162
A. Model Based Selection of Soft Magnetic Materials	163
B. Comparison of Soft Magnetic Materials	167
C. Measurement Setup for IL Characterisation	169
D. Laboratory Measurement of Power Grid Impedance	171

E. Modelling and Design Methods for EMI Filters Flowcharts	173
F. Test Bench for Characterisation of Magnetic Materials Under Saturation Conditions	179
G. Table of Mutual Couplings	181
H. Comparison of Parasitics Compensation Methods	185
I. Parameters of Passive Components Used for Filter Prototypes in Chapter 5	187
J. Hybrid Chokes	193
K. Topologies of Conventional Filters Used for System Level Experiments	197



List of Figures

1.1. Interdisciplinary allocation of EMI filters.	2
1.2. Classification of power electronics converters [195].	4
1.3. Classification of existing rectifiers.	5
1.4. Three-phase 2-level active infeed converter.	5
1.5. Classification of control strategies suitable for rectifiers.	6
1.6. Spectra of AICs operated under different control strategies.	6
1.7. CM voltage levels for different PWM patterns.	8
1.8. Common and differential mode interferences in a three-phase system.	10
1.9. A typical variable speed drive system with stray capacitors included.	12
1.10. CM impedance between AIC and the ground.	13
1.11. Measured values of CM and DM disturbances of AIC with no EMI filter connected.	14
1.12. Common mode paths within a variable drive system.	14
1.13. A typical PCB-based EMI filter.	15
1.14. Measurement setups for three-phase EMI filter characterization according to [92].	17
1.15. Π , T , $\Gamma(LC)$ and CL filter topologies.	18
1.16. Topology of a typical three-phase EMI filter.	19
1.17. CM and DM equivalent networks of the analysed EMI filter.	19
1.18. CM, DM-decoupled and DM-unbalanced insertion losses of an actual EMI filter.	20
1.19. Classification of electromagnetic disturbances by frequency.	22
1.20. EMI emission limits according to different standards	23
2.1. Classification of soft magnetic materials suitable for EMI filter applications.	28
2.2. Frequency dependency of real and imaginary permeability for a typical ferrite.	29
2.3. Microstructures of crystalline, amorphous and nanocrystalline materials [74].	34
2.4. Impedance of nanocrystalline and ferrite based chokes with the same number of turns and dimensions.	35
2.5. Comparison of the soft saturation of powder material and normal magnetization of ferrite.	37
2.6. Types of parasitic capacitors of an inductor and corresponding equivalent circuit.	39
2.7. Equivalent circuit of an inductor.	39
2.8. Field distribution of CMC.	41
2.9. CMC impedances for CM and DM paths.	41
2.10. Equivalent circuit of a capacitor.	42
2.11. Modelled and measured capacitors 0.09 nF.	43
3.1. example of a spectrum produced by a PE converter without an EMI filter.	47
3.2. Standard filter topologies.	47
3.3. IL of standard filter topologies (50 Ω /50 Ω).	48
3.4. Impact of self-parasitics on impedance of capacitors and inductors.	54

3.5. Physical parameters of the CMC for EPC calculation.	55
3.6. Standard filter topologies with included EPC and ESL.	57
3.7. Standard filter topologies with included parasitics and considered permeability degradation.	58
3.8. Comparison between the analytical model and prototype of a Γ -topology (50 Ω /50 Ω).	59
3.9. Comparison between the analytical model and prototype of a Π -topology (50 Ω /50 Ω).	60
3.10. Comparison between the analytical model and prototype of a T -topology (50 Ω /50 Ω).	60
3.11. Simulated IL of the standard filter topologies with different load and source ohmic impedance.	62
3.12. Simulated IL of the standard filter topologies with different reactive load and source impedance.	64
3.13. RLC Foster network used for representation of frequency dependent permeability.	67
3.14. Equivalent circuit of the three-phase CMC implemented in LTspice with consideration of permeability and saturation effects.	68
3.15. PCBs with soldered cores used for impedance characterization.	69
3.16. Comparison between simulated and measured core impedances.	70
3.17. Comparison between impedances of N87 ferrite under saturation.	71
3.18. Circuit of the designed three-phase EMI filter.	72
3.19. Filter used for IL measurements.	72
3.20. Impact of different non-ideal parameters on IL of an EMI filter.	73
3.21. Validation of created CMC models.	74
3.22. Resulting H-field plot after performing magnetostatic simulation.	76
3.23. Resulting E-field plot after performing electrostatic simulation.	77
3.24. Comparison between an EMI filter model in LTspice with consideration of all non-ideal factors and the reference prototype.	78
3.25. Impact of the CMC saturation on CM insertion losses.	78
3.26. Circuits of EMI filters used for FEM simulation with CST studio.	80
3.27. 3D models of EMI filters used for FEM simulation (red lines show discrete ports for lump capacitors placement).	82
3.28. Impact of geometry simplification on simulation results.	83
3.29. Comparison between simulations with waveguide and discrete ports.	83
3.30. Black-box model of an EMI filter automatically created in the schematic: for CM IL characterization on the left hand side and for DM IL characterization on the right hand side.	84
3.31. Impact of frequency dependent permeability on IL.	85
3.32. Comparison between IL of designed and simulated filters with an improvement.	85
3.33. Comparison between measured and simulated self-made filters.	86
3.34. Comparison between measured and simulated industrial filters.	87
3.35. Comparison between CM IL of designed and simulated filters with an improvement.	88
4.1. Effect of EPC on insertion losses of a conventional EMI filter.	90
4.2. Effect of ESL on insertion losses of a conventional EMI filter.	90
4.3. Resulting circuit of the CMC with an implemented EPC compensation network.	92

4.4. Measured IL of a conventional EMI filter with and without EPC compensation, based on three capacitors.	93
4.5. Measured IL of a conventional EMI filter with and without EPC compensation assisted with resistors.	94
4.6. Measured IL of the reference filter, EMI filters with EPC compensation based on single-coil and three windings methods.	95
4.7. Measured IL of a conventional EMI filter with and without EPC compensation based on the center-typed capacitor method	96
4.8. Designed EMI filter with ESL compensation based on crossed over capacitors.	97
4.9. CM and DM IL of the EMI filter with implemented compensation based on crossed over capacitors.	97
4.10. An equivalent circuit and a 3D model of the planar coupled inductor.	98
4.11. EMI filter with the coupled inductor based ESL compensation applied to X-capacitors.	99
4.12. CM and DM IL of the EMI filter with the coupled inductor based ESL compensation applied to X-capacitors.	99
4.13. EMI filter with the coupled inductor based ESL compensation applied to X- and Y-capacitors.	99
4.14. CM and DM IL of the EMI filter with the coupled inductor based ESL compensation applied to X- and Y-capacitors.	100
4.15. PCB used for EMI filters with different location of coupled inductors.	100
4.16. CM and DM IL of the EMI filter with the coupled inductor based ESL compensation, applied to X- and Y-capacitors from the opposite side.	101
4.17. EMI filter with the coupled inductor based ESL compensation, applied to Y-capacitors.	101
4.18. CM and DM IL of the EMI filter with the coupled inductor based ESL compensation, applied to Y-capacitors.	102
4.19. Possible option of compensation inductor arrangement.	103
4.20. CM and DM IL of the EMI filter with ESL and EPC compensation methods applied.	103
4.21. Single polarity couplings of a capacitor's bank.	106
4.22. DM-unbal P1 IL of the reference filter for every phase.	107
4.23. EMI filters with different component arrangements. F1 - reference arrangement, F2 - improved arrangement, F3 - filter with components spread in space.	107
4.24. Measured DM-unbal IL of the reference filter for every phase with inverted CMC.	108
4.25. Measured DM-unbal IL of the filter with rearranged components.	108
4.26. Measured DM-unbal IL of the filter with increased distance between components.	109
4.27. Measured DM-unbal IL of filters with different components arrangements.	109
4.28. Couplings between Y-capacitors.	110
4.29. Plot of a coupling coefficient between two capacitors depending on the angle and distance.	111
5.1. Equivalent circuits of filters with different capacitor connections.	116
5.2. Comparison of measured IL exhibited by the filter A with the direct capacitor connection and the filter B with the star point connected capacitors (measured).	117
5.3. Simulated IL of EMI filters with a different number of stages.	118
5.4. Measured IL of EMI filters with different topologies.	119

5.5. Simulation of Γ -, Π - and <i>CLCLC</i> -topologies optimized in order to get the minimal leakage current.	120
5.6. Measurements of Γ -, Π - and <i>CLCLC</i> -topologies optimized in order to get the minimal leakage current.	121
5.7. Various ways for high frequency components implementation.	122
5.8. <i>T</i> -topology based filters with different arrangement of HF components.	123
5.9. Comparison of two methods of high frequency capacitors implementation with <i>T</i> -topology.	123
5.10. Comparison of two methods of high frequency capacitors implementation with Π -topology.	124
5.11. Comparison of Π -topology based filter with and without resonance damping.	125
5.12. CM IL of a Π -filter with the natural resonance of the HF stage adjusted to the SRF and without adjustment.	126
5.13. Equivalent circuits of Π - and <i>T</i> -topologies, assisted with high frequency stages.	127
5.14. Comparison between IL of the <i>T</i> -filter, <i>T</i> -filter with additional HF capacitors and <i>T</i> -filter supplemented with an <i>LC</i> -stage.	128
5.15. Comparison between IL of the Π -filter, Π -filter with additional HF capacitors and Π -filter supplemented with an <i>LC</i> -stage.	129
5.16. Impedance of CMCs based on different material.	130
5.17. CM IL of an EMI filter with different CMCs.	130
5.18. DM IL of an EMI filter with nanocrystalline and ferrite CMCs.	131
5.19. IL Comparison of the enhanced EMI filters and state of the art EMI filters with the same topologies.	133
6.1. A block diagram of the test bench.	136
6.2. A picture of the test bench.	136
6.3. Spectra emitted by the self-made AIC and the AFE with no EMI filter connected.	137
6.4. Spectra of the self-made AIC operating under different PWM frequencies.	139
6.5. Spectra of the self-made AIC with reference parameters and reduced dead time.	140
6.6. Spectra of the self-made AIC, measured under different DC-link voltages.	141
6.7. Spectra of the self-made AIC measured under different load conditions.	142
6.8. Spectra of the self-made AIC connected to the global protective earthing conductor and floating.	143
6.9. Combined EMI filtering concept on the system level.	145
6.10. Impedance of a single line inductor and four line inductors in serial.	146
6.11. Spectra of a self-made AIC with conventional EMI filters based on Y-capacitors connected directly after AIC and no EMI filter.	148
6.12. Spectra emitted by a self-made AIC without EMI filter and with a conventional EMI filter including a CMC directly on the input of AIC.	148
6.13. Spectra emitted by a conventional AFE from without EMI filters and with a standard EMI filter.	149
6.14. Spectra emitted by a conventional AFE with different EMI filter connected.	150
6.15. Spectra emitted by a conventional AFE with enhanced EMI filter connected.	150
6.16. Diagram of the test setup with a motor load.	151

6.17. Spectra emitted by an inverter on the DC side with diverse stray capacitance.	152
6.18. CM equivalent circuit of the test setup with a motor load.	152
6.19. Spectra of an inverter measured under different PWM frequencies.	153
6.20. Spectra measured under different load currents.	154
6.21. Spectra of an inverter measured for two types of switches with 150 ns and 120 ns switching time.	154
6.22. Impact of the protective ground connection on EMI spectrum emitted by an inverter.	155
6.23. Spectra emitted by an inverter on the DC side with EMI filters based on different topologies including Y-capacitors connected directly after the converter.	157
6.24. Spectra emitted by an inverter on the DC side with EMI filters based on different topologies including CMC on the CM main current path.	157
A.1. Graphical explanation of k_1 , dark blue area represents a merit figure for frequency dependent permeability.	164
C.1. Measurement setup of insertion loss.	169
C.2. Noise floor of the used network analyser.	170
C.3. Internal construction of the shielded box.	170
D.1. Measured DM impedance of the power grid measured in Darmstadt(Germany).	171
D.2. Measured DM and CM impedances of the active infeed converter with a line choke and an EMI filter	172
E.1. Design of EMI filter based on simplified analytical model.	174
E.2. Design of an EMI filter based on LTspice non-ideal model.	175
E.3. Design flow of EMI filter based on FEM	176
E.4. Flowchart summarizing proposed EMI filter improvement methods	177
F.1. Test bench used for measurements of permeability under saturation.	179
F.2. Structural diagram of the measurement setup of characterisation of permeability under saturation.	180
G.1. Inductance and inductive coupling coefficients.	182
G.2. Capacitance and capacitive coupling coefficients.	183
J.1. Hybrid choke.	193
J.2. Γ -filter with included hybrid choke and Γ -filter with a series connection of two chokes.	194
J.3. Comparison Γ -filter with a hybrid choke, T -filter with the same cores and number of turns, T -filter with a smaller choke.	195
K.1. Filter 1: Π -topology for both CM and DM.	198
K.2. Filter 2: Γ -topology for CM and a $CLCLC$ -topology for DM.	198
K.3. Filter 3: T -topology for CM and a $CLCL$ -topology for DM.	199
K.4. Filter 2 improved: T -topology for CM and a $CLCL$ -topology for DM.	200



List of Tables

1.1. EMI emission limits for different equipment classed according to EN61800.	22
3.1. Measured leakage currents of the drive systems with different PWM frequencies.	50
3.2. Parameters of filter models used for validation of the proposed modelling method.	59
3.3. Parameters of RLC-network for studied soft magnetic materials.	69
3.4. Values of components used for EMI filter simulation.	71
3.5. Parameters of the filters under test.	81
4.1. Characteristics of analysed parasitics compensation methods.	104
5.1. Parameters of capacitor connection types.	114
5.2. Summary of parameters for basic and enhanced filter topologies.	133
6.1. Summary of analysed AIC parameters influencing the EMI disturbances level.	147
6.2. Summary of analysed motor inverter parameters influencing an EMI disturbances level.	156
A.1. Parameters of different core materials used for tests.	165
B.1. Parameters of available on the market soft magnetic materials.	167
H.1. Summary of analysed self-parasitics compensation techniques.	186
I.1. Parameters of the filters under test (different capacitor connection types).	188
I.2. Parameters of the filters under test.	190
I.3. Parameters of filters with and without high frequency components based improvement applied.	192



Abbreviations and Symbols

Abbreviations

Abbreviation	Description
3D	Three Dimensional
AC	Alternated Current
AFE	Active Front End
AIC	Active Infeed Converter
BNC	Bayonet Neill Concelman Connector
CISPR	Comité International Spécial des Perturbations Radioélectriques (International Special Committee on Radio Interference)
CM	Common Mode
CNS	Chinese National Standard
CSR	Current Source Rectifier
DC	Direct current
DM	Differential Mode
DPC	Direct power control
DUT	Device Under Test
EMC	Electromagnetic Compatibility
EME	Electromagnetic Emissions
EMI	Electromagnetic Interference
EN	European Norm
EPC	Equivalent Parallel Capacitance
EPR	Equivalent Parallel Resistance
ESL	Equivalent Series Inductance
ESR	Equivalent Series Resistance
EU	European Union
FCC	Federal Communications Commission (USA)
FEM	Finite Element Method
GTO	Gate turn-off thyristor
HF	High-Frequency
HVDC	High Voltage Direct Current Transmission
IEC	International Electrotechnical Commission
IGBT	Isolated gate bipolar transistor
IL	Insertion loss
LISN	Line Impedance Sabilization Network

Continued on the next page . . .

Abbreviation	Description
MIL-STD	Military Standard
MOSFET	Metal Oxide Semiconductor Field Effect Transistor
PCB	Printed Circuit Board
PCC	Point of Common Coupling
PE	Power Electronics
PEEC	Partial Element Equivalent Circuit Method
PWM	Pulse With Modulation
QP	Quasi-Peak (detector)
RF	Radio Frequency
RMS	Root Mean Square
SMPS	Switched Mode Power Supplies
SRF	Self-Resonant Frequency
THD	Total Harmonics Distortion
UPS	Uninterruptible Power Supply
VNA	Vector Network Analyzer
VOR	Voltage Oriented Control
VSD	Variable Speed Drive
VSR	Voltage Source Rectifier

Symbole

Symbol	Description	Units
A_c	Cross-sectional area of a core	m^2
B	Magnetic flux density	T
B_{sat}	Saturation flux density	T
B_{tot}	Total magnetic flux density	T
\hat{B}	Peak excitation flux density	T
C_{cab}	Stray capacitance of the motor cable	F
C_{cap}	Stray capacitance of a DC-link capacitor	F
C_{choke}	Stray capacitance of the line inductor	F
C_{com}	Compensation capacitance	F
C_{conv}	Total stray capacitance of a PE converter	F
C_{DC-}	Stray capacitance of negative busbar	F
C_{DC+}	Stray capacitance of positive busbar	F
C_{EPC}	Equivalent parallel capacitance of CMC	F
C_{grid}	Stray capacitance of the grid side cable	F
C_{motor}	Stray capacitance of the motor	F
C_p	Parasitic capacitance	F
C_{sub}	Stray capacitance of substrate	F

Continued on the next page . . .

Symbol	Description	Units
C_{tc}	Turn-to-core capacitance of CMC	F
C_{tt}	Turn-to-turn capacitance of CMC	F
$C_{tt\text{--exact}}$	Exact turn-to-turn capacitance of CMC	F
$C_{tt\text{--simpl}}$	Simplified turn-to-turn capacitance of CMC	F
C_X	X-capacitance	F
C_{InvIn}	Stray capacitance of the inverter input	F
C_{InvOut}	Stray capacitance of the inverter output	F
C_{CabMot}	Total stray inductance of the cable and motor	F
C_0	Speed of light in vacuum	m/s
d	Diameter of conductor	C/m ²
D	Electric flux density	m
D_1	Diameter of a wire without insulation	m
D_o	Diameter of a wire with insulation	m
f	Frequency	Hz
f_{SRF}	Self-resonance frequency	Hz
f_{cutoff}	Cut-off frequency	Hz
E	Electric field strength	N/C
J	Current density	A/m ²
H	Magnetic field strength	A/m
H_c	Coercivity diameter of a core	A/m
h_c	High of a core	m
H_{ext}	External magnetic field	A/m
\hat{H}	Peak magnetic field strength	A/m
I_{cm}	Common mode current	A
I_{dm}	Differential mode current	A
I_{max}	Maximum common mode current for a given core	A
I_{sat}	Saturation current	A
i_u	Current of the phase U	A
i_v	Current of the phase V	A
i_w	Current of the phase W	A
$\bar{I}_{lk}(lg)$	Line to ground leakage current	A
$\bar{I}_{lk}(sg)$	Star point to the ground leakage current	A
k_{damp}	Coefficient of the damping resistor for compensation winding	-
k_{ex}	Material specific coefficient depending on specific domain wall energy	-
l	The main path length of a magnetic core	m
L_{CMC}	Common mode choke inductance	H
L_{core}	Inductive part of a magnetic core	H

Continued on the next page . . .

Symbol	Description	Units
L_i	Initial inductance of a CMC	H
L_M	Mutual inductance	H
L_s	Series inductance	H
L_{sat}	Remaining inductance after saturation of a CMC	H
L_{Cab}	Inductance of the cable	H
L_{CabMot}	Total inductance of the motor and cable	H
L_{InvOut}	Inductance of the converter ground cable at the output	H
L_{InvIn}	Inductance of the converter ground cable at the input	H
L_{LISN}	Main inductance of line impedance stabilization network	H
l_t	Mean-turn length	m
l_{wire}	Length of conductor	m
m	Mass	kg
M_s	Saturation magnetization	A/m
N	Number of turns	-
N_{com}	Number of turns for the compensation coil	-
N_{main}	Number of turns for a phase winding	-
p_h	Hysteresis losses	W
p_e	Eddy current losses	W
p_{ex}	Excess losses	W
p_{tot}	Total losses	W
r_{cin}	Outernal diameter of a core	m
r_{co}	Internal diameter of a core	m
R_{core}	Resistive part of a magnetic core	Ω
R_p	Parallel resistance	Ω
R_s	Series resistance	Ω
R_{wire}	Frequency dependent resistance of the wire	Ω
U'_0	Signal level across the load with filter installed	V
U_0	Signal level across the load without filter installed	V
U_s	Voltage of the source	V
U_{LG}	Line-to-ground voltages voltage	V
U_{SG}	Star point-to-ground voltage	V
W	Energy stored in solenoid	J
w	Magnetic energy density	J/m
Z_0	Load impedance	Ω
Z_F	Impedance of a filter	Ω
Z_S	Source impedance	Ω
Z_C	Impedance of a capacitor	Ω

Continued on the next page . . .

Symbol	Description	Units
Z_L	Impedance of an inductor	Ω
δ_{skin}	Skin depth	m
ϵ_0	Permittivity constant	F/m
ϵ_r	Relative permittivity of coating dielectric	-
λ	Wavelength	m
μ	Absolute permeability	-
μ''	Imaginary permeability	-
μ'	Real permeability	-
μ_0	Magnetic constant	H/m
μ_a	Amplitude permeability	-
μ_i	Initial permeability	-
μ_i	Initial permeability	-
μ_r	Relative permeability	-
$\underline{\mu}$	Complex permeability	-
∇	Curl operator	-
ω	Corner frequency	rad/sec
$\Phi(I_L)$	Magnetic flux	Wb
ρ	Conductance	S
ρ_c	Resistivity of core material	Ω
θ	Angle occupied by a winding	-
Θ^*	Intersection point of the two elementary capacitances	-



1 Introduction

Power electronics (PE) systems are widely used all over the world. There is a great number of applications for PE such as adjustable speed drives, electrical energy harvesting, uninterruptible power supplies (UPS), charging devices, inductive heating systems, high voltage DC transmission lines (HVDC), aircraft power supply systems, e-mobility, switched mode power supplies (SMPS), etc. The prevalence of power electronics converters is explained by a number of benefits and new opportunities compared with older, outdated systems. High efficiency (reaching 99%), high power density, perfect controllability, bidirectional power flow and low system costs are the main advantages of PE converters. The number of PE converters continues to grow with accelerating rates as the number of applications for PE converters also increases. [1, 55, 209]. Among the PE systems is a special group of converters called active infeed converters (AIC). They provide a power factor close to 1, and their harmonic damping capabilities stand out as a result of strict demands on efficiency and energy quality [91]. Despite the fact that AICs remain more expensive than passive rectifiers, the superior technical characteristics allow us to conclude that AICs are going to replace existing passive rectifiers in the near future. [113, 154, 194]. In contrast to classical passive rectifiers, AICs allow for improvement of local power quality, control DC-link voltage and achieve very high power density. However, AICs also exhibit some disadvantageous side-effects [231]. One of the greatest shortcomings of AIC is the high-frequency electromagnetic pollution. Unacceptably high levels of electromagnetic disturbances produced by PE converters can influence other electrical and electronic systems in the vicinity. In real installations, diverse PE converters have to be connected in immediate proximity to each other as well as to some other pieces of electronic equipment. Linked together through the power grid, those devices might negatively influence each other. Therefore the level of electromagnetic interferences (EMI) produced by PE converters has to be strictly limited. A classical approach to limit electromagnetic emission involves passive electromagnetic interference filters [155].

The main purpose of EMI filters is the improvement of the electromagnetic emission level exhibited by a PE system. To that end, an alternative term "electromagnetic compatibility (EMC) filters" can sometimes be employed [92]. An EMI filter together with a PE converter create a more reliable system with better electromagnetic compatibility and susceptibility. Apart from the utilization of EMI filters, there are some other methods that allow us to decrease EMI emission of PE systems, which are also applicable to AICs. These include:

- Implementation of soft-switching techniques for semiconductors [228];
- Utilization of advanced pulse with modulation (PWM) patterns for common mode voltage reduction [78, 80, 196];
- Various control strategies with minimized EMI pollution [17, 205]
- Different types of active filters [35, 37]
- Use of multilevel converter topologies

Nevertheless, in contrast to the use of EMI filters these measures do not guarantee a reduction of the produced electromagnetic interferences below a desirable level, especially in the MHz range. Therefore, EMI filters remain the most reliable solution in the majority of practical cases [203]. Tasks related to

EMI filter design are, as a rule, quite complex and demand understanding of two fields: electromagnetic compatibility and power electronics (Figure 1.1). A lack of competence in either of these two fields leads to the development of inaccurate mathematical models. It causes many problems at the prototyping stage, because damping of EMI filters predicted in simulations does not match with reality. For that reason, in some cases the design process of EMI filters is treated as a trial and error process [155], although there are a lot of attempts to structure this procedure [21, 64, 86, 132, 145, 165, 200, 204]. Most research projects focus on EMI filters for single-phase SMPS and the filters are considered as idealized components. This assumption may lead to a flawed design or to the aforementioned trial and error process. Therefore, the exact behavioural models reflecting all relevant effects influencing characteristics of EMI filters must be developed. Moreover, IL of EMI filters are strongly affected by load and source impedances. In the ideal case, a particular EMI filter has to be analysed together with a PE converter under realistic operation conditions. An EMI filter designed independently from a PE system can exhibit even worse IL than the IL predicted for the theoretical worst case scenario [97, 117, 220].

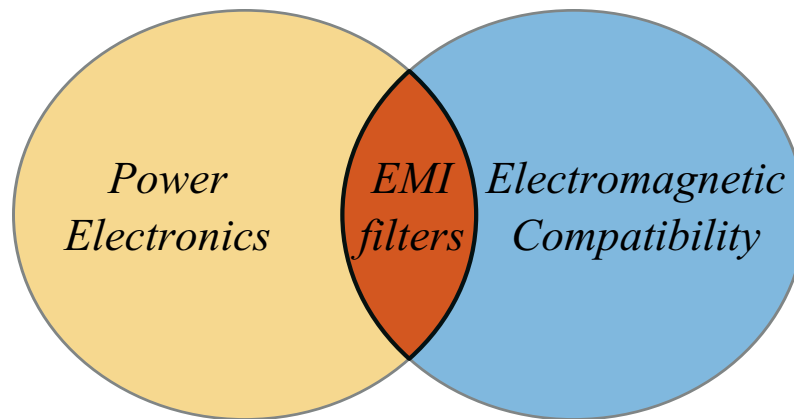


Figure 1.1.: Interdisciplinary allocation of EMI filters.

Typical EMI filter analysis involves separation of the interference types into common and differential classes [40, 70, 158, 211]. According to this approach, different noise propagation paths are analysed individually, so that the corresponding stages of an EMI filter are designed in accordance with the interference types, which they are intended to deal with [60, 65]. The same interference separation approach is used in this work.

An optimization in the field of EMI filter design is a compromise-finding process. There are two typical optimization tasks in the EMI filter design field. The first is to maximize the power density of an EMI filter, while minimizing its cost. The required IL and nominal current define boundary conditions for the optimization problem to avoid problems with overheating and core saturation. It is common to oversize EMI filters in order to be on the "safe side", but this safety comes at an additional cost. Moreover, an intended design of an oversized filter does not guarantee a fulfilment of the initial technical requirements. Obtained filter characteristics might be inappropriate due to unaccounted parasitics or mutual coupling effects between components which are growing with the size of components.

The second compromise has to be found between universal and sophisticated filter designs. A universal EMI filter can be used for all types of PE converters, but the power density and the cost are far from optimal. With a sophisticated EMI filter design approach, many different filters have to be designed and produced for specific PE systems. Each of the specialised EMI filters will have higher power density,

so that some costs can be saved. This approach requires adopting EMI filter IL for a particular PE converter.

Nowadays, a lot of companies offer PE converters for three-phase applications with comparable functionality, but completely different EMI spectra. From the point of EMI filter design it would be ideal if all existing converters have similar EMI spectra. The spectrum produced by a PE converter is affected by a large number of parameters beginning with a PWM frequency and ending with mechanical construction. Standardization of all available PE converters is not possible from both technical and marketing perspectives. Nevertheless, a design of specialised EMI filters for a group of converters selected by some particular attributes should be possible. For example, a topology of an AIC has the most significant impact on an EMI spectrum. Consequently, a specialised group of EMI filters can be developed for existing AIC topologies. Three-phase AICs can be further divided into several smaller groups in accordance with a control strategy, semiconductor parameters, utilized passive components, a mechanical design, etc. The number of specialized filters that has to be designed increases with the number of identified groups of converters. However, this approach can result in a nearly infinite number of different filters, which would increase both development and manufacturing costs. Therefore, parameters of a PE converter effecting the level of produced disturbances have to be ranked. It would allow assignment of converters to groups, in accordance with produced spectra. Then a specialised EMI filter can be used for the whole group of converters.

Future development of EMI filters should focus on higher integration with PE converters, i.e. including the filtering components and the power electronics converter on the same printed circuit board (PCB) or inside the same casing. This would allow for further optimization of EMI filters in order to achieve lower prices and higher power densities. [69, 111, 114]. Ultimately, the degree of integration of EMI filters into three-phase active infeed converters should reach the same level as in modern single-phase SMPS.

1.1 Power Electronics Converters

The key element of power electronics is a switching converter. Power electronic converters can be divided in four main categories according to performed power conversion type [167]. In a DC-DC converter a DC input voltage with a given amplitude is processed in order to obtain an output voltage with smaller or higher amplitude. An AC-DC converter, also called a rectifier, produces a DC output voltage from an input AC voltage. The amplitude of the DC output, as well as the current waveform input, may be controlled. The inverse conversion is performed by a DC-AC converter or inverter which controls an output current amplitude and frequency. AC-AC cycloconversion involves controlling of an input voltage to a given magnitude and frequency at the output [53]. Real devices are usually made by combining a few basic types of switching converters. For example, a typical three-phase frequency inverter for a motor control is a combination of AC-DC and DC-AC converters (Figure 1.2).

The heart of all PE converter are semiconductor devices [182]. Typically power semiconductors are operated in on-off or switching mode (in contrast to signal processing). Ideally a power semiconductor has a zero current in off-state and zero voltage drop in on-state. Power semiconductors such as insulated gate bipolar transistor (IGBT) or metal oxide semiconductor field effect transistor (MOSFET) have a vertical structure. Development of the power electronics applications is mainly driven by

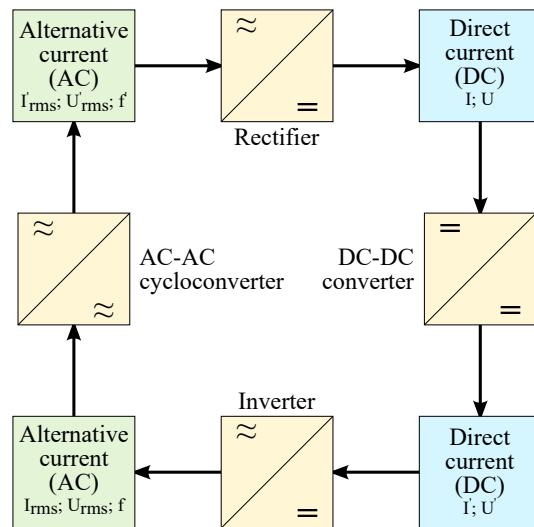


Figure 1.2.: Classification of power electronics converters [195].

an improvement of semiconductors. Nonetheless, passive components, especially power magnetics, are indispensable in power electronics systems and together can occupy up to 80 % of a PE system volume. Utilization of higher switching frequencies of semiconductors allows shrinking the size of passive components and consequently increasing power density, but it will generate a higher level of disturbances in the higher frequency range.

A classification of three-phase rectifiers, summarized from existing literature, is proposed in Figure 1.3. The simplest devices allowing AC-DC conversion are grid commutated unidirectional rectifiers, realised on power diodes. These rectifiers are particularly robust and reliable due to their simplicity. Shortcomings of this rectifier category are some undesirable effects on the power grid (high THD), unregulated output voltage and large filtering components (line inductors). Total harmonic distortion (THD) of diode rectifiers can be improved with employing of special phase-shifting transformers. It allows increasing the number of current pulses per grid period. These systems are typically used for high power applications; for instance rectifiers for aluminium smelters [195]. Diodes can be substituted by thyristors, so that the current supplied to the load can be controlled. However, improving of the power factor as well as more complex algorithms of DC-voltage control or harmonics compensation cannot be applied. The other properties of thyristor-based rectifiers are similar to diode-based rectifiers. All other rectifiers utilizing semiconductors allowing a forced turn-off (GTOs, IGBTs and MOSFETs) are called self-commutated. Self-commutated rectifiers are further divided into voltage source rectifiers (VSR) and current source rectifiers (CSR). Characteristics feature of the CSR are a fast dynamic response and a simpler topology compared to the VSR. CSRs are typically used for medium-voltage drives in the MW power range. VSRs have generally higher power density and consequently lower prices. Two last advantages lead to widespread VSR applications in power electronics. [19] VSR and CSR can be utilized in either unidirectional or bidirectional power flow. With regard to output voltage provided, rectifiers are classified as boost or buck. [174] Independent from an implementation type, AICs are superior from power density and efficiency points of view. Among AICs the most widespread topology is a classical two level three-phase active infeed converter [112, 184] (Figure 1.4). It has clear advantages in comparison with the other active rectifier's topologies such as simplicity, the smallest number of utilized semiconductors

and the lowest price [11, 17, 113, 187, 194]. AIC topology, together with utilized semiconductors, have the most significant impact on an EMI spectrum produced by a particular converter [222].

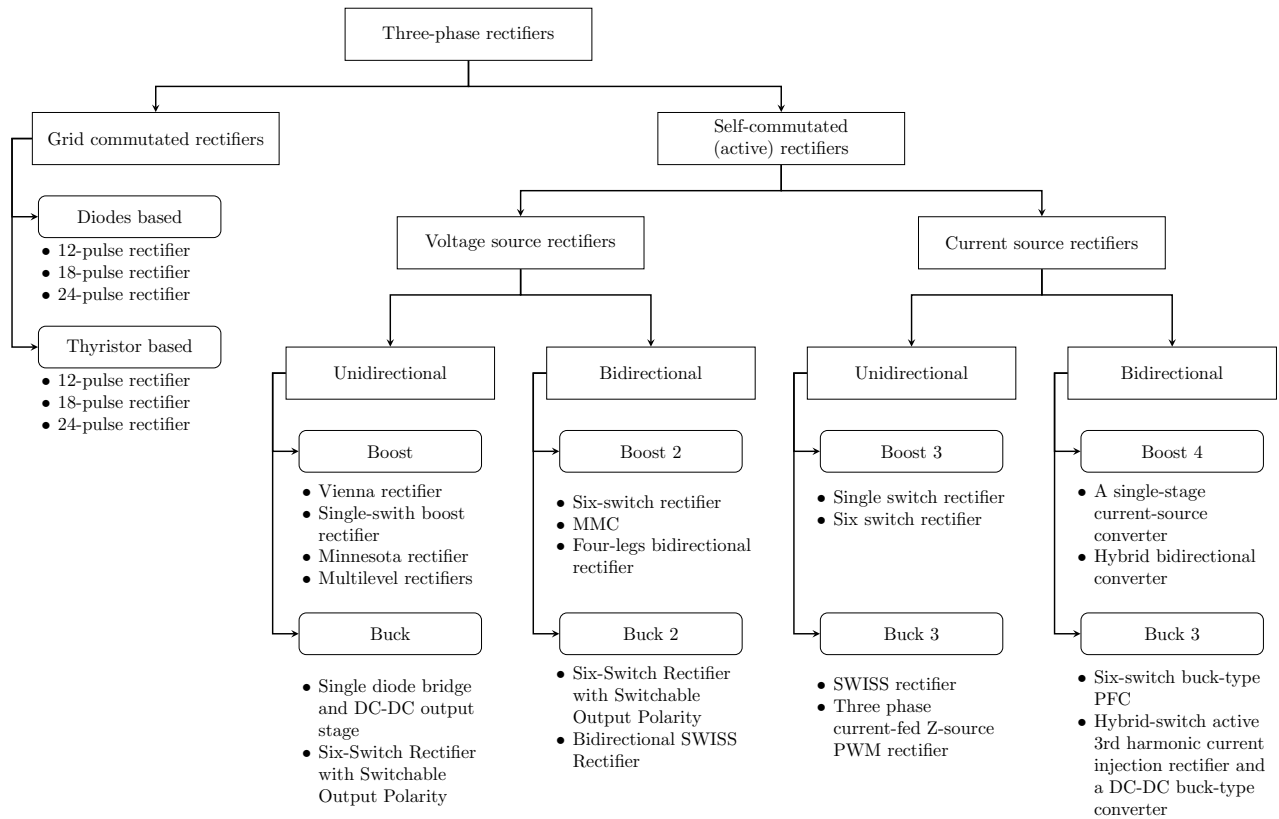


Figure 1.3.: Classification of existing rectifiers.

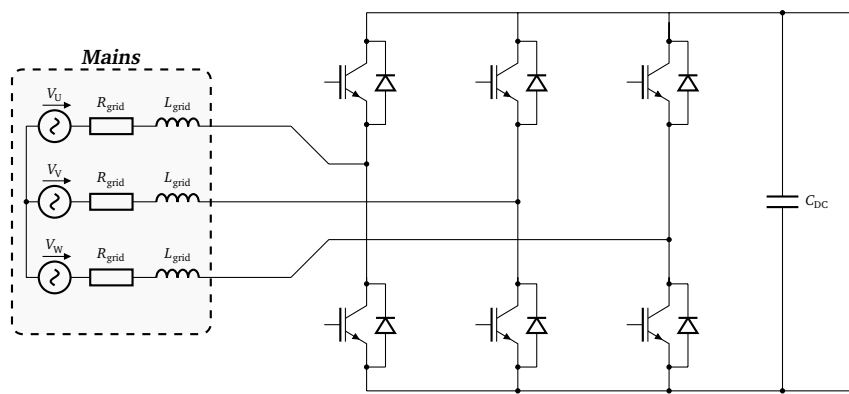


Figure 1.4.: Three-phase 2-level active infeed converter.

Control is an essential part of any power electronic systems. A typically controlled parameter is current on the output/input of a converter [53, 136]. DC voltage or a power flow can be controlled indirectly. A huge amount of different control methods starting from classical PI controllers and finishing with methods based on modern control theory (fuzzy logic, adaptive control, etc.) can be implemented in order to control a power electronics converter [17, 54, 105, 127, 175]. A classification of control methods

which are successfully utilized for self-commutated rectifiers control is proposed in Figure 1.5. Principles of rectifiers control are quite similar to principles of motor control. Rectifier control involves a power flow or DC-link voltage as the main controlled quantities. Voltage oriented control (VOC) and direct power control (DPC) are the most commonly used control strategies. The EMI spectrum of a particular AIC can vary in accordance with which control strategy is used. Figure 1.6 demonstrates spectrum of the same AIC under VOC and DPC. For a VOC, multiples of the switching frequency (4 kHz) are clearly seen in the produced spectrum. For a DPC there are no clear switching frequencies observed and a low frequency spectrum is spread out between 5 kHz and 20 kHz. A significant difference introduced in the spectrum requires considering a utilized control strategy during an EMI filter design [64, 71, 152].

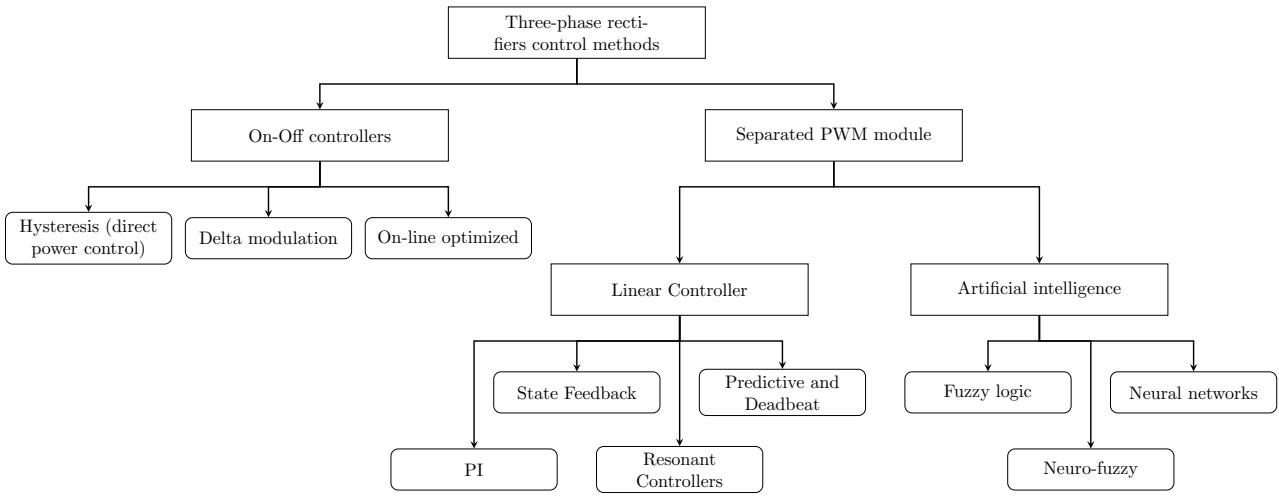


Figure 1.5.: Classification of control strategies suitable for rectifiers.

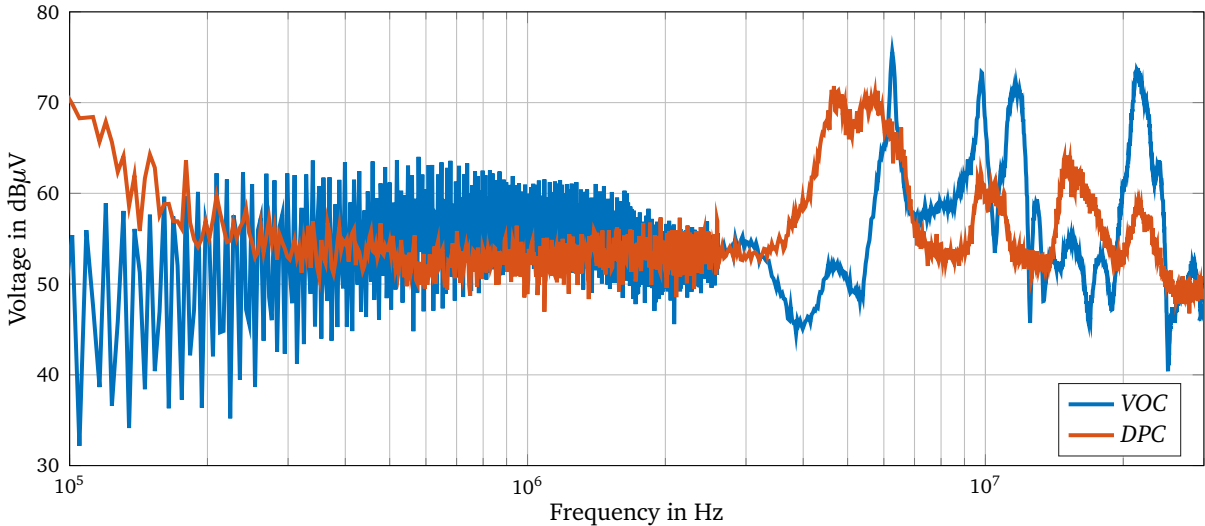


Figure 1.6.: Spectra of AICs operated under different control strategies.

While the fast switching semiconductors are the direct contributor to DM interferences, CM interferences are strongly affected by a utilized PWM pattern. In order to control phase currents of the three-phase two-level AIC, IGBTs switch between two voltage levels. An instantaneous phase current is

defined by an instant switching state of three half-bridges. In a classical space vector PWM a 0-vector is generated by a connection of a plus or minus DC-link terminal to all phases simultaneously so that a path for common mode current is created together with one of parasitic capacitors. A three-level PE converter topology makes it possible to avoid the need to use a plus or minus DC potential as a 0-vector, but requires two times more transistors when compared to a two-level topology. This topology also requires a connection of two capacitors in series to form of a middle point, hence it has a much higher price [184]. Nonetheless there is a number of special PWM patterns for a classical two-level AIC allowing the level of CM voltage to be reduced, such as active zero PWM, remote state PWM and near State PWM [80]. An EMI level is directly proportional to an amplitude of a CM voltage between a star point and the ground. Levels of CM voltages for different PWM patterns are depicted in Figure 1.7. From the diagrams on the right hand side can be seen that for all specialised PWM patterns a voltage between the middle point and the ground is $+\hat{V}_{DC}/6$ or $-\hat{V}_{DC}/6$ which is a factor of three less than for a conventional space-vector PWM.

A typical spectrum produced by a three-phase AIC is shown in Figure 1.6. As can be seen the highest amplitude of EMI is associated with side-bands of a PWM frequency and its multiples. Every next multiple of PWM frequency has 5 to 10 dBV smaller amplitude in comparison with the previous one. This dependency suggests that with higher PWM frequency the complete spectrum is shifted towards higher frequencies. Moreover with higher PWM frequency the spectrum is biased by several dB upwards. This means that in the future instead of PWM frequency harmonics of 20th-30th order, located in the EMI range (150 kHz–30 MHz), second or third PWM harmonics with much higher amplitudes are going to enter this EMI range. EMI filters with a cut-off frequency in the range 5 kHz–20 kHz and IL slope of -40 dB/decade are typically used today. For instance if the third PWM multiple has an amplitude equal to 0.5 V and IL of the EMI filter is -60 dB between 150 kHz–200 kHz. It would be insufficient for compliance with pollution norms requiring limitation of an interference level to 65 dBV at this frequency. In order to comply with the norms, required IL must be higher than -78 dB. It becomes obvious that IL of EMI filters in the frequency range up to 1 MHz must be improved due to growing switching frequencies utilized in PE converters. Additional filter stages and/or bigger values of capacitors and inductors could be used for achieving the required damping. Methods of EMI filter improvements are discussed in detail in Chapter 4.

1.2 EMI Issues in Power Electronics

In the field of electromagnetic compatibility all phenomena are handled from two perspectives: emission and susceptibility. In accordance with a propagation mechanism each of these electromagnetic phenomena are divided into conductive and radiative. Within this gradation EMI filters can be referred to a conductive emission group. It reflects the main purpose of an EMI filter to suppress emissions produced by one or more devices. In agreement with an interference gradation, provided by the international electrotechnical commission (IEC) (61000 standards group), different conductive phenomena such as flicker, harmonics, voltage fluctuations etc. [66] are added to the group of conductive interferences.

Besides conductive EMI, radiative phenomena also take place in power electronics. Therefore all parts of a power electronics converter have to be properly shielded. This task is usually fulfilled by the housing of a PE converter. After passing through an EMI filter high frequency conductive interferences

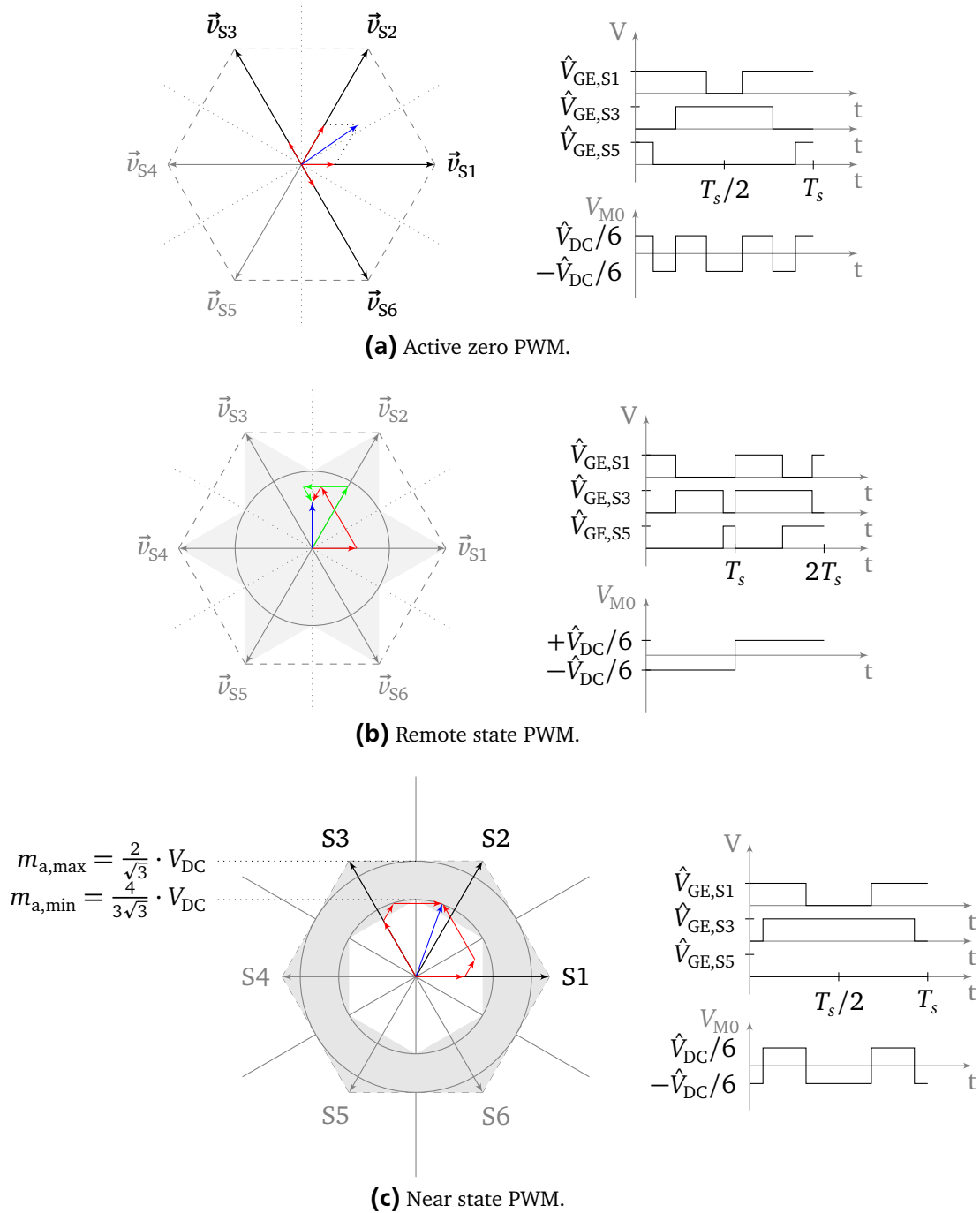


Figure 1.7.: CM voltage levels for different PWM patterns.

are attenuated and emission of the electromagnetic energy by cables should be reduced. Thus cables between a PE converter and an EMI filter should be kept as short as possible. All produced disturbances can be localized within a power electronics system by a properly selected EMI filter and good shielding.

Power electronics converters are based on switching of semiconductors between on and off states. In such way a particular voltage at the input of a converter can be transformed to any other specified voltage. For this conversion high voltages and currents have to be commutated with frequencies from several hundreds of Hz up to dozens of MHz. The switching process inevitably generates an extremely

high level of both radiative and conductive electromagnetic emission. A high level of produced EMI is one of the main disadvantage introduced by power electronics converters.

Power transistors do not switch instantaneously. For high power IGBTs the turning-on process takes several hundreds of nanoseconds. Slope rate of the given transistor can be adjusted via changing of the gate resistance. An overshoot which follows a switching event is influenced by the gate resistance as well. Longer switching time leads to a lower EMI level but higher power losses inside of a transistor and vice-versa. Thus a compromise between an EMI level and power losses for every particular situation must be found [221].

It is essential that the semiconductors used in a particular PE converter strongly affect produced EMI level. Nowadays Si-based semiconductors remain state-of-the-art in the majority of three-phase power electronics converters. Nevertheless GaN and SiC semiconductors are developing very rapidly [15, 41, 189]. Transition from Si-semiconductors to GaN and SiC may become possible if the system cost of the power electronics system based on wide-bandgap semiconductors becomes comparable with the Si-based system. The main feature of wide-bandgap semiconductors is short switching time. Turn-on time of commercial, currently available SiC 1200V MOSFETs lies in the range between 10 ns and 100 ns. For a comparison, turn-on time of a conventional Si-based IGBT is typically between 200 ns and 800 ns. [3, 176]. Consequently, PWM harmonics produced by conventional power electronics converters will be moved to higher frequencies with the spreading of wide-bandgap semiconductors. In this case IL in the range of 1 MHz and higher is going to become the main design criteria for EMI filters. Moreover fast switching of wide-bandgap semiconductors causes high $\frac{du}{dt}$ rates. Hence, requirements for EMI filter capacitors are going to be more strict with the utilization of SiC and GaN semiconductors.

Stray inductance of a busbar is going to become an even more critical parameter of GaN or SiC based PE converters [29, 30]. The voltage overshoot after transistors turn off is caused by stray components of the current path. The main contributors are the stray inductance of a laminated busbar and stray inductance inside of a power module. Together with the stray chip capacitance this stray inductance creates a resonant circuit with a resonance frequency in the range 1 MHz–100 MHz. These oscillations together with steep voltage and current slopes during the semiconductor switching process are some of the main causes of EMI problems within power electronics converters. [109, 221]. There are some special methods of busbar design allowing tangible reduction of the EMI level produced by power electronics [22, 202]. With a properly designed busbar, power density can be improved by speeding up semiconductor switching and utilizing the higher current rates [210]. Another method to reduce negative EMI effects introduced by the busbar parasitics is connecting a snubber circuit directly to the DC terminals of a semiconductor module that is in use. Capacitor-resistive snubbers are typically used [16]. Some other snubber options can be found in [221]. A snubber network is intended to mitigate an overshoot after a switching event. Energy stored in the overshoot dissipates in this case in the capacitor or resistor.

Separation of interferences into two categories in accordance with formation nature is usually used for conductive EMI analyses. Interferences can be either symmetrical or differential mode (DM) and asymmetrical or common mode (CM) [27, 34, 233]. The formation mechanism of those interference types differs significantly. Common mode EMI are caused by currents flowing in the same direction in

all conductors and a return path passing through the ground (1.1). Differential mode interferences are produced by current flowing in opposite directions in phase wires according to (1.2) [158].

$$i_{cm} = i_a + i_b + i_c \tag{1.1}$$

$$i_{a,dm} = i_a - i_{cm} = (i_b + i_c) - 2i_{cm} \tag{1.2}$$

Common and differential currents are explained with the example of a three-phase power electronics system (Figure 1.8). The switching of a power electronics converter causes production of both DM and CM interferences which are represented by corresponding voltage sources V_{DM} , V_{CM} . The direction of common mode currents is shown with red arrows and differential mode currents are shown in blue. From this equivalent circuit it is easy to see that measurements of the phase current represent a sum of DM and CM currents.

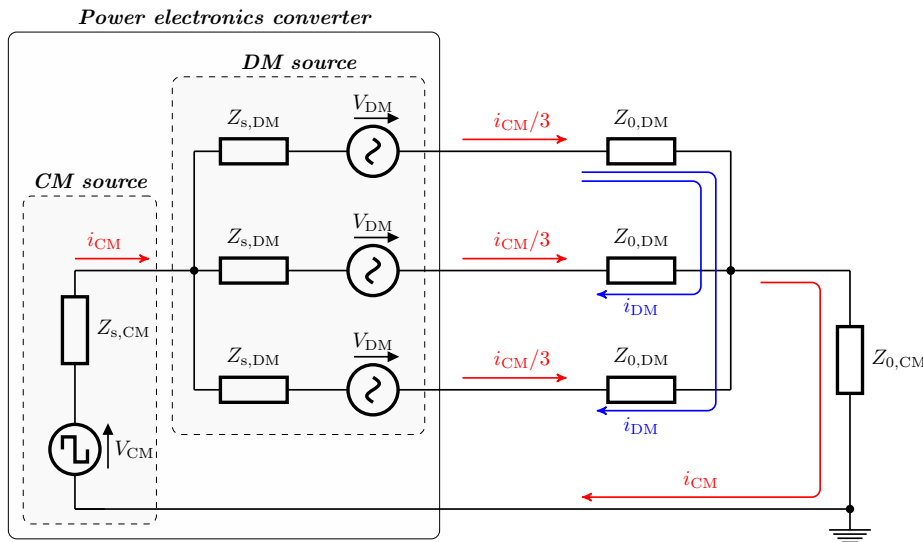


Figure 1.8.: Common and differential mode interferences in a three-phase system.

Since the path for DM currents does not differ from the path of the phase currents it is partially absorbed by the line choke and DC-link capacitor of AIC [60, 118]. Meanwhile a CM path is not affected by primary components of AIC; it is solely influenced by additionally introduced EMI filter impedance within this path. Therefore the majority of studies are focusing on the prediction and analysis of CM current paths [103, 106, 131, 144]. In order to create a closed loop for a CM current flow at least one stray capacitor within the whole drive system must participate in the CM current path. In figure 1.9 a typical variable speed drive (VDS) system including a load and a power grid is depicted. Within the VDS system several different parasitic capacitors between conductive parts of a PE converter and the ground can be isolated. C_{conv} represents a sum of the following stray capacitor types within a PE converter:

- Semiconductor substrate and a grounded heatsink(C_{sub});
- Laminated positive busbar and housing(C_{DC+});

-
- Laminated negative busbar and housing(C_{DC-});
 - DC-link capacitors and housing(C_{cap}).

The contribution of those three components can vary and depends mainly on the mechanical design. Capacitance between a heatsink and semiconductor's substrates (C_{sub}) is usually dominant [153]. Due to the specific structure of polypropylene capacitors, their stray capacitance against a housing is relatively high (several nanofarads for $2300\mu\text{F}$, 800V capacitors [44]). IGBT drivers may introduce some additional capacitance as well, though it is relatively small and can be neglected in the majority of cases. Impedance between the DC-link and the ground measured for a typical three-phase AIC ($1200\text{V}/600\text{A}$) is depicted in Figure 1.10.

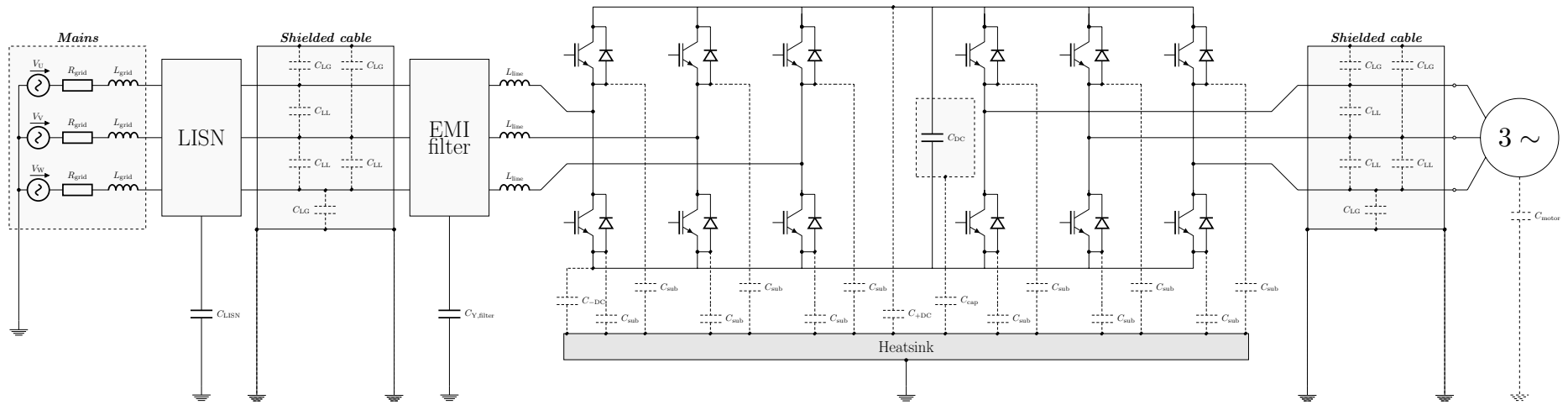


Figure 1.9.: A typical variable speed drive system with stray capacitors included.

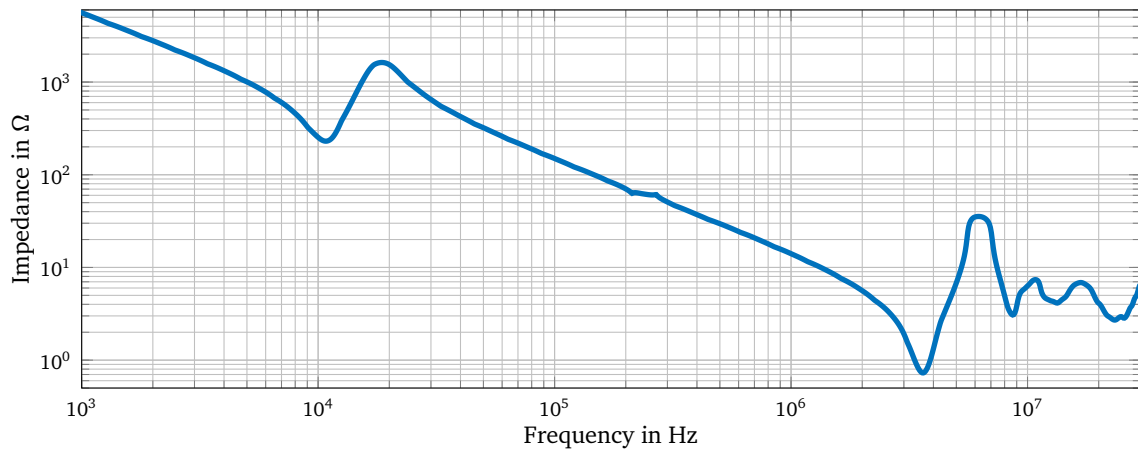


Figure 1.10.: CM impedance between AIC and the ground.

A load side of the drive system is represented by two stray capacitors between conductive wires of a motor cable and a shield (C_{cab}) and motor windings and a housing (C_{motor}). Except capacitance to the ground, cable wires are also coupled between each other. Due to these capacitive and inductive couplings a transformation of disturbances between DM and CM occurs. It can lead to formation of some additional CM currents inside of the cable. Load side stray capacitors together with C_{conv} form a CM current path on the load side. A grid side cable has the same capacitive effects as a motor cable C_{grid} . A line inductor has a core, which is typically grounded, hence stray capacitance C_{choke} participates in the forming of a CM path on the grid side. The middle point of a grid transformer is usually grounded, therefore CM current can close via a real ground wire [188, 232].

A widespread statement concerning dominance of CM disturbances at high frequency is not completely fair, especially for the grid side [62, 70, 158, 166]. The reason for this misconception is a grounded star point of a grid transformer and a long cable which form a perfect path for CM currents. Laboratory measurements show that CM currents have more significant contributions into overall disturbances level starting from a couple of kHz (Figure 1.11). Another reason for CM dominance over the whole EMI frequency range is the presence of the DC-link capacitor. Depending on the type of a DC-link capacitor it can quite significantly mitigate DM disturbances. Because its function is similar to X-capacitors, connected between paths of DM disturbances. A typical value of a DC-link capacitor is by the order of magnitude bigger than of a X-capacitor, therefore damping effects are also higher.

EMI filters can be placed between a power grid and a power electronics converter in order to eliminate EMI produced by AIC. CM current is shunted through filter capacitors to the ground so that a low impedance CM current path is formed. It does not allow passing of disturbances produced by a PE converter into the power grid. C_{choke} acts as an additional Y-capacitor of an EMI filter. An EMI filter decouples the PE converter from the grid, but the load remains affected by produced EMI. Surely, in order to eliminate EMI on the motor side, some additional filtering components (common mode chokes or EMI filters) can be included. In total six different common mode current paths exist within the VDS depicted in Figure 1.9. Determination of the contribution of the VDS capacitance into the overall CM path is a highly complex task. Attempt to localize any VDS component in order to measure CM current (impedance) in the particular branch leads to violation of the initial operation conditions. Consequently the conducted measurements or simulations do not reflect actual CM currents during a normal VDS

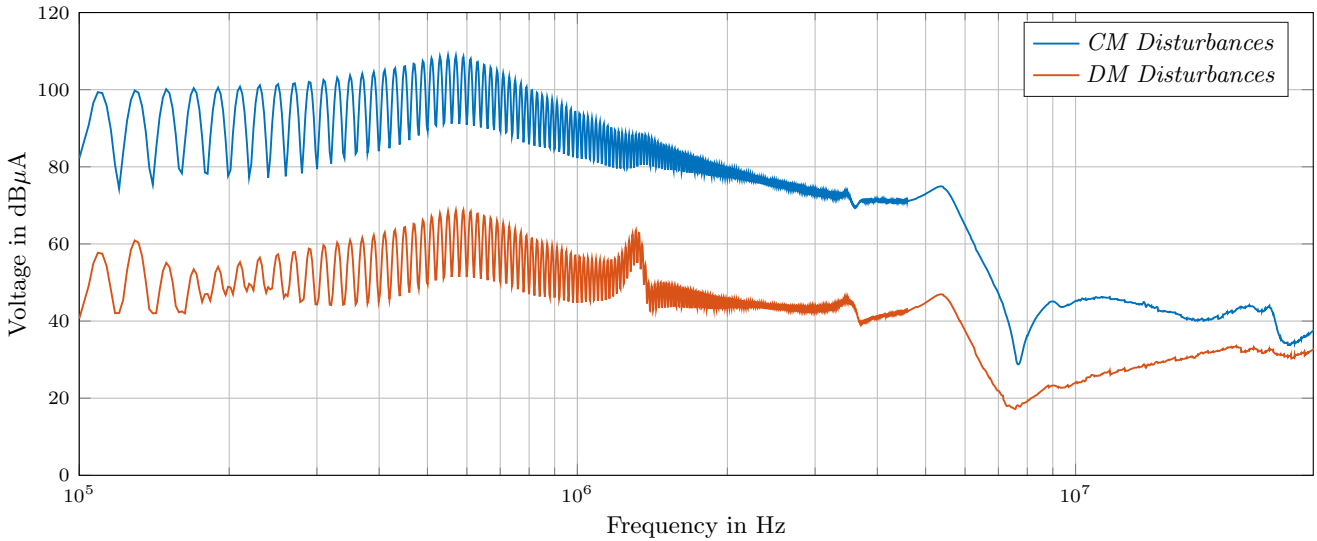


Figure 1.11.: Measured values of CM and DM disturbances of AIC with no EMI filter connected.

operation. Moreover, sharing of CM currents between VDS components can be affected by mounting or any changes in the ground connection. Nevertheless, information about it is extremely important for EMI filter design and also gives an opportunity to affect produced EMI levels during system commissioning.

A VDS depicted in Figure 1.9 can be further simplified in order to localize possible CM current paths through every component of a VDS (Figure 1.12). A source of CM disturbances is by definition located inside of the PE converter and connected to the ground via stray capacitor C_{conv} . At the load side CM current can be closed through stray capacitors of a motor C_{motor} and a motor cable C_{cab} . At the load side with no EMI filter connected, CM current flows through stray capacitance of the cable C_{cab} and the line choke C_{choke} to the ground and further toward other devices connected to mains. With an EMI filter connected, CM impedance of a power grid is increased and simultaneously an additional path for the CM current through Y-capacitors $C_{Y,flt}$ is organized. Consequently the amount of CM disturbances reaching mains significantly decreases.

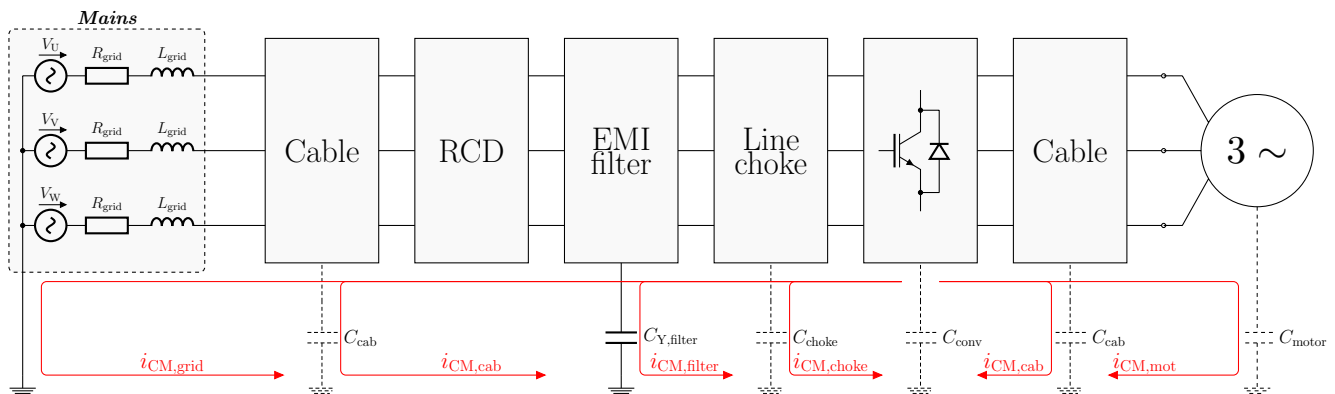


Figure 1.12.: Common mode paths within a variable drive system.

Apart from electromagnetic interferences, common mode current within a VDS can cause unintended triggering of residual current devices (RCD) [226]. Without actual faults in a system, phase currents in RCD are not compensated, due to the current which is shorted to the ground via stray ca-

capitors. Installation of EMI filters increases the leakage current of a VDS due to direct connection of conductive parts with the ground through Y-capacitors. It is usually achieved by utilizing smaller Y-capacitors and bigger common mode chokes (CMC). EMI filters with decreased leakage current are under active investigation and are already available on the market [178].

A CM current path together with a CM formation mechanism on the motor side of a three-phase drive system have been extensively investigated [56, 139, 140, 143, 169, 186, 223]. Within a motor, CM current phenomena is frequently referred to as a bearing current. There are four types of bearing current caused by utilization of power electronics inverters:

- Small capacitive bearing currents (usually considered not dangerous to the drive);
- Electrostatic discharge current (EDC) bearing currents ("Discharge currents");
- HF circulating bearing currents
- Bearing currents due to rotor ground currents.

The most significant is a circulating bearing current caused by stator to frame capacitance. This type of current is dominant in the frequency range from 100 kHz up to several MHz. A rotor ground current can also reach a few amperes even for small motors (11 kW). Frequency of these currents can reach only several 100 kHz [5] and usually it does not reach a standardized EMI range. However, a rotor ground current contributes into CMC saturation and has to be taken into account during CMC design.

1.3 EMI Filters

An EMI filter is a system presenting high impedance in a specified frequency range in order to provide sufficient insertion losses (IL) [155]. EMI filters have to minimize undesirable energy leaving an enclosure (emission) of a PE converter or entering it and causing an inappropriate operations (immunity). Nominally EMI filters have to deal solely with conductive interferences but radiated effects must be considered due to mechanisms of conversion between electromagnetic disturbance types [137]. A typical PCB based three-phase EMI filter with removed housing is shown in Figure 1.13.

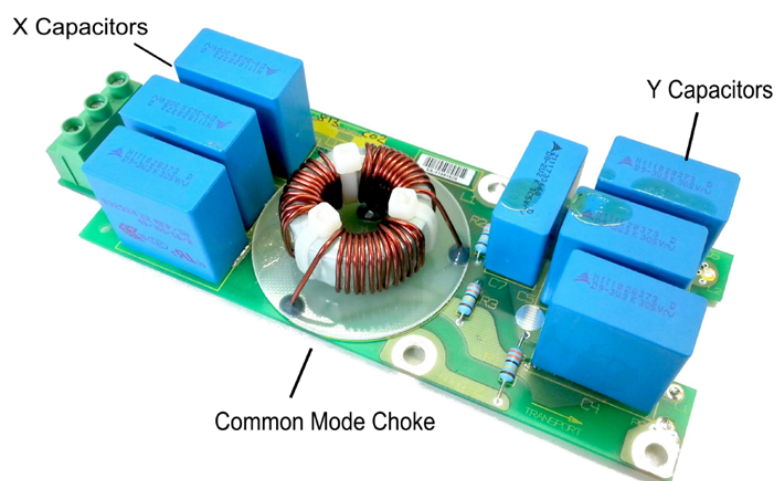


Figure 1.13.: A typical PCB-based EMI filter.

Insertion losses (1.3) is a conventional way to characterize EMI filters. IL by definition is a ratio between a signal level U_0 measured across the load of a test configuration without the filter installed and the signal level U'_0 with the installed EMI filter.

$$IL(dB) = 20 \cdot \log_{10} \frac{U_0}{U'_0} \quad (1.3)$$

EMI filter IL must be evaluated for attenuation of two interference types (CM and DM). Figure 1.14 shows a standardised measurement setup for an EMI filter IL characterization. At the first step an EMI filter is not included and the source voltage is divided between source (Z_S) and a load (Z_0) impedances. A voltage drop across the load without an EMI filter (U_0) can be easily found (1.4)

$$U_0 = \frac{Z_0}{Z_S + Z_0} \cdot U_S \quad (1.4)$$

In order to characterize CM IL of the three-phase EMI filter all inputs and outputs must be shorted and a filter is inserted in the measurement setup according to CISPR17/EN55017 [92] (figure1.14a). A voltage drop across a load $U_0(CM)$ with consideration of the included EMI filters is (1.5).

$$U'_0 = \frac{Z_0}{Z_S + Z_0 + Z_F} \cdot U_S \quad (1.5)$$

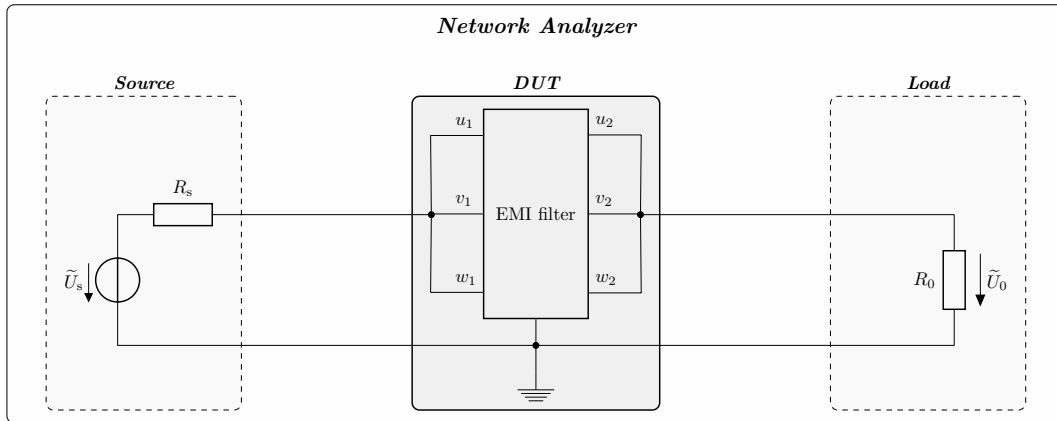
Thereafter IL of the EMI filter can be found as a relation between measurements with the filter U'_0 and without the filter U_0 . (1.6) is obtained by substituting (1.4) and (1.5) into the general equation (1.3).

$$IL(CM) = 20 \log_{20} \frac{U_0}{U'_0} = \frac{\frac{Z_0}{Z_S + Z_0}}{\frac{Z_0}{Z_S + Z_0 + Z_{F,CM}}} = \frac{Z_S + Z_0 + Z_{F,CM}}{Z_S + Z_0} \quad (1.6)$$

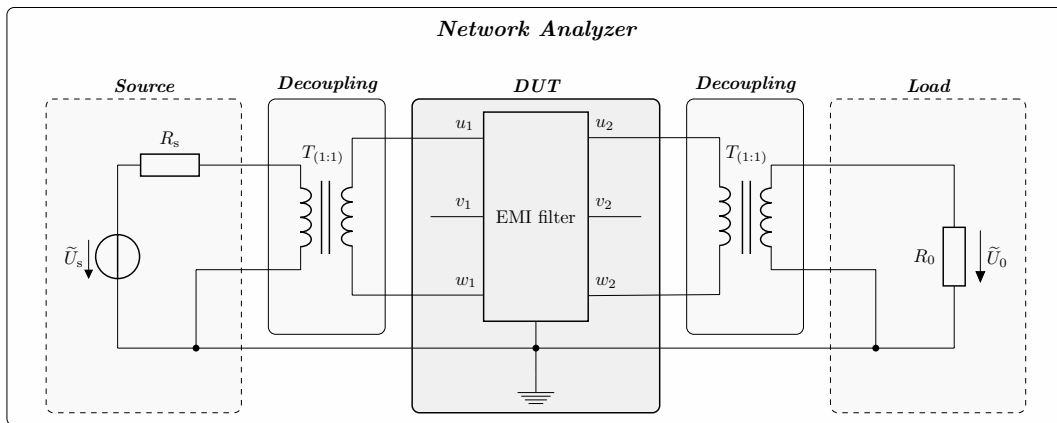
For a phase-to-phase DM filter IL characterization, additional decoupling transformers have to be used (Figure 1.14c). The transfer function of the transformers has to be as liner as possible in the frequency range of the filter characterization. Such connection allows the attainment of a close to the reality current path. During DM measurements the third filter terminal remains open.

$$IL(DM) = 20 \log_{20} \frac{U_0}{U'_0} = \frac{\frac{Z_0}{Z_S + Z_0}}{\frac{Z_0}{Z_S + Z_0 + Z_{F,DM}}} = \frac{Z_S + Z_0 + Z_{F,DM}}{Z_S + Z_0} \quad (1.7)$$

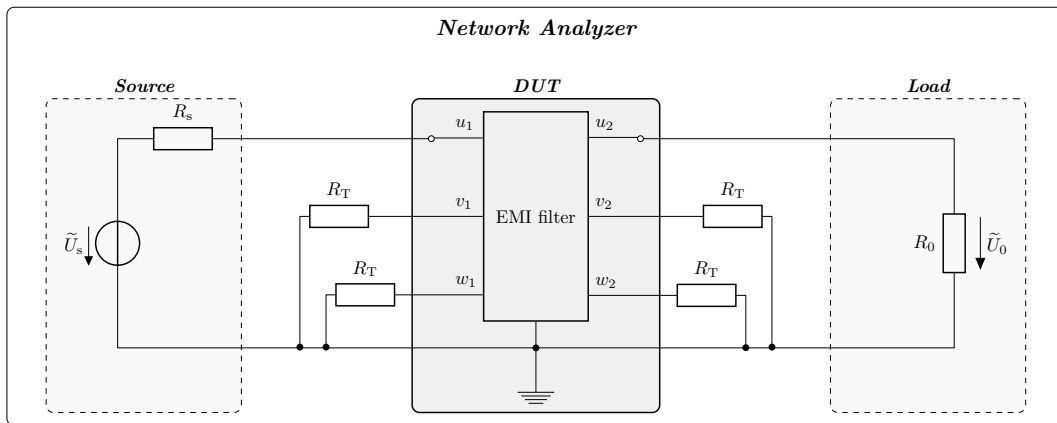
From (1.6) and (1.7) it can be seen that IL of a particular filter strongly depends on the source and load impedance. It must be emphasized that a filter characterization measurement setup is idealized. Standardized load and source impedance involved in EMI filter IL measurements allows the comparison of different EMI filters between each other but does not reflect a real IL demonstrated together with a particular power electronics converter.



(a) CM measurement setup.



(b) DM measurement setup.



(c) DM unbalanced measurement setup.

Figure 1.14.: Measurement setups for three-phase EMI filter characterization according to [92].

Four different topologies of EMI filters exist according to the classical circuit theory. All other types represent combinations of these basic topologies. The basic topologies are typically based on capacitors and inductors; resistors are rarely used due to high power losses [63, 199]. Figure 1.15 shows four types of filter topologies. T and Π topologies provide attenuation 60 dB/decade and LC and CL have 40 dB/decade. A topology of a filter has to be chosen in order to provide the maximal IL for the impedance combination exhibited by the particular system. With the series connection of several stages IL the dependency from load and source impedance diminishes. Moreover, multistage filters provide

higher IL rates. Components employed in a multistage filter can be smaller, so that the total power density of a filter can be improved. Despite these clear advantages multistage filters are not frequently used in three-phase PE converters due to the probable higher price of the filter compared to single-stage filters.

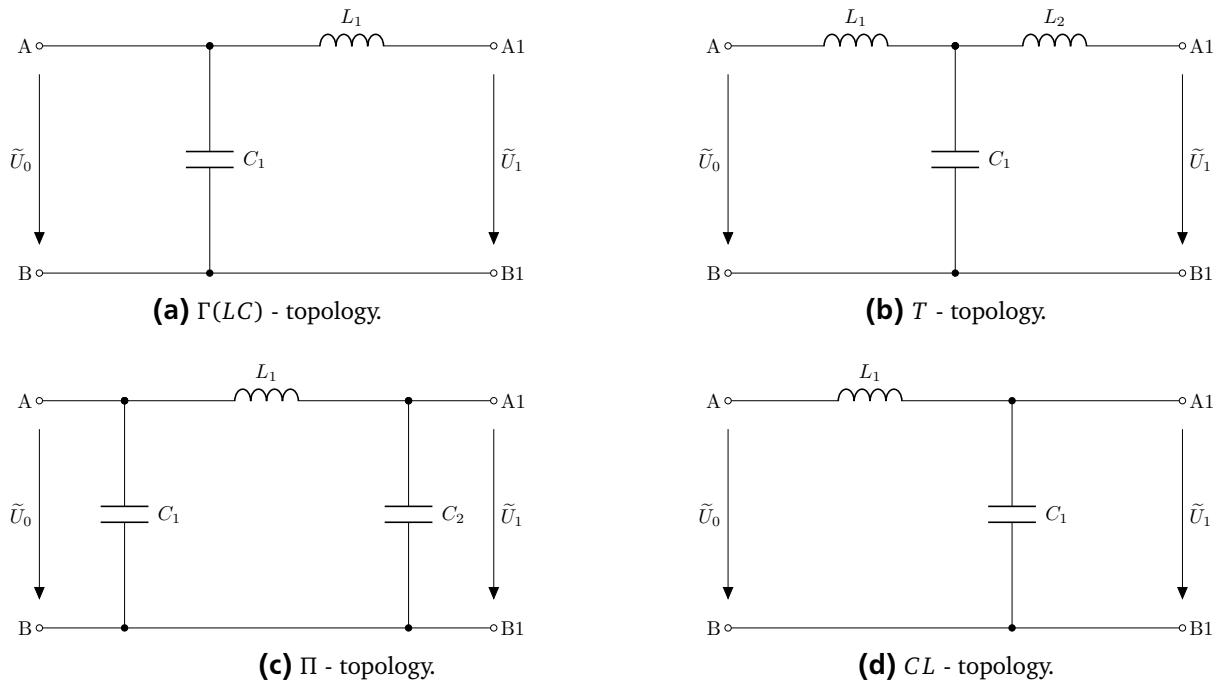


Figure 1.15.: Π , T , $\Gamma(LC)$ and CL filter topologies.

Common mode and differential mode IL exhibited by the single EMI filter installed in the PE system are not equal and should be adjusted separately according to CM and DM disturbance levels. Therefore, different filter topologies as well as component values have to be used for DM and CM damping. Typically for a power electronic converter CM impedance on the converter side is bigger than CM impedance on the grid side. For this particular case an LC configuration of a CM filter is suitable. DM signals see a PE converter as a capacitive load (DC-link capacitor in series with semiconductors) exhibiting low impedance. Hence DM filters should have a CL configuration. Since a single EMI filter must provide attenuation of both CM and DM disturbance, components responsible for attenuation of both disturbance types have to be included in the device. Figure 1.16 shows the topology of the conventional industrial three-phase EMI filter [179], where L_1 is a three-phase common mode choke. As seen from the name CMC is responsible for the CM interference attenuation. The windings of the CMC are coupled so that fluxes generated by DM currents are cancelled inside of the choke core and do not see its impedance while CM currents see the whole impedance of the CMC. Typical values of the CMC inductance are 1 mH – 10 mH. Characteristics of a CMC directly depend on utilized core material.

Capacitor C_{Y1} is called Y-capacitor. This type of capacitor is by definition connected between conductive parts and the ground. In this particular case it is placed between the star point and the ground. This arrangement is typical for three-phase EMI filters. CM noise sees the capacitor C_{Y1} in series with capacitors C_{XY1} , C_{XY2} and C_{XY3} . With this type of connection DM interferences are not affected by a Y-capacitor (it is true for ideally balanced phases). Values of Y-capacitors are limited by maximal leakage

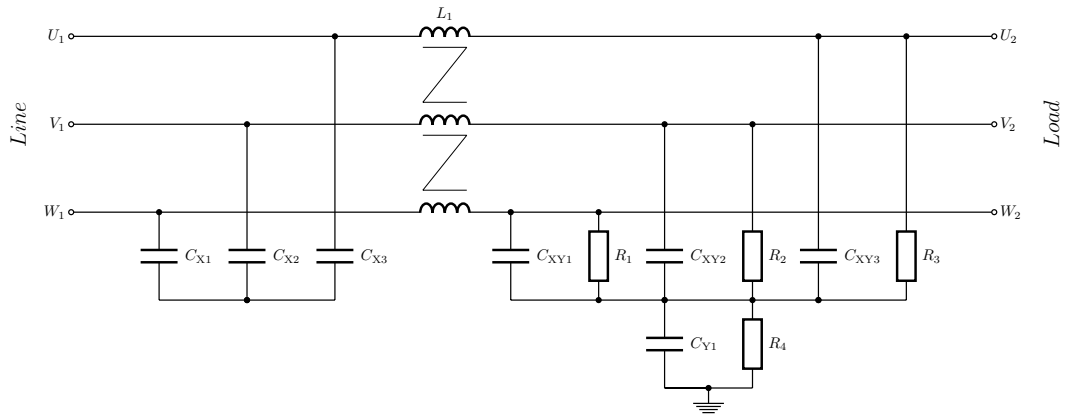


Figure 1.16.: Topology of a typical three-phase EMI filter.

current and typically do not exceed $3\mu\text{F}$. Capacitors C_{XY1} , C_{XY2} , C_{XY3} , C_{X1} , C_{X2} and C_{X3} are referred to as X-capacitors. The values of these capacitors are not restricted because of safety reasons (there is effect on leakage current). Alternatively, X-capacitors can be also placed directly between phases. In this situation nominal voltage of capacitors must be higher (400 V for low voltage applications). However, X-capacitors may affect a transfer function of a PE converter and create some resonance effects with grid inductance or with other PE devices connected to the same grid. Typical values for these capacitors lie in the range from $1\mu\text{F}$ up to $10\mu\text{F}$. Resistors R_1 , R_2 , R_3 and R_4 have no effect on IL of the filter. Their purpose is discharging of filter capacitors when voltage is removed.

The depicted Figure 1.16 topology does not include DM inductors due to non-ideal coupling between CMC windings which forms a leakage inductance. When DM currents flow in the winding some amount of flux remains uncanceled. Due to this leakage flux every winding demonstrates a small differential-mode inductance. A leakage inductance of CMC together with X-capacitors form a Π filter. However, the leakage inductance can lead to saturation of a CMC. For an analysis of an EMI filter DM and CM equivalent circuits have to be developed. Equivalent DM and CM circuits of the EMI filter depicted previously are shown in Figure 1.17.

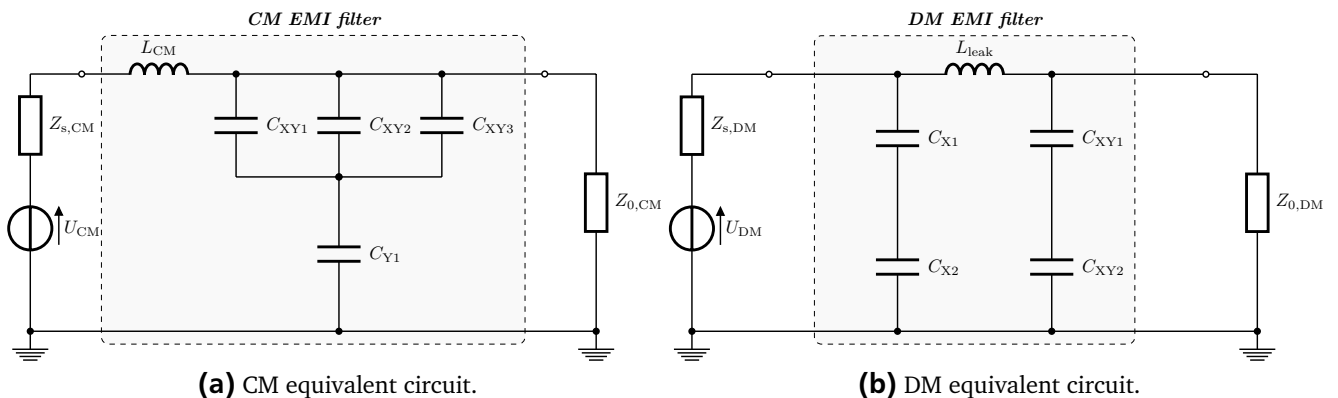


Figure 1.17.: CM and DM equivalent networks of the analysed EMI filter.

For an actual EMI filter design procedure, use of idealized filter components is as a rule insufficient. Real passive components used for a design of EMI filters have self-resonant frequencies (SRF). They are caused by parasitic parameters of passive components (ESL of capacitors and EPC of induc-

tors). Typically SRFs are located between 500 kHz and several MHz. SRF mainly depends on physical dimensions. Values of ESL and EPC normally lie in ranges 1 nH – 20 nH and 5 pF – 20 pF respectively. An example of CM, DM and unbalanced DM IL of a conventional EMI filter measured with a setup depicted in Figure 1.14 is demonstrated in Figure 1.18. Resonances caused by stray components can be clearly seen. The first resonance (45 kHz, unbalanced DM) is a consequence of an interaction between the main filter components. The second resonance (400 kHz, CM) is eventuated by a Y-capacitor and its ESL. The third resonance (1.2 MHz, CM) is between CMC inductance and EPC. As can be seen in the MHz range, IL is mainly determined by parasitics.

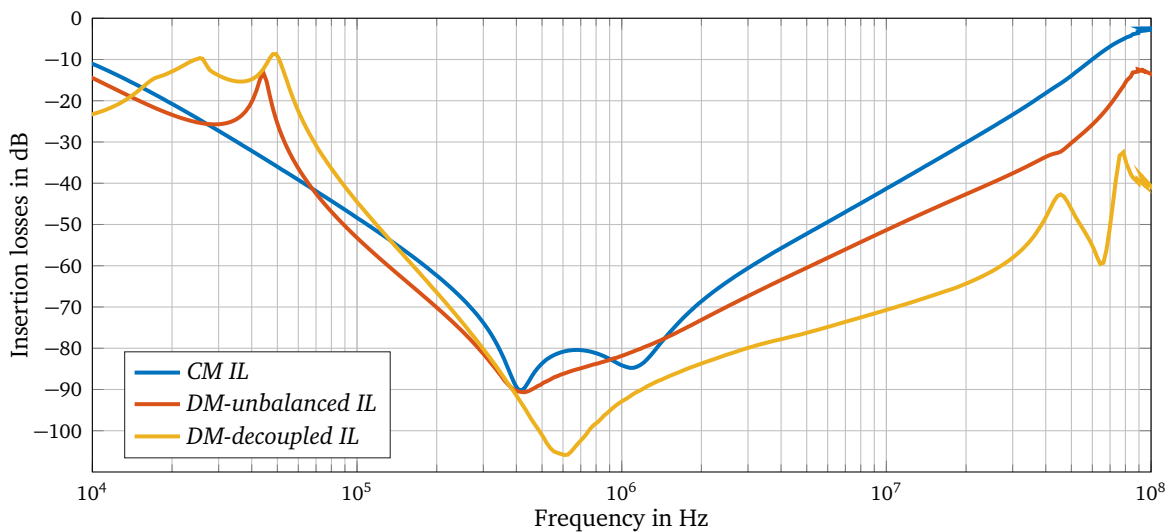


Figure 1.18.: CM, DM-decoupled and DM-unbalanced insertion losses of an actual EMI filter.

An additional important aspect indirectly related to EMI filters is mounting of the complete system. This includes a PE converter, an EMI filter, a load and cables. Inappropriate connection between an EMI filter and a PE converter significantly decreases filter effectiveness. There are three main rules how an EMI filter has to be mounted. Firstly, a filter must be located directly at the input of a PE converter. Secondly, a low inductance path must be provided between Y-capacitors of an EMI filter and the ground of the whole installation. Lastly, a capacitive coupling between the "clear" filter output and the "dirty" input must be minimized.

Different aspects related to an EMI filter design for a PE system can be found in the existing literature. In regards to filters for single-phase systems and for SMPS, much research has been completed. There is a vast body of literature available on the subject [4,10,36,40,42,115,124,129,142,155,170,190,218,219]. Authors deal with different aspects of filter design such as IL prediction and measurements, IL improvement, parasitics cancellation, elimination of mutual couplings, filter characterisation etc. From these works it can be boldly concluded that development of EMI filters is a quite complex assignment. Moreover, three-phase EMI filters are not so well investigated and plenty of scientific questions remain unanswered. There is no doubt that the issues related to three-phase EMI filters are even more complex and require detailed study and analysis.

1.4 Standards Overview

The first EMI were recognized as a serious problem in telecommunication more than a hundred years ago. At that moment development of the national and international standards institutions has began. Because of negative effects which can be caused by electromagnetic disturbances produced by a PE converter they have to be limited to acceptable levels. Therefore, a lot of standardisation committees have been constantly working on standards which establish maximum pollution levels for power electronics converters. The most influential of these are:

- International Special Committee on Radio Interference (International)
- Verband der Elektrotechnik, Elektronik und Informationstechnik VDE (Germany)
- European Committee for Electrotechnical Standardization (International)
- American National Standards Institute (US)
- Institute of Electrical and Electronics Engineers (International)
- International Electrotechnical Commission IEC (Internations)
- Federal communication commission (US)
- Radio Technical Commission for Aeronautics (International)
- China Electronics Standardization Institute (China)

A lot of the standards produced by those organizations are interlinking or even representing a translation from the language of origin. Such harmonization of standards all over the world gives the possibility of a free trade [110]. A good overview of existing standards with comments and applications is given in [137]. According to the general gradation of EMC standards the group called "high frequency conducted emission" is intended to deal with EMI filters-related issues. Besides the classification in accordance with their nature, interferences are also classified by frequency range [133, 203] (Figure 1.19). Division on conductive and radiated emission is entirely relative. It is obvious that above 30 MHz conductive emission does not dissipate and must still be taken into consideration. As can be seen from Figure 1.19, in the range from 2 kHz up to 150 kHz standardization committees have not come to consensus with industry and so it is not yet completely standardized. The majority of PE converters utilize switching frequencies in this range, therefore a standardisation of this range is very challenging. In EN 55011:2007 the following statement concerning the range is provided: "Limits for mains terminal disturbance voltages in the frequency band 9 kHz to 150 kHz are under consideration, except for induction cooking appliances". However, a compliance with standards in this range will be with high probability assigned to the future EMI filters with the extended frequency range. Because of the aforementioned reason and in order to conduct more detailed analysis of EMI filters the frequency range of interest in this work is chosen between 2 kHz and 100 MHz.

All methods of IL measurements independently from a power electronics system are described in CISPR17/EN55017 [92]. Equipment and methods necessary for disturbance testing of power electronics systems are mainly given CISPR16-1-2 [95] and IEC61000-4-6 [94]. As it is mentioned in the section 1.3, EMI filters are characterized in terms of IL. Necessary equipment and measurement setup for obtaining of DM and CM IL are also presented in CISPR17/EN55017 [92]. A measurement procedure for asymmetry between phases is given as well. In accordance with CISPR17/EN55017 the reference measurements have to be conducted with 50 Ω source and load impedances.

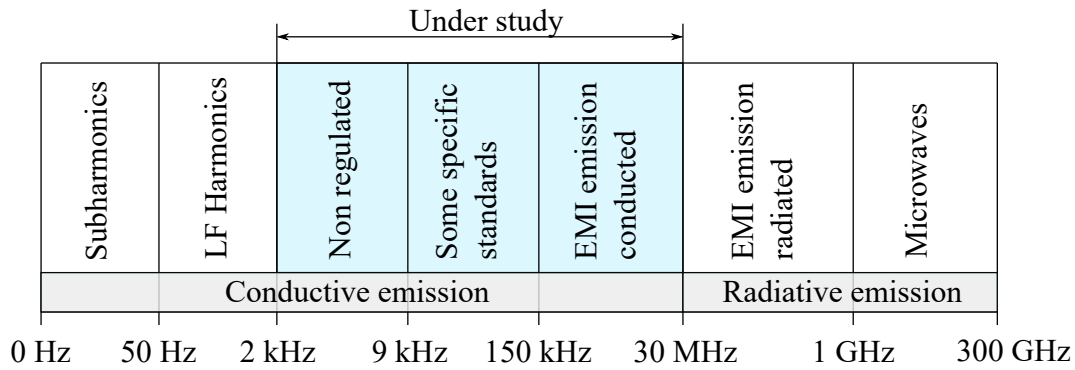


Figure 1.19.: Classification of electromagnetic disturbances by frequency.

General conductive emission limits are given in CISPR11 [96] and CISPR22 [90]. In CISPR22 two equipment classes are defined. Class B are equipment, devices and apparatus that are intended to be used in the domestic environment and meet class B emission requirements. Class A is defined as follows: equipment, devices and apparatus that do not meet the class B emission requirements, but comply with class A emission requirements. Emission levels given in FCC paragraph 15.107 and IEEE1560-2005 repeat the same disturbances levels as CISPR standards.

Special emission requirements for adjustable speed electrical drive systems are presented in IEC61800-3.2004. Drive systems are divided into four groups; categories C1 and C2 correspond to CISPR16; for categories C3 and C4 requirements are less strict. However those drives cannot be used in connection with the public electrical network. Allowed disturbance levels for adjustable speed electrical power drive systems according to EN61800 standard are shown in Table 1.1. Limits given by the most commonly used standards are summarized in Figure 1.20. The limits are designed for the general spec-

Equipment categories according to EN61800				
Frequency MHz	Category C1 (EN55022 Class B) dBuV	Category C2 (EN55022 Class A) dBuV	Category C3 I<100A dBuV	Category C4 I>100A dBuV
0.15 - 0.5	66-56	80-74	100	130
0.5 - 5	56	74	86	124
5 - 30	60	74	90-68	116

Table 1.1.: EMI emission limits for different equipment classed according to EN61800.

trum and do not deal with separation of interference types on common and differential modes, which is indispensable for a proper filter design.

As was mentioned before, Y-capacitors are connected between conductive parts of the EMI filter and the ground. Current through this capacitor is determined by the value of a capacitor and mains voltage and frequency. Worldwide requirements for the leakage current vary from 0.5 up to 5 mA depending on the application. For example, Underwriters Laboratory (UL) defines a 5 mA leakage requirement for most consumer products. In Europe the leakage current is defined by IEC60950-1 [93]. For stationary equipment it has to be lower than 3.5 mA. For hand held equipment leakage current limits are even more strict (0.75 mA) [99]. Consequently there is a maximum allowed value for Y-capacitors. Moreover, safety requirements affect the construction of Y-capacitors themselves [98]. In contrast with X-capacitors in the fault situation Y-capacitors must always become the open circuit. Otherwise conductive parts can

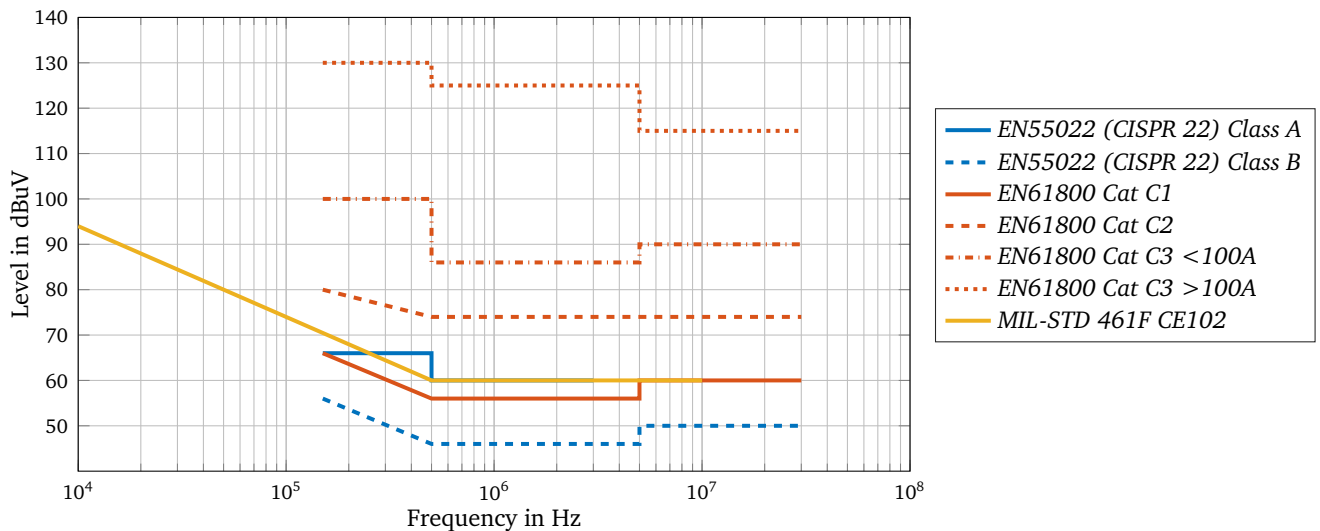


Figure 1.20.: EMI emission limits according to different standards

be shorted with the ground. According to this standard Y-capacitors can be used in position where a failure of the capacitor could expose somebody to dangerous electric shock. It means that safety standards indirectly affect an EMI filter's design and price.

1.5 Objectives and Outline of the Thesis

Within the frame of this thesis, issues directly and indirectly connected to EMI filter design and improvement are comprehensively studied. Analysis of EMI filters is conducted according to the principle "from simple to complex", starting from the simplest level of materials and components. Thereafter, EMI filters are treated within a system with idealized conditions (impedances of source and load are assumed to be 50Ω [92]). The impact of the reference impedance used for EMI filter characterisation on IL is investigated as well. Furthermore, the analysis of common and differential current paths inside of a conventional drive system is carried out. Eventually, EMI filters are considered at the system level. Moreover, behavioural models of EMI filters with different complexity are developed. Current filter improvement methods are systematized and complemented. Novel improvement possibilities are proposed. The objectives of the work can be summarized under the following points:

1. Comprehensively study three-phase EMI filters; collect and structure knowledge about this subject; create methods and models permitting accurate anticipation of IL without indispensable filter prototyping.
2. Develop methods of EMI filter improvement and adopt existing methods to three-phase EMI filters. Determine possible limits of improvement methods and create recommendations for which method should be employed for which application.
3. Define the degrees of freedom for IL improvement introduced by multistage or ladder EMI filters. Investigate technical characteristics of different filter topologies. Conduct a comparative analysis of various filter types not only from a performance point of view but also considering price, power density and realization complexity.

-
4. The final objective is to demonstrate how variation of PE system parameters effects the emitted EMI spectrum. Moreover, to show impact of PE system parameters on EMI filter design and investigate how filters with different topologies can cope with such changes.

The last two aspects are especially complex and comprehensive study of them is beyond the scope of one work. Therefore, these issues should be addressed in future scientific works.

Components of EMI filters are discussed in Chapter 2. For several reasons, the main attention is focused on magnetic materials. Firstly, magnetic materials are used as a base for CMCs, which have a crucial impact on power density and costs. Secondly, characteristics of soft magnetic materials are highly nonlinear. Lastly, there is a lack of information in current literature where soft magnetic materials are critically compared with the main focus on EMI filters. A background for further development of mathematical models of EMI filters is prepared in Chapter 2.

Several mathematical models for EMI filters with different exactness and development efforts are proposed. Factors affecting filter performance are explicitly studied in this thesis and the relevance of these factors is estimated. Every factor is sequentially included into the mathematical model of an ideal EMI filter. Particular attention is paid to mathematical modelling of CMC core materials and analysis of non ideal properties demonstrated by magnetic materials on filter IL. Exactness of developed mathematical models is confirmed with measurements of built prototypes. In such a way, significance of every non-ideal parameter on IL can be assessed. Irrelevant effects are precluded from simulation in order to accelerate modelling, allowing achievement of the desirable accuracy with adequate time costs. The most significant physical phenomena are discussed in detail. The complexity of these experiments is gradually increased, so that an optimum balance between a sufficient exactness level of a mathematical model and necessary development efforts can be chosen for every particular situation. Benefits and shortcoming of different EMI filter simulation methods are described. Maximum achievable accuracy is demonstrated for all developed mathematical models (Chapter 3).

After preparation of behavioural models and design methods for EMI filters, the main focus is switched towards design of enhanced filter topologies and systematized improvement of conventional filters. Possible degrees of freedom for IL improvement are analysed in detail. Frequency limits and the maximum possible enhancement of IL are identified. Reasons causing these limitations are explained from a physical point of view and discussed. Theoretical background of each improvement method is presented with a focus on parasitics compensation. Different combinations of improvement methodologies are applied to reference EMI filters and tested. Comparative analysis of designed EMI filter prototypes with implemented improvement measures and reference EMI filters is conducted. The most relevant physical phenomena affecting IL are reviewed and combined with the most efficient improvement methods (Chapter 4 and Chapter 5).

Necessary conditions for design of high performance EMI filters are discussed in Chapter 5. There, methods allowing the development of an EMI filter with initially superior characteristics (compared to conventional ones) are proposed. Possible connection types of filter capacitors are analysed, with the focus on improvement of power density and high frequency IL. Comprehensive analysis of multistage filters is conducted with four main points: performance, power density, costs and development complexity. Some options allowing high frequency IL enhancement with utilisation of additional high frequency components are proposed. All enhanced prototypes are compared with conventional filters. Issues related

to core material selection are addressed and systematized. Prognoses of future EMI filter development based on achieved results are made.

Parameters of power electronics systems and their impact on emitted disturbances are analysed in Chapter 6. Effects of PWM frequency variation, semiconductor switching speed, dead time, load current and other converter parameters are evaluated. Changing of some parameters has considerable influence on the emitted EMI spectrum, and consequently, on the EMI filter design. Spectra emitted by an AIC and a motor inverter are measured with different EMI filters. Comparative analysis of performance exhibited by the major EMI filter topologies is evaluated. Effects caused by utilization of diverse topologies are exposed and discussed.



2 EMI filter components

Quality of designed EMI filters is directly dependent on the employed components. Utilization of high-performance components helps to improve filter characteristics substantially. In this chapter a detailed analyses of EMI filter components is given.

The highest degree of freedom in EMI filter design is given by inductive components. Development of inductive components, such as CM and DM chokes, is usually included in an EMI filter design procedure. A number of turns, a winding type including mechanical layout, a type of the core material, a number of winding layers etc. can be adopted in order to achieve specified characteristics. In contrast with inductive components, capacitors are typically purchased, so that a designer cannot considerably influence their characteristics. Therefore, the main attention of the analysis in this chapter is focused on inductive components and soft magnetic materials suitable for EMI filters. Analysis of properties of soft magnetic materials is conducted with the main purpose estimating of existing material restrictions in the inductor design.

An overview of capacitor types employed in EMI filters is made. The main parameters of capacitors are described and analysed. Resistors are not discussed due to their insignificant impact on EMI filter IL. However, resistors are used in EMI filters for two main purposes: damping of resonances and discharge of capacitors. This chapter prepares a background indispensable for further development of EMI filter behavioural models and investigation of improvement methods. Impact of non-ideal parameters of utilized components on EMI filter IL is discussed as well.

2.1 Soft magnetic materials

There are four main types of soft magnetic materials suitable for design of inductive components used in EMI filters. Those are ferrite, nanocrystalline, amorphous and powder materials. Ferrites are used in EMI filtering applications most frequently. This is mainly because of the price of ferrite cores, which is the lowest comparable with the other materials. A wide diversity of ferrites with parameters suitable for both common and differential mode inductors is available. Nanocrystalline and amorphous materials consist of the thin type winded in a form of toroids and stadiums. This production technology is relatively expensive and thus causes the high price of cores based on these materials. Amorphous materials, which consist of cobalt are even more expensive due to the high price of cobalt itself. However, in some applications utilization of more expansive nanocrystalline or amorphous chokes leads to lower system costs. Permeability exhibited by the last two materials groups lies in the range 5000-1000000 units, hence they are perfectly suitable for CM inductors but cannot be efficiently used for DM inductor design. Specific properties of powder cores (soft saturation and low permeability) make them the best choice for DM inductors. The price of powder cores is also higher comparable with ferrites. Existing types of soft magnetic materials together with some popular trade marks are summarized in Figure 2.1. A more detailed description of every group is given hereafter. Laminated steel is not included in this classification and neither is permalloy. This is because they have an operational frequency range which is bellow 150 kHz [84].

Soft magnetic materials for EMI applications

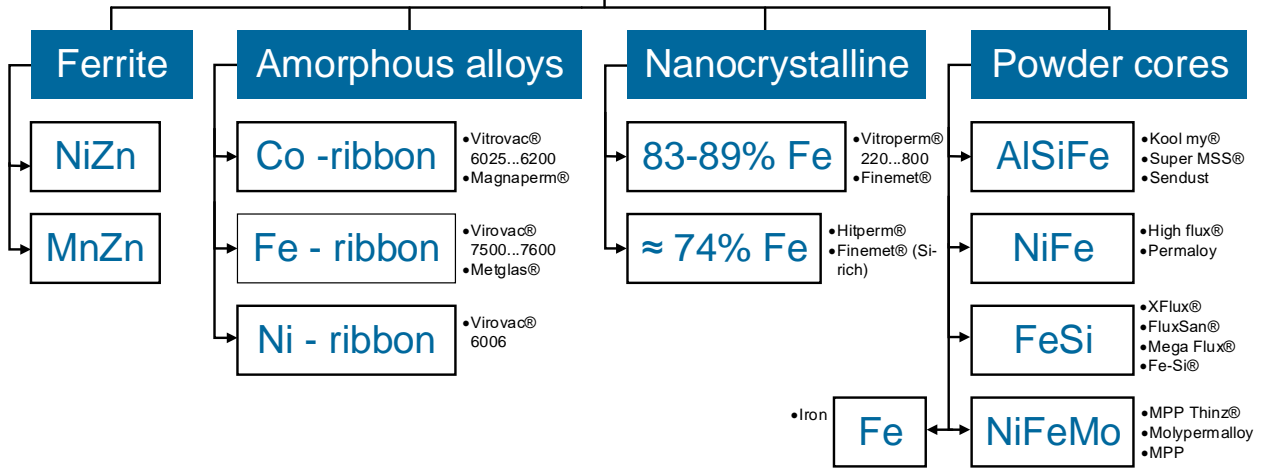


Figure 2.1.: Classification of soft magnetic materials suitable for EMI filter applications.

The following set of parameters is used for soft magnetic material comparative analysis.

Permeability or absolute permeability μ can be called the most important parameter of magnetic material. It characterizes the ratio between magnetic flux density B and magnetic field strength H

$$\mu = B/H. \quad (2.1)$$

Four types of permeability are commonly used: relative permeability μ_r , amplitude permeability μ_a , initial permeability μ_i and complex permeability $\underline{\mu}$.

- Relative permeability μ_r is defined as a ratio between magnetic constant μ_0 and absolute permeability μ

$$\mu_r = \frac{\mu}{\mu_0} = \frac{1}{\mu_0} \frac{B}{H}. \quad (2.2)$$

- Amplitude permeability μ_a is determined by the slope of the straight line extending from the origin to any point of the hysteresis curve.
- Initial permeability μ_i is described as the amplitude permeability μ_a for a relatively small magnetic field strength. This permeability is typically given in datasheets.

$$\mu_i = \lim_{H \rightarrow 0} \mu_a. \quad (2.3)$$

- Complex permeability $\underline{\mu}$ is used to characterize magnetic materials by analogy with general electrical engineering. The complex permeability comprises of a real and an imaginary part $\mu = \mu' - j\mu''$ [26]. At the high frequency the eddy currents and the magnetic losses in the core material give

rise to the phase shift between H and B . On low frequencies permeability is a real number, and consequently vectors of H and B are in phase. At high frequency the phase shift increases together with the angle between H and B . Complex permeability describes all types of core losses. Both parts of the complex permeability for a given core are expressed based on the frequency dependent resistor and inductor (2.4) and (2.5) [74].

$$\mu'(f) = L_s(f) \left(\frac{l}{\mu_0 h_c N^2 \ln\left(\frac{r_{co}}{r_{cin}}\right)} \right), \quad (2.4)$$

$$\mu''(f) = R_s(f) \left(\frac{l}{2\pi f \mu_0 h_c N^2 \ln\left(\frac{r_{co}}{r_{cin}}\right)} \right), \quad (2.5)$$

where L_s and R_s are series inductance and resistance, μ_0 is a permeability constant, N is a number of turns and h_c , r_{co} and r_{cin} are geometrical parameters of a core. As seen from (2.4) and (2.5) permeability is frequency dependent. Equation (2.4) and (2.5) are used for recalculating real and imaginary parts of impedance obtained from measurement of a choke based on 40x24 core from EPCOS [48]. Frequency dependent permeability of this core is depicted in Figure 2.2.

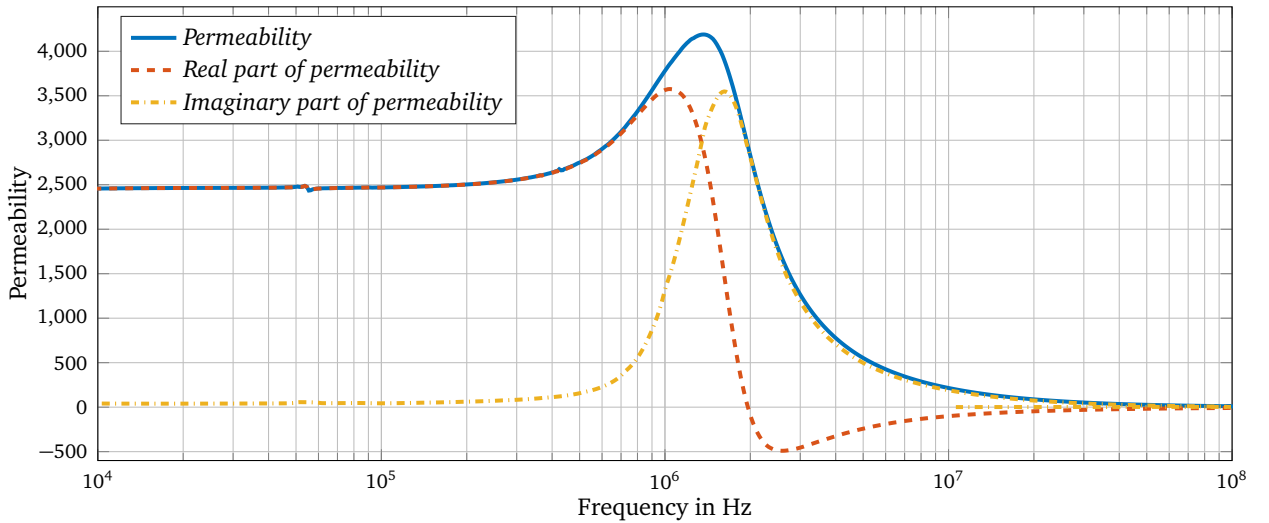


Figure 2.2.: Frequency dependency of real and imaginary permeability for a typical ferrite.

Saturation flux density (B_{sat}) is equivalent to saturation magnetization M_s . This is the state reached when applied external magnetic field H_{ext} cannot increase the magnetization inside of the core further. Together with permeability the saturation flux density defines maximum power density of a core. The trajectory of material magnetization is called hysteresis. It represents a hardy nonlinear process caused by magnetic friction inside of a core. Hysteresis modelling is a common task in material science. Some methods which can be used for consideration of saturation during EMI filter modelling are discussed in Chapter 3.

Power loss is the most complex parameter due to the diversity of physical processes causing it. It is directly related to coercivity (H_c) and operated frequency. Power losses are typically calculated for one magnetization cycle; during this cycle some energy is consumed. This energy is provided by the external field and transformed into heat inside of a magnetic material. The total power losses are comprised of hysteresis, eddy current losses and excess losses. An additional loss group which is not always included into excess losses is magnetostriction loss, caused by magnetostriction phenomena (this can be a reason for core "whistle") [207].

Hysteresis losses (p_h) include the energy used for rotation of magnetic moments of the core. It is important to notice that hysteresis losses correspond to the area enclosed by the static hysteresis loop (hysteresis measured under DC conditions). The larger the area of the hysteresis, the higher the hysteresis loss. Generally, hysteresis losses per mass m are described as (2.6)

$$p_h = \frac{4f H_c \hat{B}}{m}, \quad (2.6)$$

where \hat{B} is peak excitation flux density, f is the frequency of the excitation signal (sine in this case) and H_c is coercive force. Volumetric hysteresis power losses in W for the case of B-H curve simplified to a rectangular and with the operation point at the origin, according to [104] can be found as (2.7)

$$p_h = 4f \mu_0 \mu_r \hat{H} = \frac{4f \hat{B}^2}{\mu_r \mu_0}. \quad (2.7)$$

Eddy-current losses p_e are caused by circulative currents flowing within a core. A changing magnetic field induces voltage which causes these currents. Consequently these losses increase with frequency. The higher the resistivity of the core material, the lower the eddy-current loss. For sinusoidal excitation voltage within a toroid core eddy-current losses can be calculated as (2.8) for the skin depth δ_{skin} much bigger than h , which is a case for a considered application

$$p_e = \frac{\pi h_c f^2 \hat{B}^2 \ln\left(\frac{r_{\text{co}}}{r_{\text{cin}}}\right)}{4\rho_c} \quad \text{for } \delta_{\text{skin}} \gg h. \quad (2.8)$$

The same equation for laminated core is rewritten as follows

$$p_e = \frac{(\pi h f \hat{B})^2}{6\rho_c} \quad \text{for } \delta_{\text{skin}} \gg h. \quad (2.9)$$

Here ρ_c is resistivity of core material, h is lamination thickness, A_c is a cross-sectional area of a core.

Sometimes excess losses are called anomalous eddy-current losses. Since for the majority of magnetic materials some deviation from homogeneous and uniform permeability is observed, the total losses cannot be described as a sum of hysteresis and eddy-current loss. This type of loss is the consequence of domain wall's discontinuous movements or so-called non-homogeneous magnetization. During magnetic field variation many small discontinuous jumps occur as the domains rotate (Barkhausen effect).

Due to these jumps additional eddy-currents are induced. According to Bertotti [13, 14]. Excess losses are calculated as (2.10).

$$p_{\text{ex}} = k_{\text{ex}}(\hat{B}f)^{1.5}, \quad (2.10)$$

k_{ex} is a material specific coefficient depending on specific domain wall energy.

Finally the total core power loss density for sinusoidal waveforms is given by (2.11)

$$p_{\text{tot}} = p_{\text{h}} + p_{\text{e}} + p_{\text{ex}} = + \frac{4f\hat{B}^2}{\mu_r\mu_0} + \frac{(\pi hf\hat{B})^2}{6\rho_c} + k_{\text{ex}}(\hat{B}f)^{1.5}. \quad (2.11)$$

There are two main ways to decrease core losses, which should improve the high-frequency behaviour of the material. These can be derived from equation (2.11). The first one uses a laminated core and consequently decreases the thickness of core material. The second method is based on changing the composition of the material in order to decrease conductance of material.

Some more simple methods of power loss estimation can be used as well. For instance a sinusoidal magnetic flux density total core loss can be described with the help of Steinmetz equation

$$p_{\text{tot}} = K_c f^\alpha \hat{B}^\beta. \quad (2.12)$$

where the empirical coefficients K_c , α , and β depend on the core material and frequency range. The Steinmetz Equation is usually used for simplification of power loss calculation in engineering practice. Nevertheless, it agrees quite well with real data. Non sinusoidal excitation can be calculated with the improved Steinmetz Equation [82].

Curie temperature. After reaching this temperature ferromagnetic domains disintegrate abruptly. Ferromagnetic material loses its magnetic properties and becomes paramagnetic. Above Curie temperature thermal oscillations of the atomic magnets increase and overcome the coupling magnetic forces that maintain the alignment of the atomic magnets within domains. However, the operating temperature for most EMI filters is below 100 °C and typically Curie temperature lies in the range 200 - 250 °C

Maximum energy density. This is a generalized parameter that describes how effectively the space is occupied by the core. Energy density can be specified as a product of inductance and saturation flux density of the given core material (3.11) and (2.14)

$$L = \frac{\mu_0\mu_r N^2 A_e}{l}, \quad (2.13)$$

$$I = \frac{lB_{\text{sat}}}{\mu_0\mu_r N}. \quad (2.14)$$

Here N is the number of turns per winding; A_e cross section area; μ_0 the permeability constant; μ_r relative permeability; l the main path length of a magnetic core; B_{sat} is saturation flux density of material. and energy stored in the inductor is

$$W = 0.5L \cdot I^2 = 0.5 \frac{\mu_0 \mu_r N^2 A_e}{l} \left(\frac{l B_{\text{sat}}}{\mu_0 \mu_r N} \right)^2 = \frac{B_{\text{sat}}^2 l A_e}{2 \mu_0 \mu_r} \quad (2.15)$$

(2.15) represents the energy stored in the magnetic field of the inductor. However, the volume of the field-filled core of the solenoid is $l \cdot A$, so the magnetic energy density (the energy per unit volume) inside the solenoid is

$$w = \frac{B_{\text{sat}}^2}{2 \mu_0 \mu_r}. \quad (2.16)$$

An attempt to combine parameters of ferromagnetic material to the figure of merit, representing performance of material as a single number is made in Appendix A.

2.1.1 Ferrites

Ferrites have been known since the beginning of 20th century. Ferrites are ceramic, homogeneous materials composed of various oxides or carbonates with iron oxide (Fe_2O_4) as their main constituent. The general chemical formula is MeFe_2O_3 , where Me represents divalent transition metals (manganese, zinc, nickel, cobalt, magnesium etc). In conductive EMI field filtration manganese-zinc ($\text{MnZnFe}_2\text{O}_4$) and nickel-zinc ($\text{NiZnFe}_2\text{O}_4$) ferrites are the most common compositions. MnZn ferrite shows relatively high initial permeability and typical application frequency range is up to 10 MHz. NiZn alloys have lower conductivity and consequentially lower losses (2.11). They can be used up to frequencies of approximately 100 MHz. The initial permeability of these materials is less in comparison with MnZn alloys. Ferrite cores can be manufactured in various shapes. However, toroidal cores are the best solution for EMI filters, due to less flux leakage than other shapes. Properties of ferrites as well as the other ferromagnetic materials are caused by the existence of electron spins. All ferrite materials have natural resonance frequency due to those spins. In the low frequency range, domains inside of the material rotate normally introducing initial permeability. When the frequency of the external magnetic field and the natural resonance frequency of spins match, the precessing spins start to absorb power from the external field. As a result, the induction B produced in each cycle decreases, which means that μ degrades. Consequently inductance and high frequency IL of the EMI filter decreases as well.

Gapped cores for conducted EMI suppression are not usually ideal. This is especially true in frequencies above a few hundred kilohertz, since the stray flux in the area close to an air gap produces radiative disturbances. Secondly, extra eddy-currents are induced in the winding which adjoin to that area. They in turn heat a conductor up and lead to decreasing efficiency. A third issue is the sound noise and vibration caused by the magnetic flux which closes through an air gap. Gapped cores exhibit considerably higher noise level compared with ungapped cores.

On the physical level modern ferrites have already reached a limit of performance [59]. Nevertheless, optimization of this materials group still continues. One or two parameters can be optimised depending on specific application trends, which drive further development. Improvement of permeability at the high frequency is one of the major areas of consumer interest. Unfortunately, manufacturing ferrites is not the easiest procedure. R&D and tooling costs limit the number of materials which one company can produce. Development of a new ferrite mark can take two to three years. However, new shapes evolve more rapidly than compositions. Currently ferrite designers are working on three main areas of research [82]:

- Low profile + planar magnetic chokes. They have a lower profile than their wire wound counterparts.
- Automation of production process: new core shapes have to allow automate winding process.
- Predictable parasitics: with planar magnetics, windings are precise and consistent, yielding magnetic designs with highly controllable and predictable characteristic parameters.

The other direction in development of ferrites is 3D printing of ready to use inductance components [217]. It definitely helps to optimize components inside of the filter and allows better integration of EMI filters inside of power electronics devices. Characteristics of ferrite materials are contrasted with other soft magnetic materials in Appendix B.

2.1.2 Amorphous Alloys

Amorphous alloys are also called metallic glasses or noncrystalline alloys. Amorphous metal does not have crystalline structure. All atoms of amorphous metal are randomly arranged and due to this amorphous materials have higher resistivity compared to crystalline metals $1.2 - 2 \mu\Omega \cdot m$. Amorphous alloys are prepared by rapid cooling of the melt. In this case they are frozen in the liquid state configuration and crystallization of the melt is avoided. As a result, one gets metastable amorphous structure.

The amorphous materials were introduced in the second half of the 20th century. P. Duwez and co-workers presented the first iron-carbon-phosphorous alloy in 1967. These materials have proliferated after the invention of technology for the ribbons production in 1969 [72]. Similar technology is used for production of nanocrystalline materials. Due to absence of crystalline structure amorphous alloys are magnetically soft. They exhibit linear hysteresis loops with low coercivity. The reason for low coercivity is an increasingly low level of magnetostriction (almost 0). The saturation induction can vary from 0.7 – 1.8 T, at the same time initial permeability can reach 150000. Due to the amorphous structure and ribbon based design these materials exhibit good behaviour on frequencies around 1 MHz. The biggest disadvantage of Co-based amorphous materials is the price of cobalt, which is higher than conventional iron by a factor of five. Since Co is the main component in the material composition the price of core is relatively high and is driven by the cobalt price.

Typical composition for amorphous soft magnetic materials is described by $Me_{70-85}X_{15-30}$. Most soft magnetic materials are based on ferromagnetic elements Fe, Co and Ni. X denotes metalloids elements such as B, Si and C. For the conductive EMI filtration Co-based materials are the most suitable. Fe-based have the highest saturation flux density (1.5 – 1.7 T) but with increasing of the Fe portion magnetostriction increases and as a result the material loses its benefits. Ni-based alloys are mostly used for

sensor strips of a very short length. They are not suitable for EMI filters due to low cure temperature and relatively low saturation flux density (≈ 0.5 T). Metglas inc. and Vacuumschmelze are the biggest suppliers of amorphous alloys. Complicated manufacturing process and high price are the main reasons of a limited number for core suppliers for amorphous alloy. Amorphous materials for EMI filters might be a good solution for high-performance application when the price is not the critical factor. In the EMI filters field amorphous alloys have been almost completely supplemented by nanocrystallines.

2.1.3 Nanocrystalline Alloys

Nanocrystalline materials occupy the gap between amorphous and conventional crystalline materials. Nanocrystalline is a material with amorphous structure which consists of small crystallized grains (grain size for most alloys can vary between 10 – 100 nm). Figure 2.3 shows structures of different material types. The unique properties of nanocrystalline directly depend on the manufacturing technology (rapid solidification with annealing treatment).

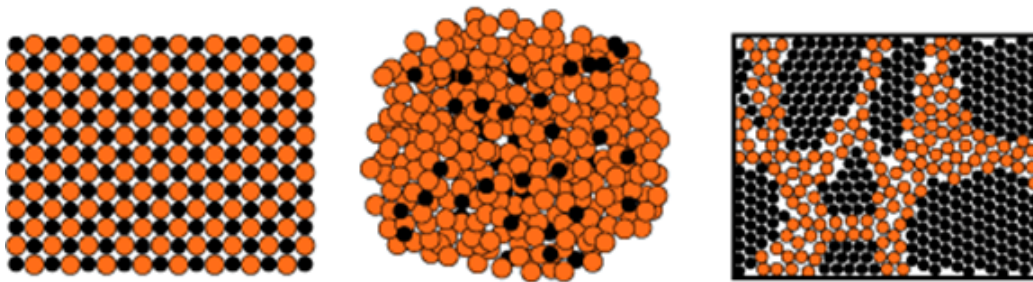


Figure 2.3.: Microstructures of crystalline, amorphous and nanocrystalline materials [74].

Nanocrystalline alloys are the last invention in soft magnetic materials suitable for conductive EMI filtration. They were invented in 1988 by Yoshizawa and coworkers [229]. The material had the standard amorphous composition $\text{Fe}_{73.5}\text{Cu}_1\text{Nb}_3\text{Si}_{13.5}\text{B}_9$ which was transformed to the nanocrystalline state. The nanocrystallines simultaneously exhibit relatively large magnetic permeability and maximum magnetization, as well as low coercivity. Superior soft magnetic properties of nanocrystalline are the consequence of the magnetocrystalline anisotropy constant tending to zero [73]. There is a wide range of nanocrystalline alloys with round rectangular or flat hysteresis loops and coercivity H_c smaller than 2 A/m. Saturation flux density of different nanocrystallines is 1.2 – 1.5 T, that is three times higher than in ferrites and twice as high as Co-based amorphous alloys. Permeability can vary from 20000 up to more than 150000. High permeability of nanocrystalline materials helps to decrease the number of turns of the inductor. As a result, the stray capacitance between turn connections might be reduced. Due to low ribbon thickness around 20 μm and relatively high electrical resistivity 1.15 – 1.2 $\text{m}\Omega \cdot \text{m}$, nanocrystallines exhibit low core losses, especially in frequencies above 100 kHz. The dependence of the initial permeability on temperature is almost linear. In the temperature range from 40 up to 120 $^{\circ}\text{C}$ the deviation of initial permeability is 5-6%. Impedances for ferrite and nanocrystalline based common mode chokes with 15 turns are depicted in Figure 2.4

There are several shortcomings of nanocrystalline materials, such as brittleness, small choice of core configurations and price. Because of brittleness additional mechanical protection is required. Most

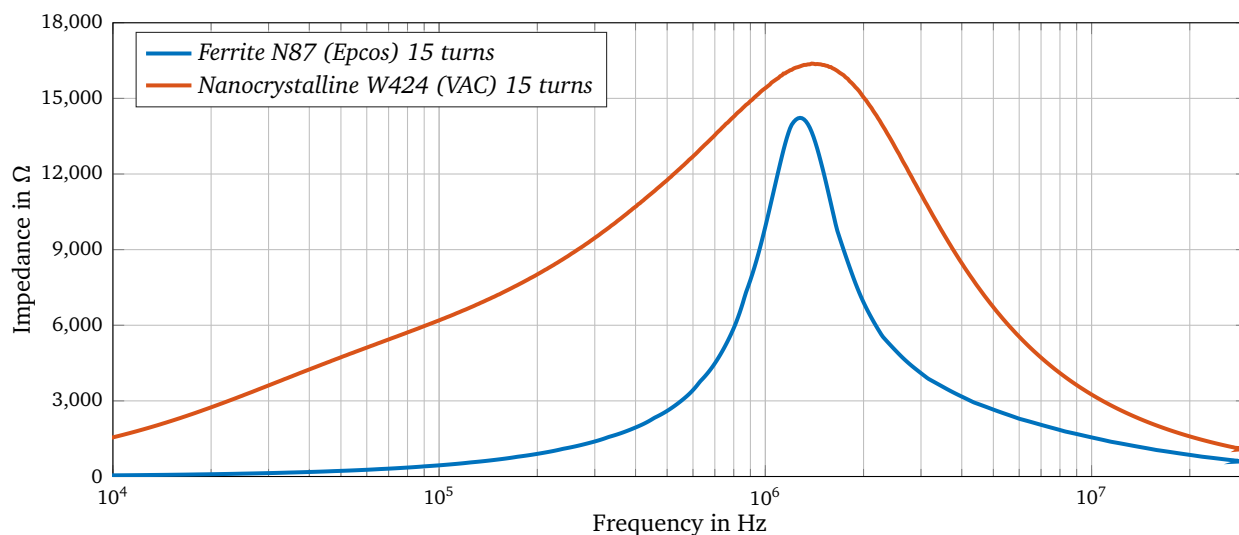


Figure 2.4.: Impedance of nanocrystalline and ferrite based chokes with the same number of turns and dimensions.

often for increase of mechanical stability epoxy coating or plastic core boxes are used. The low number of core configurations is caused by the production process (the material represents a ribbon). Toroid cores, stadium cores, U-shape and air gapped cores are available. The average price of nanocrystalline materials remains relatively high compared with ferrites. A sample of nanocrystalline core is on average 50-100 % more expensive compared to the ferrite analogue. Theoretically due to the high permeability of nanocrystalline a designer can decrease the number of turns and therefore the price of the wire, or save some space: therefore the final difference between ferrite and nanocrystalline based inductors can be reduced. In spite of the fact that a few decades have passed from the moment of nanocrystalline invention, just a few companies in the world have mastered production of these materials (Vacuumschmelze, Magnetec, Hitachi, MK-magnetics). Nowadays two generations of nanocrystalline exist. Finemet and Vitroperm alloys represent first generation ($\approx 74\%$ Fe) and second generation is represented by Nanoperm or Hitperm with higher Fe concentration ($\approx 83 - 89\%$ Fe). More detailed characteristics of nanocrystalline materials and comparison with other material types according to previously mentioned parameters are summarized in Appendix B.

There are some possibilities for improvement of soft nanocrystalline composition in the future. This is because any changes of nanocrystalline composition or changing of the grain size increase magnetostriction in the negative or positive direction, so that coercivity increases and the material loses its soft magnetic properties. Changing of composition or grain size with a goal to improve some of the material parameters needs a relatively time consuming adjustment of magnetostriction to zero. Because of D^6 dependency between grain size of nanocrystalline and coercivity it makes no sense to produce materials with grain size bigger than 30 nm. However at the same time, for grain size below 10 nm coercivity becomes independent of the grain size. This makes improvement of the high frequency material properties via variation of the grain size almost impossible. The main direction of nanocrystalline improvement is stretching of hysteresis loop, decreasing of permeability and increasing energy storage capabilities. This is aimed at applications in storage inductors of SMPS. Gapped nanocrystalline core versions for these applications are already available, however due to previously discussed reasons this is

not the best option for EMI filters. For further enhancement of high frequency properties and reduction of losses, minimization of ribbon thickness or increasing of material's electrical resistance is necessary. Decreasing of ribbon thickness will lead to the complication of the manufacturing process due to a high tendency towards tearing. Moreover, a filling factor of the core decreases with a thinner ribbon. Ribbon thickness normally lies between $18\mu\text{m}$ and $22\mu\text{m}$. Further decreasing of the ribbon thickness shifts μ'' components to higher frequency as a consequence of the increased Wolman frequency.

It is worth mentioning that in spite of the relatively low power loss exhibited by nanocrystalline's materials at the frequency of several kHz, power loss increases rapidly with frequency. On 150 kHz power loss of nanocrystalline are significantly higher as compared to ferrite. It also can be observed from Figure 2.4 where μ' of nanocrystalline becomes dominated after 40 kHz. On the one hand, the energy carried in disturbance form is converted to heat within a magnetic core causing overheating of an inductor. On the other hand, disturbance energy is completely eliminated from conductive parts; it is not stored in the form of a magnetic field or reflected back to the disturbance source. The maximum power dissipation must be limited during choke design in order to avoid overheating.

Manufacturing technology is the main driver in improvement of nanocrystalline and all ribbon-based magnetic materials in general. Unfortunately equipment for manufacturing ribbons requires significant investment. Despite the issues, new shapes of nanocrystalline cores should become available in the near future. Manufacturing of nanocrystalline planar cores is possible in theory, and the price of the planar nanocrystalline cores is the question. Therefore price reduction is the most practical direction for research.

2.1.4 Powder Materials

Powder cores are made by the milling down of high permeability alloys into powder, followed by pressing them together with a non-magnetic binder (organic or inorganic) into the desired shape. Afterwards, cores are sintered in an oven. This structure allows the isolation of magnetic material powder particles from each other, creating a non-permeable gap. The material then becomes suitable for higher frequencies. Due to the small size of the magnetic powder particles, the skin effect does not occur. As a result of effects caused by air gaps between particles, permeability of the resulting material becomes considerably smaller. The main feature of powder cores is a naturally distributed air gap. A magnetization curve typical for materials with soft saturation is compared with a normal ferrite curve in Figure 2.5. Permeability is relatively stable with increasing frequency, since the size of particles is small and degradation due to skin effect is minimized.

Powder material cores were invented in the beginning of the 20th century in the USA. The first toroidal powder iron cores were used in telecommunications. Permeability of powder cores was about 30 units with manufacturing technology quite similar to the modern day. Magnetic and electric properties of powder cores depend on several factors, namely, the permeability of the powder material, particle size and shape, fill factor, insulation binder content, moulding pressure and heat treatment processes. Main powder soft magnetics materials are:

- Pure iron (Iron powder cores);
- Iron-nickel alloy class of soft magnetic (High flux, Permalloy);
- Iron-nickel-molybdenum powders (MPP, Molypermalloy cores);

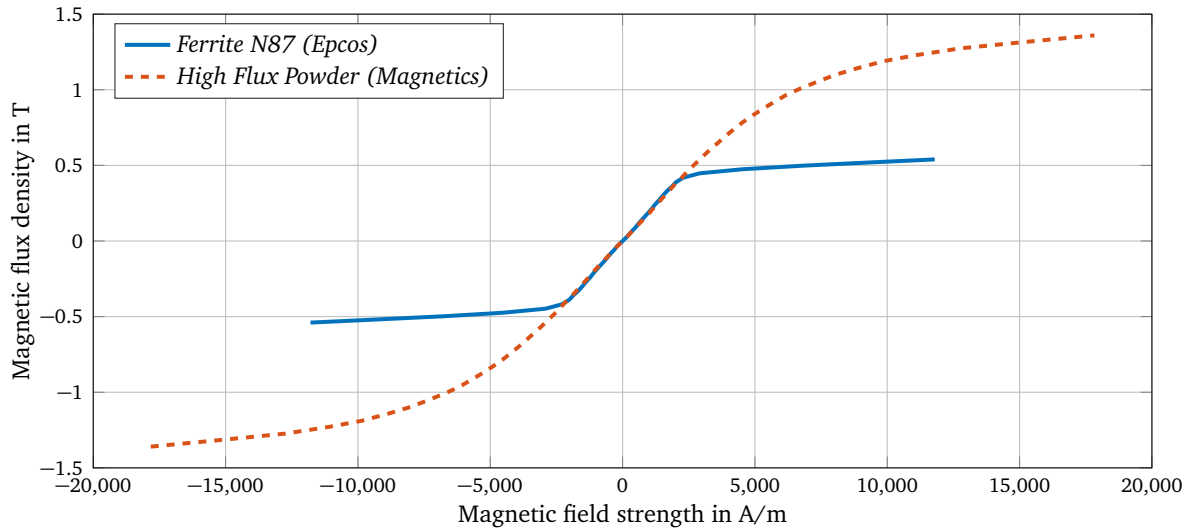


Figure 2.5.: Comparison of the soft saturation of powder material and normal magnetization of ferrite.

- Iron silicon aluminium class of soft magnetic powders (Kool my, Sendust Super MSS cores);
- Silicon steel (XFlux, FluxSan, Mega Flux, Fe-Si).

Pure Iron cores exhibit high saturation flux density and cure temperature (1.5 T and 770 °C correspondingly). But all other parameters are relatively poor ($\mu \approx 100$, losses 840 mW/c³m). Nevertheless, price of powdered iron based cores is the lowest among powder materials. Iron-nickel alloys are the best among powder materials in terms of saturation flux density 1.5 T and relatively good initial permeability ($\mu \approx 30 - 90$). MPP cores offer the highest permeability of $\mu \approx 30 - 200$, the lowest power loss and sufficiently high saturation flux density. All properties of iron-silicon-aluminium cores are average compared to other powder materials except costs; the price is comparable with iron powder. Silicon steel is not the best decision for EMI filter application due to its low permeability ($\mu \approx 25 - 60$). All powder cores exhibit considerable good temperature stability of permeability (deviation $\pm 2\%$ in the range from -40 to 770 °C).

As can be seen from Table B.1 powdered cores can rival the other materials in terms of saturation flux density, temperature stability and cost. At the same time significantly lower initial permeability make these cores not a preferable solution for CM inductors. However, from the aforementioned properties it is seen that powder materials are ideally suited for DM inductors, especially in comparison with gapped ferrite cores. The best powder cores for EMI filter applications are based on iron-nickel-molybdenum and iron-nickel materials. Unfortunately these two types are the most expensive among powder materials.

2.2 Inductive Components

Inductive components used for EMI filters are typically based on toroidal cores. This core shape has several benefits for EMI filter applications:

- Magnetic flux which closes outside of the core is low. Hence, the mutual couplings inside of the EMI filter are minimized;
- Good heat transfer in comparison with closed cores;

- It does not require some additional mechanical components for fastening. An inductor can be made of toroid core and wire;
- Toroids are usually not gapped. It has some advantages for EMI inductive components mentioned previously.

Due to these reasons toroidal cores are considered as the standard form within this thesis.

Characteristics of inductive components are mainly derived by two phenomena. The first one is the magnetic core properties such as frequency dependant permeability and magnetic hysteresis. The second is a self-resonant frequency caused by self-capacitance (also called equivalent parallel capacitance (EPC)). For a toroid core DC inductance, when the amplitudes of magnetic flux density close to the origin is equal to (3.11), equation (3.11) allows only a rough estimation of inductance due to nonlinear nature of permeability characteristics. The general formula can be supplemented by frequency and current dependent permeability $\mu(f, I)$. Some ways to include a frequency dependent permeability as well as the saturation effects to the mathematical mode of an inductor are discussed in following chapters. However, for the simplest case a series resistor, representing ohmic losses inside of the magnetic core, and a series inductor are included into an equivalent circuit.

Any conductive structures separated by dielectric material represent a capacitor. Whenever a charged conductor is placed in the proximity of other conductors, the lines of electric field leave one conductor and terminate on the surrounding conductors. In general capacitance of a parallel-plate capacitor is equal to the ratio of the charge stored on one plate to the voltage difference between two plates. Of course, geometry of winding is more complex than a simple two plate capacitor. But it is clear that undesirable capacitors can be found between turns as well as between winding and core. These capacitors influence behaviour of inductive components in a MHz range.

Distributed turn-to-turn capacitance can be represented like shunt capacitance of an inductor, which conducts high-frequency currents and bypasses inductance of the inductor. A typical core-based inductor contains three different types of self-capacitance which are summarized as a lump capacitor in parallel with an inductor. Figure 2.6 shows three adjacent turns of an inductor with a magnetic core. C_{tt} is a turn-to-turn capacitance between these adjacent turns, which is divided into the capacitance through the air between two adjacent turns C_{tt-air} and capacitance through two layers of wire insulation material of two adjacent turns C_{tt-iso} . C_{tc} is capacitance between a turn and a magnetic core. An equivalent circuit (Figure 2.6) represents three turns of inductors including the following effects: self-inductance, core losses and parasitic capacitances. Inductors consisting of two or more winding (CMC) have one more stray capacitor, namely winding to winding capacitance (C_{ww}). The last one is typically small compared to C_{tt} due to the longer distance between windings which is required because of isolation requirements.

After simplification of the equivalent circuit depicted in Figure 2.6b with the star-mesh transform (Y to Δ transform in this particular case) resulting EPC is obtained as a product of all capacitances listed above. From Figure 2.7 it becomes obvious that inductive components together with their own EPC represent a resonance circuit. Self-resonant frequency caused by EPC of inductive components employed in EMI filters typically lie in the range 1 MHz–10 MHz. EPC of multilayer inductors is bigger than EPC of one-layer samples [32]. This is the main incentive for utilization of one-layer inductors for EMI applications, where good high-frequency characteristics are indispensable. Moreover, one-layer winding ensures low impact of the proximity effect, so that it can be taken out of consideration.

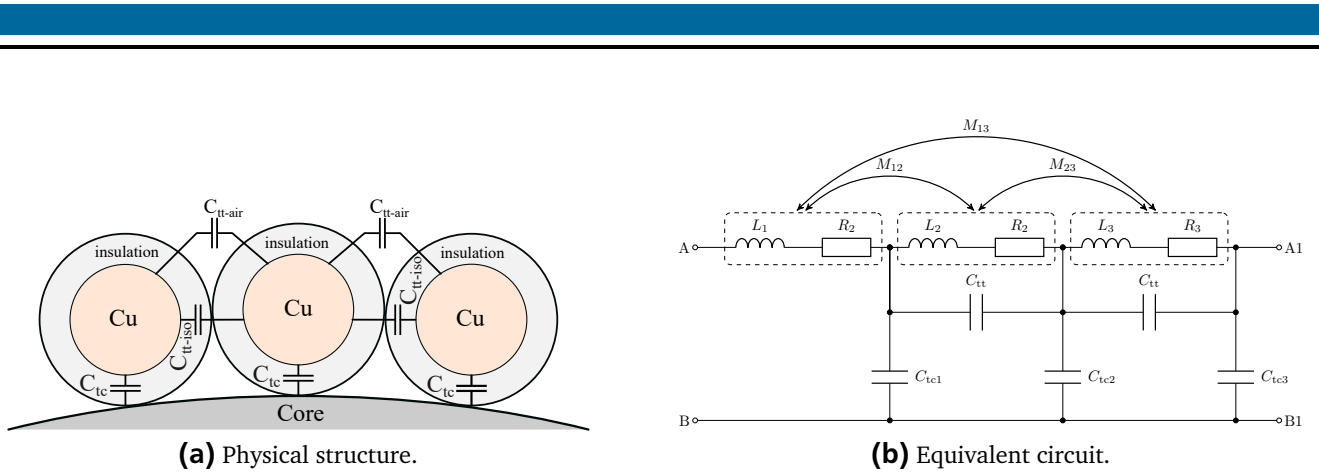


Figure 2.6.: Types of parasitic capacitors of an inductor and corresponding equivalent circuit.

In order to create an adequate inductor model wire effects must be included. Inductors for EMI filters are typically wound using a one-wire cable. There are two reasons for using a one-wire cable. Firstly, due to the skin effect energy of the high frequency disturbances is partially converted to heat and is not propagated further. Obviously, it can negatively influence the thermal mode of a conductor as a side effect. Secondly, it exhibits lower EPC, since adjacent turns from a litz wire with the same active cross-section as a solid wire have larger contact surface. Therefore, only two physical effects should be included into the mathematical model of an inductor, such as skin effect and ohmic resistance. Resistance of a solid wire conductor is given by (2.17).

$$R_{\text{wire}} = \frac{4l_{\text{wire}}\rho}{\pi d^2}, \quad (2.17)$$

where ρ is conductance, l is the length of conductor and d its diameter. For a round conductor with a diameter much larger than the skin depth, current flowing through a conductor is pushed from the middle of a conductor to the conductor surface due to non-linear distribution of the electromagnetic field. With this assumption, a conductive area of a wire can be reduced, leading to (2.18).

$$R_{\text{HW}} = \frac{l_{\text{wire}}\rho}{\pi d \delta_{\text{skin}}}, \quad (2.18)$$

where δ_{skin} is the skin depth. Finally, an equivalent circuit, consisting of L_{core} and R_{core} representing a magnetic core, R_{wire} and EPC can be created (Figure 2.7). This equivalent circuit describes only a choke itself but does not take into account possible coupling with the other EMI filter components.

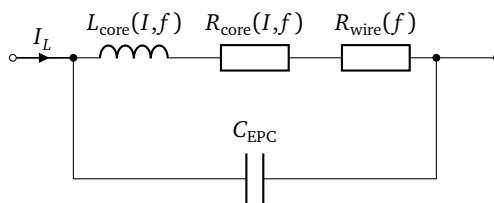


Figure 2.7.: Equivalent circuit of an inductor.

After some simplification an equivalent circuit depicted in Figure 2.7 can be converted to the impedance Z_L which can be used further for analytical calculation of insertion loss

$$Z_L = \frac{R_{\text{core}} + R_{\text{wire}} + j\omega L_{\text{core}}}{1 - \omega^2 L_{\text{core}} C_{\text{EPC}} + j\omega C_{\text{EPC}}(R_{\text{core}} + R_{\text{wire}})} \quad (2.19)$$

Saturation is one of the most critical properties of the core based inductive components. When a core of inductive components is driven into saturation only inductance of a wire (a hundred times smaller) stays. With a saturated core, IL of an EMI filter degrade significantly. Even for ideally designed EMI filters with consideration of all non ideal effects saturation will nullify all efforts. Therefore, special attention must be paid to this effect.

2.2.1 Common Mode Chokes

A common mode choke is the cornerstone of filter design and is an indispensable component of any EMI filter. The first CMC for three-phase application was presented in 1971. By definition a CMC represents a special case of a transformer with specifically arranged windings. For instance current flowing at phase U induces magnetic flux in a clockwise direction. The back path of current is split up between phase V and W, so that the flux caused by these currents is in counter-clockwise direction as shown in Figure 2.8. Ideally, magnetizing forces caused by differential (phase currents) cancel each other completely (2.20), (2.21).

$$i_u + i_v + i_w = 0 \quad (2.20)$$

$$\frac{Ni_u}{l} + \frac{Ni_v}{l} + \frac{Ni_w}{l} = 0 \quad (2.21)$$

The flux distribution in an ideal three-phase CMC is depicted in Figure 2.8.

Toroid based construction of a three-phase CMC exhibits some advantages, and therefore is frequently used. Low core price, no additional mechanical chassis required, small leakage flux and low thermal resistance are the main of benefits. However, the winding process of toroids requires special tools which can be very costly.

Because of existing safety limitations of the maximum leakage currents, value of Y-capacitors is restricted. Moreover, leakage current can cause of unintended triggering of residual current protection devices (RCD). One more limitation for Y-capacitors is high $\frac{du}{dt}$ of power electronic devices. More expansive capacitors must be used in order to survive under these rapid voltage changes. $\frac{du}{dt}$ rates for GaN and SiC devices reach 3000 V/ μ s. Although, the best samples of Y-capacitors are able to withstand only 800 V/ μ s - 1000 V/ μ s and cannot be used. Therefore, a CMC remains the only component responsible for dimpling of CM disturbances. A CMC presents high impedance for common mode noise in the k Ω range,

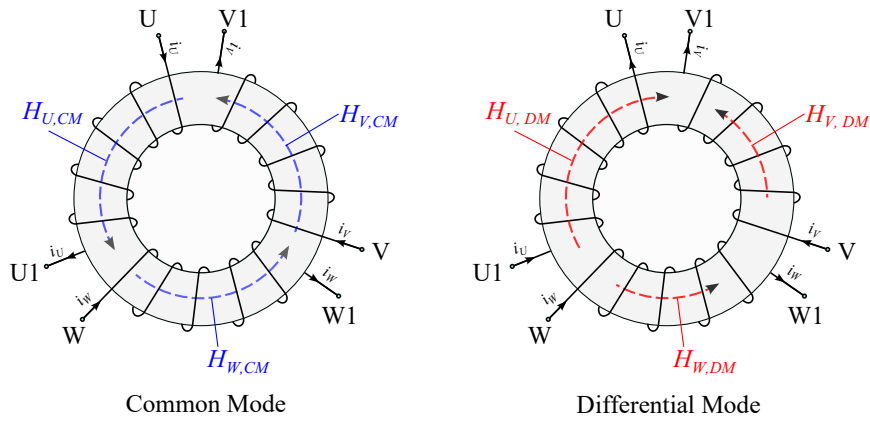


Figure 2.8.: Field distribution of CMC.

but small impedance against differential mode current which is also referred to the leakage inductance. Figure 2.9 shows measured impedance of CMC for DM and CM disturbances.

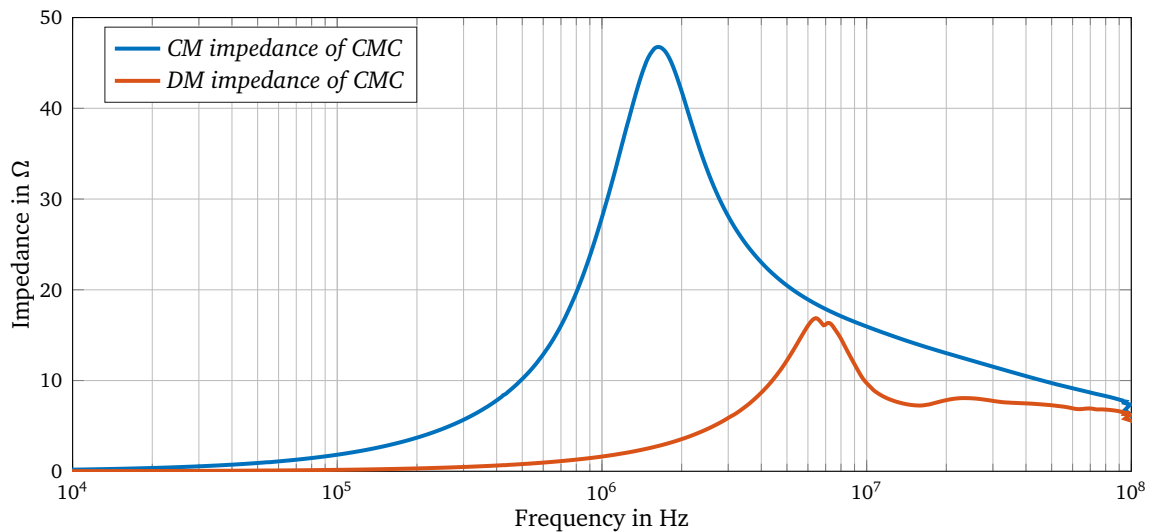


Figure 2.9.: CMC impedances for CM and DM paths.

In contrast with DM inductors CMC has one more important parameter: the leakage inductance caused by leakage flux. The leakage flux is a result of the H-field which is not coupled to the core. This leakage H-field results in the leakage B-field. Since the leakage B-field leaves the core (by definition), effective permeability of the leakage path is much lower than the permeability of the main core path. Therefore, the leakage flux is much lower than the flux induced inside of the core. The leakage inductance in fact is desirable and responsible for DM disturbance damping. Nevertheless, the leakage flux contributes to the core saturation. The part of flux caused by a leakage inductance has to be taken into account during B_{tot} calculation.

$$B_{tot} = \frac{\mu_0 \mu_r I_{cm} N}{l} + 3 \frac{\mu_0 I_{dm} N}{l_{eff}}. \quad (2.22)$$

Here N is the number of turns per winding; A_e cross section area; μ_0 the permeability constant; μ_r relative permeability; l the main path length of a magnetic core, I_{cm} and I_{dm} are common and differential mode currents and l_{eff} is given by (3.15)

$$l_{eff} = l \sqrt{\frac{\theta}{2\pi} + \frac{1}{\pi} \sin \frac{\theta}{2}}, \quad (2.23)$$

where θ is the angle occupied by a winding and l is the main path length of a magnetic core. (3.15) is valid for $\theta > \pi/6$.

2.3 Capacitors

Capacitors are the second main component of filters. Due to the absence of complex magnetic materials, high frequency behaviour of capacitors is affected mainly by self-parasitics. Consequently, performance of an EMI filter is strongly influenced by these parasitics. A relatively simple equivalent circuit reflects a film capacitor behaviour in the wide frequency range (Figure 2.10). Resistor R_p represents the leakage under DC operation. R_s is ohmic resistance of conductive plates and leads. ESL and C are main capacity and equivalent series inductance. Together they cause a self-resonant frequency of the capacitor.

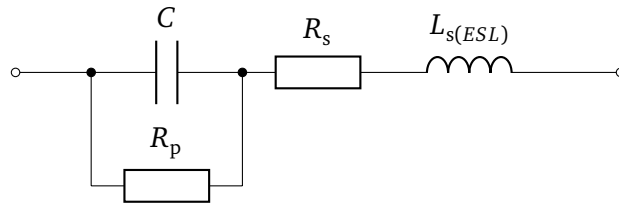


Figure 2.10.: Equivalent circuit of a capacitor.

An equivalent circuit depicted in Figure 2.10 is represented with equation (2.24)

$$Z_C = R_s + j\omega L_s + \frac{R_p}{1 + j\omega R_p C}. \quad (2.24)$$

For the vast majority of situations an even simpler model without R_p is sufficient. A comparison between measured capacitor characteristics and a simplified model is shown in Figure 2.11. The match is almost ideal. From this characteristic it can be concluded that the IL of an EMI filter will be strongly affected by the ESL of a capacitor. It must be mentioned that due to ESL of capacitors it is coupled with the other components inside of a filter. Therefore, the high frequency characteristics of capacitors placed in the EMI filter are strongly affected by adjacent components.

Film capacitors are used in three-phase EMI filters the most often. This is mainly because of low price and moderate ESL. Filters with film capacitors can be supplemented with additional ceramic capacitors, which have lower ESL. This solution allows improvement of the high frequency IL of a filter.

Two types of capacitors are employed in EMI filters. X-capacitors are connected across the phases. In this case a failure does not lead to the hazard of electric shock to people. Connection of X-capacitors between a phase and the ground is not allowed. Y-capacitors are connected between conductive parts and

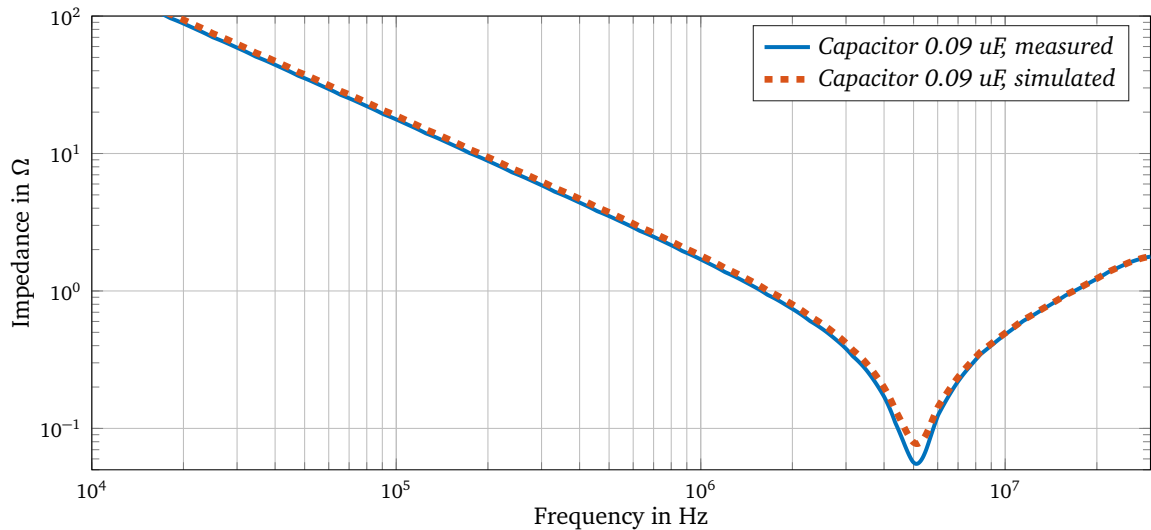


Figure 2.11.: Modelled and measured capacitors 0.09 nF.

the ground. In accordance with demands of IEC 60384-14 Y-capacitors under a failure condition must represent an open circuit. Safety demands on Y-capacitors lead to the lower power destiny and higher prices of this capacitor type compared to X-capacitors. Depending on the surge voltage amplitude, which is used during qualification tests, bought X- and Y-capacitors are subdivided into seven classes; X1, X2, X3 and Y1, Y2, Y3, Y4 according to IEC 60384-14 [98].

2.4 Mutual Couplings

Mutual couplings are not the actual components of an EMI filter but they have to be taken into consideration during filter design. Effects caused by electromagnetic fields inside of an EMI filter represent one more reason of IL degradation at the high frequency. Typically, inductive couplings are dominant over capacitive couplings. The most significant couplings are associated with the leakage flux of a CMC. Magnetic field closing outside of the core strikes through the other filter components and PCB traces in vicinity with a CMC. This magnetic field induces current in components, organizing a path for high frequency disturbance transmission. Therefore, arrangement of components inside of an EMI filter affects resulting IL [76].

Effect of mutual couplings can be demonstrated by employing two similar filter topologies with the same components but diverse layouts [61, 190]. Importance of such couplings has already been shown in the example of single-phase filters used in SMPSs [23, 160, 219]. In contrast with single-phase filters for SMPSs construction of three-phase filters is better balanced by definition. A number of components in three-phase filters assume correct placement of components by default. The best solution is the simplest one in this case. Besides mutual inter component couplings, couplings between components and PCB traces as well as a coupling between input and output trace loops in the case of a PCB-based filter must be considered [138].

However, mutual couplings do not always have parasitic effects. For instance a capacitive coupling between conductive parts and a housing represents a distributed Y-capacitor. Interaction between X-capacitors connected between different phases can improve balancing within an EMI filter etc. The

leakage flux of a CMC can be used for compensation of ESL of capacitors located nearby. The most dangerous consequences are represented by the inductive coupling between an input and an output of an EMI filter. By definition this coupling shorts an input and an output of an EMI filter, so that disturbance can freely migrate from an disturbance source to the power grid.

3 Modelling and Design Methods for EMI Filters

Modelling and design of EMI filters is one of the most important tasks in modern power electronics. In fact, there is no PE converter that can comply with norms without additional filtering. Development of an EMI filter seems to be rather trivial; nevertheless, fulfilment of this task can take a long time and requires a multitude of simulations, prototypes and tests.

The normal level of abstraction and simplification, which gives precise simulation results for the majority of applications, is usually not sufficient for EMI filter design and modelling. Therefore, the necessity to develop modelling approaches that are dedicated to the design of EMI filters for power electronics converters is clearly recognisable. The majority of the existing design procedures of EMI filters can be referred to as structured "trial and error" methods. They require the "looped" design and testing procedure. Developed EMI filters have to be tested together with a PE converter until the level of disturbances emitted by this converter complies with particular norms. Obviously this approach can lead to an infinite number of iterations and very high development costs. Moreover, every iteration requires prototyping of the previously simulated EMI filter in order to improve the accuracy of the model. Thus, mutual couplings and nonlinear permeability effects are extracted from a built prototype. Thereby an equivalent circuit of the filter is fine-tuned in accordance with measurements. A finely tuned mathematical model reproduces IL of the EMI filter quite precisely, but even then minor changes in a specification require restarting the whole procedure. This approach has some clear shortcomings. Firstly, the time required for suitable design is almost impossible to predict. Secondly, building a prototype is not always possible due to lack of some required components. Lastly, a PE converter for the designed filter utilization can be unknown or under development, so that validation of the electromagnetic compatibility (EMC) concept can be started only after the first converter prototype has been built. However, no fundamental description of the "trial and error" approach, which would characterize in detail the entire algorithm required for EMI filter design, is summarized in research literature.

The main goal in this chapter is to develop EMI filter modelling and design procedures with distinctly described algorithms. Proposed mathematical methods allow moving away from the "trial and error" approach and consequently decreases the number of prototypes needed to obtain an EMI filter with specified characteristics. Effects introduced by modification of EMI filter parameters and their correlation are discussed. The most important nonideal properties of a filter, which are caused by self-parasitics and the nonlinear character of permeability, are included into the proposed mathematical models. Moreover, relevance of mutual coupling is determined so that only the most important mutual couplings are considered in the mathematical models - since only a few mutual couplings inside of a filter have a substantial impact on IL.

Different simulation methods are evaluated from different points of view such as exactness, design efforts and time. Every proposed design method is discussed in detail, so that it can be easily reproduced. Accuracy of those methods is assessed experimentally on examples of built three-phase EMI filter prototypes. All proposed models can be extended and utilized for further optimization and improvement.

3.1 Design of EMI Filters Based on a Simplified Analytical Model

Utilization of an analytical model is the simplest way to estimate IL of the EMI filter. The most relevant effects inside of an EMI filter can be described with relatively simple mathematical equations. However, a well prepared analytical EMI filter model might demonstrate accurate results even in comparison with more complex simulation methods. The model of a three-phase EMI filter proposed in this section is based on the classical electric circuits theory. In order to create a reliable analytical model, relevant physical processes must be determined and reflected in components of an equivalent circuit.

The first part of any EMI filter design process is estimation of desirable IL for both symmetrical and asymmetrical modes. This task is usually quite challenging for several reasons. Most importantly, a power electronics converter, which must be equipped with an EMI filter, is not always available for EMI spectrum measurements. This is because the filter and converter are designed simultaneously by different developers, or it is unknown which exact converter will utilize the designed filter. Moreover, in accordance with the standard procedure of conductive emission testing, only a superposition of CM and DM has to be measured. Different components of an EMI filter are responsible for CM and DM disturbance damping. For correct utilization of measured data during filter design, DM and CM disturbances must be separated. This issue can be solved mathematically, during data processing. In this case DM and CM signals have to be measured simultaneously. Alternatively, a special interference separator can be applied [62, 70, 168].

Typically, a measured spectrum contains several critical resonances which have to be mitigated in order to comply with standards as shown in Figure 3.1 (Critical frequencies are 1.2 MHz, 11 MHz and 14 MHz). Dashed lines in Figure 3.1 show the maximum conductive disturbance level for classes A and B according to EN55022. Let's assume that for the PE converter with the spectrum depicted in Figure 3.1 a CM EMI filter has to be designed. In order to comply with standards, IL in the frequency range 400–1300 kHz must be 60 dB and CM IL in the frequency range 3–14 MHz must be higher than 30 dB. DM IL in the range up to 800 kHz must exceed 70 dB with ≈ 30 dB up to 30 MHz. A few more simplifications have to be done before building an analytical model of the filter. Firstly, it is assumed that there is no unbalance between phases. Secondly, the load and source impedances are 50Ω (impact of load and source impedances on the filter IL is discussed in Section 3.1.2). Lastly, mutual interactions between filter components are discarded.

When required damping of the filter under development is known, a topology can be selected. Equivalent circuits for three standard topologies (Γ - type, T - type and Π - type) are depicted in Figure 3.2. All other topology types represent a series connection of those standard networks. Any three-phase EMI filter can be analysed as a ladder network consisting of several standard stages connected together. In accordance with a specification, two different filters (one for CM and the other for DM) have to be designed. With an approximation that there is no phase unbalance, only one phase can be simulated. Equivalent filters are simplified to two four-port networks and analysed under 50Ω source and load conditions similar to Figure 1.14. Equivalent filters for CM and for DM disturbances as a rule employ different topologies and component values. When a required CM and DM filter IL are obtained for a 50Ω system, these two equivalent filters have to be combined into one physical device. Obviously, the components of equivalent circuits must be substituted with three-phase equivalents in an actual construction. Values of DM components for a three-phase EMI filter must be recalculated according to

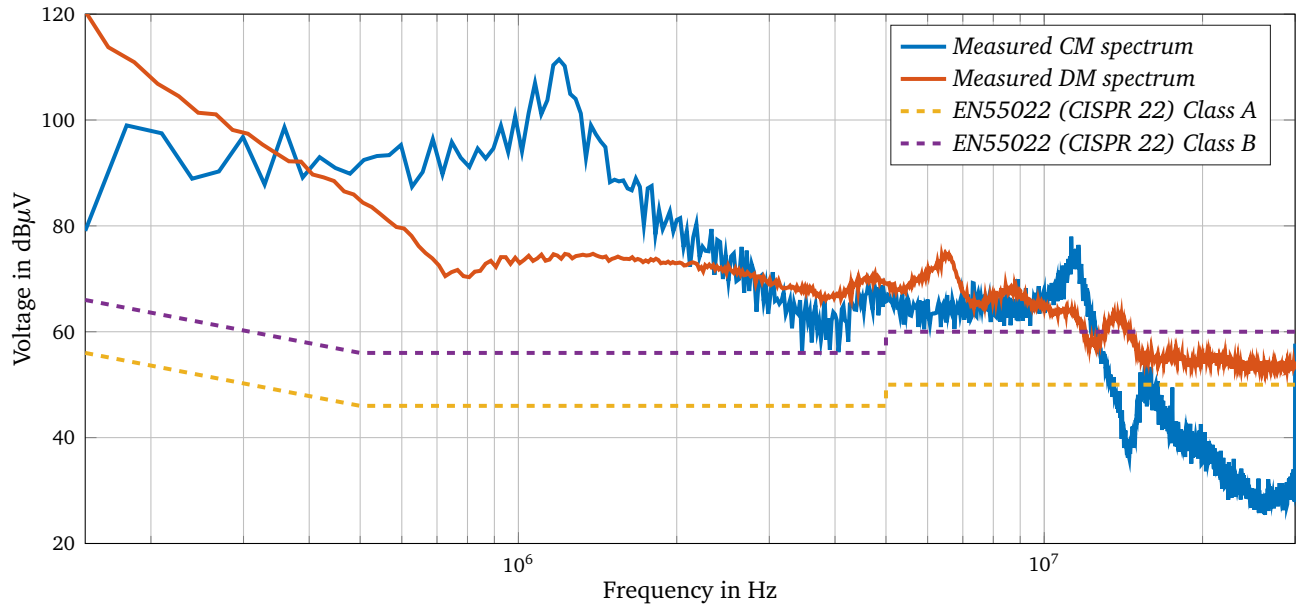


Figure 3.1.: example of a spectrum produced by a PE converter without an EMI filter.

a connection type (phase-to-phase, phase-to-artificial star point). Development of equivalent circuits which reflect real behaviour of an EMI filter under CM and DM conditions is the most complicated stage of filter design. Insertion loss of any topology can be calculated if impedances of load Z_L and source Z_S

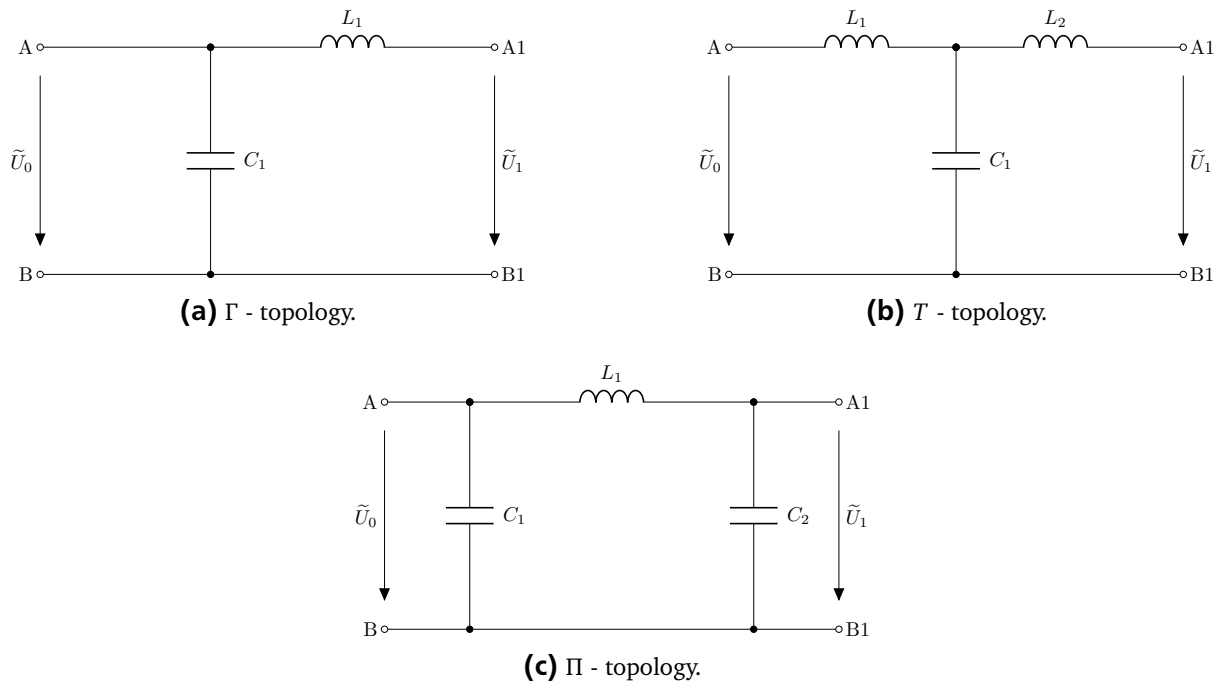


Figure 3.2.: Standard filter topologies.

are known. The general case of IL is (3.1)

$$IL = 20 \log_{10} \left(A_1 \frac{Z_L}{Z_S + Z_L} + A_2 \frac{1}{Z_S + Z_L} + A_3 \frac{Z_L Z_S}{Z_S + Z_L} + A_4 \frac{Z_S}{Z_S + Z_L} \right), \quad (3.1)$$

where A_1, A_2, A_3 and A_4 are coefficients determined by the filter topology. From (3.1) is clearly seen a direct dependency of IL from the load and source impedance term. Particular cases of (3.1) for standard topologies (Γ , T and Π - types) depicted in Figure 3.2 are as follows:

$$IL_{\Gamma} = 20 \log_{10} \left(\frac{Z_{C1}(Z_S + Z_L + Z_{L1}) + Z_S Z_L + Z_S Z_{L1}}{Z_{C1}(Z_S + Z_L)} \right), \quad (3.2)$$

$$IL_T = 20 \log_{10} \left(\frac{Z_S + Z_L + Z_{L1} + Z_{L2}}{Z_S + Z_L} + \frac{Z_S Z_L + Z_S Z_{L2} + Z_L Z_{L1}}{Z_{C1}(Z_L + Z_S)} + \frac{Z_{L1} Z_{L2}}{Z_{C1}} \right), \quad (3.3)$$

$$IL_{\Pi} = 20 \log_{10} \left(\frac{Z_S + Z_L + Z_{L1}}{Z_S + Z_L} + \frac{Z_L Z_{L1} + Z_L Z_S}{Z_{C2}(Z_S + Z_L)} + \frac{Z_S Z_{L1} + Z_L Z_S}{Z_{C1}(Z_S + Z_L)} + \frac{Z_S Z_L Z_{L1}}{Z_{C1} Z_{C2}(Z_L + Z_S)} \right). \quad (3.4)$$

Some other cases of IL characterisation for single-phase filters can be found in [124].

The main cut-off frequency is presented in frequency characteristics of every filter. This frequency is caused by interaction between reactive components included in a filter. After a cut-off frequency a slope representing impedance (or insertion losses) begins to change rapidly. From literature it is known that the rates of change are 40 dB/decade for Γ -topology and 60 dB/decade for T - and Π -topologies. Frequency characteristics of ideal filters are shown in Figure 3.3. Parameters used for calculation of those characteristics are listed in the legend.

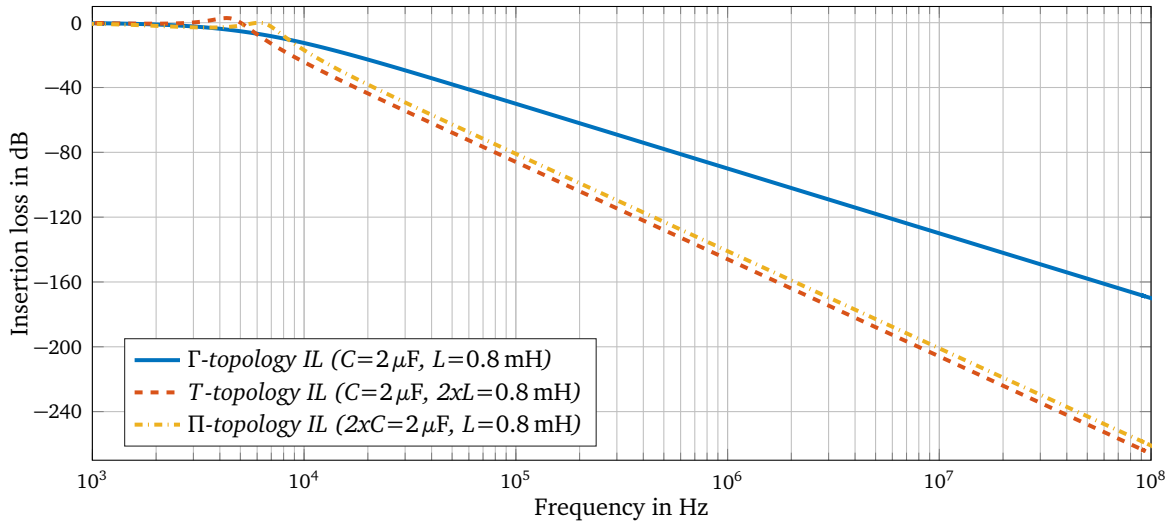


Figure 3.3.: IL of standard filter topologies (50 Ω /50 Ω).

As can be seen from Figure 3.3, utilization of T - and Π -topologies is most efficient. In this case the total value of the required inductance and capacitance is smaller. Due to a higher rate of change (60 dB/decade) a cut-off frequency can be shifted towards higher frequencies, although desirable IL at the frequency of interest is still achieved. However, some disadvantages are also present. Firstly, the

total number of components in EMI filters with Π - or T -topologies is higher, which is also true for multi-stage filters. Secondly, a sharper resonance at the cut-off frequency comparable with a Γ -type is typical for T - and Π -topologies. Those resonances are seen in Figure 3.3, although they are well damped by $50\ \Omega$ load and source impedance. The resonances can be occasionally met by one of PWM frequency multiples (harmonics) produced by a power electronics converter. In this situation PWM harmonics will be amplified, so that an EMI level at this particular resonance frequency increases. Therefore it might be necessary to include an additional resonance-damping network. Similar effects can be achieved with utilization of magnetic materials with a high imaginary part of permeability, which introduces extra ohmic losses and damps a resonance at the cut-off frequency as a side effect. A cut-off frequency of any filter topology can be found as a following

$$f_{\text{cutoff}} = \frac{1}{2\pi\sqrt{LC}}. \quad (3.5)$$

where L and C are the total inductance and total capacitance of the stage. From (3.5) it is seen that changing of the component's size shifts a cut-off frequency of a filter. When two stages are connected in series a resulting filter has two cut-off frequencies. Since components of a filter are typically balanced (the total capacitance and inductance are split up evenly between all stages), cut-off frequencies of different stages match. If different component values are used, two resonances become explicitly seen.

During analytical modelling of multistage filters several cut-off frequencies (one for every stage) have to be found. Every following cut-off changes a rate of IL change by 40 dB/decade. For example, a $LCLCLC$ -filter has two cut-off frequencies. After the first cut-off IL decreases with 40 dB/decade. After the second cut-off the rate of change increases up to 80 dB/decade, the third cut-off changes the rate of change to 120 dB/decade, etc. Consequently, there are two ways to achieve some specified damping in the particular frequency range; either to use components with smaller values connected in series, which gives a higher rate of IL change, or to shift a cut-off frequency toward a lower frequency range. The first method prescribes implementation of additional components but might be considerably better in terms of power density. The second way allows to use of a simple filter structure, but used components are quite bulky. Eventually a compromise between the number of components and their size must be found in every particular case. However a desirable damping cannot always be achieved with a simple filter topology, even when extremely large components are used. Firstly, increasing of component size leads to increase of self-parasitics. As a result a SRF is shifted to the kHz range and high frequency IL degrade. Secondly, high IL (above 100 dB) in the low frequency range is not achievable due to the slow rate of IL change. Thirdly, Realization of CMCs with inductance higher than $100\ \mu\text{H}$ requires utilization of huge cores and a high number of turns, so that multilayer windings are unavoidable. It leads to significant increase of EPC and degradation of high frequency IL. Fourthly, high capacitance and inductance can negatively influence stability of a PE control system. Moreover, utilization of Y-capacitors higher than several mF results in leakage current exceeding the permitted value (3.5 mA, according to [93]). It becomes clear that high performance of an EMI filter can be only achieved with use of multistage topologies. Detailed analysis of different filter topologies is conducted in Chapter 5. It shows superior properties of multistage filters in terms of IL, power density and price.

When idealized frequency characteristics of the filter under development satisfy all requirements, values of passive components have to be derived from the pre-calculated impedances. During this process it must be kept in mind that the maximum size of Y-capacitors is limited by the maximum leakage current 3.5 mA [93], with a sidenote "Leakage currents greater than 3.5 mA are allowed under certain conditions". The simplest analytical method, which allows estimating leakage current of a filter is defined in [99] as (3.6) for a direct line-to-ground connection ($I_{lk,ig}$) and (3.7) for three-phase applications with Y-capacitors connected between a star point and the ground ($I_{lk,sg}$):

$$I_{lk,ig} = 2\pi f U_{LG} C_Y, \quad (3.6)$$

$$I_{lk,sg} = 2\pi f \frac{0.06 U_{LG} C_X}{3C_X + C_Y} C_Y, \quad (3.7)$$

where U_{LG} is line-to-ground voltage; C_X and C_Y are values of X- and Y-capacitors in farads. The origin of these equation is not rather hard to follow. On one hand in the ideal system leakage current must be equal to zero. On the other hand in the non-ideal system leakage current has to be defined by the source of common mode disturbances. This current is also influenced by the other parameters of CM path within a PE system.

It should be noted that the main contributor to leakage current is the main grid frequency. Nevertheless, harmonics produced by the switching frequency of a particular PE converter contribute to the leakage current as well. It is especially notable if a PWM frequency is rather high (above 8 kHz). For example I_{lk} for a filter with Y- and X-capacitors 3.3 μ F has a leakage current of 6.2 mA according to (3.7). Harmonic voltage with an amplitude 1 V at the frequency 8 kHz results in additional 2.5 mA. With increase of the PWM frequency up to 12 kHz the part of leakage current caused by the first PWM harmonic increases up to 3.7 mA. Laboratory experiments confirm that leakage current of a drive system depends on the switching frequency of a PE converter. Table 3.1 demonstrates a dependency between leakage current and a PWM frequency measured for two different converters with the same EMI filter. It is clearly seen that leakage current increases proportionally with the switching frequency in both experiments. The dependency between leakage current and PWM frequency is not linear in reality, but investigation for exact reasons of such behaviour is out of scope of this work.

<i>Parameter</i>	<i>PWM frequency in kHz</i>			
	2	4	8	16
Converter 1	2.0 mA	2.66 mA	3.7 mA	7.33 mA
Converter 2	2.1 mA	2.48 mA	5.04 mA	6.93 mA

Table 3.1.: Measured leakage currents of the drive systems with different PWM frequencies.

In accordance with a dependency presented above the total leakage current of an EMI filter can be found as (3.8)

$$I_{lk,Tot} = I_{lk,50} + 1.5I_{lk,PWM} \quad (3.8)$$

where $I_{lk,50}$ and $I_{lk,PWM}$ are leakage currents caused by the main grid frequency and PWM frequency. The coefficient 1.5 considers the impact of sub-harmonics of the main PWM frequency. The obtained value $I_{lk,Tot}$ is quite close to reality, so that it is recommended to use it for further C_Y assessment. When the maximum allowed leakage current for the particular system is specified, the maximum value of C_Y can be derived from (3.6) and (3.7) as following (3.9) and (3.10)

$$C_{Y,lg} = \frac{I_{lk,Tot}}{2\pi f C_X U_{LG}} \quad (3.9)$$

$$C_{Y,sg} = \frac{3C_X I_{lk}}{2\pi f 0.06 U_{LG} C_X - I_{lk}}. \quad (3.10)$$

Since there is no safety limitation for X-capacitors, the value of these capacitors is typically quite high. This is also caused by rare use of additional DM inductors, so that DM IL of the particular EMI filter has to be ensured only by X-capacitors and the relatively tiny leakage inductance of a CMC. Consequently the value of X-capacitors can be as large as possible, in order that the specified IL is reached. However, utilization of high capacitance negatively influences a SRF. This effect must be considered at later design stages. An alternative to simply increasing X-capacitors could be distribution of X-capacity among different stages of the filter.

With known Y-capacitor size indispensable CMC inductance can be derived from

$$L_{CMC} = \frac{1}{(2\pi f)^2 C_Y}. \quad (3.11)$$

Alternatively approximated attenuation of the EMI filter for frequencies much higher than the cut-off frequency [66, 145] can be found as (3.12).

$$IL = 20 \log_{10} \left(\frac{\frac{R_L}{R_S + R_L}}{\left(\omega^{2N} \prod_{j=1}^N L_j C_j \right)} \right). \quad (3.12)$$

Resulting IL obtained with this method are similar to the method presented before but it is more complicated to get the values of components which are required for given IL.

The next stage of design includes passive component selection based on impedances obtained previously and modelling of a CMC. Size of Y-capacitors is already known, so that they can be chosen from the available types. During this process the required voltage class and safety type have to be

considered. Design of a CMC can be split up into several phases. Firstly, a core has to be selected. Secondly, with known CMC inductance the necessary number of turns must be calculated. A resulting sample has to be examined to ensure that does not exceed B_{sat} . Finally, EPC can be estimated and included to an equivalent circuit. Apart from CMC inductance, several more initial parameters have to be specified such as current which a CMC can withstand without saturation I_{sat} , saturation flux density B_{sat} (defined by a core material) and leakage inductance L_{dm} . The main contributor to I_{sat} is CM current I_{cm} . The problem of common mode current assessment in a drive system is beyond the scope of this work. However, some approximated value of CM current has to be taken for analytical EMI filter design. Typically it lies within 5% of the nominal phase current. For a given core and with known CM inductance the number of turns is given in (3.13).

$$N = \sqrt{\frac{L_{\text{cm}}}{\mu_0 \mu_r l_{\text{eff}} A_e}}. \quad (3.13)$$

The number of turns equal to the next integer bigger than received N has to be taken in order to achieve satisfactory inductance. Here N is the number of turns per winding; A_e cross section area; μ_0 the permeability constant; μ_r relative permeability; l the main path length of a magnetic core. Thereafter a differential mode inductance or leakage inductance is found as (3.14).

$$L_{\text{dm}} = \frac{\mu_0 N^2 A_e}{l_{\text{eff}}}, \quad (3.14)$$

here l_{eff} is given by (3.15)

$$l_{\text{eff}} = l \sqrt{\frac{\theta}{2\pi} + \frac{1}{\pi} \sin \frac{\theta}{2}}, \quad (3.15)$$

where θ is the angle occupied by a winding and l is the main path length of a magnetic core. (3.15) is valid for $\theta > \pi/6$. Alternatively, leakage inductance can be assessed in accordance with methods presented in [146].

Due to non-ideal effects of a CMC, DM current contributes to the core saturation too. Thus it has to be taken into consideration during B_{sat} estimation. Contribution of CM and DM currents into overall flux can be found as (3.16) and (3.17) respectively.

$$B_{\text{cm}} = \frac{L_{\text{cm}} I_{\text{cm}}}{N A_e} = \frac{\mu_0 \mu_r I_{\text{cm}} N}{l}, \quad (3.16)$$

$$B_{\text{dm}} = \frac{L_{\text{dm}} I_{\text{dm}}}{N A_e} = 3 \frac{\mu_0 I_{\text{dm}} N}{l_{\text{eff}}}, \quad (3.17)$$

I_{cm} is the CM current flowing through the CMC (it is given in initial conditions) and I_{dm} is the DM current, which can be approximated by the nominal phase current. The factor 3 in (3.17) is valid for CMCs with three windings and describes contribution of phase currents to the total flux. On the one hand B_{dm} is considerably smaller than B_{cm} , therefore the factor 3 does not increase the total flux significantly. On the other hand it allows staying on the safe side and avoiding saturation caused by B_{dm} . Finally, a sum of magnetic fluxes induced in a core by I_{cm} and I_{dm} is found as (3.18)

$$B_{tot} = \frac{\mu_0 \mu_r I_{cm} N}{l} + 3 \frac{\mu_0 I_{dm} N}{l_{eff}}. \quad (3.18)$$

B_{tot} must be lower than saturation flux density of the used core material B_{sat} . Nevertheless, in order to get high core utilization a margin between B_{tot} and B_{sat} should be kept above 30% of B_{sat} (3.19)

$$(B_{sat} \cdot 0.7) \leq B_{tot} < B_{sat}. \quad (3.19)$$

Alternatively, if the core material is known, the maximum common mode current is calculated as follows (3.20).

$$I_{max} = \frac{l B_{sat}}{\mu_0 \mu_r N}. \quad (3.20)$$

If the resulting CMC can not withstand the maximum required current and the core is saturated, a core with bigger dimensions has to be taken and the whole CMC choke design procedure has to be repeated. It can take several iterations until all specified conditions are satisfied. In order to safe time use of special computational software such as Matlab or similar is recommended.

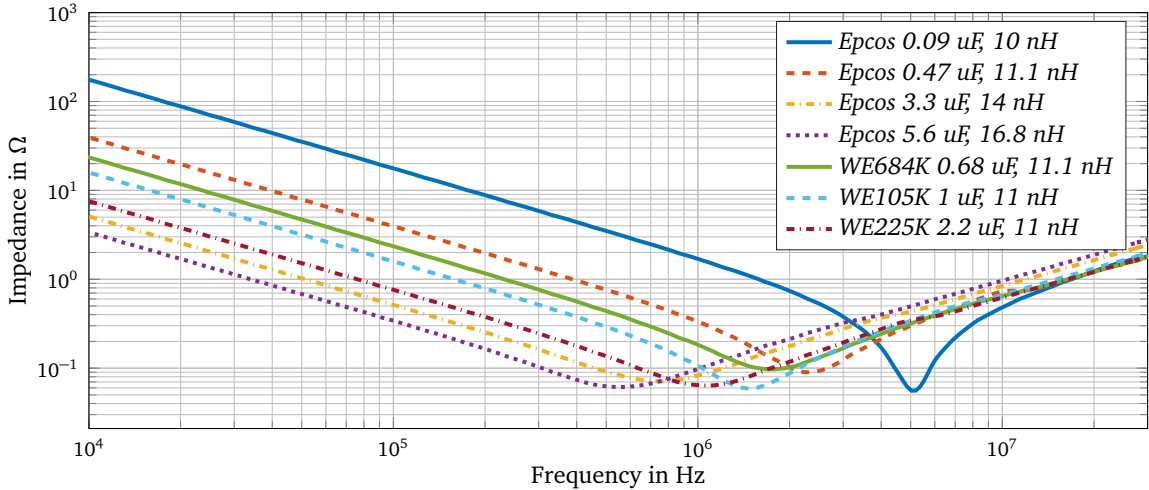
The leakage inductance L_{dm} of a CMC is used for evaluation of DM IL. With known L_{dm} the value of X-capacitors can be found in order to satisfy an initial specification. If required conditions can not be fulfilled by a Γ -topology of a DM-filter an additional group of X-capacitors might be employed. It corresponds to a Pi -topology. Following improvement of IL requires utilization of DM chokes, which is not mandatory in the vast majority of cases.

Thereafter, non-ideal characteristics of components have to be included into the model. Self-parasitics depend mainly on geometry. Value of ESL for film capacitors used in EMI filters is typically in the range 8–18 nH. ESL of capacitors in most cases can be found in a datasheet or can be derived from a measured resonance frequency according to (3.21)

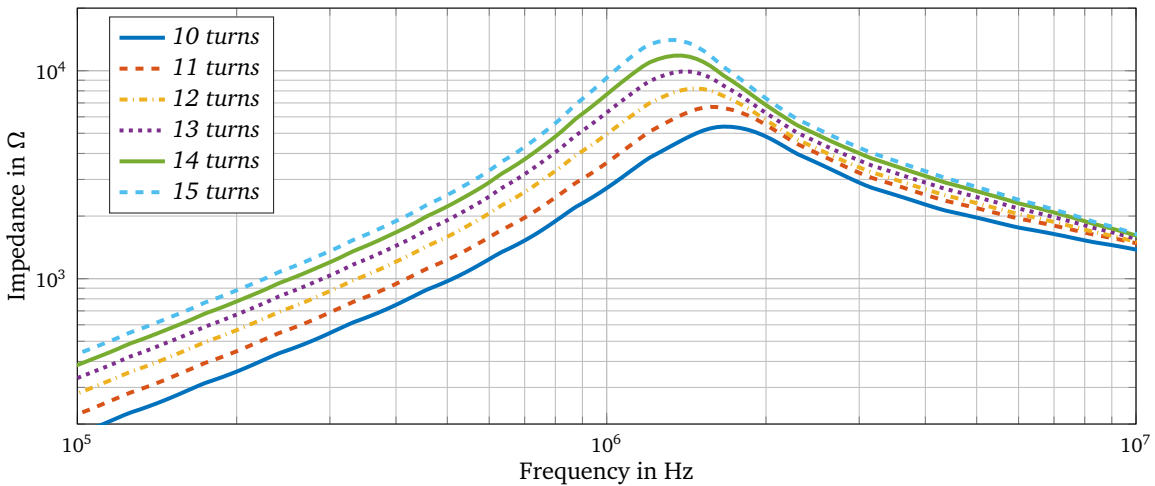
$$L_{ESL} = \frac{1}{(2\pi f_{SRF})^2 C}. \quad (3.21)$$

According to equation (3.21) increasing of main capacitance shifts SRF of a capacitor toward the lower frequency range. It can be concluded that increasing of capacitor values leads to improvement of low frequency IL but negatively affects high frequency IL. Measured characteristics of conventional film capacitors with different capacitance values are depicted in Figure 3.4a. Neither analytical nor FEM esti-

mation of ESL are often used, because capacitors are typically purchased and all parameters are given by manufacturers. However, some methods of ESL estimation based on 3D electromagnetic modelling can be found in literature [33, 118]. In contrast to capacitors, CMCs are usually designed during filter devel-



(a) Impedance of capacitors with different ESL and capacity values (measured data).



(b) Impedance of a CMC (ferrite N87) with different turn numbers (measured data).

Figure 3.4.: Impact of self-parasitics on impedance of capacitors and inductors.

opment. Therefore, EPC estimation of a CMC requires more detailed discussion. EPC vary depending on geometry and the number of turns. Total EPC of a CMC consists of turn-to-turn C_{tt} and turn-to-core C_{tc} capacitors. From Figure 3.4b it can be seen that the number of turns has minor impact on the SRF of a CMC. The resonance frequency is shifted due to decrease of inductance, but for all studied cases (10...15 turns) EPC is changed insignificantly. These effects are explained by the series-parallel connection of C_{tt} and C_{tc} capacitors [157]. Physical parameters indispensable for calculation of EPC are shown in Figure 3.5.

According to [157] the exact turn-to-turn capacitance consists of the coating capacitance and the capacitance of the air gap between two adjacent turns connected in series and can be estimated with

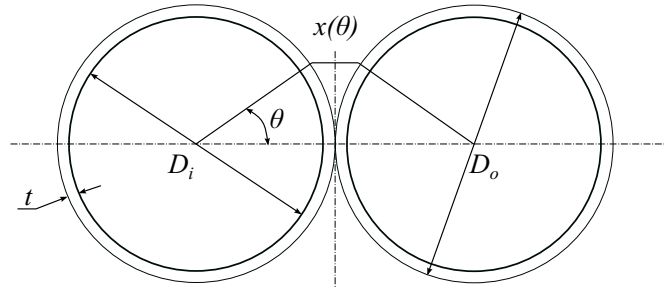


Figure 3.5.: Physical parameters of the CMC for EPC calculation.

equation (3.22). In accordance with laboratory measurements for an actual enamelled cable the coating thickness lies in the range from 2% up to 10% of a cable diameter.

$$C_{tt\text{-exact}} = \frac{2\epsilon_0 l_t}{\sqrt{\left[1 + \frac{1}{\epsilon_r} \ln \frac{D_o}{D_i}\right]^2 - 1}} \arctan \left[\sqrt{\frac{2 + \frac{1}{\epsilon_r} \ln \frac{D_o}{D_i}}{\frac{1}{\epsilon_r} \ln \frac{D_o}{D_i}}} \right] \quad (3.22)$$

and a simplified model according to [135] leads to (3.23)

$$C_{tt\text{-simpl}} = \epsilon_0 l_t \left[\frac{\epsilon_r \theta^*}{\ln \frac{D_o}{D_i}} + \cot\left(\frac{\theta^*}{2}\right) - \cot\left(\frac{\pi}{12}\right) \right] \quad (3.23)$$

$$\theta^* = \arccos \left[1 - \frac{\ln \frac{D_o}{D_i}}{\epsilon_r} \right] \quad (3.24)$$

where θ^* is given by (3.24); $\epsilon_0 = 8.85 \times 10^{-12}$ in F/m free space permittivity; ϵ_r relative permittivity of the coating dielectric; l_t the mean-turn length; D_o and D_i are diameters of a wire with and without insulation respectively. EPC of several CMCs was assessed using (3.23) and measured with a network analyser. Resulting deviation between measured and calculated data lies within 25%.

A stray capacitor between a turn and a core is seen as a capacitor between a plane and a conductor. Then the path length of the electric field line is only half as long as in the case of two adjacent turns. Capacity is inversely proportional to the distance between plates and consequently C_{tc} should be twice as big as C_{tt} according to (3.25), as can be seen in Figure 2.6.

$$C_{tc} = 2C_{tt} \quad (3.25)$$

the overall EPC can than be represented by means of equivalent circuits consisting of parallel and series connection of C_{tt} and C_{tc} . For a single-layer winding the value of EPC is decreasing with increase of the number of turns, starting from $C_{EPC}(2N) = 2C_{tt}$ for the two turns choke. C_{EPC} of the choke with three

turns (an equivalent circuit is shown in Figure 2.6a) after several star to delta transformations is (3.26).

$$C_{\text{EPC}}(3N) = \frac{4C_{\text{tt}}12/5C_{\text{tt}}}{4C_{\text{tt}} + 12/5C_{\text{tt}}} = 1.5C_{\text{tt}}. \quad (3.26)$$

The general equation for calculation of the stray capacitance for coils consisting of any number of turns is expressed as (3.27).

$$C_{\text{EPC}}(nN) = \frac{C_{\text{tt}}}{2 + \frac{C_{\text{tt}}}{C_{\text{EPC}}(n-2)}} + C_{\text{tt}}. \quad (3.27)$$

Eventually C_{EPC} stops to grow at the constant, which is equal to $1.366C_{\text{tt}}$ for the number of turns, which is higher than 10 the following is true (3.28) [135].

$$C_{\text{EPC}} \cong 1.366C_{\text{tt}}, \quad nN \geq 10 \quad (3.28)$$

(3.28) confirms that the number of turns has a minor effect on EPC of a choke. In contrast with expectations, increasing the number of turns leads to lower overall EPC C_{EPC} . Figure 3.4b shows that decreasing the turn number insignificantly influences an SRF. However, an SRF of a CMC with a lower number of turns is shifted towards high frequency due to decrease of inductance. According to (3.28) the SFR of the CMC with a turns number higher than 10 is only affected due to change of inductance, which corresponds to a factor of 1.5. As it is seen in Figure 3.4b the difference between the SRF of the choke with 15 turns (1.83 MHz) and the SRF of the choke with 10 turns (1.24 MHz) is 1.475. It adheres to the theory described above. In some cases decreasing a turn number can lead to worse core utilization, so that the maximum power density for a given core cannot be achieved.

With known ESL and EPC, the equivalent circuits depicted in Figure 3.2 can be redrawn as shown in Figure 3.6.

Since every soft magnetic material has a natural resonance of permeability, degradation of permeability can be roughly modelled by means of a second order transfer function. Nevertheless, if permeability is implemented in a filter mathematical model as a reactive network, components of it start to interact with the other reactive components of the filter. It leads to the appearance of extra resonances which do not exist in reality. However, effects caused by permeability degradation can be considered with utilization of a simple capacitor-resistive branch in parallel with an inductor (Figure 3.7). Certainly, this solution does not accurately represent real permeability characteristics. A proposed type of a network is derived from experiments. Value of the capacitor can be found as C_s multiplied by 5. Value of the resistor should be between 1 k Ω and 50 k Ω for ferrite materials and 0.5 k Ω -20 k Ω for nanocrystalline. Resistor value has to be found empirically, as no dependency on the other parameters of the filter mathematical model has been found. This value strongly depends on the core material used and a particular CMC geometry. Prototyping is one of the possible solutions for this issue, so that values of components can be adjusted in accordance with a prototype. The final equivalent circuits for standard filter topologies with simplified permeability characteristics are shown in Figure 3.7. It is worthwhile to mention that for a

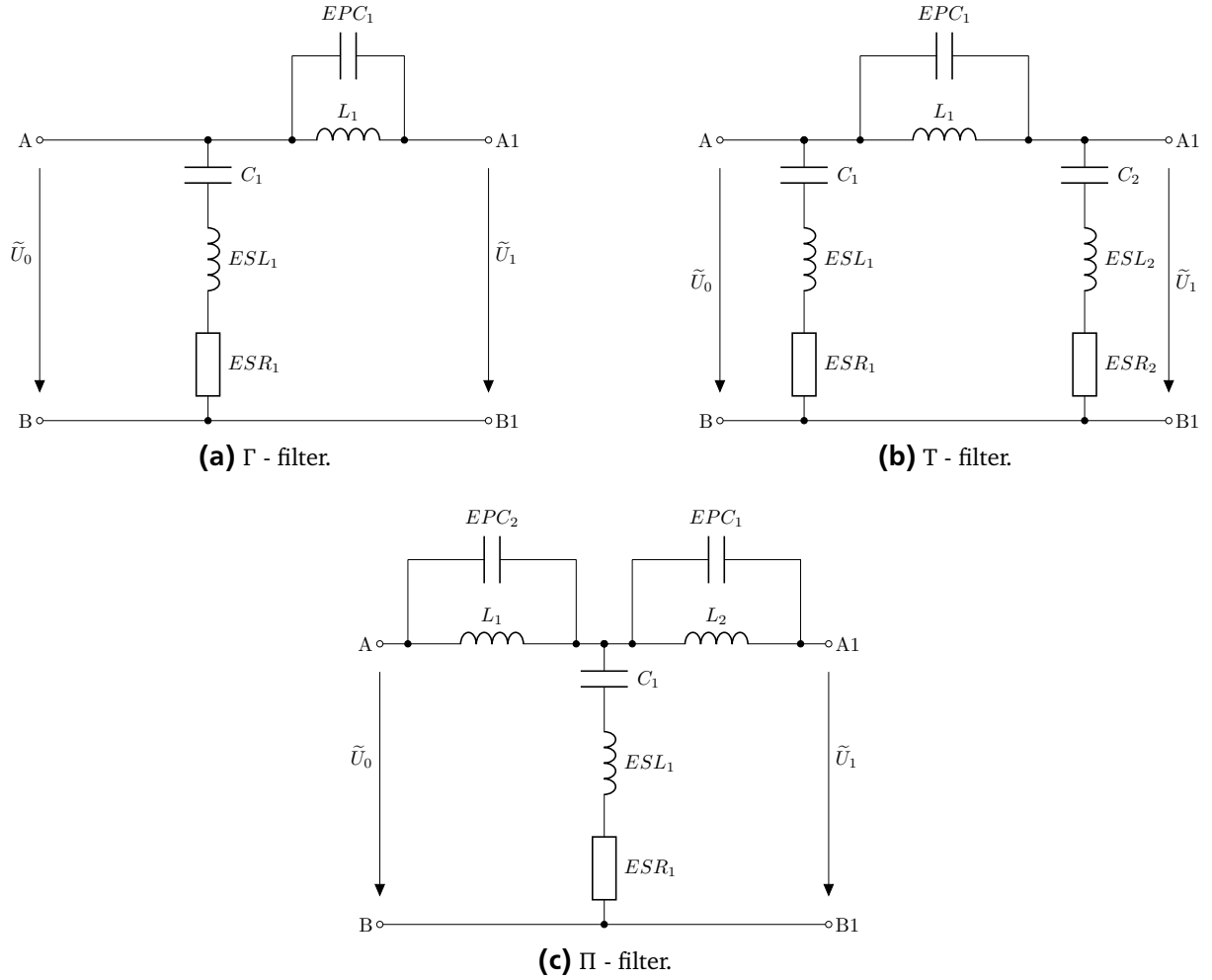


Figure 3.6.: Standard filter topologies with included EPC and ESL.

rough estimation of IL a filter model without exact consideration of permeability effects is sufficient, as degradation of the CMC impedance is ensured by EPC.

Eventually differential and common mode IL of the filter are modelled employing equivalent circuits from Figure 3.7. All parameters necessary for this model are obtained analytically, without involvement of extra simulation tools. In order to model IL of the standard circuits depicted in Figure 3.7 respective impedances in (3.2), (3.3) and (3.4) must be substituted with (3.29) for inductors and (3.30) for capacitors

$$Z_C = \frac{1}{j\omega C_1} + j\omega L_{ESL} + R_{ESR}, \quad (3.29)$$

$$Z_L = \frac{1}{\frac{1}{j\omega L} + j\omega C_{EPC} + \frac{1}{(1/j\omega C_{core} + R_{core})}}. \quad (3.30)$$

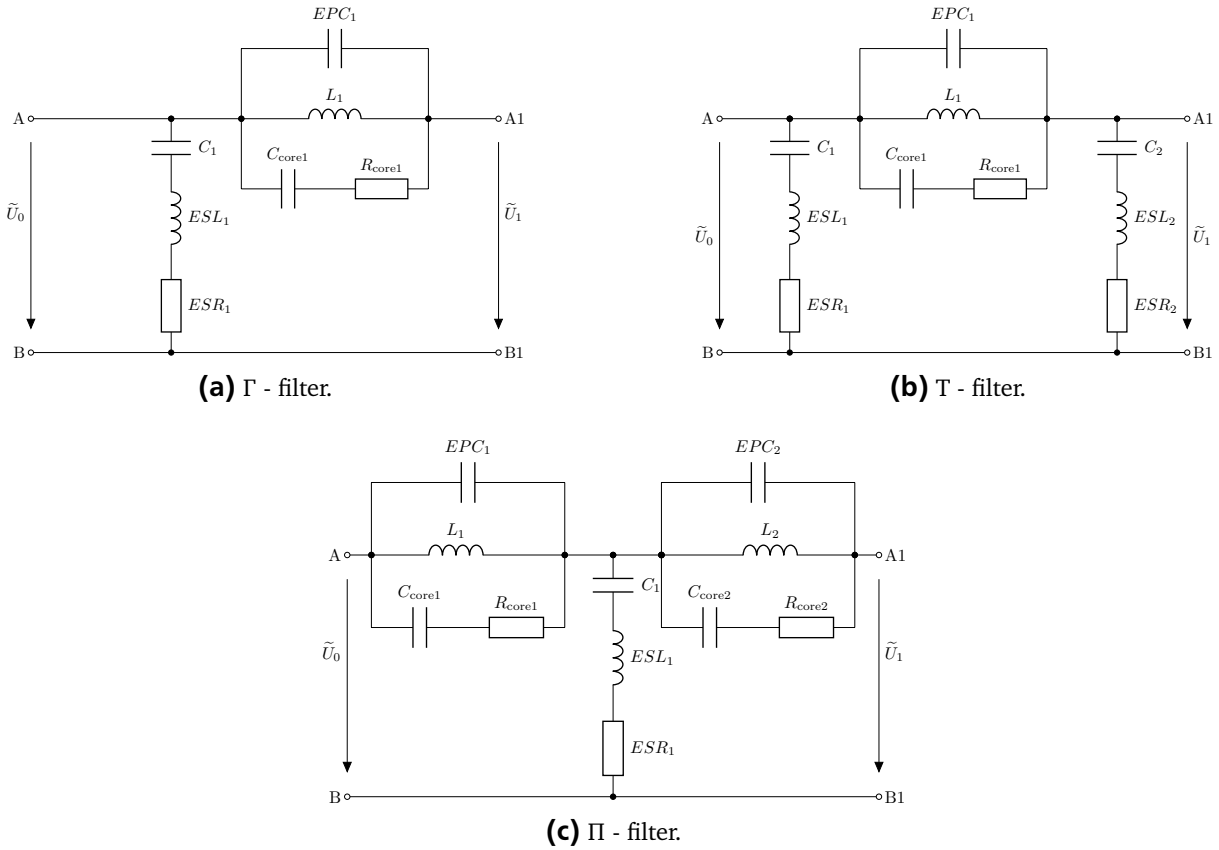


Figure 3.7.: Standard filter topologies with included parasitics and considered permeability degradation.

In order to achieve better results, core characteristics have to be modelled more precisely. In this case networks of higher complexity must be used. More important is the fact that parameters of those networks are extremely complicated to figure out analytically, without building a prototype. From conducted simulations it is concluded that representation of a core material as a simple resistor in series with the main inductance (as it recommended in some references) does not give good results, especially in the high frequency range. The final IL modelled utilizing equations (3.2), (3.3) and (3.4) with (3.29) and (3.30) takes into account degradation of IL due to stray components and permeability diminishing at the high frequency. For any other filter topology IL can be found using the same principles presented in this section. In this case coefficients of (3.1) have to be derived from corresponding equivalent circuits. Finally, if the initial specification is not fulfilled by the results obtained from simulation with non-ideal parameters, one of the following options can be applied:

- Change a material used for CMC;
- Increase values of inductors/capacitors;
- Apply EPC and ESL compensation methods;
- Utilize other filter topologies;
- Increase the number of stages.

This step requires comprehensive understanding of processes within a filter in order to chose an appropriate improvement method for every particular situation. Filter improvement methods are discussed in detail in Chapter 4 and Chapter 5.

3.1.1 Analytical Model Validation

The proposed analytical model is validated with EMI filter prototypes built and measured in a laboratory. It is important to note that IL were obtained from measurements with a vector network analyser (VNA) Keysight E5061B [108] with an accuracy of 10 %, related to the dB scale. A more detailed description of the measurement setup that was used can be found in Appendix C.

Measurements of three filter prototypes, which represent Γ -, Π - and T -topologies were carried out. The resulting comparisons with the corresponding analytical models are shown in Figure 3.8, Figure 3.9 and Figure 3.10. The error between the Γ - filter model and the measured prototype lies within ± 15 dB. Generally the model shows correct tendency in the entire frequency range with almost ideal agreement in the range 1–600 kHz. Some disagreement in the range 600 kHz–1 MHz is provoked by the simplified model of soft magnetic material used for a CMC. A resonance at 25 MHz is primarily caused by properties of a PCB which has not been included in the presented analytical model. Similar resonances are seen in IL of filters based on T - and Π -topologies. Parameters used for simulation with the proposed filter models are summarized in Table 3.2.

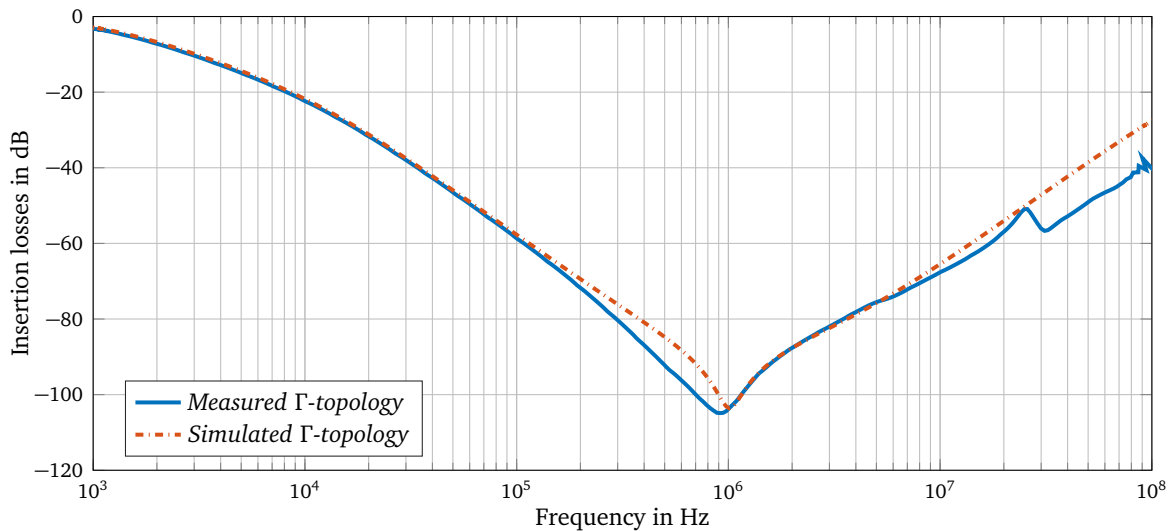


Figure 3.8.: Comparison between the analytical model and prototype of a Γ -topology (50 Ω /50 Ω).

Topology	Main components		Axillary components				
	C_1, C_2	L_1, L_2	$ESL_1,$ ESL_2	$ESR_1,$ ESR_2	$EPC_1,$ EPC_2	$C_{Core1},$ C_{Core2}	$R_{Core1},$ R_{Core2}
Γ - topology	2.1 μF *3	0.62 mH	3 nH	63 m Ω	21 pF	21 pF	3500 Ω
Π - topology	0.1 μF *3, 0.68 μF *3	0.62 mH	1.3 nH, 9 nH	150 m Ω , 180 m Ω	21 pF	21 pF	1700 Ω
T - topology	0.1 μF *3	0.62 mH	9 nH	150 m Ω	21 pF	21 pF	3500 Ω

Table 3.2.: Parameters of filter models used for validation of the proposed modelling method.

Measured insertion losses of T - and Π -topologies extend the measurable range of the used network analyser. Therefore tolerance of resulting measurements in the range under 100 dB might be

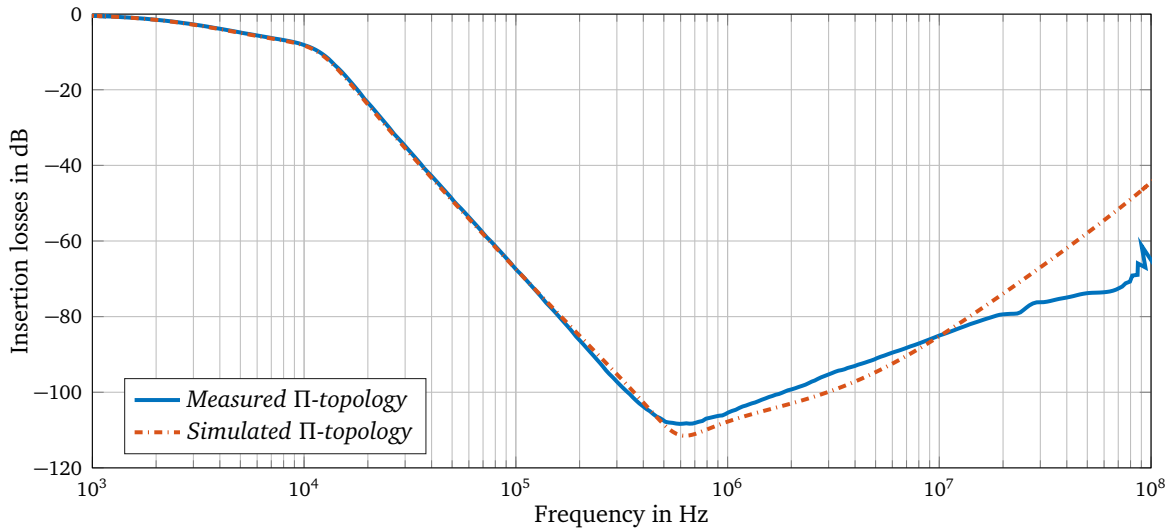


Figure 3.9.: Comparison between the analytical model and prototype of a Π -topology ($50 \Omega/50 \Omega$).

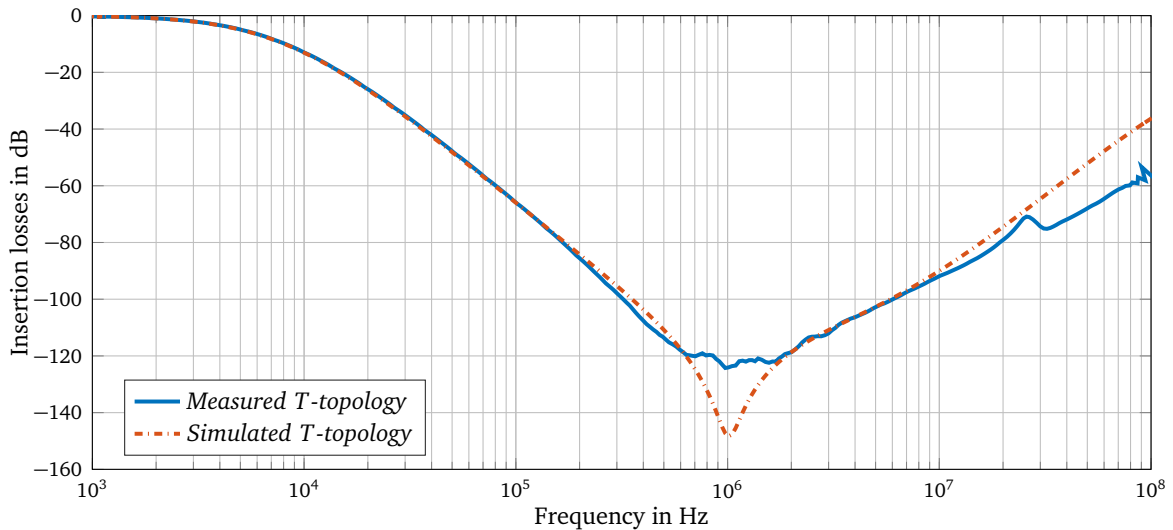


Figure 3.10.: Comparison between the analytical model and prototype of a T -topology ($50 \Omega/50 \Omega$).

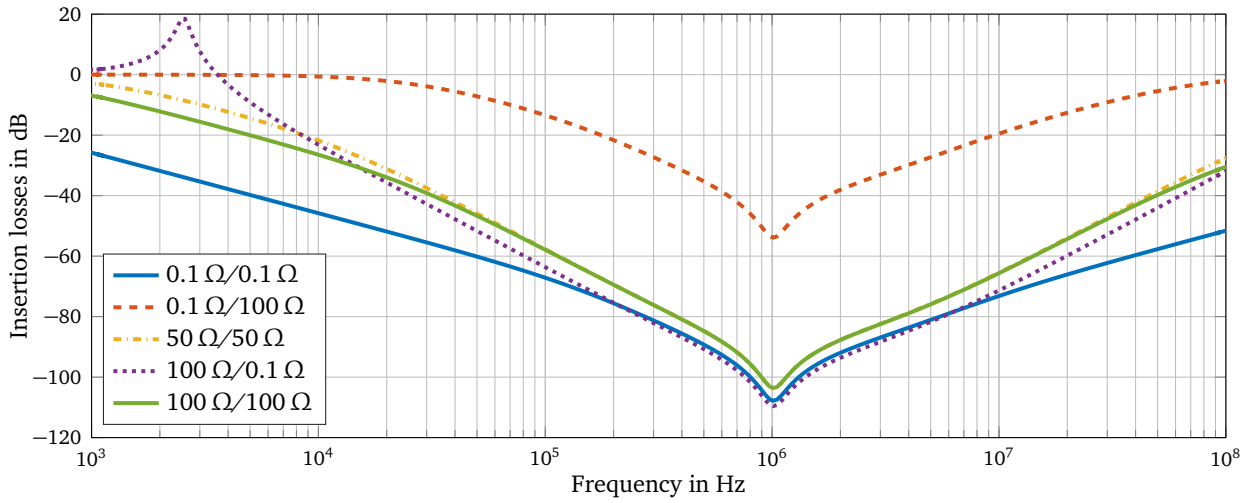
insufficient and after 120 dB a signal amplitude is so small that it is not possible to sense. Analytical models for all three topologies agree well in the low frequency range (up to 0.7 kHz). For a T -topology it is not possible to compare simulated and measured IL in the range 0.7–2 MHz due to instrumentation reasons. Resonances caused by parasitics match quite well for all topologies. In the range 1–100 MHz the models do not reflect the actual behaviour perfectly, although they exhibit the same tendency as measured prototypes. The observed mismatch is caused by simplifications made earlier. Even EMI filter prototypes with eliminated mutual couplings, used for the model validation, demonstrate strongly non-linear behaviour at the high-frequency. These effects are explained by phenomena such as soft magnetic material properties, PCB effects, mutual couplings and the tolerance of measurements. Most importantly, in the proposed analytical model the degradation of IL with frequency is reflected. From conducted simulation and measurements it is seen that EMI filters can be modelled utilizing the proposed method with an excellent proportion between time and accuracy.

3.1.2 Impact of Load and Source Impedances on Insertion Loss

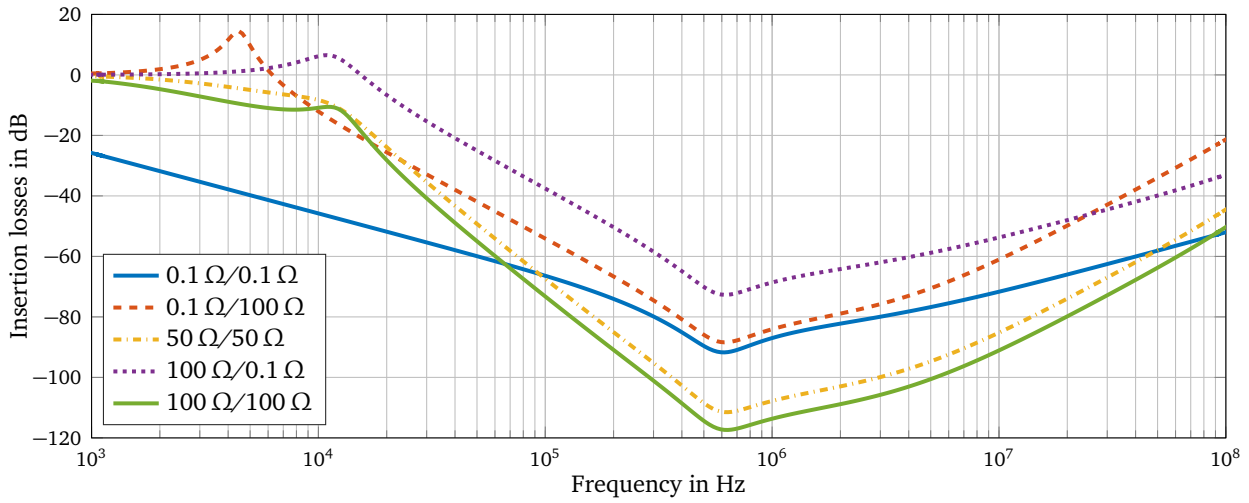
From equations (3.2), (3.3) and (3.4) it becomes obvious that IL are strongly affected by source and load impedance (sometimes referred to as characteristic impedance). In order to determine significance of the system impedance impact on IL, behavioural models of Γ -, Π - and T -topologies are characterized for the following standard combinations of load and source ohmic impedances: $50\ \Omega/50\ \Omega$; $100\ \Omega/0.1\ \Omega$ and $0.1\ \Omega/100\ \Omega$. The last two impedance combinations are referred to as the worst case scenarios in CISPR17/EN55017 [92]. Those cases of study do not demonstrate the exact damping of the filter connected to a PE system, but allow comparison of different types of EMI filters under similar conditions. According to standard definition, a tested filter should show the worst IL when it is connected to the $0.1\ \Omega/100\ \Omega$ system [92, 117]. But this is completely correct only for a Γ -topology, since it exhibits the lowest IL under $0.1\ \Omega/100\ \Omega$ conditions. A T -topology demonstrates the worst IL with $0.1\ \Omega/0.1\ \Omega$ impedance and a Π -topology has the lowest IL with $100\ \Omega/100\ \Omega$ impedance. Both aforementioned cases are not taken into account in the existing standards. Figure 3.11 demonstrates characteristics of the simplified analytical filter models validated earlier, which were simulated with five different sets of source and load impedance. All parameters of the models remain as shown in Table 3.2.

The combination of load and source impedance, which results in the worst IL, is different for every considered filter topology (Figure 3.11). It contradicts CISPR17/EN55017, where the impedance combination $0.1\ \Omega/100\ \Omega$ is referred to as a combination for the worst case scenario IL evaluation. Furthermore, with variation of the source and load impedances IL changes dramatically. For example, the difference between IL of a Γ -topology characterized under $50\ \Omega/50\ \Omega$ impedance and $0.1\ \Omega/100\ \Omega$ exceeds 50 dB and in the worst case the maximum IL hardly reaches $-50\ \text{dB}$ (Figure 3.11a). Consequently, employment of filters with a Γ -topology in the systems with high load impedance is inefficient. A Π -topology is less influenced by impedance variation, and the maximum degradation from $50\ \Omega/50\ \Omega$ in the worst case does not exceed 40 dB. IL demonstrated by a Π -topology remains quite high with all possible source and load impedances, reaching $-70\ \text{dB}$ under the worst conditions (Figure 3.11b). It makes the Π -topology a good candidate for power electronics systems with unknown source and load impedances. The best behaviour in terms of IL stability with variation of system impedance is exhibited by a T -topology. With the worst case impedance combination ($100\ \Omega/100\ \Omega$ for T -topology) IL remains quite high (up to $-100\ \text{dB}$) and the maximum deviation from $50\ \Omega/50\ \Omega$ does not exceed 50 dB (Figure 3.11c). Finally, it can be concluded that dependency of IL on system impedance lowers with increasing filter complexity.

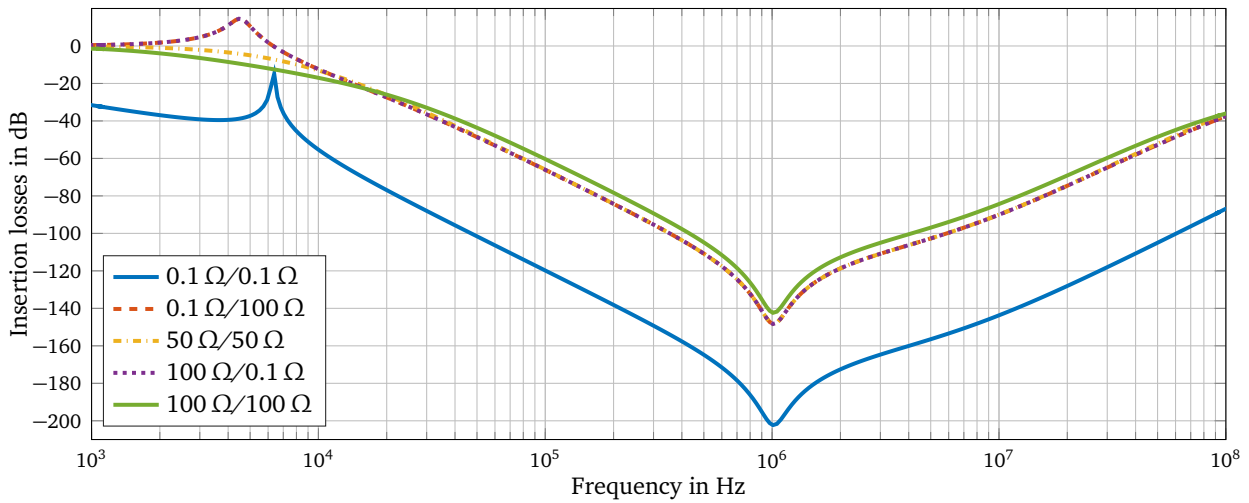
In reality impedances of the power grid and consumers being connected to the grid are extremely complex, and significantly differ from resistive systems standardized for EMI filter characterization [92]. DM impedance of the power grid in Europe is determined as 90th percentile value for supply impedance (for residential customers who are mostly fed by overhead LV distribution) as $0.4 + jh0.25\ \Omega$, where h is the harmonic order [88]. In [89] values for the mains impedance at 50 Hz are given for distribution networks with a load up to 16 A/phase. The values for the phase conductors are $(0.24 + 0.15i)\ \Omega$ and the impedance for the neutral wire is slightly smaller $(0.16 + 0.1i)\ \Omega$. It means that both standards assume resistive-inductive behaviour of the grid, which still does not reflect the real grid impedance (especially on high frequencies). Moreover it does not include the excessive installation of shunt capacitors as part of



(a) Γ - topology.



(b) Π - topology.



(c) T - topology.

Figure 3.11.: Simulated IL of the standard filter topologies with different load and source ohmic impedance.

EMI filters of power electronics in the grid. CM current primarily via stray capacitors of the drive system. Hence the capacitive nature of CM load a source impedances can be assumed (Appendix D).

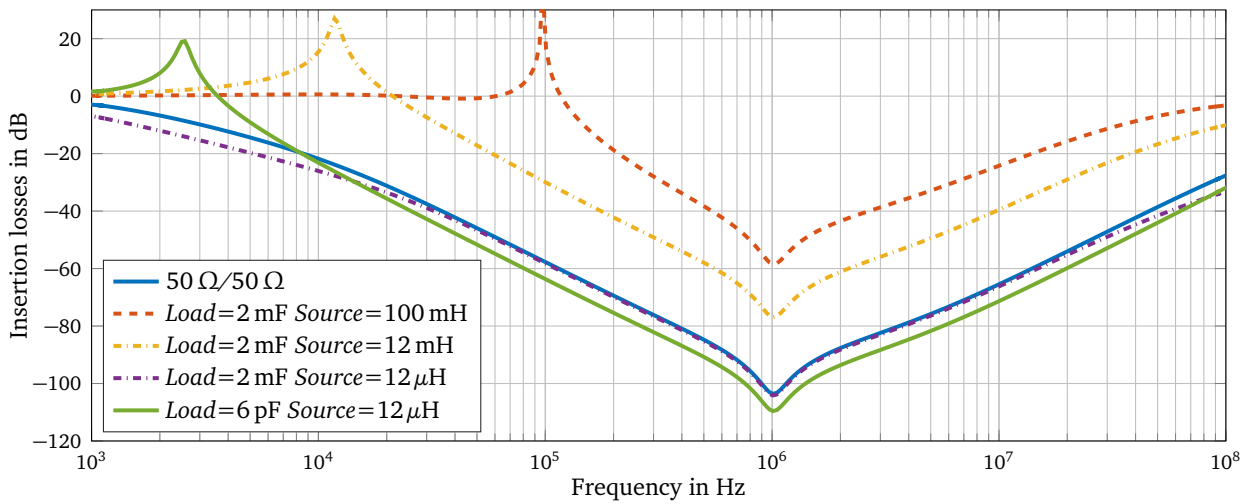
Previously made assumptions concerning power grid and AIC impedance can be used in order to estimate behaviour of standard filter topologies under conditions close to the reality. Load and source resistors in the filter models are replaced with capacitive-resistive load and inductive-resistive source impedances. IL determined under these load and source conditions are shown in Figure 3.12. Values of components are chosen in order to find the maximum possible deviation from IL of a filter connected to the $50\ \Omega/50\ \Omega$ system. The source side is represented by R and L connected in series (R is $0.01\text{--}10\ \Omega$ and L is $0.01\ \mu\text{H}\text{--}5\ \text{mH}$). The load side is an RC series network with capacitance equal to a DC link capacitor, which lies typically in the range $0.05\text{--}10\ \text{mF}$ and R in the range $0.01\ \Omega/1\ \Omega$. IL exhibited by three typical filter topologies is once again estimated under the aforementioned load and source parameters. Resulting IL for cases with the maximal deviation from the $50\ \Omega/50\ \Omega$ system are depicted in Figure 3.12. Some undesirable effects like additional high- and low-frequency resonances are observed. Nevertheless, a common tendency of IL shown by filters connected to the system with reactive impedance remains similar to the pure resistive system.

IL of Γ -, Π - and T - topologies characterized under reactive source and load impedance conditions is similar to IL obtained under resistive source and load conditions, with an exception of aforementioned resonances. In some cases IL exhibited by the typical filter topologies under the reactive load and source impedances are better than for the resistive system. Conducted experiments once again confirm that use of resistive load and source impedance does not reflect the real filter behaviour due to reactive character of components in the actual PE system. In order to assess IL under the real worst case conditions a filter under development must be characterised using reactive, instead of purely ohmic impedance. Nevertheless, the resistive system is sufficient for rough IL estimation, since behaviour of filters under ohmic and reactive load and source impedance is similar. Surely, characterisation of an EMI filter with ohmic load and source impedance can be used for IL comparison. Due to the undoubted importance of grid impedance for the EMI filter design, simulation of EMI filters with power grid and PE converter models is one of the most important activities for future studies.

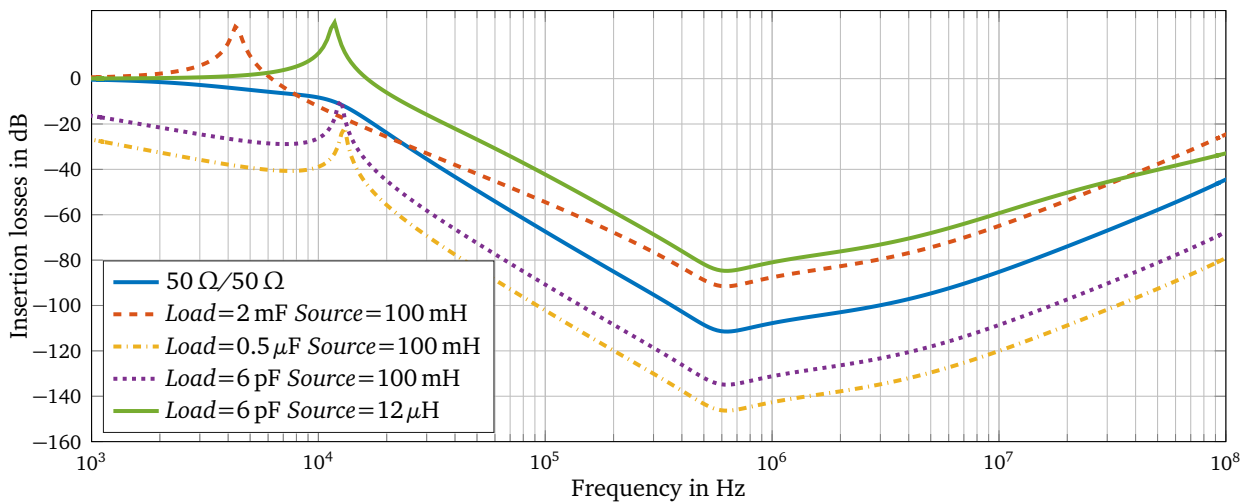
IL of the filter under design can be quite easily estimated under different load and source conditions using the proposed analytical approach assisted with reactive load and source impedances. In this case some critical system topologies can be considered during a design phase. The complete methodology of EMI filter design based on the simplified analytical approach is summarized in a flowchart depicted in Figure E.1.

3.2 SPICE Based EMI Filter Design Assisted with FEM Modelling

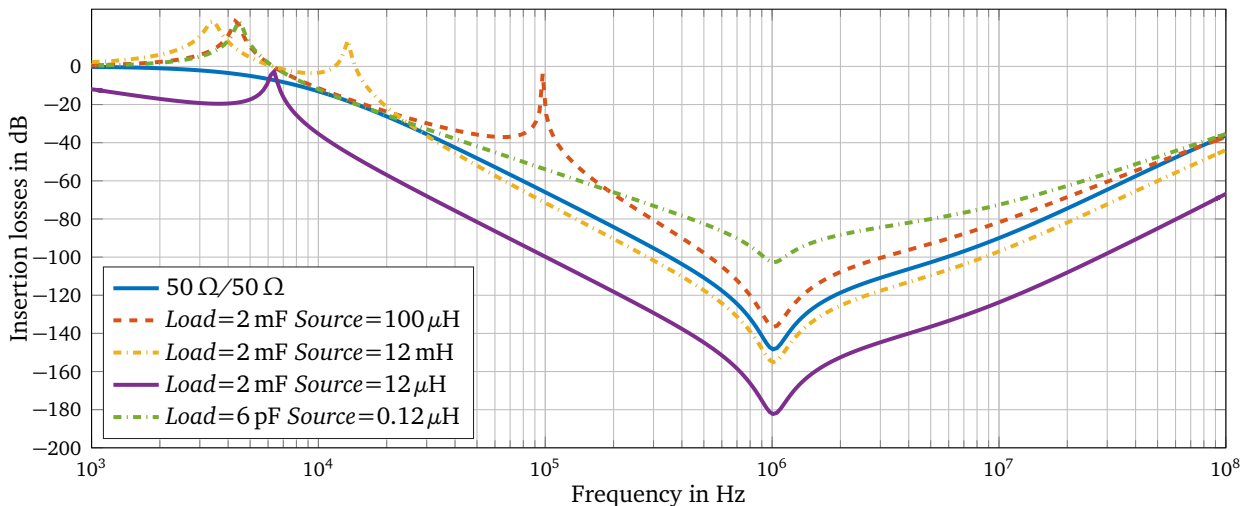
The analytical model presented in Section 3.1 is more suitable for the first estimation of IL than for detailed EMI filter simulation, as it does not allow simulating IL of an EMI filter accurately. Moreover, consideration of nonideal effects in the analytical model is rather difficult. Thus, a model based optimization and improvement of IL size or costs cannot be performed. Saturation effects, frequency dependent variation of permeability, self-parasitics and mutual couplings between filter components are crucially important and must be taken into account for building of an accurate behavioural model. The modelling method, presented in this section, considers all listed non-ideal phenomena. Resulting behavioural mod-



(a) Γ - filter.



(b) Π - filter.



(c) T - filter.

Figure 3.12.: Simulated IL of the standard filter topologies with different reactive load and source impedance.

els of EMI filters are quite complex and it is more convenient to develop such models with specialised circuit analysis software. The SPICE language, which is dedicated to the simulation of analog electronic circuits, is one of the most widespread programs in the field of electrical engineering. A default SPICE frequency sweep function is perfectly suitable for EMI filter design. Moreover, both the frequency and time domain analyses can be conducted without any changes in the model if the behavioural model is properly prepared.

Similar to the analytical approach presented in Section 3.1, the starting point for a three-phase EMI filter modelling based on SPICE is estimation of idealized IL. Hence, only ideal elements are included into a filter equivalent circuit, which was prepared in the LTspice environment. Since DM and CM IL must be evaluated separately, some changes in schematics must be made; connection of the filter model to the reference impedance has to be selected in accordance with simulated IL type (Figure 1.14). It allows utilization of the same EMI filter mathematical model for DM and CM IL characterisation. Thereafter, self-parasitics of passive components are included into the filter circuit as lump components. Self-parasitics can be calculated according to analytical methods presented in Section 3.1. Alternatively, they can be directly measured with a network analyser. A simple model of a three-phase CMC can be created with the help of a coupling coefficient (default function in LTspice). This coefficient can be adjusted according to mutual inductance between the windings of a CMC. At this stage, particularization of filter characteristics should be similar to results obtained from the simplified analytical model, as was shown in Figure 3.8, Figure 3.9 and Figure 3.10. For further enhancement of a filter mathematical model, the simple CMC model has to be substituted with an advanced one. Such advanced CMC models must precisely reflect variation of permeability with increase of the frequency. Saturation effects of a CMC have to be included into the same model, so that degradation of IL caused by core saturation can be prevented at the design stage.

3.2.1 Novel Behavioural Model of CMC

There is a lack of mathematical models of CMCs which treat high frequency phenomena, caused by permeability degradation combined with core saturation effects. Since the main focus of this work is three-phase EMI filters, a behavioural model of a three-phase CMC is proposed. Nevertheless, the proposed three-phase model can be, when it is required, simplified to a single-phase CMC. The majority of existing CMC models assume permeability to be a constant [123, 129, 130]. Typical impedance based CMC models consist of a series inductor and a parallel resistor, which represent the leakage inductance and power losses within a core, respectively, and a capacitor, which represents EPC. In this case, the high-frequency behaviour of a CMC is defined solely by EPC. Such models are not very accurate. Moreover, consideration of saturation effects is not possible [102]. The second commonly used type of CMC models is based on a network consisting of a group of active and reactive components. The values of components are selected according to measurements of the choke prototype. This type of model is quite accurate, but they are not flexible in terms of core dimensions and the number of turns. This means that a model must be redesigned for every variation of a CMC [116]. A look-up table with the linear interpolation of measured core characteristics is also used from time to time. Poor scalability and principle impossibility for considering saturation in such models are the main disadvantages of the last method. Some attempts towards building CMC behavioural models that consider frequency dependent permeability and satura-

tion have been reported. However, those models are not applicable for three-phase EMI filters and not easily scalable [2, 141, 173].

Several mathematical models of frequency dependent permeability are presented in literature. Landau and Lifshitz models, first and second order Debye models, losses based and polynomial models can be used for mathematical modelling of permeability. The most widespread models are based on the complex permeability $\mu = \mu' - j\mu''$ [26]. On low frequencies permeability is a real number and therefore, vectors of H and B are in phase. On the high frequencies phase shift increases and the angle between H and B increases too. This phase shift is caused by eddy currents and magnetic losses in a core material. Two components of the complex permeability can be represented in terms of the frequency dependent resistor and inductor. For the majority of materials a parallel connection of the resistor and inductor is used [26]. The main disadvantage of those models is relatively complicated implementation in circuit simulators. Alternatively, frequency dependency of permeability can be described in S-domain as a transfer function with an even number of poles and zeros [122]. According to the classical control theory any transfer function can be represented as an equivalent network, which is rather simple to simulate with circuit analysis software. The proposed CMC behavioural model is based on a similar approach.

Similar to permeability, magnetic hysteresis is a heavily non-linear effect. Nevertheless, a great variety of magnetic hysteresis models exist in literature [100, 141, 181]. The most well-known mathematical models are simple tangential, exponential and additive models [38], as well as more complex ones like Jiles-Atherton and Preisach models [12]. The simple hysteresis models are fully sufficient for EMI filters, since permeability degradation with increasing current is the most important aspect in this application. Nonetheless, more complicated hysteresis models can be implemented in the proposed CMC behavioural model with a moderate investment of time.

Due to their physical nature, soft magnetic materials represent a system with four pairs of poles and zeroes. Two pole-zero pairs describe real and imaginary components of domain wall motion and two other pairs are responsible for real and imaginary components of gyromagnetic spin motion. However, experiments show that good results can be achieved by employing a network with only two poles and two zeros. Resulting soft magnetic material characteristics represent a vector sum of all components. These permeability characteristics of a soft magnetic material are used as a base for building a CMC behavioural model.

Comprehensive permeability characteristics of a material are necessary for preparation of a mathematical model. Unfortunately, the majority of suppliers do not provide $\mu(f)$ characteristics and therefore magnetic materials have to be parametrized by a filter designer. Measurements of permeability can be accomplished either in terms of the frequency dependent resistive and inductive components or complete one-turn impedance. Thereafter, coefficients of a mathematical function describing the measured characteristics have to be found. Since the frequency dependency of permeability can be described as a second-order transfer function (two poles and two zeros), the general equation suitable for any material is (3.31)

$$H(s) = \frac{as^2 + bs + c}{a's^2 + b's - c'} \quad (3.31)$$

Coefficients a , b , c , a' , b' , c' for a given material are found with Matlab System Identification Toolbox. The obtained transfer function can be directly used in LTspice for CMC simulation in the frequency domain. However, it is not possible to conduct the time domain simulation with the S-parameter based CMC model. For further consideration of saturation effects the transfer function has to be transformed into the form of an electrical network. The RLC electrical network, which represents the transfer function, is synthesized using the Foster network synthesis method (Figure 3.13). The same transfer function can be alternatively represented as a Cauer network. Basically, there is an infinite number of electrical networks, which can describe a single transfer function. The synthesized network includes two inductors, representing poles, and two capacitors, representing zeros of the given transfer function. From the measured impedance it can be seen that the poles do not lie directly on the imaginary axis, which means that some energy dissipation is introduced. Therefore, some additional resistors are added for damping purposes (Figure 3.13).

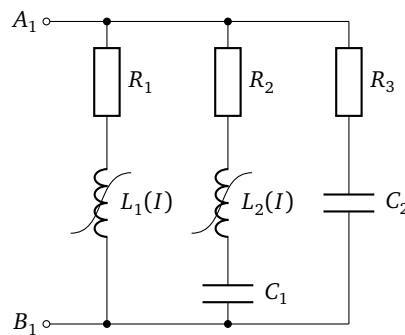


Figure 3.13.: RLC Foster network used for representation of frequency dependent permeability.

The synthesized network is implemented in LTspice. All phases of CMC are simultaneously connected to the RLC-network representing magnetic properties of the core. The connection is realized by means of voltage dependent voltage sources. In order to realize a principle of magnetic flux compensation for a differential mode (DM) current and calculate common mode (CM) current, measurements of the phase currents are performed. The sum of all phase currents is applied between the ground and the RLC-network utilizing current controlled current sources. By default the implemented summation network does not exhibit any leakage flux, and an ideal compensation of DM currents at all phase conductors can be observed, as $i_u + i_v + i_w = 0$. Due to the ideal compensation no core impedance is seen by the phase currents. In the case where CM current is introduced, the sum of phase currents does not equal zero anymore; the part which differs from zero is by definition CM current $i_u + i_v + i_w = i_{cm}$. In the developed behavioural CMC model the CM current flows to the synthesized RLC-network which creates artificial magnetic flux, which reproduces permeability characteristics of the particular material. Impedance of the RLC-circuit becomes visible only for CM current. The same voltage drop caused by core impedance is seen for CM currents at all phases. In addition, leakage inductance can be modelled through implementation of a non-ideal phase currents compensation. The whole principle is realized by a parallel connection of the voltage-controlled voltage sources between an RLC-network and a ground. The voltage applied by the voltage sources at every phase is equal to the CM voltage drop across the RLC-network. Realization of the three-phase CMC model in LTspice based on the method described above is shown in Figure 3.14.

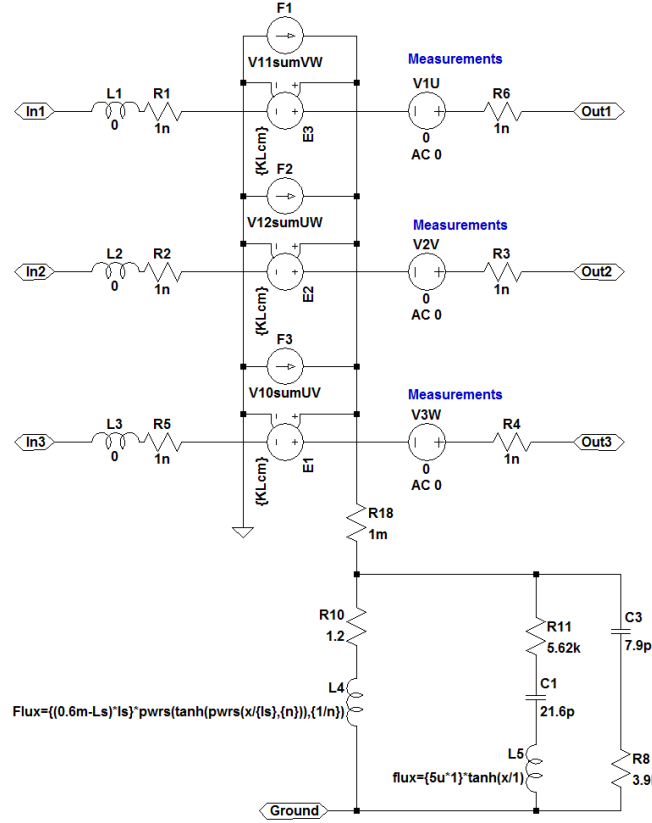


Figure 3.14.: Equivalent circuit of the three-phase CMC implemented in LTspice with consideration of permeability and saturation effects.

In order to realize saturation behaviour of $L1$ and $L2$, depicted in Figure 3.13, a function which reflects degradation of inductance with increase of current (magnetic field strength) has to be implemented instead of ideal inductance. The simplest method to accomplish this task in LTspice is to use an inverse tangential model based on the anhysteretic function of the Preisach model with a "sharpness" control (3.32). This saturation model is suitable for EMI filter modelling, since change of material susceptibility has a major effect on IL and the permanent magnetization effects can be disregarded.

$$\Phi(I_L) = (L_i - L_{sat})I_{sat} \left(\arctan \left(\frac{I_L}{I_{sat}} \right)^K \right)^{1/K}, \quad (3.32)$$

where $\Phi(I_L)$ is the resulting flux, L_i initial inductance, L_{sat} remaining inductance after saturation. I_{sat} is saturation current, I_L is the sum of all currents seen by the CMC, I_L and K is a coefficient regulating a "sharpness" of saturation. The complete current I_L consists of two components I_{cm} and $3 \times I_{dm}$. In such a way the contribution of DM currents to saturation is taken into account. A portion of I_{dm} current equal to 1% of the phase current is taken. The percent of the non-compensated phase current can be adjusted in accordance with a technical specification.

Validation of the proposed permeability model is provided in the example of four different cores. Ferrites T65, N87 (TDK Epcos) [46, 47] and Nanocrystallines W424 (Vacuumschmelze) [206], M006 (Magnetec) [134] are selected for further studies. The core under test is soldered on a specially designed PCB. The PCB itself together with several wires connected in parallel and a magnetic core realize

a one turn choke. Such construction allows elimination of a turn-to-turn capacitance and to minimization of the leakage flux. Resulting constructions used for core parametrization are depicted in Figure 3.15. The choke characterisation board is connected to a network analyser, so that frequency characteristics of a core can be obtained via shunt-through measurements. Core impedance is characterized in terms of the frequency dependent resistance and inductance. A sum of these components gives overall impedance for the choke consisting of one turn. Values of components in the Foster network are adjusted according to data obtained by measurements. Table 3.5 summarizes components of the Foster network used for modelling of previously selected soft magnetic materials. Comparison between real material characterised with the presented setup and the proposed behavioural model is shown in Figure 3.16 for four different materials. As it can be seen from this diagram mathematical models for all materials show good agreement with real characteristics and impedance drops dramatically after several MHz. Behaviour of nanocrystallines is defined by a reactive component of the complex permeability, therefore accuracy of the nanocrystalline models is worse compared to ferrite. An ideal choke has much higher impedance in the high frequency range, showing the importance of the frequency dependent permeability modelling. The difference between simulated and measurement impedance is mainly caused by tolerance of measurements and not ideal adjustment of parameters for the Foster network.

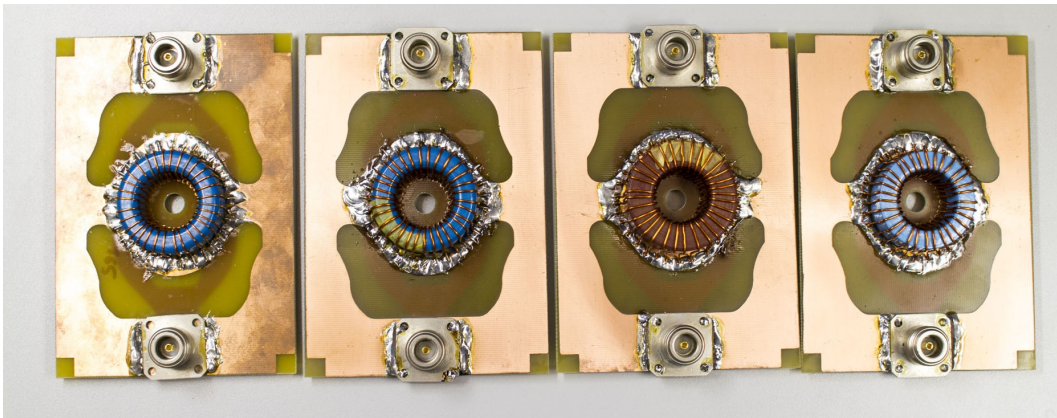
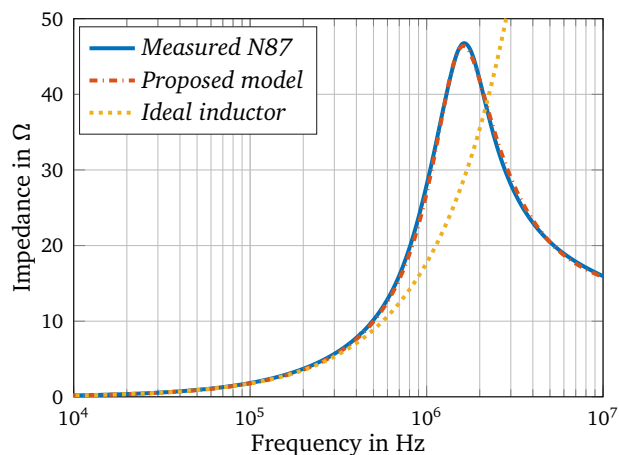


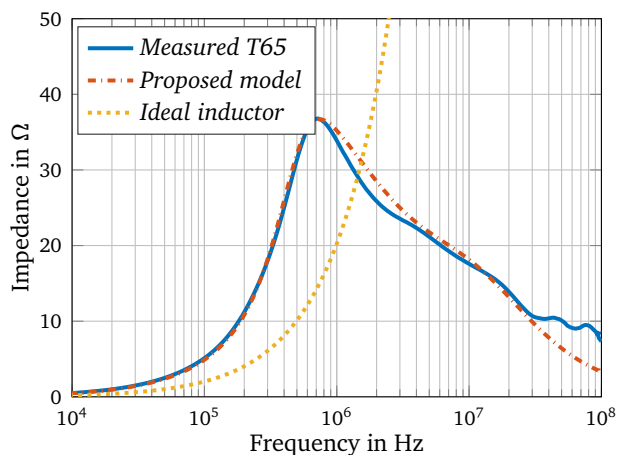
Figure 3.15.: PCBs with soldered cores used for impedance characterization.

<i>Parameter</i>	<i>Soft magnetic material</i>			
	<i>N87</i>	<i>T35</i>	<i>W424</i>	<i>M006</i>
R1	1.2 Ω	10 Ω	55 Ω	25 Ω
L1	0.42 mH	1.16 mH	3.8 mH	1.1 μ H
R2	5.62 k Ω	5.15 k Ω	2.4 k Ω	4 k Ω
L2	5 μ H	4 μ H	900 μ H	185 μ H
C1	21.6 pF	83 pF	8000 pF	925 pF
R3	3.9 k Ω	10 k Ω	4.2 k Ω	4.9 k Ω
C2	1.6 pF	5.5 pF	400 pF	275 pF

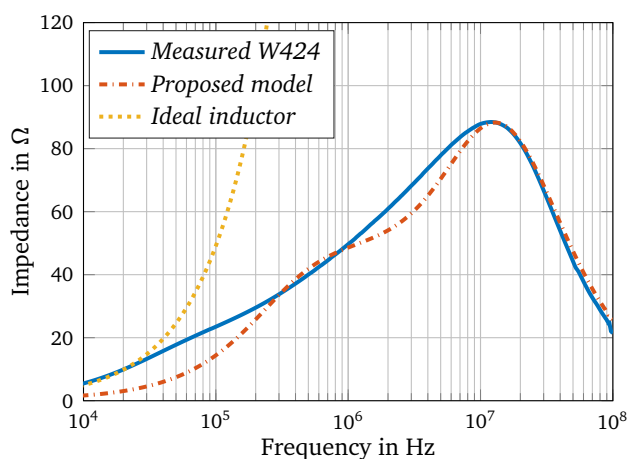
Table 3.3.: Parameters of RLC-network for studied soft magnetic materials.



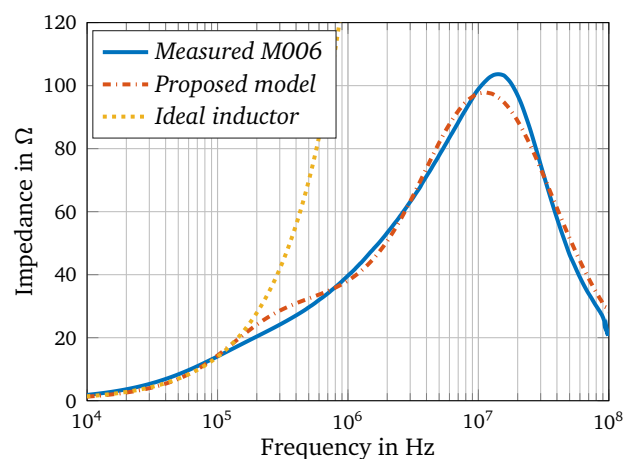
(a) Ferrite N87.



(b) Ferrite T65.



(c) Nanocrystalline W424.



(d) Nanocrystalline M006.

Figure 3.16.: Comparison between simulated and measured core impedances.

Impedance of the cores under test is characterized with applied DC bias. A setup for permeability measurements is supplemented with a DC source, which supplies saturation current. An additional cable is stretched through a toroidal choke, so that permeability can be measured independently from the high current network. More detailed description of the test bench used for cores characterisation is given in Appendix F. Saturation current is applied with small steps, which depends on initial permeability of the characterized material. Degradation of the core inductance with increase of the applied current is demonstrated in the example of an N87 material in Figure 3.17. Saturation current is changed with a step of 1 A and ten measurements are made from 1 up to 10 A. It is possible to see that under saturation conditions an agreement between measurements and simulation is not ideal in the deep saturation region due to the simplicity of the implemented saturation model and the significant impact of a current source used for saturation measurements. However, on the frequencies above 5 MHz effects of the EPC become dominant. Therefore this accuracy is adequate for prediction of CMC impedance degradation in EMI filters.

The proposed CMC model is easily scalable. Characteristics of the particular material, which are modelled, can be further used for modelling of cores with different forms and dimensions. CMC

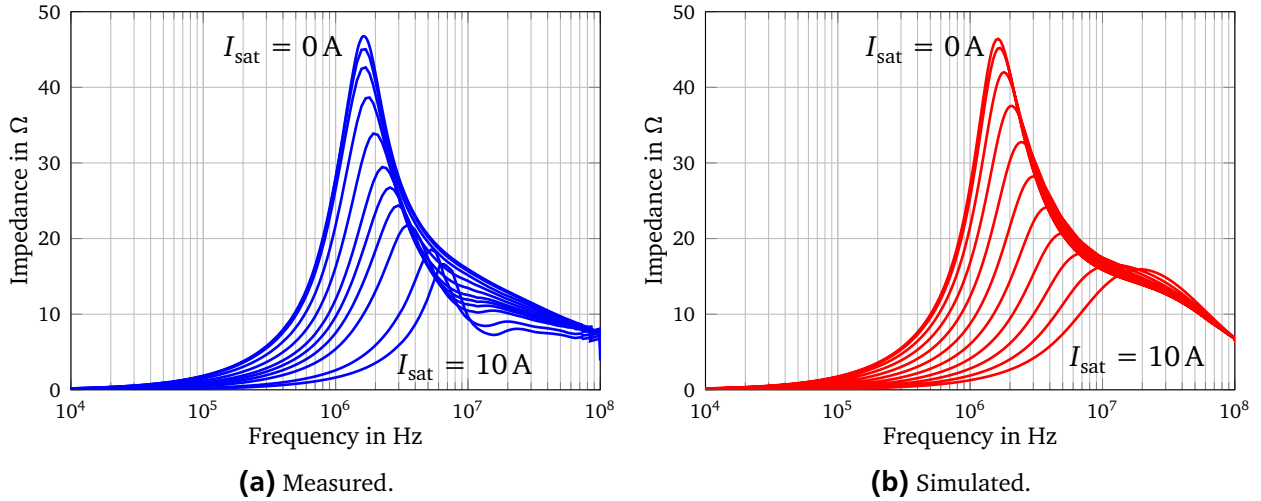


Figure 3.17.: Comparison between impedances of N87 ferrite under saturation.

parameters including core cross section, magnetic path length and the number of turns can be changed without need of additional prototyping and validation of the scaled CMC. For example when the number of turns is scaled up through changing a variable N , CMC impedance is increased quadratically. The same parameter affects the maximum saturation current linearly. The scalability is a huge benefit of the proposed model in comparison with existing numerical models, which are fully based on measurements of prototypes. A database of the most popular materials can be created rather quickly and, thereafter, used for three-phase EMI filter development in all required power ranges. It must be mentioned that the CMC model does not include EPC. This parameter can be assessed analytically in accordance with geometry of the particular choke and included into a filter model. Analytical calculation of EPC is discussed in detail in Section 3.1.

A simple one-stage topology of an EMI filter has been chosen in order to investigate effects of frequency dependent permeability and validate the proposed CMC behavioural model. Schematics of the filter are demonstrated in Figure 3.18. Values of used components as well as size of self-parasitics are summarized in Table 3.4. The investigated EMI filter is based on the special laboratory setup. Components of the filter are arranged as shown in Figure 3.19, so that stray couplings between components are minimized [33, 192]. Hence, effects caused by mutual couplings can be neglected at this stage. For all conducted simulations and measurements characteristic impedance is 50Ω , according to [92].

<i>Filter component</i>	<i>Value</i>	<i>Self-parasitic</i>
L_1	0.66 mH	6 pF, 42 k Ω
C_X	2.2 μ F	13 nH, 0.03 Ω
C_Y	2.2 μ F	13 nH, 0.03 Ω
C_{XY}	0.56 μ F	25 nH, 0.04 Ω

Table 3.4.: Values of components used for EMI filter simulation.

In order to show an impact of different non-ideal properties on the EMI filter IL a simulation with ideal components is conducted in the beginning and used as a reference. Ferrite core N87 (40x24x16)

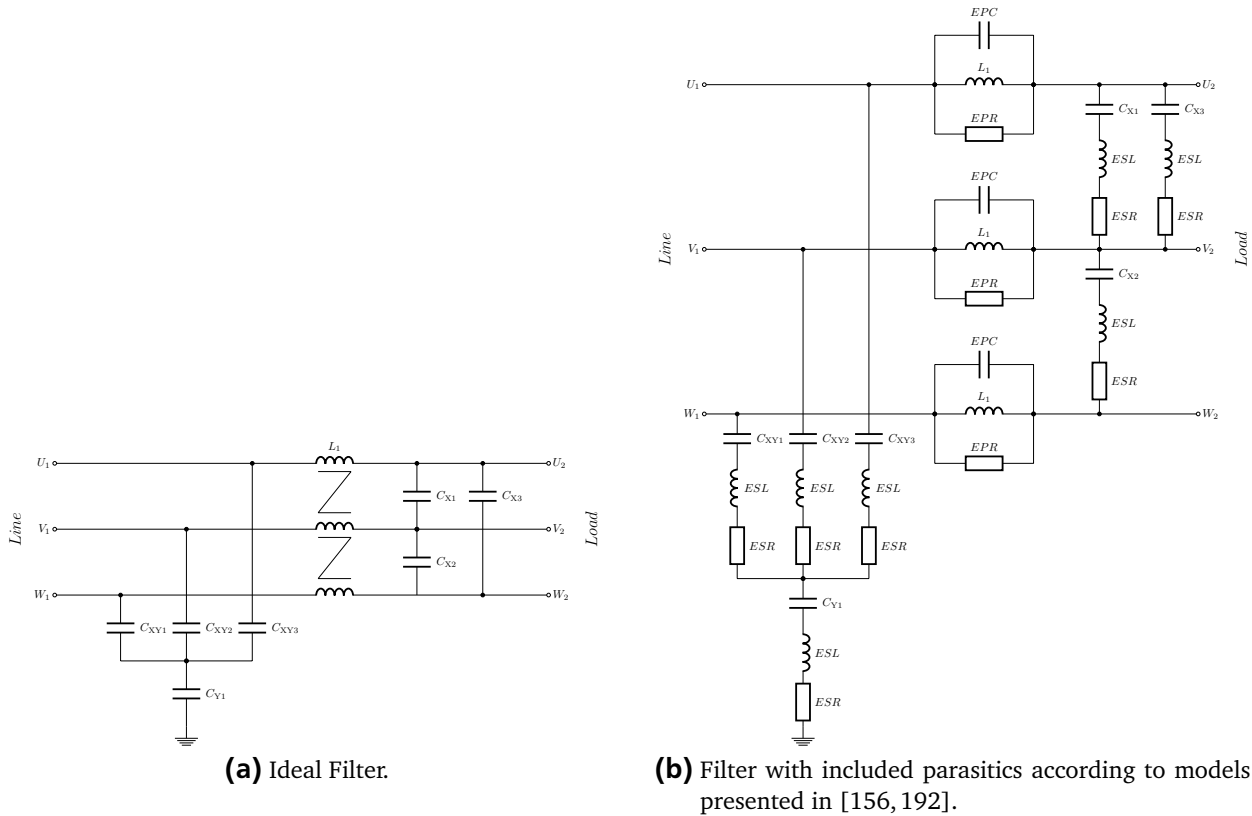


Figure 3.18.: Circuit of the designed three-phase EMI filter.

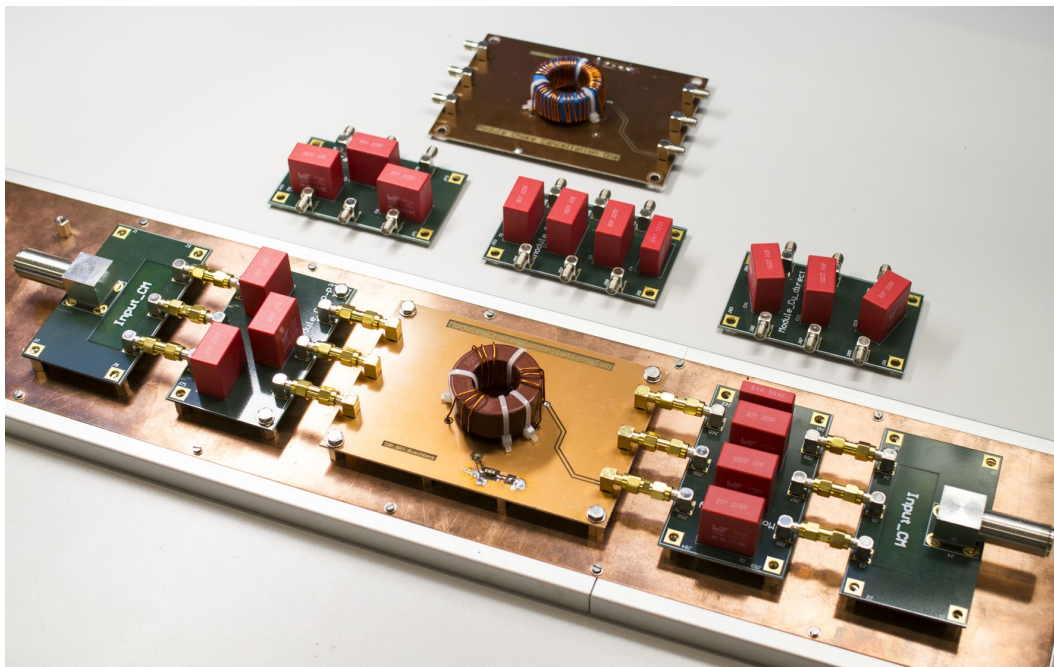


Figure 3.19.: Filter used for IL measurements.

is used as a reference at this stage. The idealized EMI filter model is, thereafter, supplemented with self-parasitics as shown in the equivalent circuit Figure 3.18b, which is measured separately for every passive component. Resulting common mode IL of the idealized filter in contrast with the filter including

self-parasitics are shown in Figure 3.20. In the next experiment a CMC used in the idealized EMI filter model is substituted with the developed CMC behavioural model (Ferrite N87). Parameters of the CMC model are adjusted in accordance with the values given in Table 3.4. Resulting IL of the filter with the CMC behavioural model alone (self-parasitics are not included) and the filter with self-parasitics alone (a simple CMC model is used) are shown in Figure 3.20. Finally, self-parasitics and the CMC behavioural model are included into the EMI filter model simultaneously (Figure 3.20).

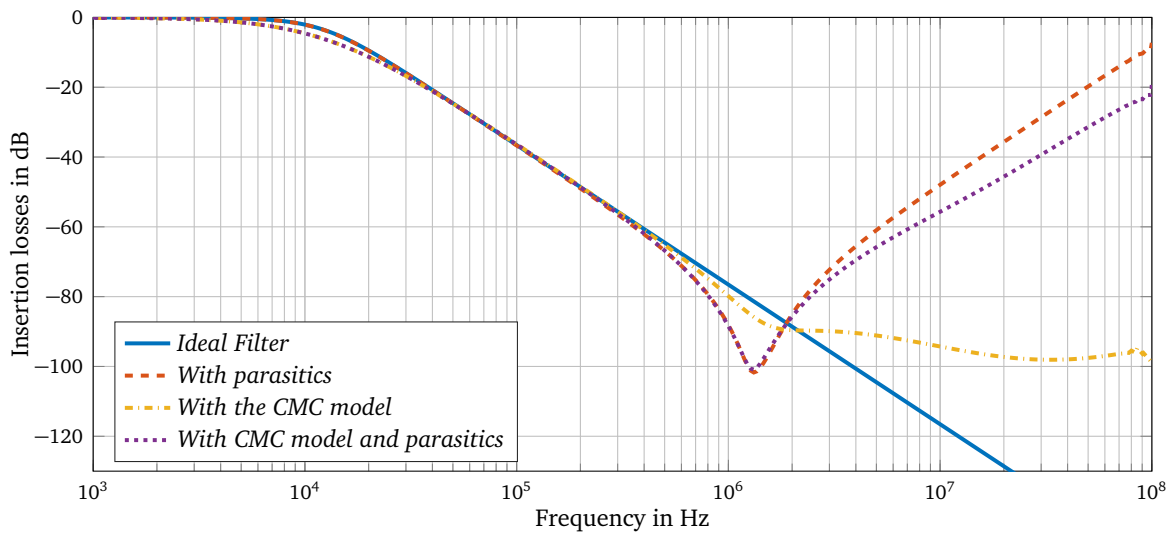
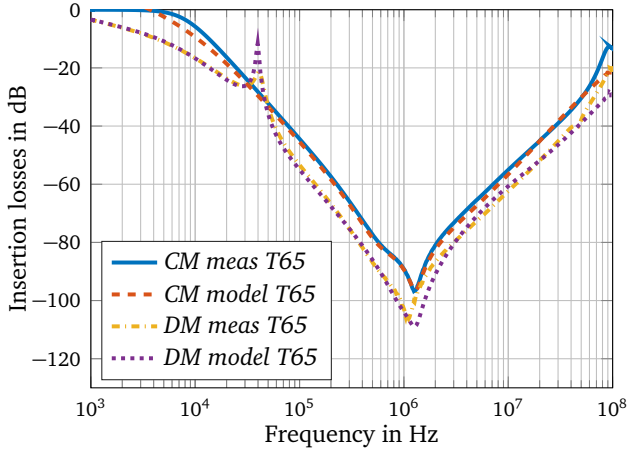


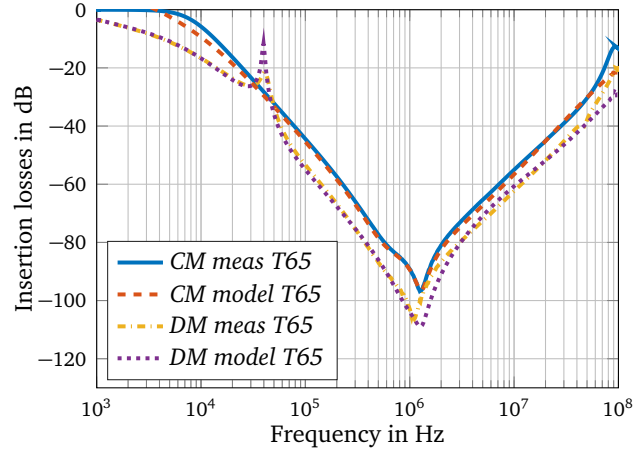
Figure 3.20.: Impact of different non-ideal parameters on IL of an EMI filter.

The characteristics of the simulated EMI filter with all included non-ideal properties are compared with measurements of a prototype. In order to validate all four CMC models as a part of an EMI filter, the same filter topology is used. CM and DM IL of the filter under test are characterized with the four previously modelled CMCs, which are based on different soft magnetic materials. Comparison of measured IL for those filters and simulation results are presented in Figure 3.21. All simulated CM IL are agree almost ideally with measurements. Some deviation is explained by absence of mutual parasitic couplings between components in the filter model as well as non-ideal matching of modelled CMC impedance. DM IL demonstrated by prototypes shows some deviation from measurements. This is caused by higher impact of mutual couplings at the high frequency DM IL and by non ideal symmetry of a real filter. Moreover leakage flux, which causes differential mode inductance, is partially affected by core properties. It makes DM inductance dependent from the core permeability but in the proposed CMC model the leakage inductance is assumed to be ideal. It is especially notable in nanocrystalline materials. In any case, filters simulated with included CMC behavioural models exhibit much better agreement with the built prototypes compared to the models based solely upon parasitics [87].

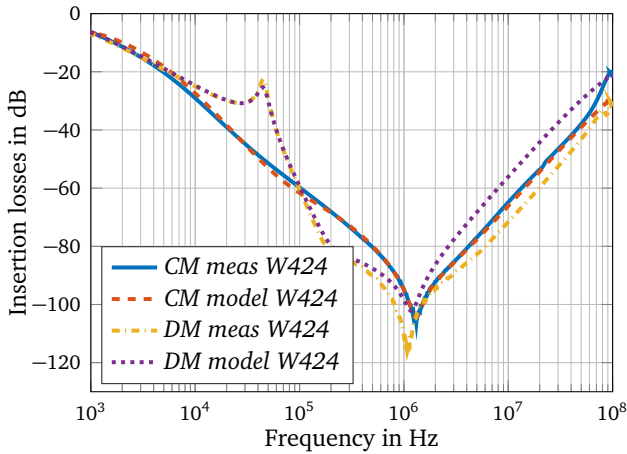
The proposed behavioural models can be easily used for simulation and design of EMI filters of any size due to the scalability of CMC parameters. They will improve the quality of filter simulations and reduce the probability of design mistakes compared to filter design procedures based on ideal CMC models. However, more precise saturation models can still be implemented. More complex EMI filter topologies consisting of two or more CMC can be designed for further tests.



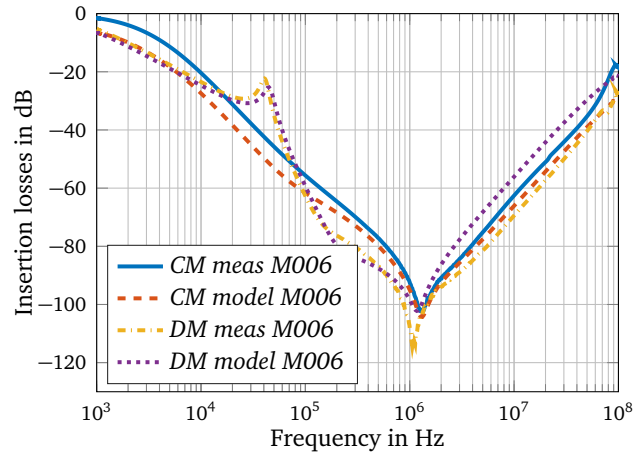
(a) EMI filter based on Ferrite N87.



(b) EMI filter based on Ferrite T65.



(c) EMI filter based on Nanocrystalline W424.



(d) EMI filter based on Nanocrystalline M006.

Figure 3.21.: Validation of created CMC models.

3.2.2 Mutual Coupling Determination

The last phenomenon influencing non-ideal properties of EMI filters is mutual couplings. In contrast with self-parasitics, which are relatively simple (Section 3.1), determination of couplings is much more challenging. The size of every such coupling can be derived either from a prototype (as shown in [159, 163, 177, 193, 214]) or from 3D electromagnetic simulation [24, 119]. The first methodology is well documented, but some questions related to 3D simulation remain open.

For determination of mutual couplings ANSYS Maxwell is used. Magnetostatic and Electrostatic simulations have to be performed in order to define inductive and capacitive couplings, respectively. A magnetostatic solver from Ansys Maxwell solves the Gauss's Law (3.33)

$$\nabla \cdot \mathbf{B} = 0 \quad (3.33)$$

and the Ampere Circuital Law (3.34)

$$\nabla \times \mathbf{B} = \mu \left(\mathbf{J} + \epsilon \frac{\partial \mathbf{E}}{\partial t} \right) \quad (3.34)$$

in which \mathbf{B} is the magnetic flux density, \mathbf{J} is the total current density and \mathbf{E} is the electric field strength. The term $\epsilon \frac{\partial \mathbf{E}}{\partial t}$ representing the time changing electric field is neglected for a magnetostatic analysis. It is assumed, than all magnetic effects are determined only by current densities within a simulated model. The inductances can be calculated from the magnetic energy stored in the field as (3.35)

$$E = \frac{LI^2}{2} = \frac{1}{2} \int_V \mathbf{B} \cdot \mathbf{H} dV. \quad (3.35)$$

From known inductances the coupling factors can be derived as (3.36)

$$k = \frac{L_M}{\sqrt{L_1 L_2}}. \quad (3.36)$$

For a single-phase EMI filter it is rather simple to set a current loop, but for three-phase filters this task is not so trivial. All current must enter and exit a simulation volume or close inside of it. One variant of current assignment is separately setting it inside of capacitors, winding of CMC and other conductive parts. Few bodies can be connected together for simplification of resulting coupling matrices. Since mutual coupling obtained from an FEM simulation have to be implemented in the filter equivalent circuits, all simulated couplings have to be assigned to components, which are already represented in the equivalent circuit. When only normal phase current is assigned it flows just through PCB traces and CMC, avoiding Y-capacitors. Therefore, one extra current flowing to the ground should be attached. It must be mentioned that accuracy of mesh should be adopted in accordance with specification. It is always a trade-off between the size of the mesh, the desired level of accuracy, and the amount of available computing resources. Although an adaptive meshing algorithm is used in ANSYS Maxwell by default, it is recommended to check the mesh manually and regenerate it for some important places, such as the inter-turn spaces of CMC.

For the electrostatic solution in ANSYS Maxwell, it is assumed that all objects are stationary, there is no time variation of any of the electromagnetic quantities and there is no current flow in conductors. The electrostatic solver of Maxwell solves the Poisson equation (3.37) and is applied to the electric potential through integration

$$\nabla \cdot \mathbf{E} = \nabla \cdot (-\nabla \phi) = -\nabla^2 \phi = \frac{\rho}{\epsilon}. \quad (3.37)$$

With knowledge of the free charge density ρ or of the electric potential ϕ it is possible to solve the partial differential equation for the electric field. In order to calculate the values of the electric field, setting the voltage in the components of the filter is necessary. Charges of all conductive components inside of the filter (capacitors, CMC windings, PCB traces etc.) are assigned to 100 V. The type (AC or DC) and

the amplitude of the voltage are not relevant for calculation of inter-component capacitance. Setting a ground surface is needed in order to determine the capacitances of the components to the ground, so the housing is assigned zero voltage potential. Preparation of the model for electrostatic simulation is rather simple compared to magnetostatic simulation. The values of stray capacitances are derived from the electric fields as in equation (3.38).

$$C = \frac{2E}{U^2} = \frac{1}{U^2} \int_V \mathbf{D} \cdot \mathbf{E} dV. \tag{3.38}$$

Magnetostatic and electrostatic simulation are carried out for the same reference three-phase filter with a circuit depicted in Figure 3.18. For this simulation a simplified 3D model is prepared. In Figure 3.22 the magnetic field intensity vector is plotted. It is possible to see how the flux lines close through observation of the rotation and the divergence of the field vectors. This plays a crucial role in the mutual coupling. When a flux line crosses two components, it creates a coupling between them. For example, when current flows in one of the capacitors and creates a flux line which crosses one of the CMC coils, voltage in the coil and therefore current is also induced. The higher the mutual inductance (and therefore the coupling coefficient), the higher the induced current, in relation to the initial current. From a conducted magnetostatic analysis it is possible to identify the locations with the strongest magnetic field. In the region between each capacitor of the X- or the Y-capacitors bank and between each coil of the CMC the highest absolute values for the H-field, with an amplitude in the range from 400 A/m up to 500 A/m is observed, in the scale of the magnetic field 2 A/m - 500 A/m. Therefore one can predict that the mutual couplings inside the capacitor's banks should introduce impact on the filter IL.

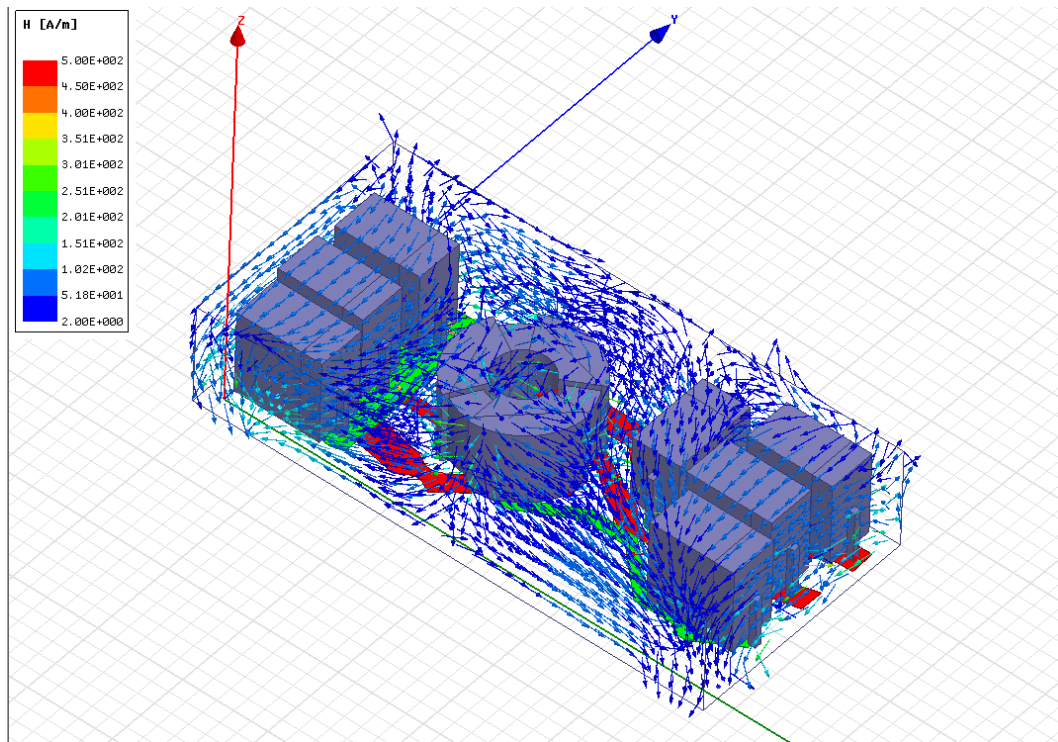


Figure 3.22.: Resulting H-field plot after performing magnetostatic simulation.

In Appendix G a table with inductances and coupling factor matrices is found. In the inductance matrix, the values in mH for self and mutual inductances for all components in the model are represented. The values of the inductances have a very wide range, starting from a few nH and going up to values in the mH range. They have influence on the filter attenuation in the MHz and GHz range. In the coupling coefficient matrix, a value of 1 means perfect coupling and a value of 0 means no coupling at all.

In Figure 3.23 the electric field vectors are plotted. The vectors are mostly aligned in the direction of the ground potential, parting from the components with voltage excitation. Practically, the capacitance between the CMC and the capacitors to the ground is the only relevant capacitance in this case. In Appendix G the values of the capacitances in pF and the coupling factors between the components of the filter are listed. Similar to inductive couplings an absolute value for the coupling coefficient of 1 is associated with an ideal coupling and 0 represents no coupling at all.

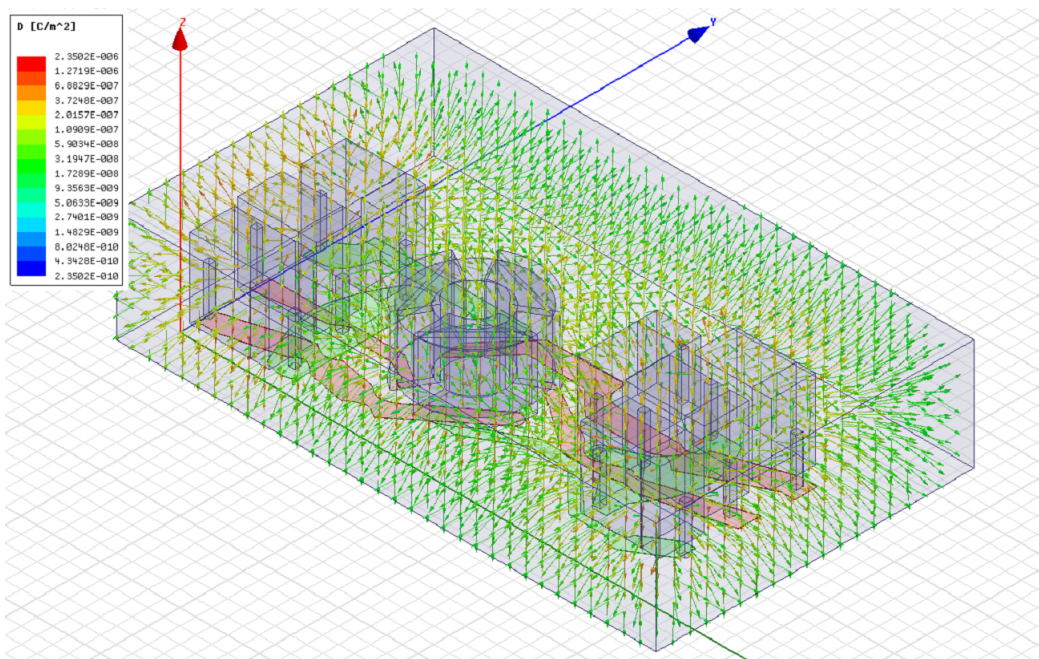


Figure 3.23.: Resulting E-field plot after performing electrostatic simulation.

Obviously, not all coupling inside of the EMI filter have considerable impact on IL degradation. Most coupling are not relevant in the frequency range of interest (1 kHz–100 MHz) and can be disregarded. Detailed analyses of the mutual coupling as well as mutual coupling minimization methods can be found in Section 4.2. IL of the reference filter model, with consideration of all non-ideal parameters, is compared with IL of a prototype in Figure 3.24. Agreement between modelled and measured IL is close to ideal. Moreover, the developed behavioural model of a CMC allows modelling the IL of the filter during saturation. Unfortunately, it is extremely difficult to validate the developed prototype of an EMI filter with a saturated core. Since the behavioural model of the core was validated for several different soft magnetic materials separately from the filter, it can be assumed that the previously validated behavioural model of the core acts correctly within a filter as well. Several steps of common mode current are applied to the reference filter model in LTspice, which already considers all non-ideal effects. IL

degradation caused by core saturation is shown in Figure 3.25. Degradation of CM IL is distinctly seen in the whole frequency range. For the common mode current above 1 A only capacitors contribute to IL. Validation of the proposed EMI filter model under saturation conditions should be considered in future research.

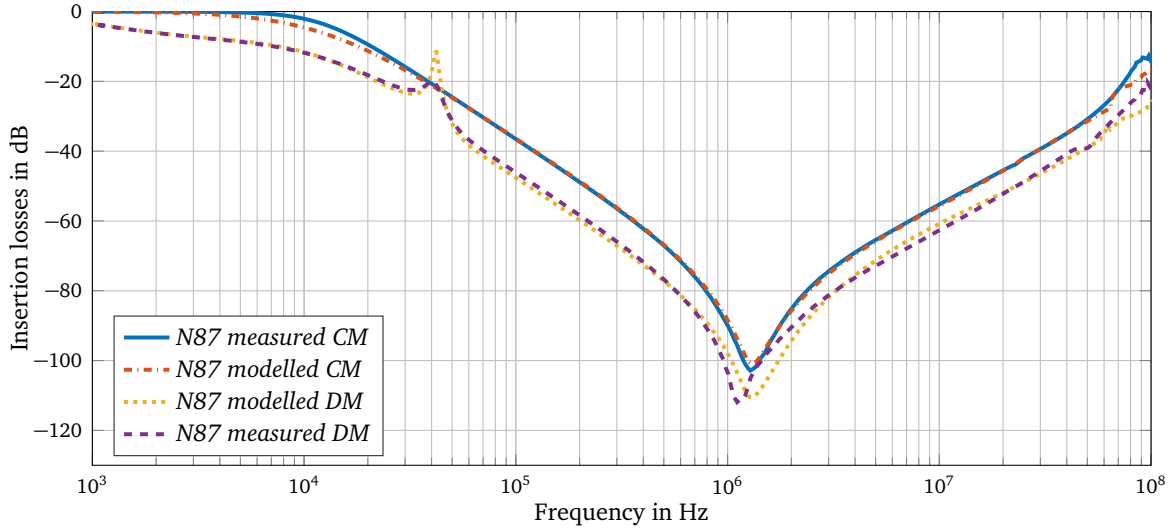


Figure 3.24.: Comparison between an EMI filter model in LTspice with consideration of all non-ideal factors and the reference prototype.

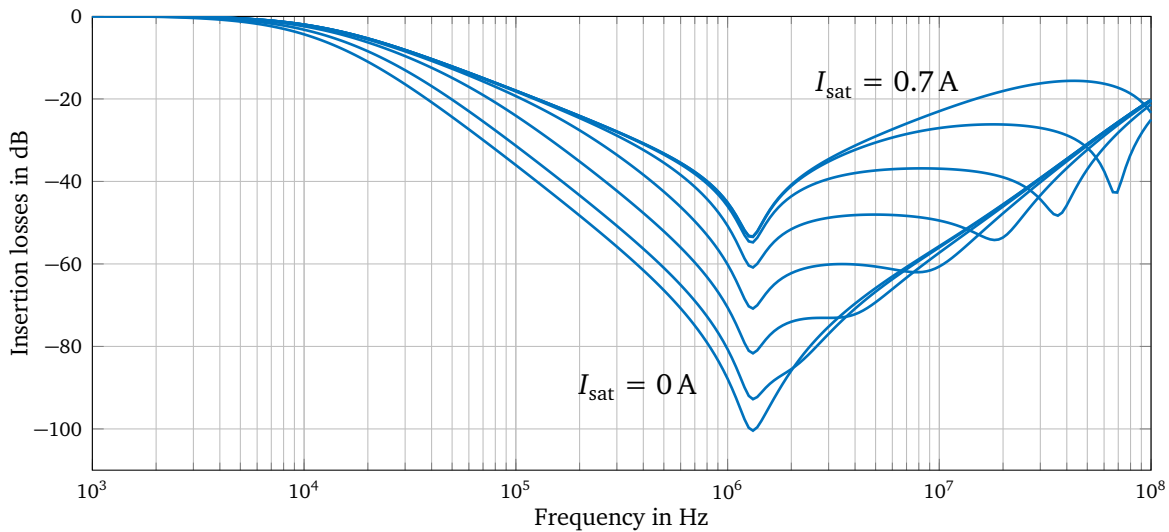


Figure 3.25.: Impact of the CMC saturation on CM insertion losses.

Unfortunately, the methodology presented in this subsection is rather complex, therefore the time cost required for preparation of an EMI filter mathematical model is quite high. Moreover, complexity of the proposed method based on SPICE simulation with parasitics extraction leads to the high probability of mistakes. Nevertheless high modelling accuracy and the scalable CMC model with included saturation effects makes this method quite attractive, when enough time is available. The complete methodology of EMI filter design based SPICE with consideration of non-ideal effects is summarized in the flowchart depicted in Figure E.2.

3.3 Combined FEM Simulation in CST Microwave Studio

As it was shown in Section 3.1 neither analytical EMI filter modelling with idealized components nor with included EPC and ESL provides a sufficient IL prediction. Methodology based on development of an EMI filter behavioural model (Section 3.2) gives simulation results closest to reality. The biggest disadvantage of this method is its complexity: good understanding of magnetic materials is required for development of a CMC mathematical model; analytical assessment of parameters like leakage inductance and EPC is quite time consuming; 3D electro- and magnetostatic FEM simulation have to be carried out, etc. In this section one more alternative method of filter simulation and design, which can be considered as a compromise between two methods that were presented earlier is described. Electromagnetic modelling based on FEM has already been used in Section 3.2 for mutual couplings evaluation and now precise CMC and self-parasitics modelling is conducted with FEM. All design procedures are performed in a CST microwave studio, and several steps are automated or can be simplified without loss of precision. The main scope of the methodology proposed in this section is to reduce the number of prototypes or, ideally, completely eliminate the necessity of EMI filter prototyping. Nowadays, 3D electromagnetic modelling represents the only alternative to prototyping, allowing improvement of the exactness for EMI filter modelling.

A virtual electromagnetic prototyping of EMI filters based on FEM is not widely used nowadays. The most likely reasons for this are the relatively high price of FEM CAE and the preconceptional relation of electrical engineers to 3D modelling. Nevertheless, it has a number of advantages in comparison with the aforementioned EMI filter simulation IL methods. FEM simulation enables a comprehensive EMI filter analysis, considering effects of self-parasitics, frequency-dependent permeability $\mu(f)$, mutual couplings, PCB layout, etc. Values of passive components can be adjusted using built in optimization tools in order to maximize IL of a particular filter without building prototypes. Moreover, IL can be easily assessed not only for the standard $50\ \Omega$ load and source impedance but for the worst case scenario as well. Improvement measures are quite simple to implement and validate using FEM simulation [83, 85].

EMI filter analysis with the parallel element equivalent circuit (PEEC) method is already well investigated and is being used. PEEC simulation shows quite good agreement with behaviour of a real system in the non-ferromagnetic environment and good computational speed [118–120]. As the PEEC method is based on Biot-Savart's law according to (3.39) the relative permeability term is absent in the equation. It means that permeable materials in vicinity with conductors cannot be handled [33, 151]. Hence soft magnetic cores cannot be modelled, which is critical for EMI filters.

$$\mathbf{B}(r) = \frac{\mu_0}{4\pi} \int_l I \frac{d\vec{l} \times \vec{r}}{|\vec{r}|^3} \quad (3.39)$$

In contrast with PEEC, FEM based prototyping requires more computing power but allows relatively simple modelling of nonlinear effects [121].

For EMI filter simulation the classical FEM is used. The complete 3D model is divided into smaller parts. Each part is defined by a differential equation and these equations are combined in the system which describes an entire problem; in our case an EMI filter. All simulation steps including circuit analysis are conducted with the help of CST microwave studio. Filter 3D models are designed in SolidWorks and

imported to CST studio later on. Two three-phase EMI filters are analysed using the proposed FEM based design procedure. The first reference filter is self-made and the second filter is a conventional three-phase EMI filter [180]. Parameters of both filters are summarised in Table 3.5 and equivalent circuits are shown in Figure 3.26.

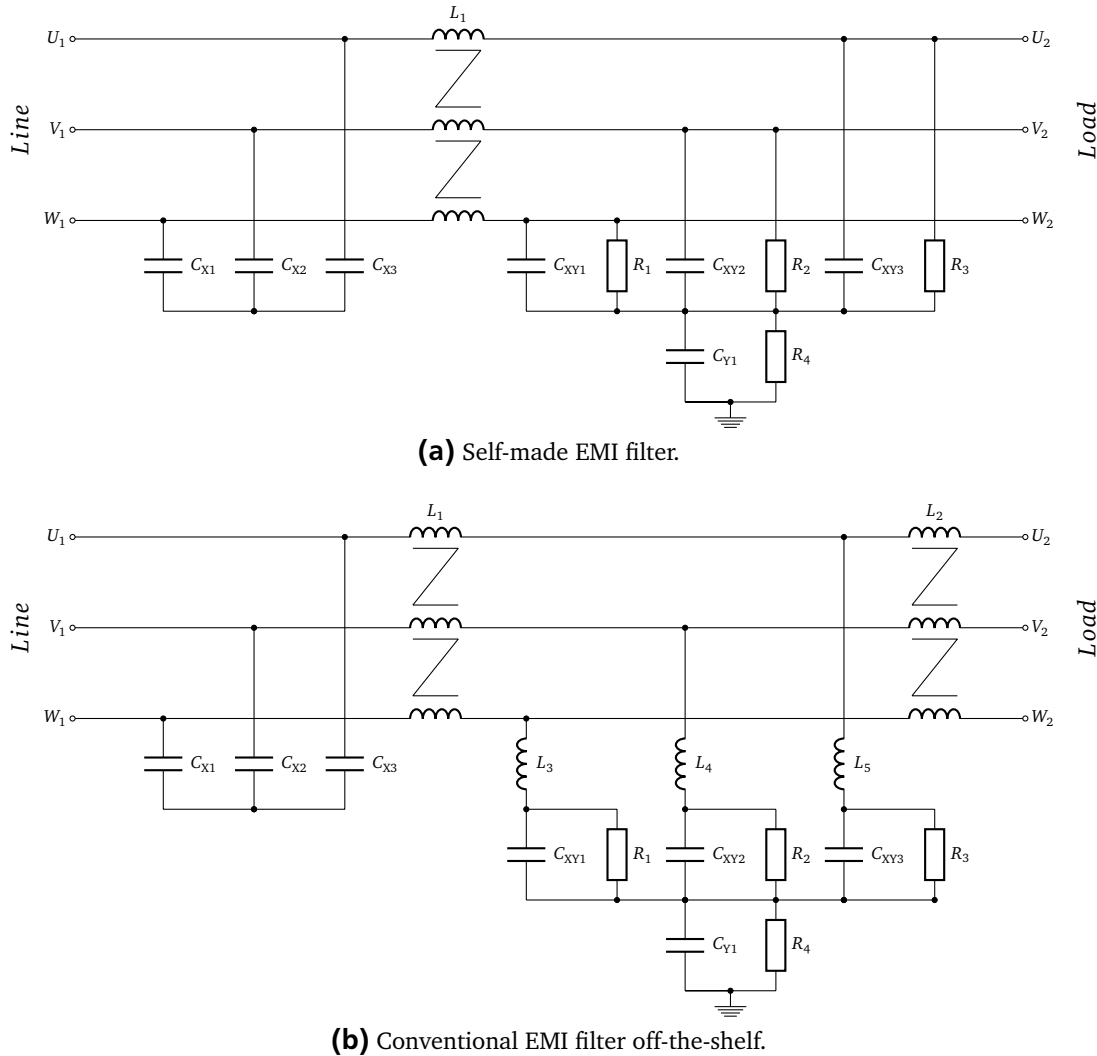


Figure 3.26.: Circuits of EMI filters used for FEM simulation with CST studio.

3.3.1 Model Preparation

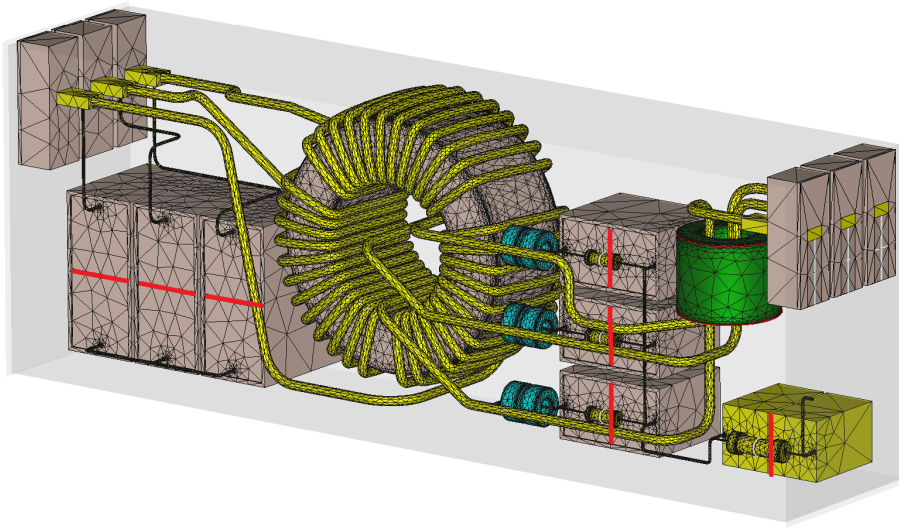
Obviously, in order to reduce simulation time, the 3D model has to be kept as simple as possible. On the other hand, simplification of a 3D model can lead to inaccurate modelling results. Therefore, a compromise between model accuracy and computation time should be found. An initial 3D model of the EMI filter has to be properly adapted for FEM simulation. The majority of non-conductive parts inside of the filter do not influence the electromagnetic field's propagation and therefore can be simplified (except PCBs). In the case of winded film capacitors an internal structure can be simplified to a rectangle. This simplification of the internal capacitor structure has been investigated in [9]. The main outcome is that the internal structure of a capacitor does not have any considerable impact on the simulation accuracy

<i>Filter type</i>	<i>3-phase grid-side</i>	<i>3-phase grid- or motor-side</i>
Nominal Current	6 A	30 A
Nominal Voltage	230 V phase to ground	275 V phase to ground
Y-capacitors	EPCOS B3202 Y2 0.47uF	HJC 310-250V 3.3 uF
X-capacitors	EPCOS B32924 X2 3.3uF	HJC 310-250V 3.3 uF
XY-capacitors	EPCOS B32924 X2 3.3uF	Pilkor 6.8 uF
Common mode choke 1	15 turns 820 uH	11 turn 1.87 mH
Common mode choke 2	none	1 turn 9uH
CMC material	EPCOS N87 40x24x16	NCD

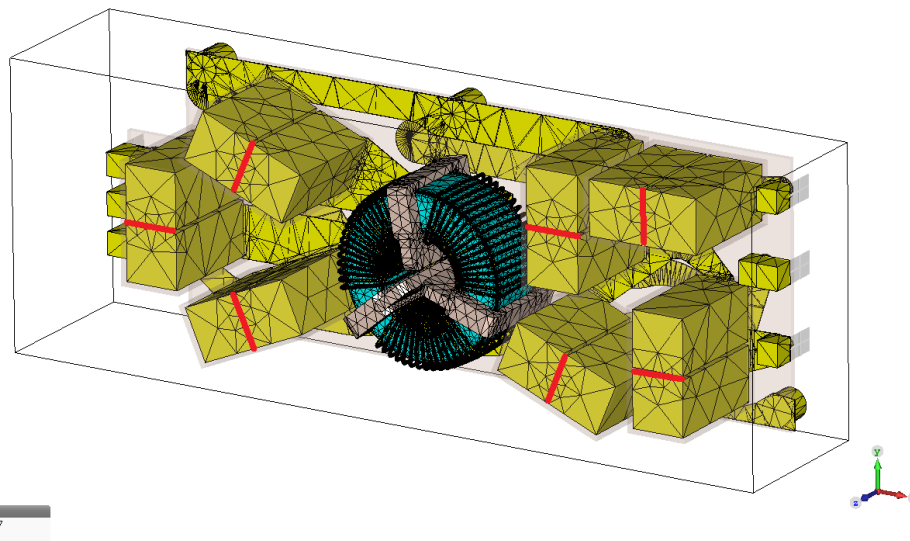
Table 3.5.: Parameters of the filters under test.

with FEM. A rectangle representing a capacitor must contain a gap which is used for placement of a discrete port. This discrete port is also reflected in the schematic, where a lump capacitor can be connected. Utilization of lump components allows optimization of component values at the final simulation stage, and also making some adjustment to IL. Lastly, a degree of simplification for CMC windings has to be chosen in order to get adequate EPC. Capacitors with simplified internal structure and CMCs with simplified winding geometry produce quite good results. 3D models used for further modelling are depicted in Figure 3.27. The number of cells after the meshing process is 361000 for the self-made filter and 530000 for the conventional filter. In order to determine the impact of the geometry simplifications on the model accuracy, several further measures (e.g. round wires of CMCs could be substituted with rectangular, or PCB traces could be approximated etc.) are applied. These measures allow reduction of the number of cells by a factor of 1.8 and the simulation time is reduced by a factor of 2.5, although modelling results are less precise. Figure 3.28 demonstrates the difference in simulated IL between reference and simplified 3D models. Despite the relatively small mismatch between characteristics obtained from reference and (over)simplified models, some instability of simulation, especially on low frequencies, is observed. Therefore, no further simplification of the model depicted in Figure 3.27 is recommended.

By definition, electromagnetic field energy is transmitted within an EMI filter between its terminals. Ideally this process takes place only between inputs and outputs of a particular phase. In reality, all six terminals of an EMI filter (for a three-phase filter) are coupled. For characterisation of such a system, a multiport network can be utilized. There are two types of ports in CST studio: discrete and waveguide ports. A discrete port represents a lump element connected between two edges of a 3D model. A waveguide port represents an infinitely long waveguide with negligibly small reflection. Use of a waveguide port is recommended for high frequency models (from hundreds of kHz up to GHz range). But the standardized range for conductive EMI pollution does not exceed 30 MHz. Therefore, modelling with waveguide ports might be unstable, especially in the kHz range. Moreover, the duration of a simulation with waveguide ports is almost by a factor of two longer than with discrete ports, so that use of discrete ports is recommended. The difference between IL obtained from simulations with waveguide and discrete ports for the same reference filter is shown in Figure 3.29. Results from a simulation with discrete ports are more stable. Also, there is a mismatch on the low frequencies when waveguide ports



(a) 3D model of the conventional EMI filter.



(b) 3D model of the self-made EMI filter.

Figure 3.27.: 3D models of EMI filters used for FEM simulation (red lines show discrete ports for lump capacitor placement).

are utilized. It can be concluded that discrete ports are more suitable for modelling of EMI filters from both accuracy and computation time points of view.

3.3.2 Simulation and Post-Processing

For comprehensive understanding of processes in an EMI filter, analysis of IL is conducted in the frequency range from 1 kHz up to 100 MHz, which is wider than the standardized conductive EMI range. A general purpose frequency domain solver with no adaptive meshing is used. Results of the 3D simula-

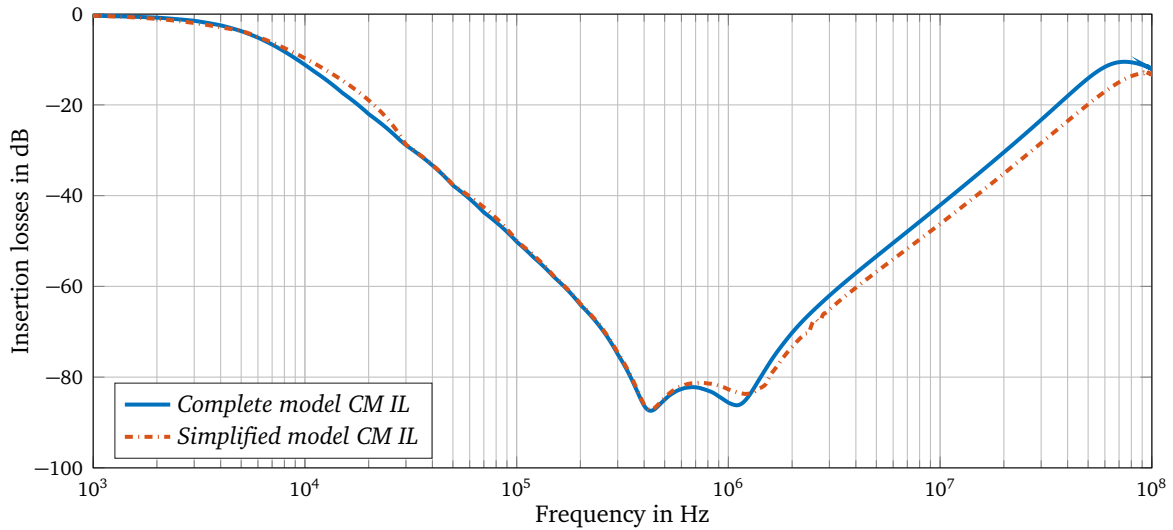


Figure 3.28.: Impact of geometry simplification on simulation results.

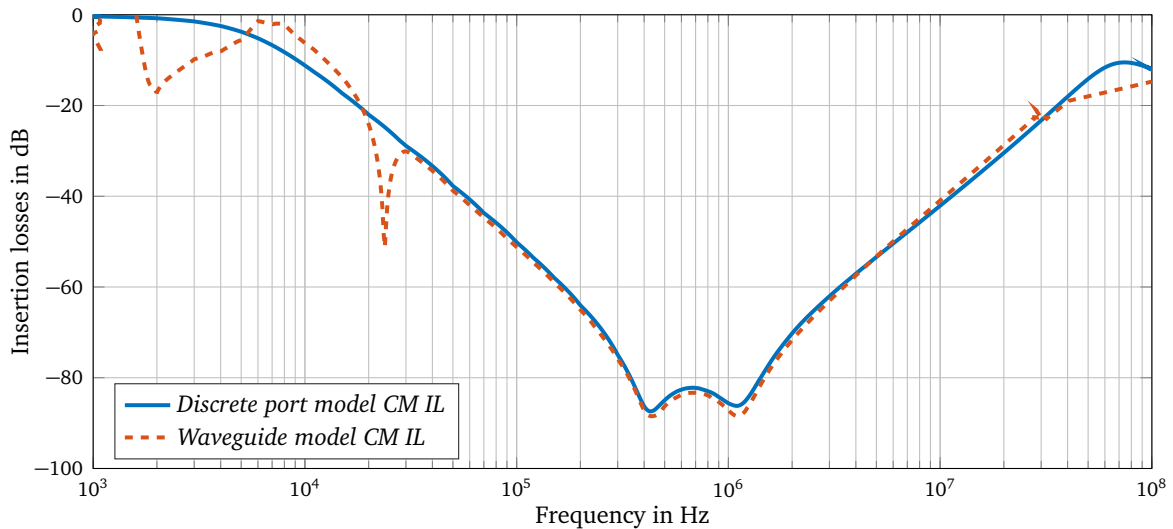


Figure 3.29.: Comparison between simulations with waveguide and discrete ports.

tion in CST studio are represented as a frequency dependent matrix consisting of scattering parameters. This matrix can be used for further simulation of both CM and DM IL of a filter in combined simulation. The black-box model obtained from 3D modelling is automatically integrated into the schematic, where all necessary lumped component can be included. All ports previously assigned in 3D modelling are reflected in a black-box model as outputs in Figure 3.30. After normalization of the S-parameters matrix to 50Ω , DM and CM IL can be calculated based on previously calculated scattering parameters. When all necessary lumped components are included into the schematic, the modelled filter is connected to external ports in series with $50 \Omega/50 \Omega$ load and source impedance. This circuit reproduces a measurement setup from CISPR17/EN55017 [92] (Figure 1.14a). Schematics of the three-phase EMI filter implemented in CST studio is shown in Figure 3.30. It must be mentioned that a connection of lump components between a port and the ground on the schematic is interpreted by software as a lump component connected between two sides of the same port in the 3D model.

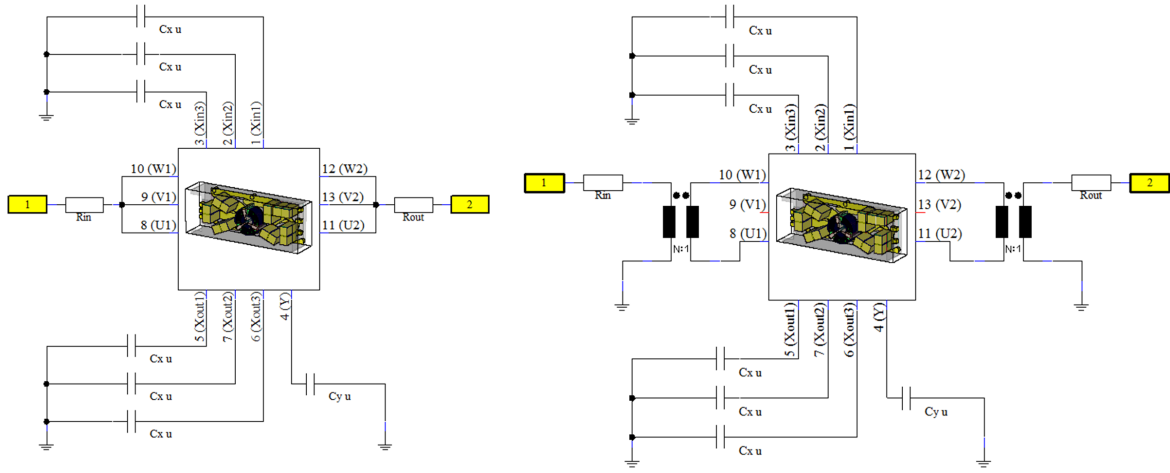


Figure 3.30.: Black-box model of an EMI filter automatically created in the schematic: for CM IL characterization on the left hand side and for DM IL characterization on the right hand side.

Frequency dependant permeability $\mu(f)$ is typically simplified during the design and simulation process to initial permeability μ_i . In order to evaluate the importance of frequency dependent permeability effects, simulations with idealized and real frequency-dependent permeability are conducted. Initially core permeability is modelled as a constant equal to μ_i . In order to obtain frequency dependant permeability, real and imaginary permeability parts are measured and approximated in accordance with the Lorentz-Drude Model [126]. N87 ferrite is used for the reference filter [46]. It has to be mentioned that measured values of permeability differ notably from those given in the datasheet, but remain within a 25% tolerance. This data is used in the magnetic dissipation fit, which uses a model of 6th order for this material. The difference IL simulated for two filters with ideal and frequency dependent permeability models is quite significant (Figure 3.31). IL obtained from simulations with idealized permeability is better for both CM and DM. Non-linear permeability leads to lower IL at the range 1–100 MHz compared to the idealized scenario. It can be concluded that utilization of the real permeability characteristics is indispensable for EMI filter design. Simplification at this stage can lead to significant simulation errors. For improvement of CM IL of the filter a ferrite core is substituted with a nanocrystalline core. In this case several effects corresponding to theoretical expectations are observed. Firstly, the low frequency CM IL is improved since μ_i of nanocrystalline is much higher. High frequency CM IL remains basically without change. Secondly, DM IL degrades due to the drop of leakage inductance of a CMC. Consequently, a nanocrystalline core with higher permeability does not give significant improvement in the high frequency range.

In order to improve high frequency IL, a black-box model of a filter can be supplemented with idealized stages and simulated only in schematic. Values of those components are automatically selected by an integrated optimizer, according to boundary conditions given for IL. Minimization of IL in the range 5–10 MHz is given as a task. Stray parameters of components used for IL improvement are taken from datasheets and included into the schematic for improvement of accuracy. In this way an improvement potential can be estimated before building a new 3D model. For the same experiment a CMC with inductance $9\mu\text{H}$, creating an LC-stage together with the above mentioned capacitors, is added. Improvement

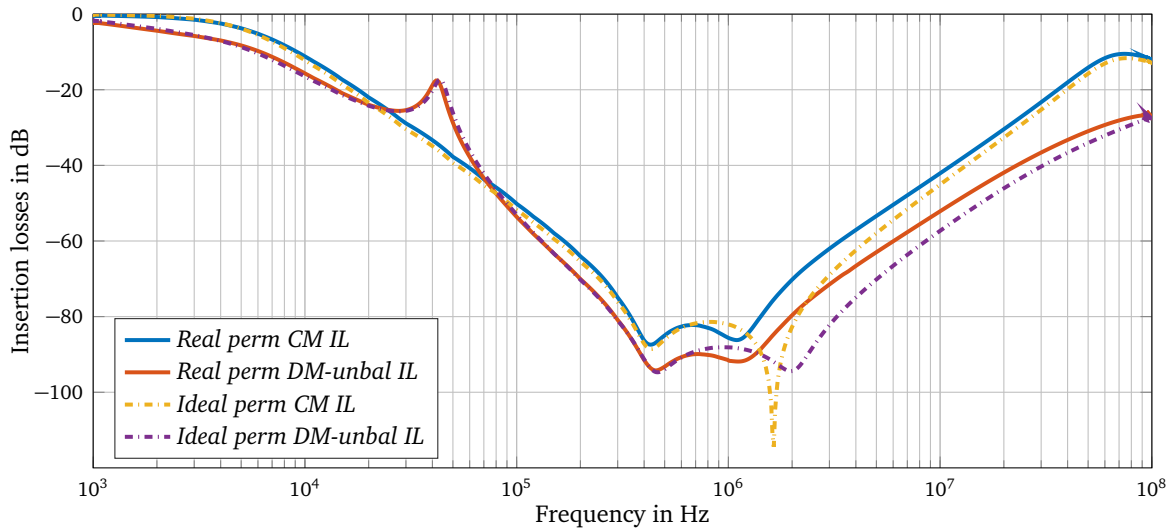


Figure 3.31.: Impact of frequency dependent permeability on IL.

of IL at high frequency is seen in Figure 3.32. Simple boosting of capacitor values causes degradation of IL at high frequency as was mentioned earlier.

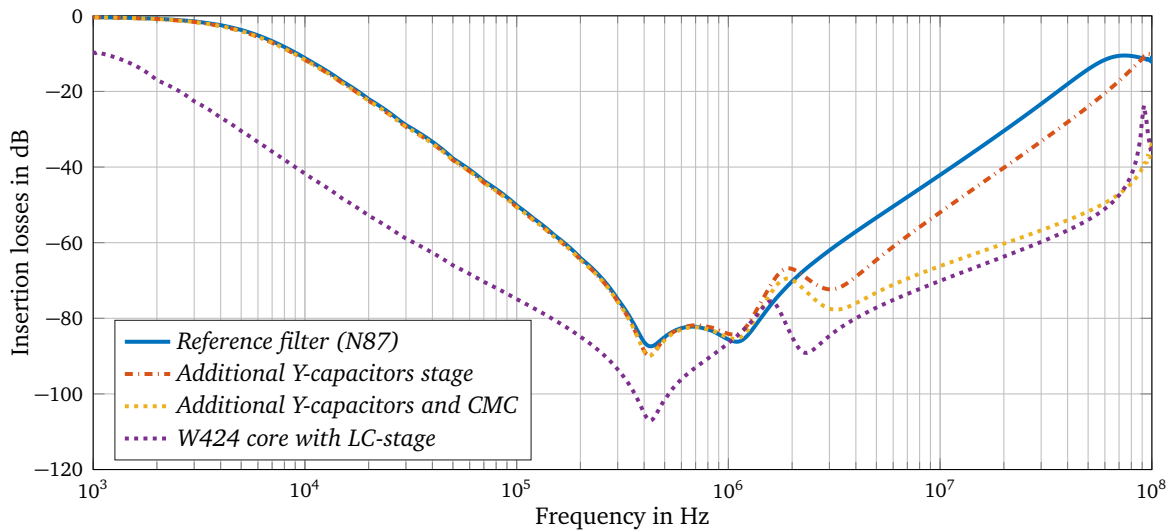
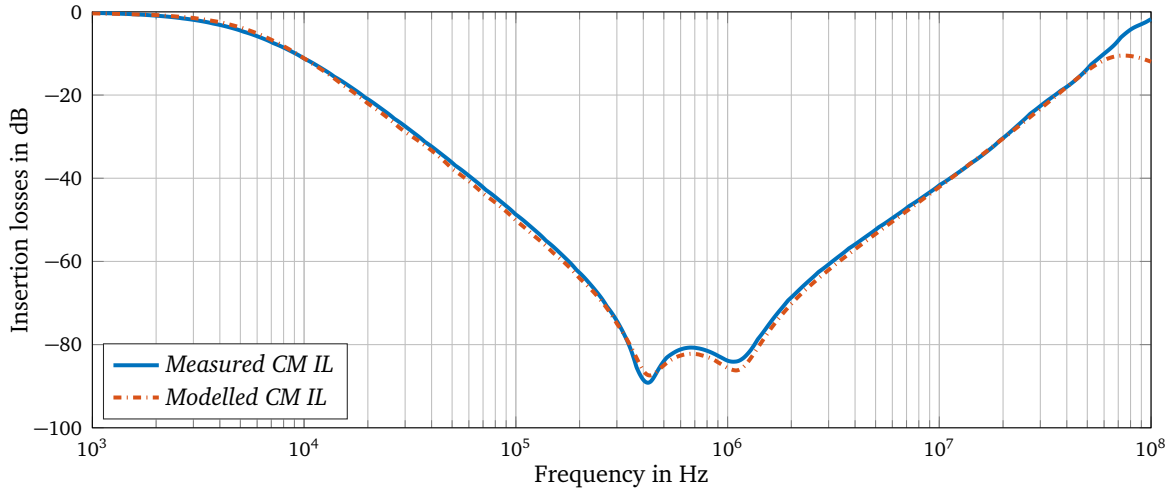


Figure 3.32.: Comparison between IL of designed and simulated filters with an improvement.

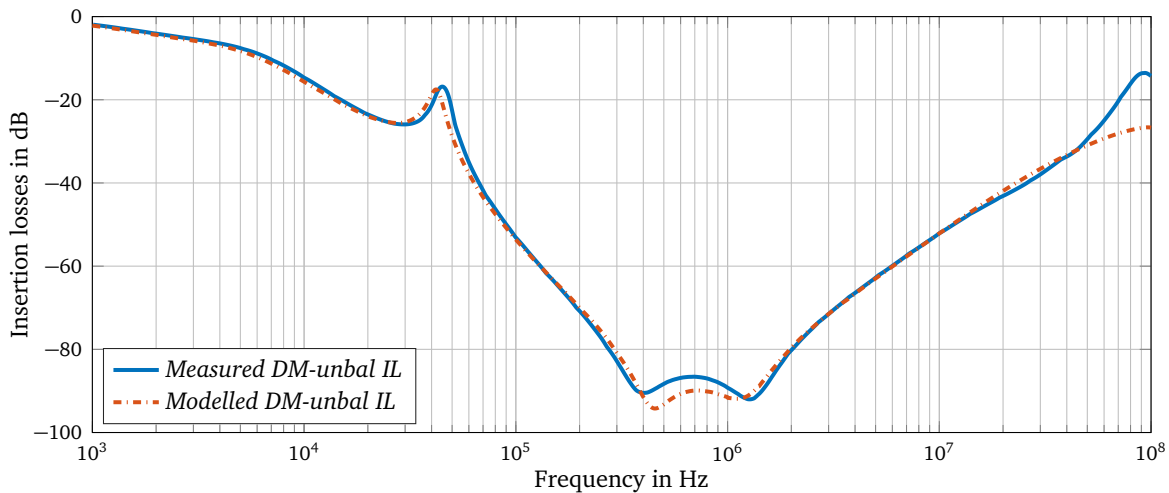
3.3.3 Validation

Resulting measurements for DM and CM IL compared with IL received from simulation are shown in Figure 3.33 and Figure 3.34. Both measurements and simulation are conducted according to CISPR17/EN55017. Measured characteristics of both self-made and conventional filters are in good agreement with simulation. However, an unexpected resonance is seen in DM IL of the conventional filter. Three different toroidal cores with unknown characteristics are utilized in the conventional filter. The mistake probably appeared during the permeability analysis, as there was no possibility to use the core characterization method developed in Section 3.2.1. The small mismatch by CM and unbalanced

DM IL can be explained by a non-ideal measurement setup and by some unaccounted inductance of the ground path.



(a) Common mode IL.



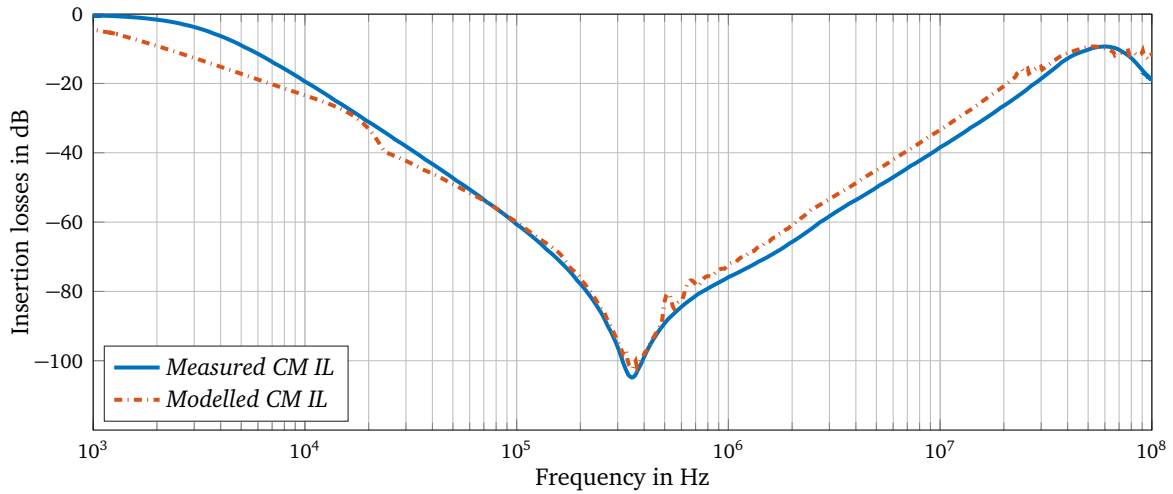
(b) Differential mode unbalanced IL.

Figure 3.33.: Comparison between measured and simulated self-made filters.

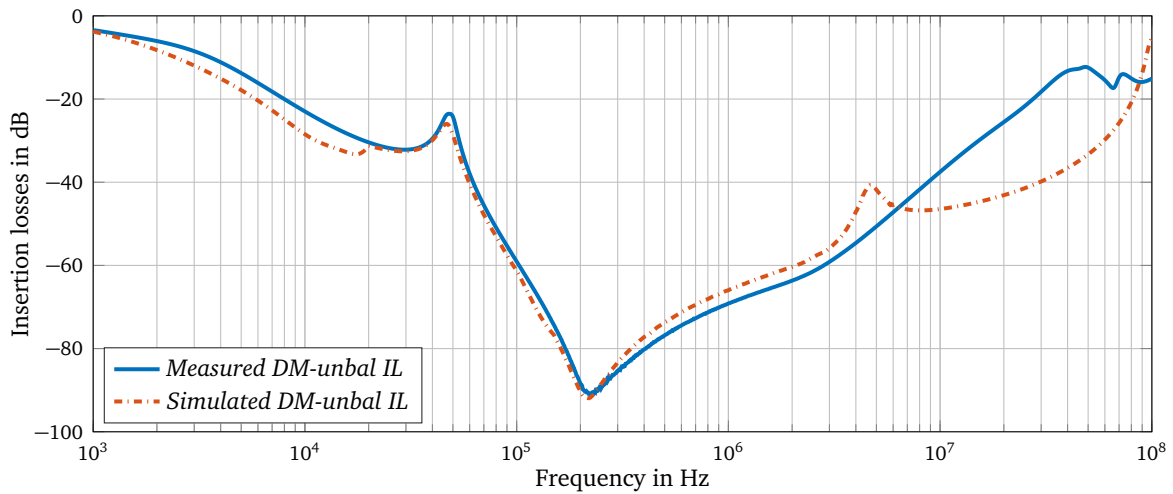
Two different improvement measures (according to optimization conducted previously) are implemented in the self-made EMI filter. The CM IL improvement predicted in simulation is confirmed with measurements of the improved prototype. Despite mismatch between measured and simulated IL, the general tendency is similar (Figure 3.35). This mismatch is caused mainly by sketch based implementation of extra stages (no parasitics are optimized).

The entire procedure of three-phase EMI filter design with FEM simulation is summarised in a flow chart, depicted in Figure E.3. Resulting characteristics of the EMI filters designed in accordance with this flow are very close to simulated IL. Characteristics of the simulated filter can be included into a model of a complete PE system.

The proposed method based on FEM electromagnetic modelling is a step towards EMI filter optimization. Practically all information required for IL modelling is contained in the 3D model with the addition of $\mu(f)$ in the form of numerical data. Good simulation results can be achieved without a deep



(a) Common mode IL.



(b) Differential mode unbalanced IL.

Figure 3.34.: Comparison between measured and simulated industrial filters.

analysis of processes inside of the EMI filter. Such time consuming steps as analytical calculation of EPC or evaluation of the parasitics relevance obtained from magneto- and electrostatic simulation are skipped. A built in optimisation tool of CST studio allows acceleration of selection of components suitable for a filter, based on the specified IL. This simulation method can be used in the case when there is not time for preparation of a SPACE model, especially when impact of mutual couplings on IL might be rather significant.

It must be mentioned that the design procedure proposed in this section does not include parasitics compensation methods. These compensation methods can be included during future development of this modelling method. Moreover adjustment of CMC parameters such as L_{cm} , L_{dm} , C_{EPC} is not flexible and requires changing of the 3D model for every following simulation step.

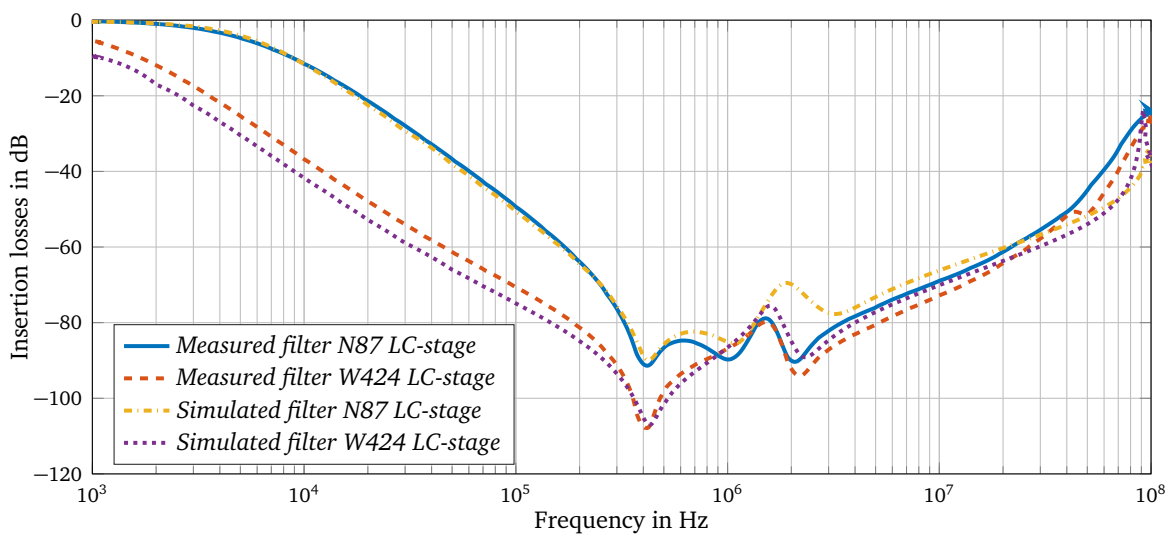


Figure 3.35.: Comparison between CM IL of designed and simulated filters with an improvement.

4 Parasitics Management in Three-Phase EMI Filters

An approach that achieves a required IL by either increasing the number of stages or by utilizing bigger passive components can be described as traditional. Filters with a higher number of stages exhibit a higher rate of IL change, thereby the required attenuation level can be reached more quickly. With employment of bigger components the main cut-off frequency of a filter is shifted toward lower frequencies and the rate of IL change remains without any changes. Nevertheless, those two methods are usually ineffective and lead to non-optimal filter design, especially for high frequency IL. Together with the size of filter components, self-parasitics increase as well. Therefore, an improvement of IL on the high frequency cannot be achieved by means of straightforward increase of component values. Multistage filters definitely have better performance at high frequencies when compared with single-stage filters. However, they degrade because of the same reason as single-stage filters. In addition, the price of a filter might increase with a higher number of stages.

Sophisticated filter design methods, which take into account effects causing IL degradation and allow to predict filters behaviour (Section 3) can be supplemented with specialized parasitics compensation techniques. Comprehensive analysis of EMI filters based upon dedicated behavioural models highlights the main reasons for IL degradation. These are: self-parasitics of passive components, mutual couplings and nonideal magnetic core properties. In this chapter the main attention is concentrated on studying the first two. Self-parasitics compensation methods allow reduction of EPC and ESL and shift the SRF of passive components toward higher frequencies. Mutual couplings can be optimized through a proper arrangement of filter components. Moreover, parasitic magnetic fields can be used for self-parasitics compensation.

Currently available parasitics compensation methods are analysed and supplemented with several novel ideas, which introduce some additional advantages. These methods are critically evaluated and tested. A detailed study of every parasitics compensation technique is conducted in terms of efficiency, costs and power density. Physical limits are determined and discussed in detail. Effects caused by mutual couplings in three-phase EMI filters are comprehensively analysed, with the main scope on the relevance assessment. After identification of the most and the least relevant coupling, recommendations concerning filter layout and component arrangement inside of an EMI filter are formulated.

4.1 Parasitics Compensation of The Filter Components

Previously conducted analysis of EMI filters (Chapter 3) shows that the main contributors to degradation of an EMI filter IL are ESL and EPC. In order to demonstrate these effects, the values of ESL and EPC in a mathematical model are changed in the range from 1 up to 100 picofarad or nanohenry respectively. In Figure 4.1 and Figure 4.2 the impact of ESL of capacitors and EPC of the CMCs on IL of the conventional three-phase one-stage EMI filter are demonstrated. Higher ESL leads to shifting of the SRF toward the lower frequency range and simultaneously lifts high frequency IL up. Degradation of IL can also be clearly seen by growing EPC, but shifting of the SRF is not certain due to damping introduced by the magnetic core. Core materials with a lower imaginary part of permeability demonstrate an explicit SRF.

It can be concluded that reduction of EPC and ESL can give significant improvement of IL at the high frequency. It is clear from these diagrams that in spite of completely compensated parasitics (it is not possible to achieve in practice), IL continues to diminish due to permeability degradation of the core material.

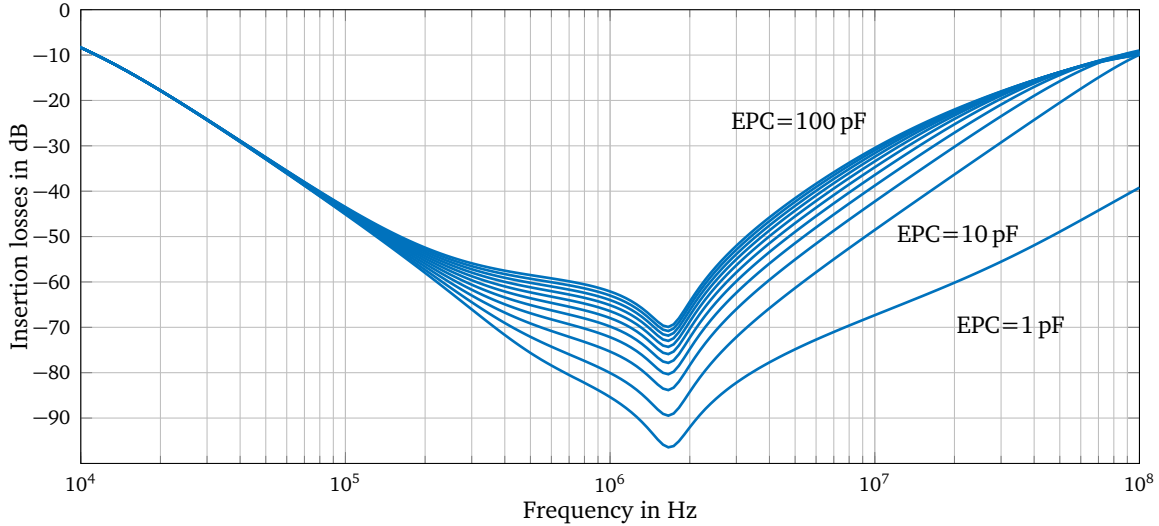


Figure 4.1.: Effect of EPC on insertion losses of a conventional EMI filter.

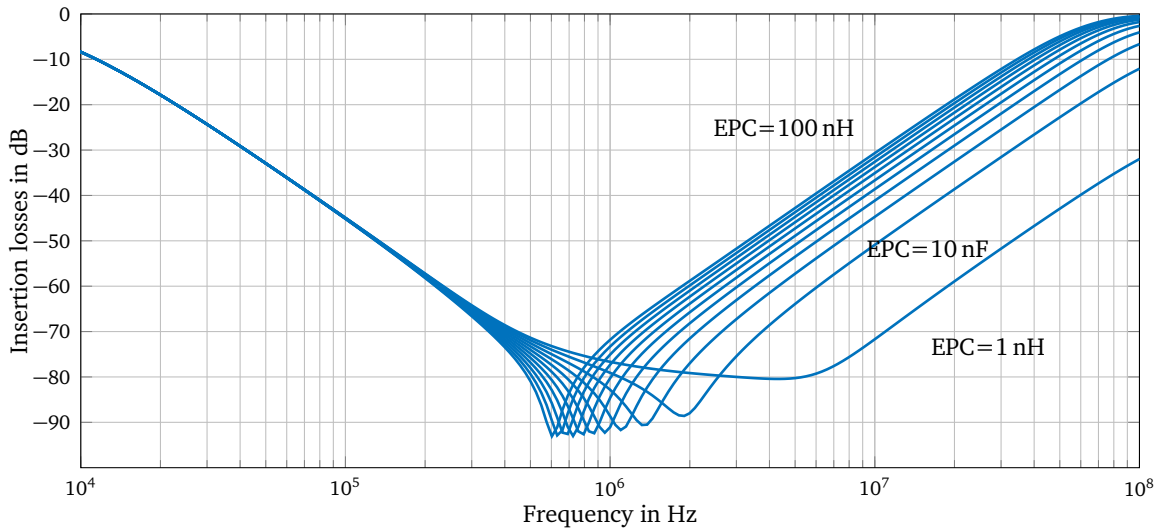


Figure 4.2.: Effect of ESL on insertion losses of a conventional EMI filter.

There is a huge amount of articles and dissertations dealing with improvement of EMI filter performance. The majority of authors focus either on the mutual couplings or on the stray components of single-phase filters [61, 147, 148, 170, 190]. Only a couple of publications are related to improvement of three-phase filters [7, 68]. For implementation of EMI filter improvement methods, either additional components or specialized PCBs are needed. Some special EMI filter components already include parasitics compensation in the construction. Those components can be directly used for improvement of the high frequency performance of EMI filters [162]. Adaptation of existing parasitics compensation methods to three-phase filters is a very challenging and sometimes impossible task. It must be mentioned that

the entire cancellation of ESL and EPC cannot be achieved with any of the proposed methods, due to secondary parasitics and nonideal magnetic material properties.

4.1.1 Compensation of EPC

EPC of a CMC can be either directly affected with variation of windings arrangement or compensated with special methods. Changing of a coil arrangement is an effective method to reduce EPC. According to (3.23) and (3.28) decreasing of a turns number does not lead to diminishing of EPC. However, moving of adjacent turns apart and utilization of a cable with lower insulation permittivity does decrease EPC. The most effective way for the EPC reduction is to increase the distance between turns. Unfortunately, cores with bigger diameter have to be utilized in this case. As a result, the size of a CMC increases, which results in lower power density. However, this could be avoided if progressive winding techniques, such as reversed, bifilar or split windings can be used. For example, a split winding allows decreasing the stray capacitance of multilayer transformers quite significantly (up to a factor of two), but the majority of CMCs have only one layer. Hence, positive effects exhibited by a split winding of a CMC are rather moderate. External mutual couplings of a CMC to other filter components can be regulated by means of specialized windings as well. Nevertheless, shortcomings of these winding types limit their use in practical applications and make them unpopular among both engineers and scientists. Some information about windings types for CMC can be found in [2, 66]. Moreover, a conventional turn-to-turn winding technique performs rather well in terms of stray capacitance. Along with the aforementioned EPC improvement approaches, which have a direct impact on EPC, an EMI filter can be supplemented with specialized compensation networks. Then EPC remains without any changes, but the total impedance of a system is improved.

It must be mentioned that the SRF is a product of EPC and self-inductance of a CMC. Therefore, increase of inductance leads to a shift of the SRF to the lower frequency, although EPC remains without changes. Due to this reason CMCs with higher inductance have lower SRF. Much better results can be achieved with use of two- or multistage filters. For instance, two CMCs with smaller inductance, which are connected in series have a noticeably lower SRF than a single inductor with the same sum inductance. This can be considered as an argument in favour of multistage filters.

In [57] the idea of a coupled inductor employed for capacitor scaling was introduced. This principle was extended further in [148] with the main focus on EPC compensation. The coupled inductor principle was adopted for EPC compensation of conventional inductors and single-phase CMCs. A coupled inductor used for compensation can be either provided as an extra component or included into the construction of a CMC. An extra compensation coil has to be wound in the same direction with the main winding. An input terminal of the extra coil is, thereafter, connected to a phase conductor and an output is shunted to the ground through a compensation capacitor. Thereby, an alternative low impedance path for interferences, (which bypassed a CMC due to EPC), is provided.

In order to implement a similar compensation method for a three-phase CMC, three compensation coils must be added. One terminal of each compensation coil is connected to a phase winding and the second terminal is connected to the compensation capacitor, similar to single phase inductors. The resulting circuit of the three-phase CMC with implemented EPC compensation network is depicted in Figure 4.3a. Compensation coils must have a smaller number of turns than the main windings. This

diminishes EPC of the compensation coil and decreases voltage applied to compensation capacitors. Each of the compensation capacitors C_{com} must be bigger than a parasitic capacitance C_p of the particular winding. The value of a compensation capacitor can be assessed with (4.1)

$$C_{com} = \frac{C_p}{N_{com}/N_{main}(1 - N_{com}/N_{main})}. \quad (4.1)$$

N_{com} is the number of turns for the compensation coil, N_{main} is the number of turns for a phase winding. From (4.1) it is seen that the number of turns of the compensation coil has a direct impact on the value of the compensation capacitor. In order to show possible IL improvement, a three-phase CMC with an implemented compensation network is designed and integrated into a conventional EMI filter. The resulting comparison between IL of the reference EMI filter with no parasitics compensation and the EMI filter with implemented EPC compensation is shown in Figure 4.4.

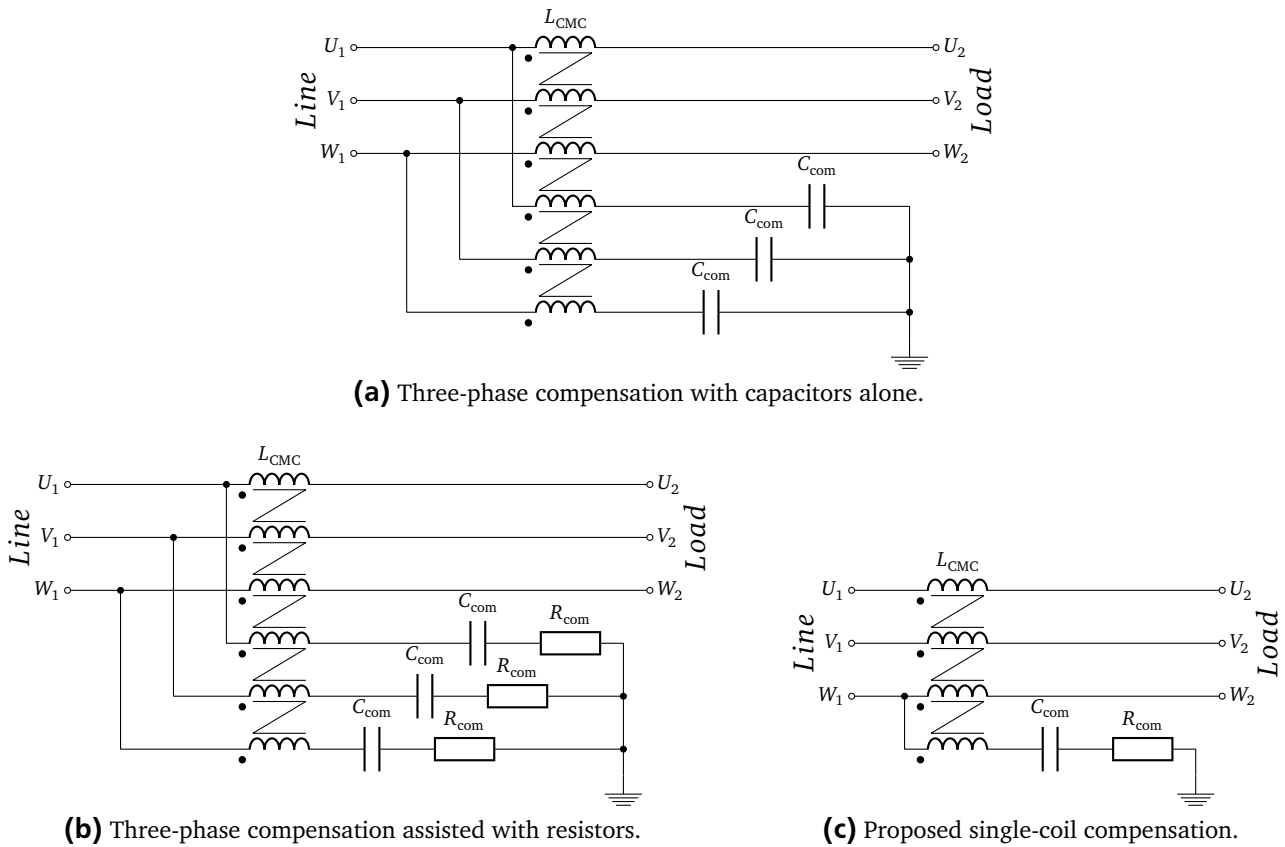


Figure 4.3.: Resulting circuit of the CMC with an implemented EPC compensation network.

Since there are no changes introduced by the compensation technique below 100 kHz, IL in this range are not shown. With the compensation coil, consisting of eight turns and measured EPC ≈ 3.1 pF of the CMC under test, the necessary compensation capacitance is ≈ 12.4 pF per phase. In Figure 4.4 an improvement of CM IL in the frequency range starting at the SRF and going up to 20 MHz, which reaches 10 dB, is observed. One extra resonance is introduced by the compensation network on about 22 MHz. Due to this resonance degradation of IL, it is comparable to the reference IL. The resonance can be damped with resistors, connected in series with compensation capacitors (Figure 4.3b). Effects

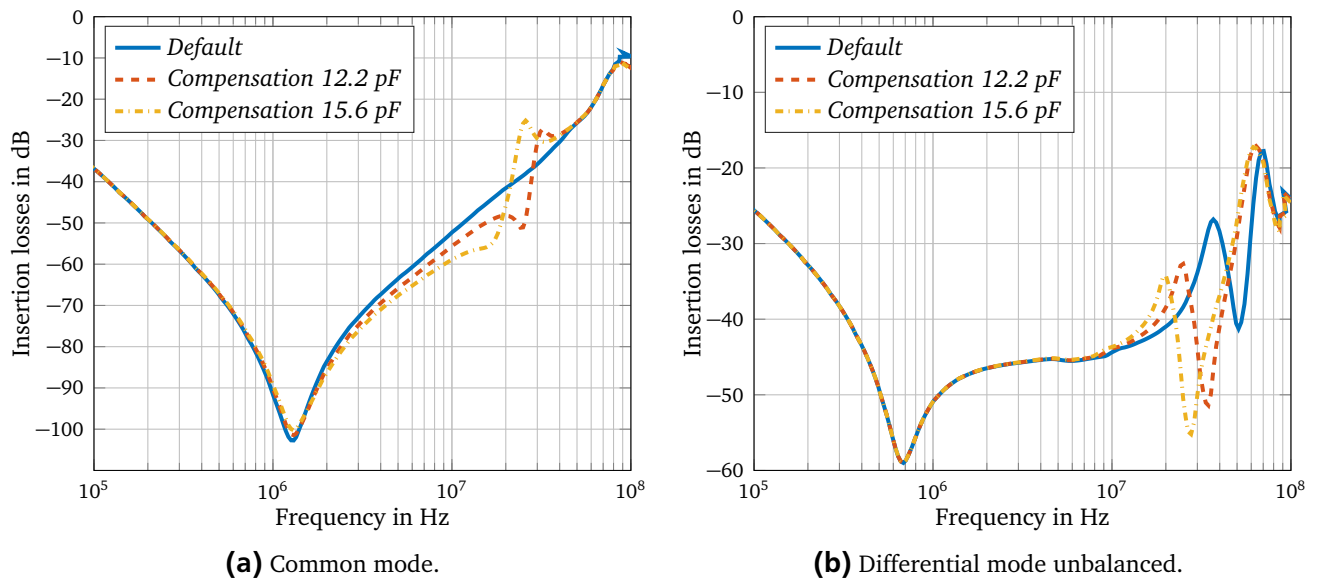


Figure 4.4.: Measured IL of a conventional EMI filter with and without EPC compensation, based on three capacitors.

of the implemented EPC compensation on DM IL are difficult to assess unambiguously. However, those effects barely touch the standardized EMI diapason (150 kHz–30 MHz) and can be neglected. If the value of the cancellation capacitor that is selected is bigger than the calculated capacitance according to (4.1), degradation of IL caused by overcompensation is observed. Measurements with a ≈ 15.4 pF capacitor demonstrate this scenario (Figure 4.4). The other situation with lack of compensation capacitance (≈ 5.6 pF) is shown in the same figure. Under this scenario IL improvement is considerably smaller.

In spite of positive results exhibited by this compensation method, achieved improvement is not so significant as expected in accordance with the simulation that was carried out. There are several reasons causing this mismatch. Firstly, CMC impedance deteriorates at the higher frequency as a result of permeability degradation. Thus, even perfect compensation does not help to keep behaviour of a CMC close to ideal. It is important to emphasize that effects caused by permeability degradation are the main contributor to CMC impedance degradation. Secondly, degradation of permeability with frequency causes reduction of coupling between a compensation coil and the main windings. Changing the coupling coefficient from 0.999 to 0.98 almost nullifies compensation effects [148]. Lastly stray inductance of the compensation network, consisting of ESL of the compensation capacitor and cable parasitic inductance, increases impedance of the cancellation network. As a result, high-frequency currents cannot flow through the compensation capacitor.

Much better results are achieved with a resistor, connected in series with the compensation capacitor. With no resistor connected, the resonance introduced by the compensation capacitor is rather narrow. The additional series resistor dampens the resonance, so that IL come back slightly to the conventional characteristic in the range 15 MHz–25 MHz as demonstrated in Figure 4.5. A circuit of a CMC used in this experiment is depicted in Figure 4.3b.

Due to the damping presented by a magnetic material, the necessary value of the damping resistor is difficult to determine precisely. For a practical design it can be roughly estimated with an empirically founded coefficient $k_{\text{damp}} = (1 - e^{-(L_{\text{cmc}} \cdot 10^3)}) \cdot 250 + 100$. CM inductance of a CMC used in the experiment is

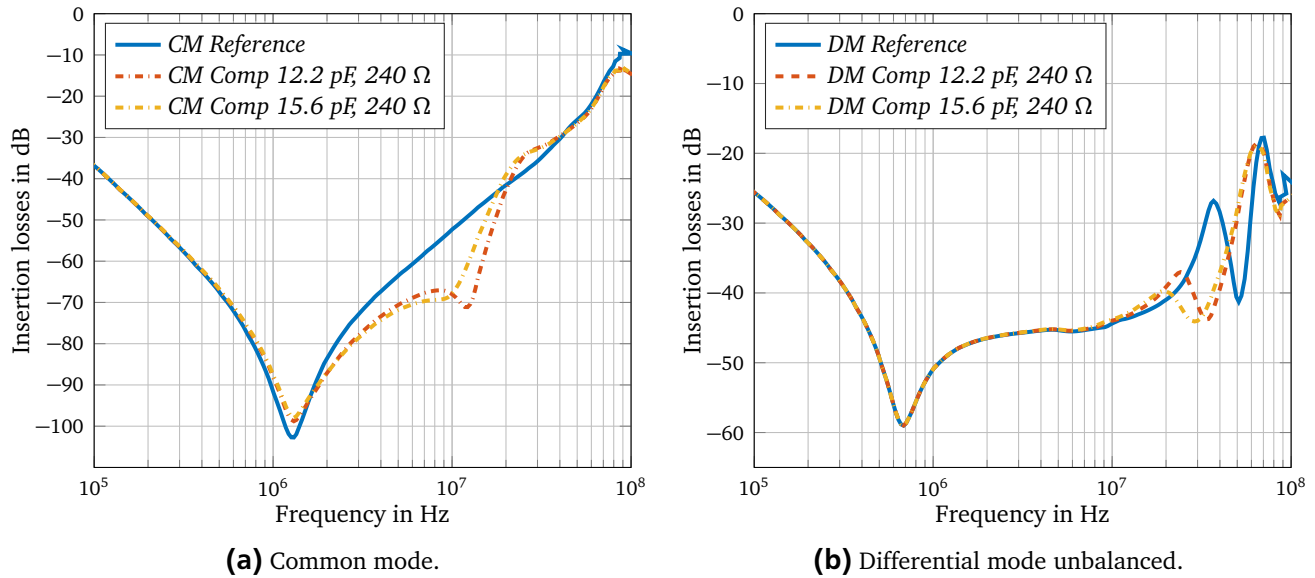


Figure 4.5.: Measured IL of a conventional EMI filter with and without EPC compensation assisted with resistors.

0.82 mH. Consequently, the damping resistor should be 240 Ω . A resonance, caused by a compensation network on 22 MHz, is mitigated with this resistor (Figure 4.5). The tendency of a CM IL curve remains similar to the previous case of study, with the maximum improvement reaching 16 dB. In contrast with the case of study without mitigation, DM IL are improved.

Assuming that a CMC has nearly ideal coupling between windings, a singular compensation coil can be used in a three-phase CMC. Phase unbalance caused by the compensation capacitor, which is connected only to one phase, is minimal since current flowing through this capacitor is negligibly small, compared to phase currents. When single capacitor compensation is employed, a sum of stray capacitors of all phase windings must be used for calculation of the necessary compensation capacitor C_{com} . The same equation (4.1) can be used for C_{com} calculation. Current which flows through the compensation capacitor remains small, so that a thin wire can be used for winding of a compensation coil. Experiments conducted with three compensation coils prove that utilization of damping resistors positively influences IL. Therefore, the proposed single-coil compensation network is also assisted with a damping resistor (Figure 4.3c). IL of the reference filter without compensation, a filter with the three-coils EPC compensation and the single-coil EPC compensation are compared in Figure 4.6. Values of utilized components are equal for both compensation methods.

When only the standardized EMI frequency range (150 kHz–30 MHz) is considered, a remarkable improvement of CM IL exhibited by both compensation methods (single-coil compensation and three-winding compensation) can be observed. For a properly designed compensation network improvement of CM IL reaches 20 dB. The IL improvement exhibited by the single-coil EPC compensation method makes it useful for practical application in three-phase EMI filters. The single-coil based compensation method has several advantages from the complexity and core utilization points of view: it is quite compact and requires only two additional passive components and a winding; furthermore, the price of implementation is by definition three times lower compared to the three-winding compensation method. Nevertheless, for CM IL improvement in the frequency range between 8 MHz and 20 MHz a three-winding compen-

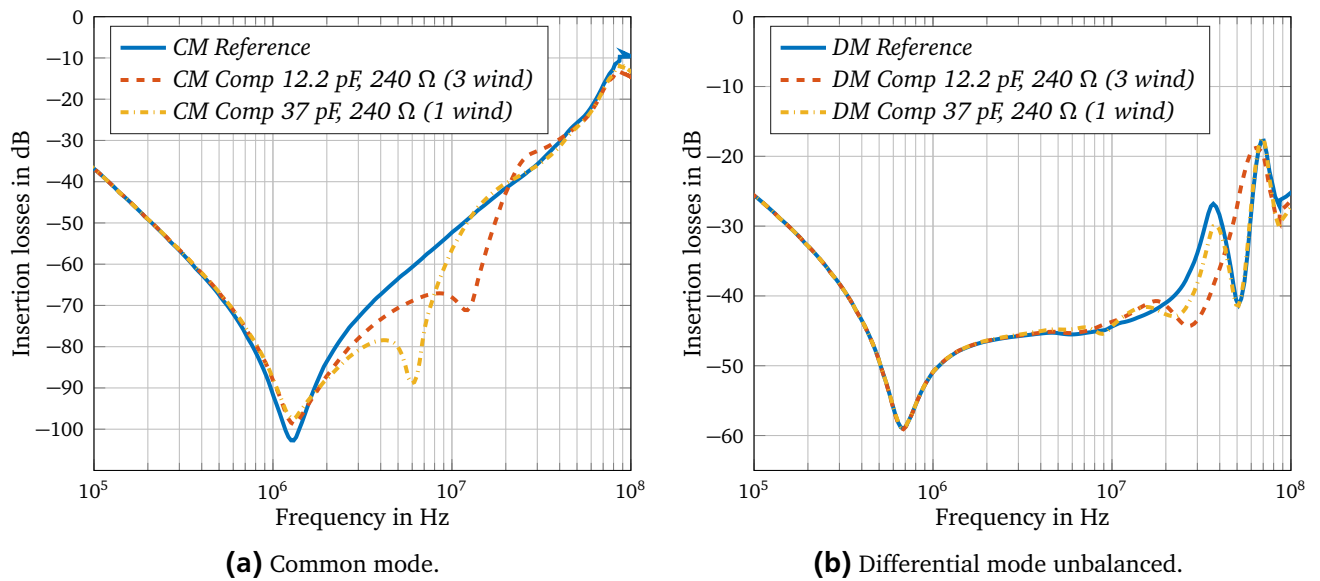


Figure 4.6.: Measured IL of the reference filter, EMI filters with EPC compensation based on single-coil and three windings methods.

sation is recommended due to its better performance in this range. For improvement in the frequency range 1 MHz–8 MHz the single-coil compensation is a better option.

Alternatively to the aforementioned methods a "center tapped capacitor" method can be employed for EPC compensation [212, 215]. The main idea of this method is to connect a small compensation capacitor between the center point of a winding and the ground. With a properly selected capacitor impedance of a CMC becomes purely inductive. A center tapped capacitor method was further developed in [68]. It was shown that for the coupling coefficient between phase windings of a CMC close to 1, a single capacitor connected to one phase winding is sufficient. It provides some benefits for production, since the central points of the two remaining phases do not need to be accessible. Compared to the coupled-coil compensation method, the center tapped capacitor method does not have an extra compensation coil and practical realization might be simpler. However, practice shows that connection to the central point of a winding must be very precise. It is difficult to achieve even during experiments in the laboratory. This issue might limit practical use of this method. Moreover, voltage across the compensation capacitor connected between the center of a winding and the ground is nominal phase voltage. It caused higher price and size of the capacitor. CM and DM IL of a three-phase EMI filter assisted with the center tapped compensation method are depicted in Figure 4.7.

DM IL are barely affected by the center tapped compensation method. Exhibited CM IL improvement is rather significant, reaching 20 dB. The best results are exhibited in the frequency range 5 MHz–30 MHz. For better stability it is recommended to stabilize the entire construction with compound. Basically, use of the center tapped capacitor method involves the same limitations due to secondary parasitic effects. Therefore, an ideal EPC compensation cannot be achieved with any of these methods.

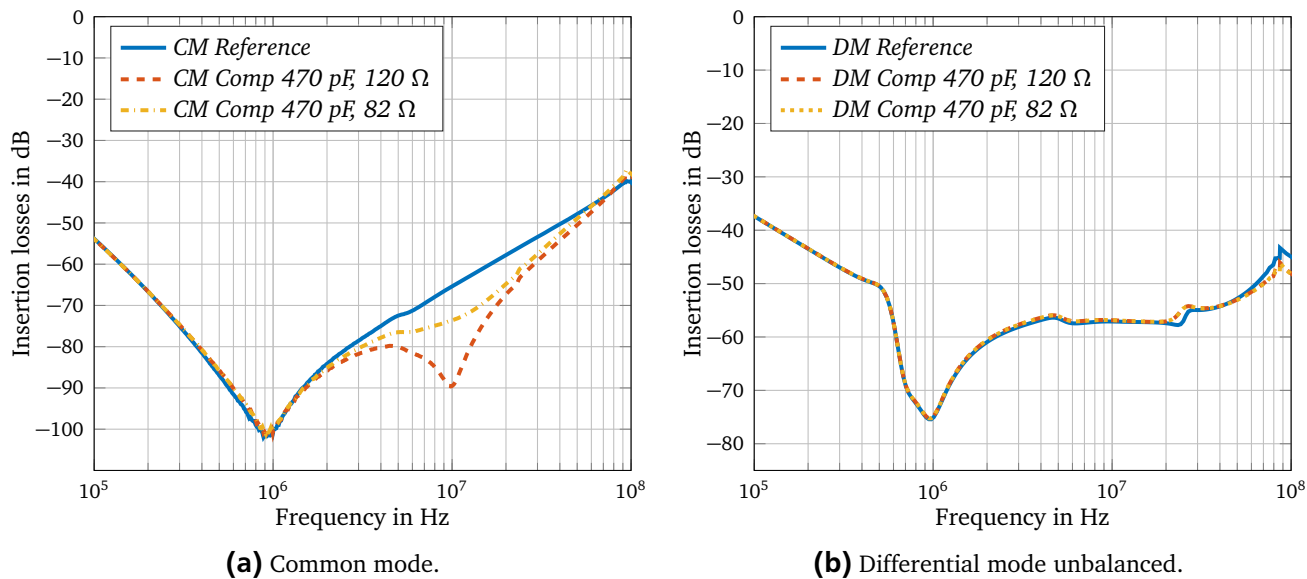


Figure 4.7.: Measured IL of a conventional EMI filter with and without EPC compensation based on the center-typed capacitor method

4.1.2 Compensation of ESL

ESL of the filter capacitors represents the second most important parasitic effect of an EMI filter. In contrast with inductive components, capacitors are typically purchased elements and there are no possibilities to influence their technical parameters. Several ESL compensation techniques for single-phase applications are presented in literature. Basically, there are two different types of ESL compensation: the method based on crossed over capacitors [191] and the coupled inductor method [149, 161]. The first is based on supplementation of conventional filter structure with coils, connected between terminals of crossed over capacitors. Compensation coils together with respective capacitors exhibit negative impedance, so that the current flowing through capacitors will not be affected by ESL. In order to use this compensation method in three-phase EMI filters, the quantity of employed capacitors has to be doubled. Moreover, the crossed over capacitors method cannot be used with Y-capacitors and series connected X-capacitors. This is because that compensation coils together with capacitors must create a balanced network. In three-phase filters this method can be applied only to X-Capacitors connected between phases.

For practical validation of this method an appropriate three-phase EMI filter is designed. An equivalent circuit of the filter is depicted in Figure 4.8a. Necessary inductance of a compensation coil is equal to 16 μ H for X-capacitors 2.2 nF each. Resulting IL of the designed EMI filter with and without compensation are depicted in Figure 4.9. For the reference measurements compensation coils are manually shorted. In the other cases IL are measured with ESL compensation coils. The filter with implemented ESL compensation is shown in Figure 4.8b. As it is expected, CM IL are not affected by EPC compensation of X-capacitors. Improvement of DM IL, which does not exceed 8 dB in the range 1–20 MHz is observed. Above 20 MHz IL of compensated filters come back towards uncompensated characteristics. This is quite similar to results obtained with the single-phase filter in [191]. The relatively poor outcome of this method can be explained by inferior tolerance of compensation coils. Obviously, ESL cannot

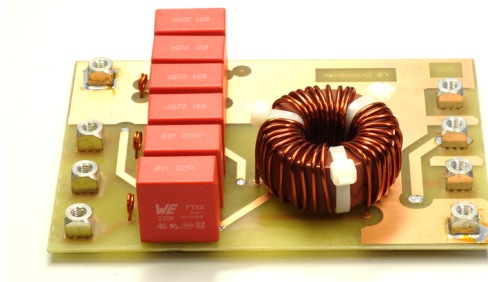
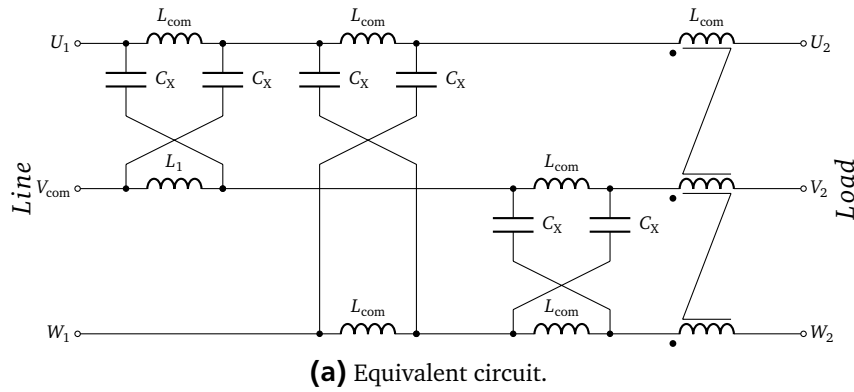


Figure 4.8.: Designed EMI filter with ESL compensation based on crossed over capacitors.

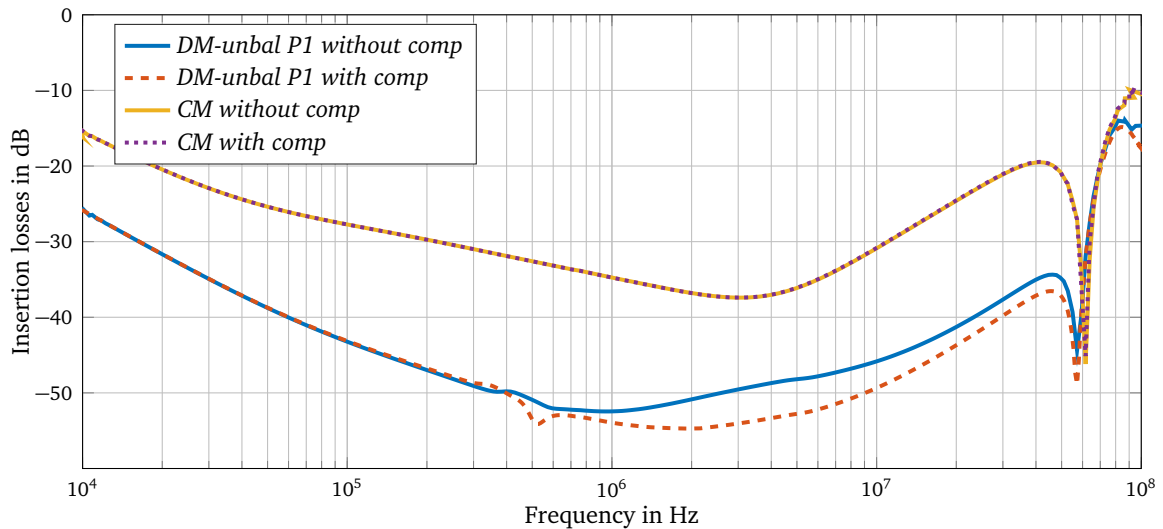


Figure 4.9.: CM and DM IL of the EMI filter with implemented compensation based on crossed over capacitors.

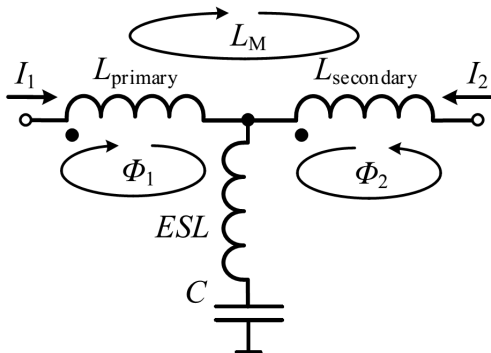
be compensated entirely and capacity degrades further due to high-frequency effects of a foil capacitor. Combined with high implementation efforts and doubly increased quantity of capacitors, it makes this compensation method not competitive in practical applications, particularly in three-phase EMI filters.

The second ESL compensation method involves utilization of a magnetically coupled inductor. [185]. A coupled inductor forms "negative inductance" in one of three terminals. One of the possible configurations of the coupled inductor is shown in Figure 4.10a. This configuration of the coupled inductor can be realized as a single planar coil tapped at the appropriate place. For the inductor depicted

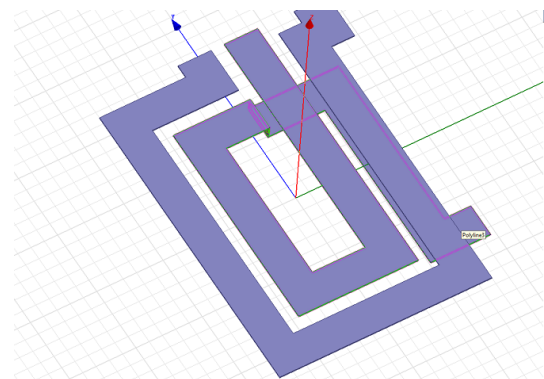
in Figure 4.10a, negative inductance is equal to the mutual inductance L_M . In order to achieve ideal compensation, negative inductance $-L_M$ and L_{ESL} must be equal, or ΔL in (4.2) must be 0. It must be mentioned that this method is very sensitive, so that the difference between L_M and L_{ESL} must not exceed 5%.

$$\Delta L = -L_M + L_{ESL} \quad (4.2)$$

A 3D model of the planar coupled inductor in ANSYS Maxwell is shown in Figure 4.10b. The mutual inductance can be adjusted by changing of the distance between coils and the turn size. This implementation is quite robust, and therefore it is suitable for practical applications. Negative inductance of the depicted coupled inductor is 16 nH.



(a) Equivalent circuit.



(b) Prototype in ANSYS.

Figure 4.10.: An equivalent circuit and a 3D model of the planar coupled inductor.

Phase-to-phase connected X-capacitors of an EMI filter is the simplest capacitor arrangement for implementation of coupled inductors. In this situation it does not matter which terminal of a capacitor is connected to the coupled inductor. A designed EMI filter with the ESL compensation applied to X-capacitors and an equivalent circuit are shown in Figure 4.11. As expected, there is no impact of compensation on CM IL. DM IL are improved by ≈ 10 dB in the range 700 kHz–20 MHz (Figure 4.12). Depicted results are close to improvement obtained with the crossed over capacitors method. Since there are no extra components needed, utilization of the coupled inductor based compensation method should be much better for practical applications than the crossed over capacitors method.

The most significant performance improvement exhibited by the coupled inductor compensation technique is observed in the case of star-connected X-capacitors followed by a Y-capacitor connected between the star point and the ground. CM and DM IL are improved simultaneously. DM IL with applied compensation gain from 10 dB to 25 dB in the range 1–80 MHz. This can be achieved due to series connection of two X-capacitors with compensated ESL, so that inductance of a current path between two phases is significantly lower. The improvement of CM IL is approximately 5 dB in the frequency range above 1 MHz. An equivalent circuit, exhibited IL and a picture of a designed EMI filter with this compensation are shown in Figure 4.13 and Figure 4.14.

It is worth mentioning that a coupled inductor must be connected to a terminal of a X-capacitor on a phase side and a compensation inductor of a Y-capacitor is connected on the star point side. The

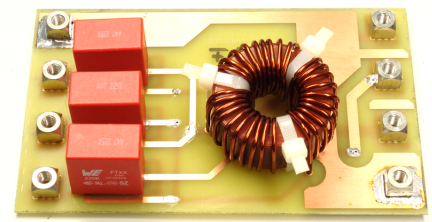
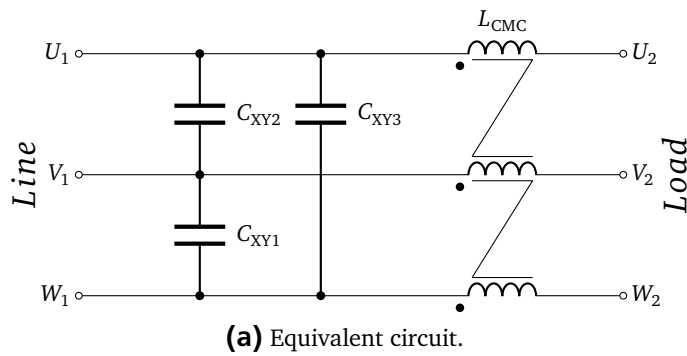


Figure 4.11.: EMI filter with the coupled inductor based ESL compensation applied to X-capacitors.

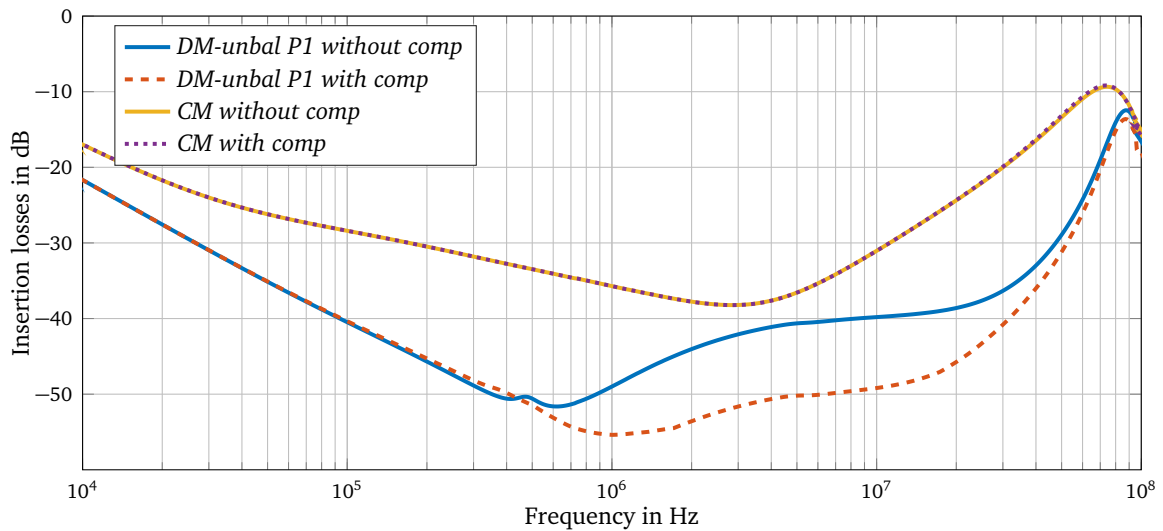


Figure 4.12.: CM and DM IL of the EMI filter with the coupled inductor based ESL compensation applied to X-capacitors.

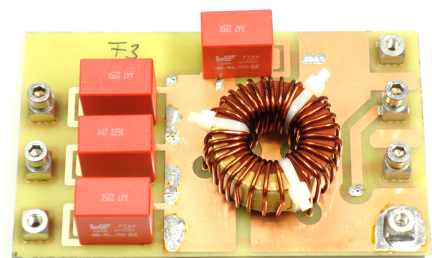
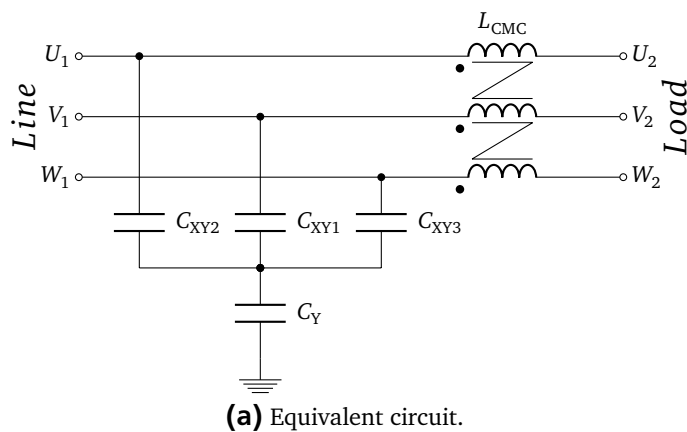


Figure 4.13.: EMI filter with the coupled inductor based ESL compensation applied to X- and Y-capacitors.

previous statement is proved by following laboratory experiments; coupled inductors are reconnected to the opposite terminal of capacitors, resulting in compensation inductors of X-capacitors which are placed on the star point side, and the coupled inductor of a Y-capacitor is located on the ground side. Aside from that, an employed circuit of the EMI filter reproduces an equivalent circuit depicted in Figure

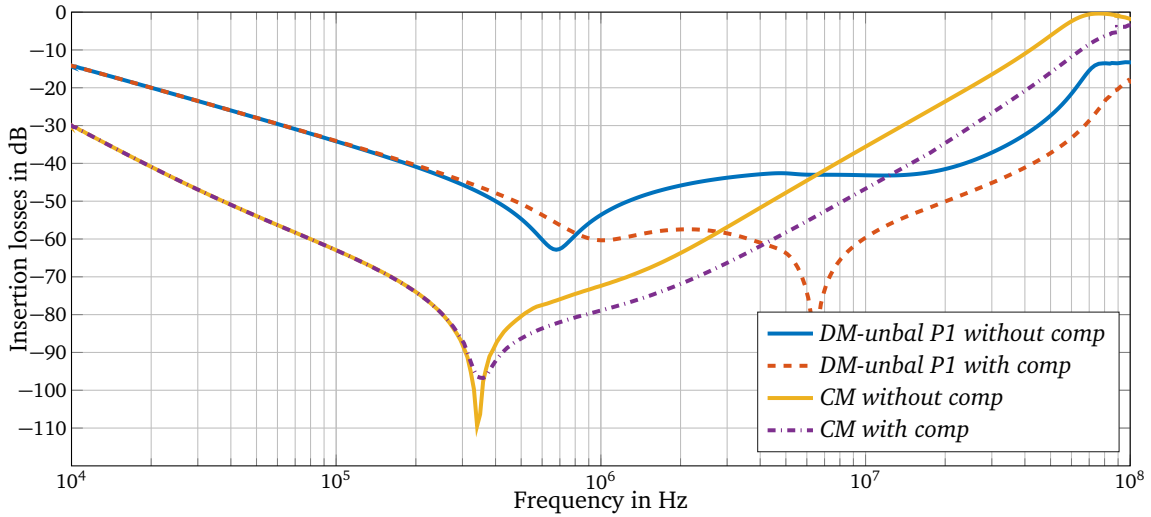


Figure 4.14.: CM and DM IL of the EMI filter with the coupled inductor based ESL compensation applied to X- and Y-capacitors.

4.13. PCB layouts with the appropriate and wrong connection of coupled inductors are depicted in Figure 4.15. Measured characteristics of the EMI filter with incorrectly connected coils are depicted Figure 4.16. For this experiment no positive effects are observed. The behaviour of this compensation inductor arrangement is explained by the following: ESL of every path become bigger, as a ground(star) side traces include self-inductance of planar inductors; primary L_1 and secondary L_2 winding of every inductor is ≈ 60 nH with a relatively poor coupling coefficient k (around 0.3), so that according to (4.3), mutual inductance cannot be higher than L_1 and L_2 .

$$L_M = k\sqrt{L_1L_2} \tag{4.3}$$

Consequently, ESL compensation does not work due to the increased size of parasitic inductance.

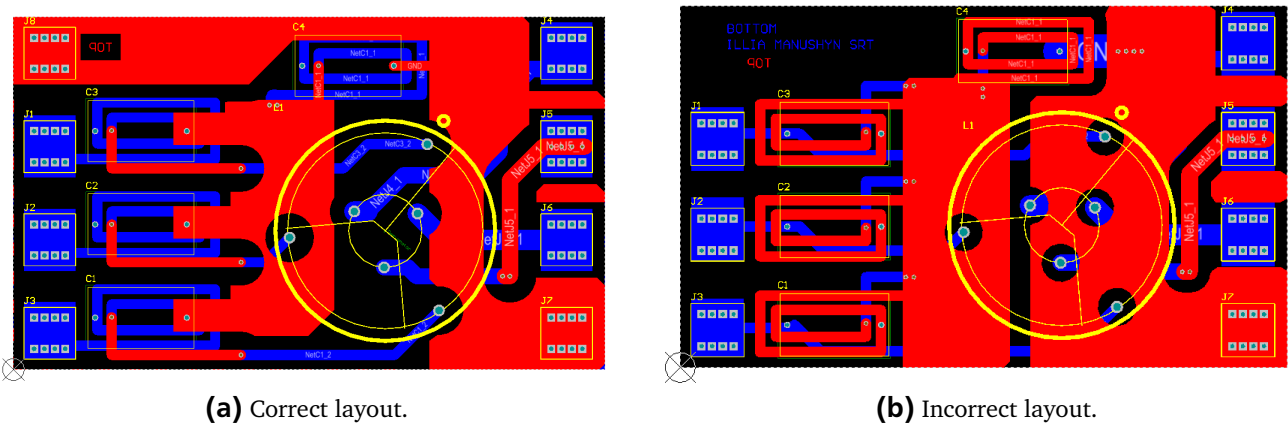


Figure 4.15.: PCB used for EMI filters with different location of coupled inductors.

The compensation technique based upon the magnetically coupled inductor is applied to another filter topology with directly connected Y-capacitors between phases and the ground (Figure 4.17). CM IL

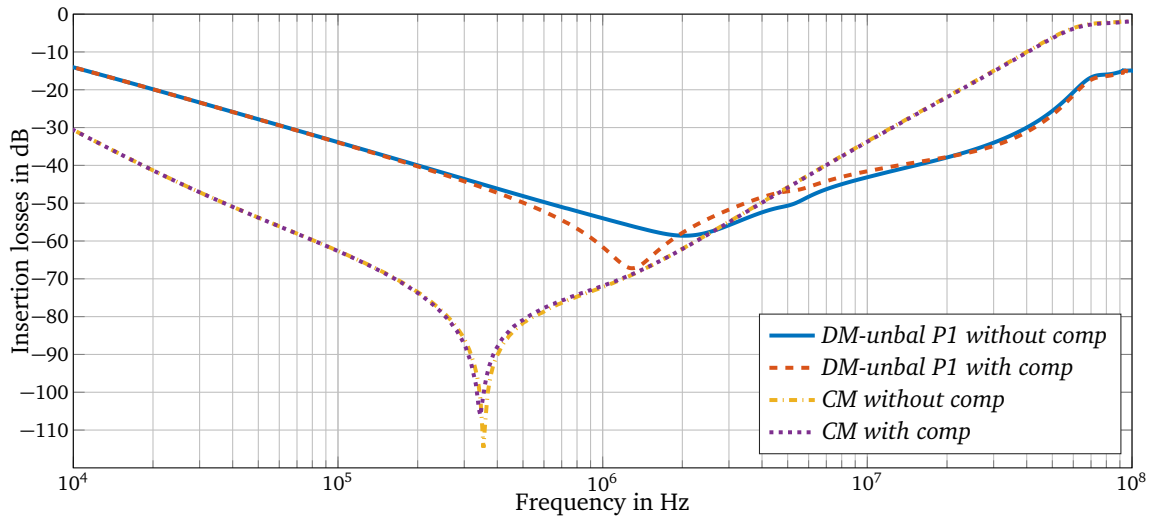


Figure 4.16.: CM and DM IL of the EMI filter with the coupled inductor based ESL compensation, applied to X- and Y-capacitors from the opposite side.

are slightly improved due to additional inductance of a current path which is hard to consider during design of the coupled inductor. As was mentioned before compensation inductance must deviate from ESL by no more than 5%. Otherwise, no positive effects will be obtained. The issue of CM path inductance consideration is seen on this example: even a well designed compensation coil cannot cover effects of the CM current path. Nevertheless compensation is quite effective as seen in DM IL and reaches 25 dB in the range 0.6–20 MHz (Figure 4.18). However this improvement is still far away from the theoretically expected results. Unfortunately, exactness of the coupled inductor design must be much higher in order to achieve better results. High exactness demand is the biggest disadvantage of this compensation method.

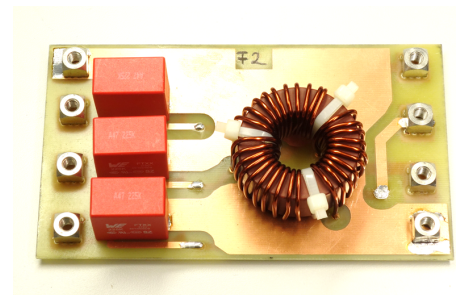
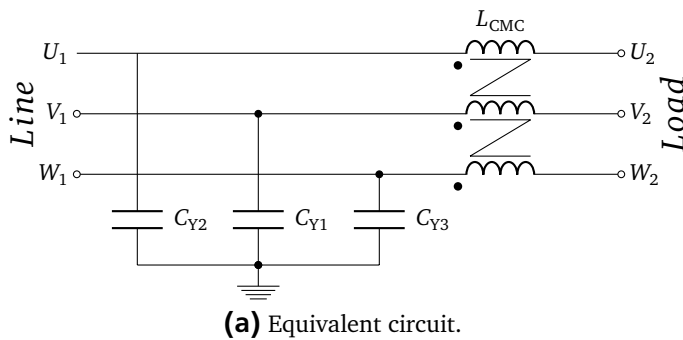


Figure 4.17.: EMI filter with the coupled inductor based ESL compensation, applied to Y-capacitors.

Implementation of the coupled inductor based compensation technique in three-phase filters has several limitations. Similar to the method based on crossed over of capacitors, ESL of Y-capacitors connected between phases and the ground directly is barely influenced due to inductance of the CM current path. Nonetheless, DM IL independent from the connection type can be improved by several decibels. In summary, the compensation method based on the coupled inductor is effective for X-capacitors when placed directly between phases and for star connection of X- and Y-capacitors. The main advantage of the coupled inductor based compensation method is that no extra elements are required and a coupled

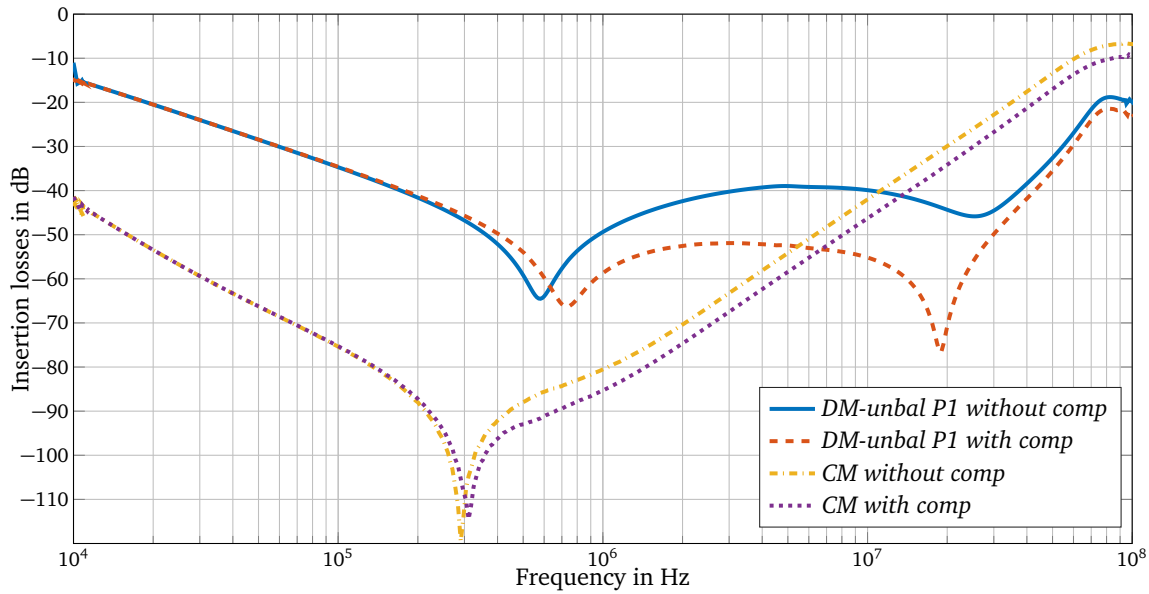


Figure 4.18.: CM and DM IL of the EMI filter with the coupled inductor based ESL compensation, applied to Y-capacitors.

inductor can be realized as a planar structure. Since even in EMI filters with higher power rates capacitors are usually placed on a PCB, implementation of a coupled inductor should not be a big issue, because PCBs that already exist and can be simply redesigned. Furthermore, additional compensation modules can be used for EMI filters with nominal power extending 25 kW [161]. This is a big advantage compared to a crossed capacitors method, where a coreless compensation coil must carry the nominal current of a filter. However, none of the studied compensation methods completely eliminate ESL.

All aforementioned compensation methods are based on schematic solutions, where lump components are compensated utilizing the other lump components. By definition ESL is self-inductance, therefore the magnetic field of the ESL can be influenced by the external magnetic field. In order to compensate ESL an inductor which creates a magnetic field in the opposite direction to the field of the capacitor has to be implemented. Simulations in FEM software show principle potential of this idea. Two different implementations of the compensation inductor are shown in Figure 4.19. Terminals of these compensation inductors can be either connected between two phases or coupled with a CMC as an additional coil. The magnetic field produced by the compensation inductor can be regulated by current flowing in it with a serial resistor. Prototypes to test this method were not built, but this idea can be further investigated.

Compensation methods can be applied simultaneously to EPC and ESL. A reference EMI filter (an equivalent circuit, Figure 4.13a) is used for demonstration of possible IL improvement, when both EPC and ESL are compensated. Demonstrated in Figure 4.20, enhancement is achieved by means of a coupled inductor method, applied to all capacitors and the single-winding compensated EPC of a CMC. The combination of those two compensation techniques gives a quite feasible DM IL improvement in the high frequency range 2–100 MHz. Results achieved in CM IL improvement are more modest and enhancement is slightly better than the option with a single winding EPC compensation alone. Costs of the components required for such improvement make up nearly 8 % of the filter price. Size of the filter is also increased by $\approx 15\%$. IL of the filter with EPC and ESL compensations are demonstrated in Figure

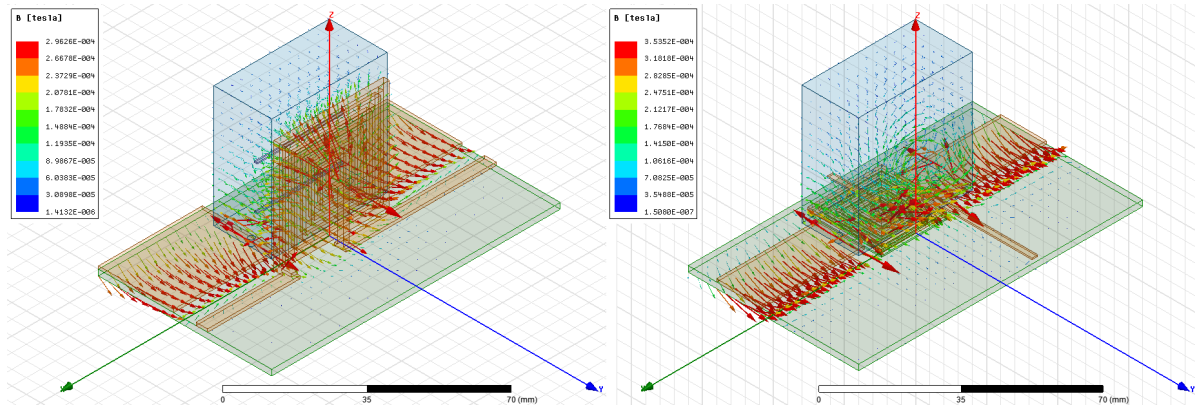


Figure 4.19.: Possible option of compensation inductor arrangement.

4.20. It can be considered as the maximum achievable improvement with use of different parasitics compensation methods.

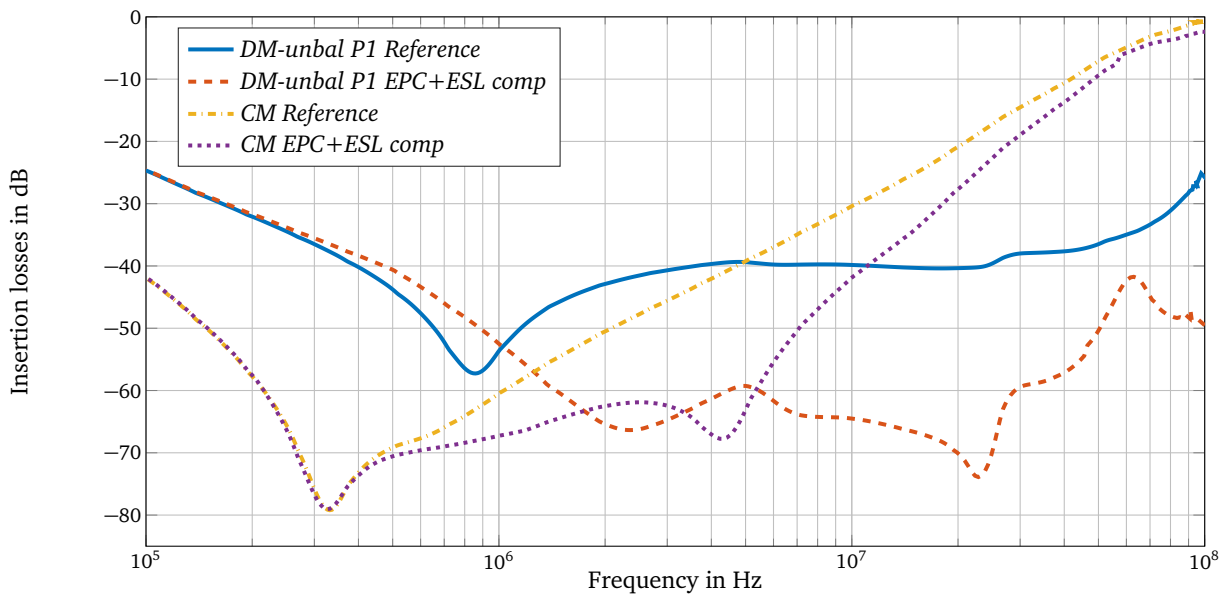


Figure 4.20.: CM and DM IL of the EMI filter with ESL and EPC compensation methods applied.

A summary of all parasitics compensation methods currently available, as well as those developed within this thesis, is given in Appendix H. Analysis is conducted in terms of required compensation components, maximum possible IL improvement and costs. Costs are estimated based upon an example of a three-phase EMI filter with a nominal current 10 A (the circuit is depicted in Figure 1.16). Only the costs of utilized components are considered for cost assessment. Recommendations concerning the field of possible utilization of compensation techniques are summed up in Table 4.1. This table can be used in order to quickly estimate the possibility of IL improvement for a given prototype.

It must be mentioned that employment of ESL compensation techniques, when mutual couplings are not considered, can lead to unexpected results. Firstly, mutual couplings either add or substitute inductance from ESL, according to the direction of current in phases. It deflects the value of ESL, which is measured for a stand alone capacitor, when capacitors are installed to a filter. Secondly, with a parallel arrangement of three capacitors the central capacitor always has the highest mutual coupling.

<i>Comp. method</i>	<i>Freq. range</i>	<i>Max. CM improvement</i>	<i>Max. DM improvement</i>	<i>Possible implementation</i>
EPC comp. with extra winding	0.2 MHz - 30 MHz	up to 25 dB (close to resonance frequency)	minor improvement can be neglected	common mode chokes and differential mode inductors
EPC comp. with a center tapped capacitor	0.2 MHz - 60 MHz	up to 25 dB (close to resonance frequency)	no changes	common mode chokes and differential mode inductors
ESL comp. based on crossed over capacitors	0.2 MHz - 20 MHz	no changes	up to 20 dB (without a distinct resonance)	phase-to-phase connected X-capacitors
ESL comp. based on the coupled inductor	0.2 MHz - 100 MHz	up to 6 dB (star connection), diminutive changes (phase-to-ground Y-cap)	up to 30 dB (star connection), up to 10 dB (phase-to-ground Y-cap), up to 10 dB (phase-to-phase X-cap)	star connection (the best results), phase-to-ground Y-cap (good results), phase-to-phase X-capacitors (similar to crossed over capacitors)

Table 4.1.: Characteristics of analysed parasitics compensation methods.

Therefore, capacitors located in vicinity with each other require individual design of coupled inductors. Although ESL of every used capacitor is identical to every other capacitor, it is recommended to design compensation coils for every capacitor with consideration of the complete filter structure and relevant mutual couplings for achievement of the best results.

4.2 Minimisation of Mutual Couplings

There is a significant number of studies discussing mutual coupling within various EMI filters types [8,61,81,156,160,192,201,213,216,230]. This literature allows an intuitive understanding of the nature of mutual coupling. Some publications even contain recommendations about component placement, so that the couplings can be minimized during a design process without involvement of any numerical methods [75, 128]. However, most of the existing works focus on single-phase EMI filters. An in-depth analysis of three-phase EMI filters, with simultaneous consideration of self-parasitics and mutual couplings between filter elements, together with an analysis of the economic aspects, has not been discussed in detail until now. Design and modelling methods of EMI filters supporting mutual coupling have already been proposed in Chapter 3. Now procedures reducing negative impact of mutual coupling on IL of three-phase EMI filters can be proposed and analysed. Relevance of every type of mutual coupling within a three-phase EMI filter to IL variation can be assessed.

From the physical point of view all components inside of the EMI filter are mutually coupled. The main issue is to detect mutual couplings that are most and least relevant to IL degradation. Three-phase EMI filters demand special treatment, since couplings differ considerably from single-phase filters. First of all, a three-phase EMI filter must handle more power, thus a PCB based design (regular for single-phase filters) cannot always be utilized. Secondly, as a result of the greater number of components a three-phase filter occupies more space. Luckily it leads to longer distances between components, and

mutual couplings might be reduced by default. Thirdly, in contrast with single-phase filters, some mutual couplings of three-phase EMI filters, like coupling within a Y-capacitors group, do not have negative effects on a filter IL, but convert interferences between CM and DM. Relevance of mutual couplings is comparison with self-parasitics is more complicated to figure out. For instance: a typical three-phase EMI filter, which contains one CMC and two stages of capacitors (Figure 1.16) has, depending on component arrangement, up to a hundred inter-component couplings.

In order to conduct objective evaluation of mutual couplings relevance, numerous simulations using an FEM analysis and electronic circuit simulations are carried out. Using this empirical data the following list of relevant criteria for mutual couplings can be identified:

- Impact in the insertion losses is bigger than 2 dB (at any frequency);
- The frequency range 10 kHz–100 MHz;
- Inductive coupling coefficient obtained from FEM modelling is bigger than 0.05;
- Capacitive coupling coefficient obtained from FEM modelling is bigger than 0.05.

Seven groups of coupling types can be localized in the conventional three-phase EMI filter based on Π -topology. For the following mutual coupling analysis an industrial three-phase PCB-based EMI filter with nominal current of 6 A has been taken as a reference.

- Inductive coupling within a group of X-capacitors;
- Inductive coupling between Y-capacitors;
- Inductive coupling between CMC and capacitors;
- Capacitive coupling between conductive parts (including filter components) and the housing;
- Inductive coupling between PCB traces;
- Inductive coupling of PCB traces and the other component;
- Inductive coupling between input and output capacitor's stages;
- Inductive coupling between input and output traces (wires).

According to the identified relevant criterion only the first two are relevant for the chosen reference filter. It must be emphasized that the last two couplings are always negligibly small for an adequately designed EMI filter (inputs and outputs are on opposite sides). However, it is crucially important to keep them low. Depending on the mutual inductance within a capacitor group, ESL in one of the branches might increase or decrease, and than ESL of the other two branches are changed respectively. The coupling between two capacitor groups (before the CMC and after the CMC) leads to the most destructive effect, namely, it shorts the CMC. This outcome is clearly seen from (4.4), when equivalent inductance of the filter L_{equiv} , seen by CM currents, depends on the mutual coupling M between the input and output capacitor groups

$$L_{\text{equiv}} = \frac{L_{\text{CMC}} \cdot (ESL_1 \cdot ESL_2 - M^2)}{M \cdot L_{\text{CMC}} + ESL_1 \cdot ESL_2 - M^2}. \quad (4.4)$$

Where ESL_1 and ESL_2 are equivalent series inductances of the input and output capacitor groups and L_{CMC} is inductance of a CMC. For the extreme case, with coupling coefficient equal to one, a CMC is completely shorted and resulting L_{equiv} is eliminated. A similar situation occurs when the input and

output traces (wires) are strongly coupled. As a result of these effects, it is recommended to split inputs and outputs of a filter in space and to avoid placing the input and output capacitor stages in vicinity with each other. Luckily, it corresponds with one of the simplest layouts of a filter.

The most significant mutual couplings are introduced within X- and Y-capacitor stages. Typically three capacitors, which compose a capacitor bank, are arranged in parallel as depicted in Figure 4.21a. As a result of this, couplings are unsymmetrical and a coupling between the first and the last capacitor is weaker than the other two. According FEM simulations that were carried out, coupling coefficients within capacitor banks typically lie in the range 0.01-0.1, depending on the distance between capacitors.

Figure 4.21 demonstrates an inductive coupling between components of the X-capacitor's bank. Assuming a positive DM current direction in the phase U and negative currents in phases V and W, signs of mutual couplings can be defined. Equivalent impedance of every capacitor branch with consideration of mutual couplings is calculated based on the equivalent circuit in Figure 4.21. Resulting ESL, and thus SRF of capacitors, change correspondingly to the distribution of mutual couplings. Asymmetrical coupling between X-capacitors is reflected in the difference between unbalanced DM IL of every phase of the reference filter. The occasion of this mismatch reaching the maximum of 10 dB is depicted in Figure 4.22. It is assumed that the phase U has only positive mutual coupling with other phases and, therefore, IL differ considerably from remaining phases.

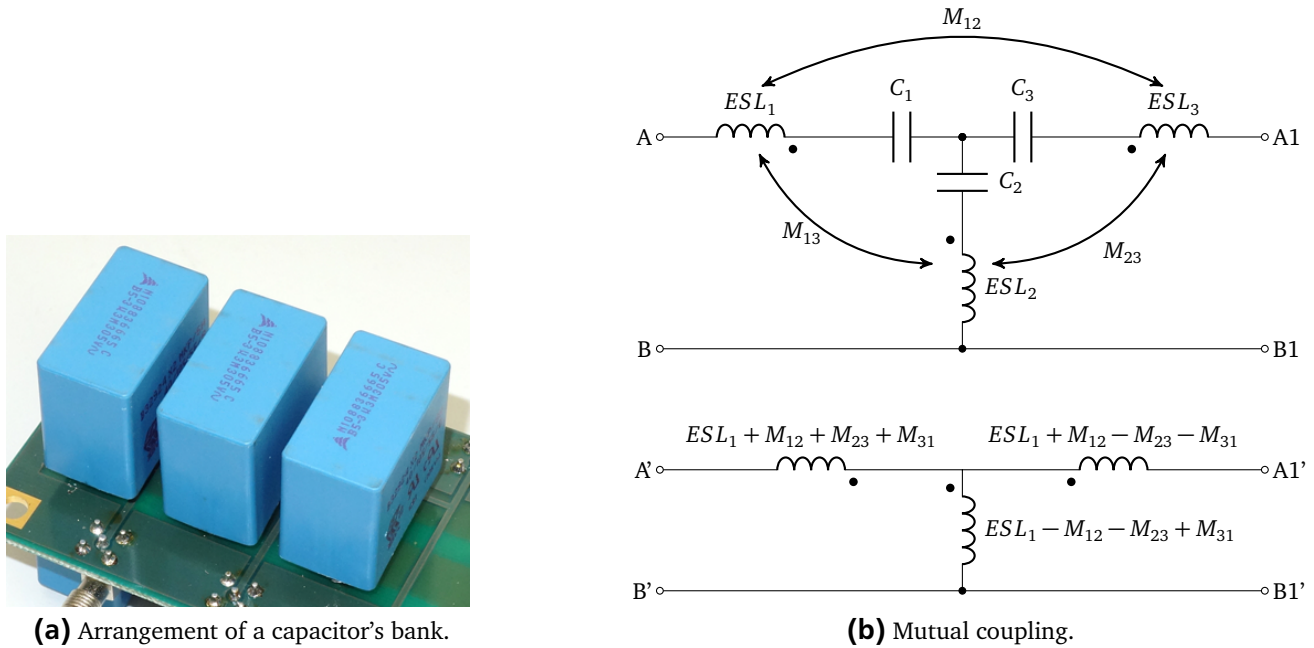


Figure 4.21.: Single polarity couplings of a capacitor's bank.

In practice mutual couplings are difficult to localize. Therefore, simulation based conclusions are difficult to confirm experimentally. For example, the phase unbalance shown in Figure 4.22 can be theoretically caused by any other mutual coupling except for the coupling between components of the X-capacitor's bank. In order to validate the aforementioned conclusions three experiments are carried out. EMI filters used for these experiments are depicted in Figure 4.23. In the first study the CMC of the conventional filter (on the left hand side in Figure 4.23) is relocated to the other side of the PCB.

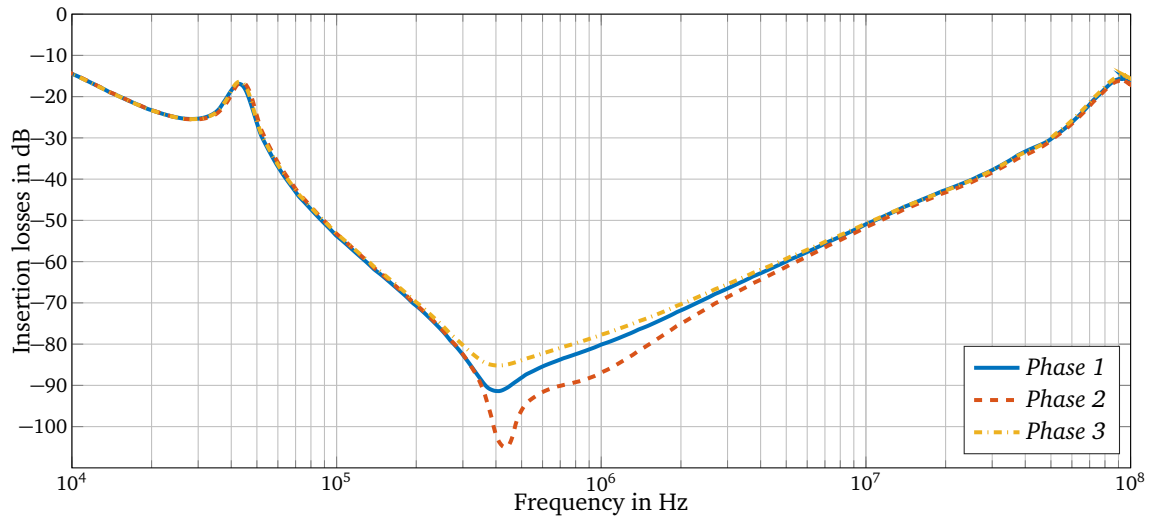


Figure 4.22.: DM-unbal P1 IL of the reference filter for every phase.

Since the CMC is removed from capacitors, mutual couplings between the CMC and capacitors became negligible. However, the phase unbalance remains quite significant and the phase symmetry is barely improved (Figure 4.24). The difference between results depicted in Figure 4.24 and Figure 4.22 is explained by changed polarity of the CMC, so that signs of mutual couplings within capacitor groups are changed.

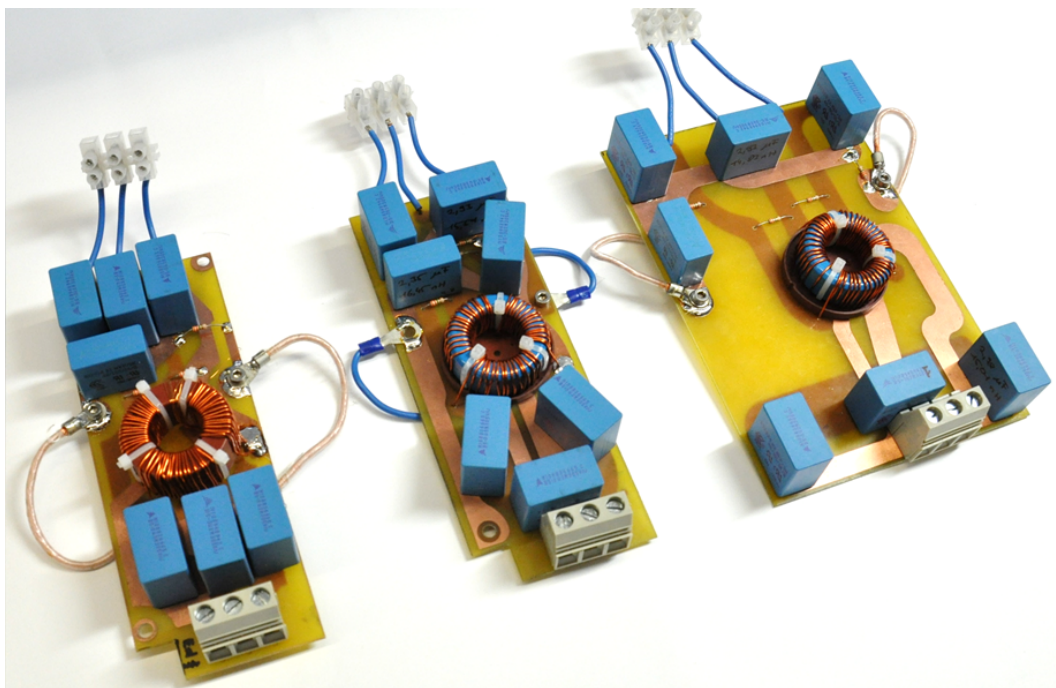


Figure 4.23.: EMI filters with different component arrangements. F1 - reference arrangement, F2 - improved arrangement, F3 - filter with components spread in space.

For the second study, filter sample with rearranged capacitors is built (Figure 4.23, F2). Capacitors are allocated in order to achieve the lowest possible mutual couplings and a symmetrical configuration. For this study the balance between phases is considerably improved and at maximum it makes up only

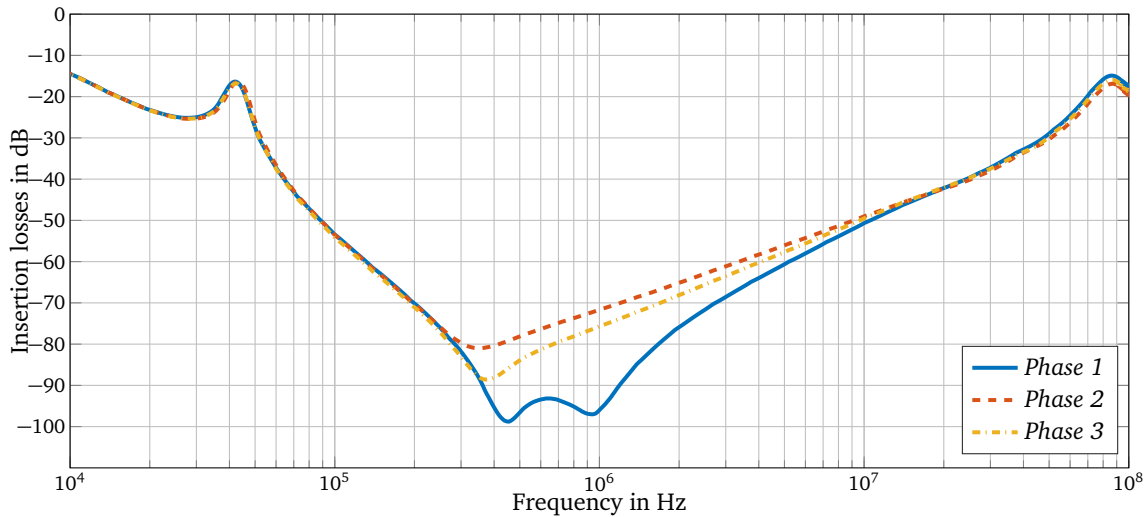


Figure 4.24.: Measured DM-unbal IL of the reference filter for every phase with inverted CMC.

6 dB (Figure 4.25). The results obtained corroborate that the main contributor to the phase unbalance is a coupling within a capacitor’s group.

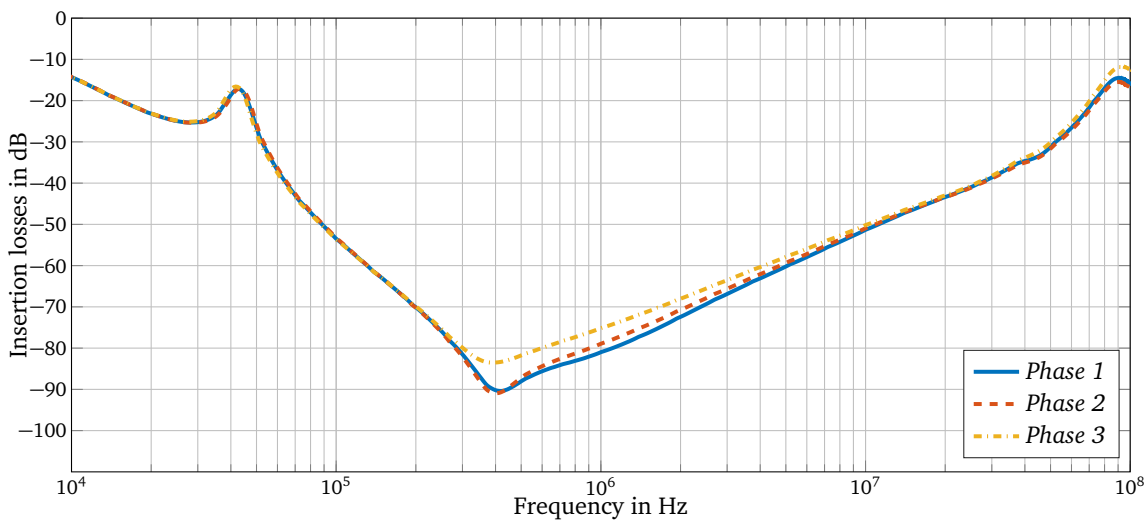


Figure 4.25.: Measured DM-unbal IL of the filter with rearranged components.

For the third and final study, all components are located on a bigger PCB (Figure 4.23, F3), so that the distance between capacitors is at least 25 mm (Figure 4.23, F3). For this design all types of mutual couplings are negligibly small. Certainly, some unbalance between phases due to non-ideal windings of the CMC, imperfect symmetry of a PCB traces and component placement remains. However, all phases have highly symmetrical IL with the difference, which does not exceed 2 dB (Figure 4.26).

It can be concluded that the unbalance effects are caused entirely by the mutual couplings within a capacitor stage and cannot be confused with the other mutual couplings. The mutual couplings between X-capacitors cannot be unambiguously classified as negative. For the symmetrical capacitors arrangement mutual couplings with correct polarities may provide improvement of IL. However, when one of the couplings is negative, resulting ESL of at least one capacitor branch decreases significantly, causing considerably bigger unbalance between phases. Unfortunately, in the case of phase-to-phase

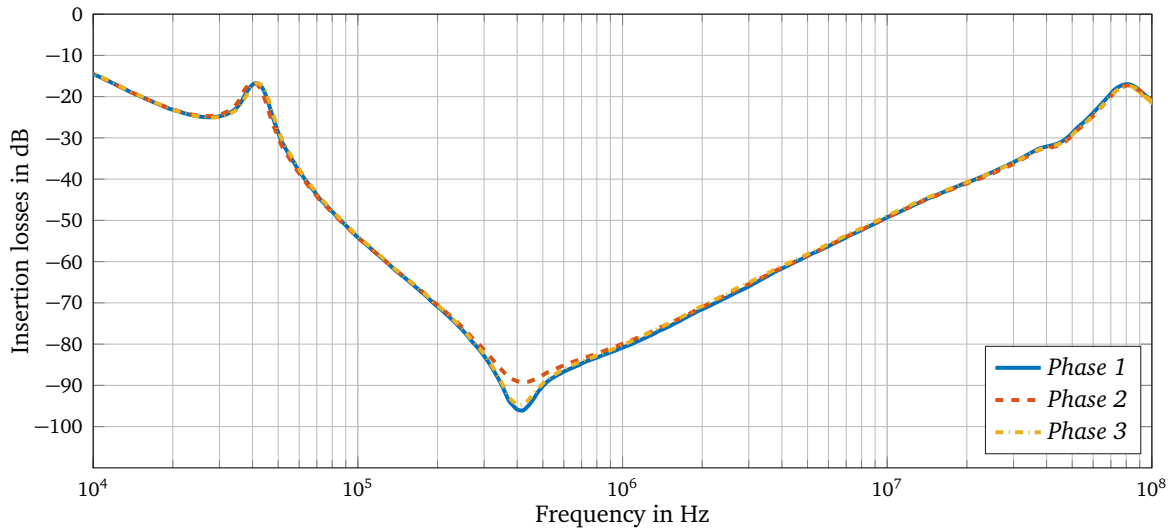


Figure 4.26.: Measured DM-unbal IL of the filter with increased distance between components.

X-capacitors, which are located in parallel, a single polarity connection cannot be achieved by definition. CM IL are barely influenced by the couplings within the X-capacitors bank. Since mutual couplings within a capacitor group do not influence CM IL and couplings between capacitors and the CMC are weak, CM IL of the filters depicted in Figure 4.23 demonstrate insignificant difference (Figure 4.27). In

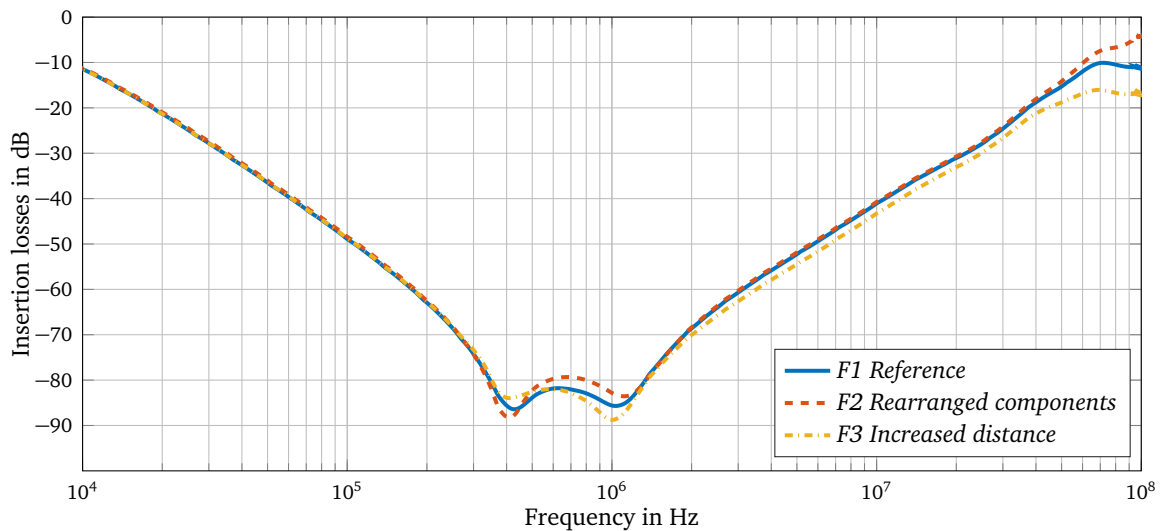


Figure 4.27.: Measured DM-unbal IL of filters with different components arrangements.

contrast with couplings inside of the X-capacitors group, mutual inductive couplings within the group of Y-capacitors unambiguously degrades performance of the filter. Besides effects similar to mutual couplings in the X-capacitors group, a mutual coupling between Y-capacitors causes conversion of disturbances from DM into CM. When current flows in one of the branches with Y-capacitors it induces currents in two other capacitors in the opposite direction, which creates a common mode disturbances (Figure 4.28a). This phenomenon is true for both directly connected Y-capacitors and for star point connected Y-capacitors. Impact of the coupling coefficient within the Y-capacitors stage on IL is studied based on the mathematical model and demonstrated in Figure 4.28b.

This conversion is more intense on higher frequencies, as the mutual coupling impedance is the product of the angular frequency and mutual inductance. The common mode conversion factor is proportional to the coupling coefficient between Y-capacitors as the higher this coupling coefficient the higher the portion of CM. Besides increasing of CM disturbances the conversion can cause saturation of a CMC. It is because the portion of DM current, which is converted to CM current in the Y-capacitors, is added to the total CM of the system. Theoretically, coupling within a capacitor's stage can be used for ESL compensation, but it is rather complicated to adjust the coupling properly even in an ideal laboratory environment. Because of this, practical utilization of such compensation methodology is very limited.

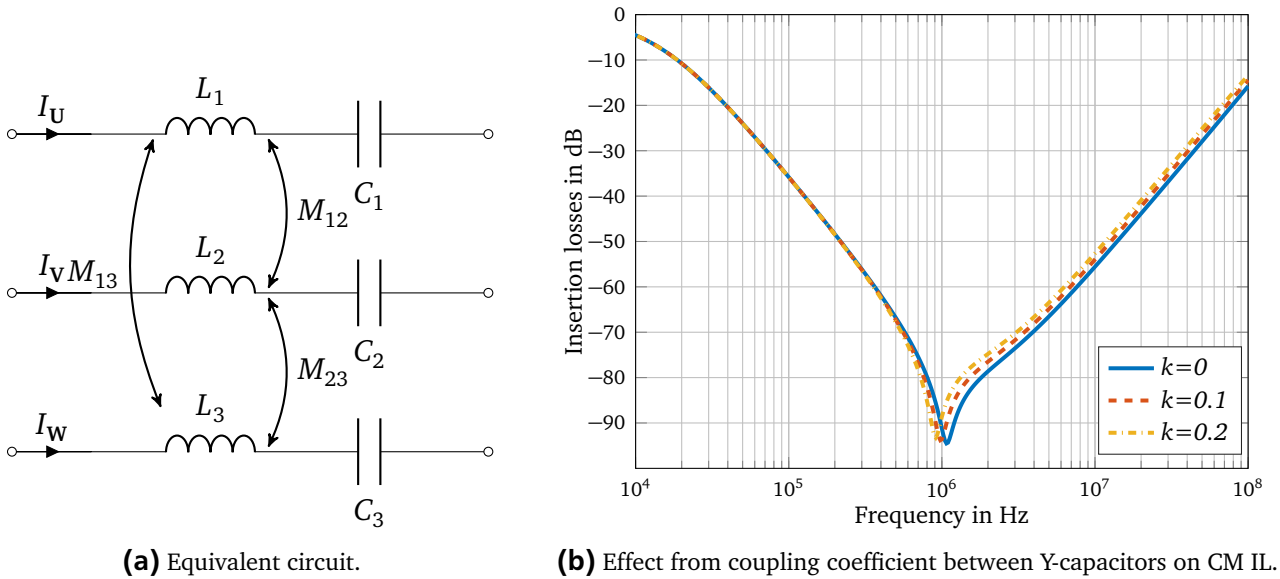


Figure 4.28.: Couplings between Y-capacitors.

According to theory, the inductive coupling between a CMC and capacitor groups can considerably affect IL. Nevertheless, for the analysed filter this coupling is negligibly small. This means that this type of a mutual coupling can be easily avoided without any specific measures. For a practical filter design the inductive coupling between the CMC and capacitor stages is typically highly asymmetrical. Basically, if all components are placed on a PCB, there is no possible situation when fields created by the CMC and capacitor are well coupled. Therefore, the coupling between the CMC and capacitors must be relatively small by default. However, the only way to decrease this coupling (besides shielding) is separation of components. An insignificant impact of couplings between the CMC and capacitors on CM IL is shown in the example of the filter with considerably increased distance between elements as shown in Figure 4.23 (F3). Resulting CM and DM IL are depicted in Figure 4.26 and Figure 4.27. More detailed information concerning this type of mutual couplings can be found in [61].

The coupling between the grounded housing and conductive parts of the filter acts like a distributed Y-capacitor and creates an additional higher-frequency resonance peak. The value of this coupling is typically in the range 10 - 100 pF. Nevertheless, effects caused by this coupling exceed the standardised EMI range. If the frequency range up to 100 MHz is considered, this coupling can be used to increase the IL at the very high frequency.

A summary of recommendations for proper EMI filter designs which allow avoiding negative effects of mutual couplings is as follows:

1. The most important rule is to keep the input and output of a filter decoupled: ideally they should be located on opposite sides. This is true for input and output groups of capacitors as well.
2. In order to reduce the coupling within a capacitor group, two approaches are possible: increase the distance and/or angle between them, or implement a shield. On the one hand, increasing of the distance between capacitors increases volume of a filter and changing of the angle between the capacitor requires some changes in filter design. On the other hand, currents induced in the shield increase losses of a filter. To determine effects of capacitor positioning, the parametric sweep with the distance and angle between two capacitors is modelled. Results of the sweep are plotted in Figure 4.29. Therefore it is recommended to combine both methods for the best results.

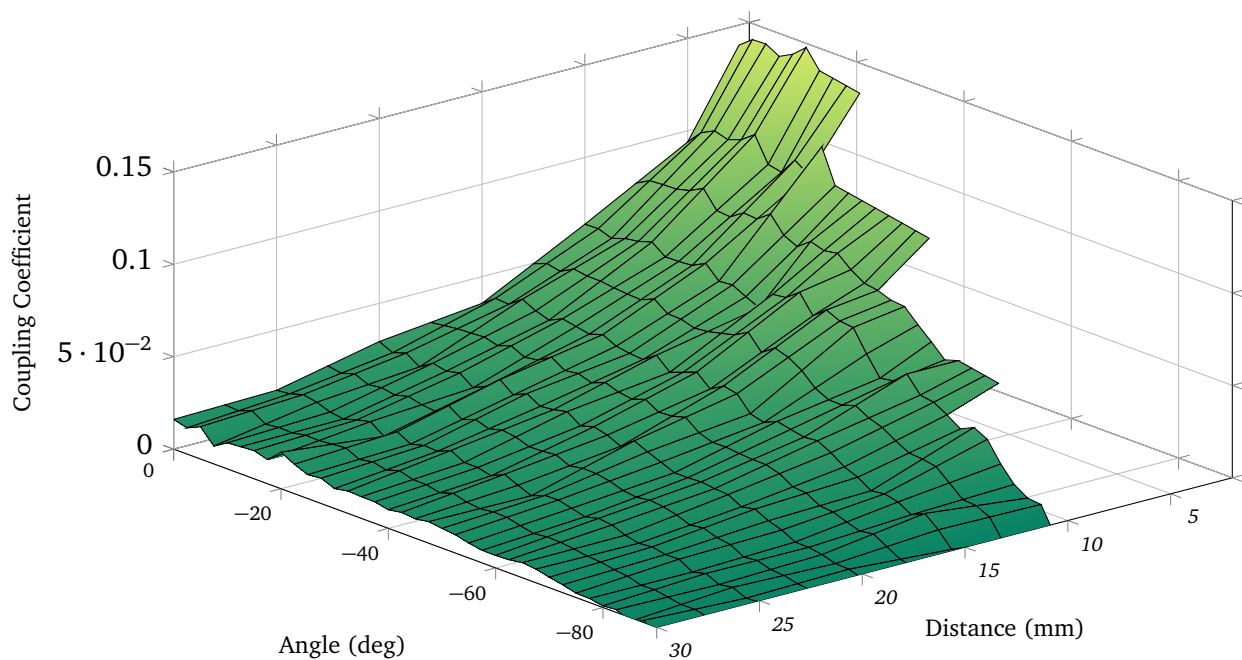


Figure 4.29.: Plot of a coupling coefficient between two capacitors depending on the angle and distance.

3. If capacitors cannot be separated or turned against each other, particular attention has to be paid to symmetrical arrangement. Polarity of placement should be kept the same in all branches. Moreover, symmetrical location of capacitors in one group allows the decrease of asymmetry between phases and conversion between different types of disturbances. A symmetrical connection is recommended for all capacitor connection types (direct phase to the ground connection, phase-to-phase connection, and the star point connected). For some particular cases when a location of components is specified by the other objectives and no rearrangement is allowed, shielding is a possible option [64].
4. Horizontal placement of a CMC is superior from the mutual couplings point of view. Although, a sufficient distance must be kept between CMC and capacitors. Practice shows that 20 mm is the ensured safety distance in the majority of cases. Recommendation concerning arrangement of DM chokes can be found in [218]. It must be mentioned that the stray flux of a CMC can be used for ESL compensation. In that case, the stray flux of a CMC and magnetic field produced by capacitive current have to point in opposite directions.

-
5. The stray capacitance between the filter components and the housing creates a distributed capacitor, which affects the high frequency IL of a filter. This means that through the increase of this parasitic component it is possible to improve damping of the filter in frequencies in the range of 100 MHz. Decreasing the distance between components and the housing increases the stray capacitance.

Luckily, from the point of view of the mutual couplings, an optimal allocation of three-phase EMI filter components corresponds to the conventional arrangement, when all components are placed in the similar order as at the equivalent circuit. That is input terminals are followed by the first stage, the second stage, etc., and output terminals. Then the coupling between inputs and outputs is automatically avoided. Basically, mutual couplings in adequately designed three-phase EMI filters cause phase unbalance, but do not have critical influence on IL. Negative effects can be completely eliminated by sticking to the general rules of filter design.

5 Design of High Performance EMI Filters

Along with parasitics compensation, there are some methods to design a filter with a priori superior characteristics compared to conventional ones. Proper selection of a topology, assisted with appropriately chosen components and management of non-ideal properties, leads to excellent results. Aspects related to performance, power density and costs of a designed filter have to be considered, forming a holistic approach to EMI filter design.

IL of an EMI filter are divided into high frequency (HF) and low frequency (LF), in accordance with filter parameters and improvement methods, which have direct impact in a particular frequency range. For instance LF IL (up to ≈ 1 MHz) are effected by a number of main stages and values of main components, which is rather straightforward. HF IL (1–100 MHz) is influenced by a considerably higher number of filter parameters and can be improved with a great variety of methods. IL degradation caused by non-ideal magnetic core properties is addressed by proper core material selection. Some additional HF stages, consisting of capacitors with reduced parasitics, inductive components based on high frequency magnetic materials and various capacitor connection types are intended to improve high frequency IL. Combination of those procedures with parasitics compensation methods gives a diversity of potential EMI filters with improved high frequency characteristics.

Obviously the complexity of enhanced filters grows with the number of filter components, but capacitors and inductors with considerably smaller nominal values can be employed. The total capacitance and inductance which is utilized in more complex topologies might be smaller than in basic Γ -topology based filters. It leads to superior results not only from the performance point of view, but it is also advantageous in terms of power density and cost. In this chapter is shown that diverse possibilities for filter improvement and optimization with competitive costs and efforts can be found for every particular situation.

5.1 Filter Structure Analysis and Advanced Topologies

In contrast with signal electronics where ten-stage filters are state of the art, conventional EMI filters in the power electronics field typically consist of one or two stages. However, multistage filters introduce several benefits for power electronics applications, even though development of multistage filters is more complex. Classical ladder networks, which contain similar stages, can be used equally with conventional single stage EMI filters assisted with special components, which are responsible for high frequency IL. The last group exhibits some additional degrees of freedom, especially if the power density is the main design criterion. Moreover, high frequency stages can be used as an alternative to EPC and ESL compensation for final tuning of IL.

Before a detailed discussion about multi-stage filter and complex topologies, the possible options for building three-phase EMI filter stages have to be reviewed and analysed. In contrast with single-stage EMI filters the number of possible topologies in three-phase filters is considerably larger. Furthermore, previously introduced compensation methods extend the number of possible options for three-phase filter design even further. In some situations EMI filters might require special damping stages [52, 227].

Due to safety reasons, discharge resistors have to be connected in parallel with capacitors. Resistor utilization is out of scope in this thesis but must be taken into account during the design process.

Generally, there are two types of building blocks for EMI filters, namely, inductive and capacitive. The number of possible options for inductive building blocks is rather small. Common mode and differential mode chokes with or without parasitics compensation represent four available inductive stages. Additional inductive stages can be assisted with a parallel damping network. In contrast with inductive components there are different possibilities of capacitor arrangements, based on various connection types. Furthermore, capacitor groups can be assisted with resistors in series in order to regulate interaction between different stages and mitigate resonances. The main capacitor connection types are:

- X-capacitors between phases ($C_{XUV}, C_{XVW}, C_{XUW}$)
- X capacitors connected to the star point (C_{XU}, C_{XV}, C_{XW})
- Y-capacitors placed directly between phases and the ground (C_{YU}, C_{YV}, C_{YW})
- Y-capacitors between the star point of X-capacitors and the ground (C_Y)

Small capacitors with an improved SRF can be used within the same stage for enhancement of the high frequency characteristics. Every connection type has its own benefits and shortcomings. The most important properties of the connection types are summarized in Table 5.1.

Connection type	Equivalent ESL (ESL_{eqv})	Nominal voltage	Power density*	Price of one item**
X-cap. phase-to-phase	$ESL_{eqv} = ESL_{XU}$	phase-to-phase (400 V) (X1 category)	nominal	reference price (100 %)
X-cap. phase-to-star	$ESL_{eqv} = ESL_{XUV} + \frac{ESL_{XVW} \cdot ESL_{XUW}}{ESL_{XVW} + ESL_{XUW}}$	phase-to-artificial star point (230 V for a balanced system) (X1 category)	higher power density in complex with an additional star-to-ground Y-capacitor.	75 % from the reference price
Y-cap. phase-to-ground	$ESL_{eqv} = \frac{1}{(1/ESL_{XU} + 1/ESL_{XV} + 1/ESL_{XW})}$	phase-to-ground (230 V)	lower due to a higher component number	reference price (100 %)
Y-cap. star-to-ground	$ESL_{eqv} = \frac{1}{(1/ESL_{XU} + 1/ESL_{XV} + 1/ESL_{XW})} + ESL_Y$	artificial star point-to-ground (up to 230 V for an unbalanced system)	higher if a single Y-capacitor is used	74 % from the reference price (only for a single Y-capacitor)

* All analysed capacitors have the same dimensions [49–51] but different safety categories

** Prices are taken from leading distributors for a 1000 item order

Table 5.1.: Parameters of capacitor connection types.

Stages with phase-to-phase connected X-capacitors are simpler to design as only one category of disturbances is affected. Moreover, since only one capacitor is connected between any two phases, equivalent ESL (ESL_{eqv}) is minimal and equal to ESL of a used X-capacitor. In turn, the phase-to-star X-capacitor connection involves two series connected capacitors per arm. It leads to an increase of

ESL_{eqv} and diminishing of equivalent capacitance. On the other hand for the phase-to-phase connection, capacitors with higher isolation requirements must be used (phase-to-phase voltage is applied to every capacitor). This increases the price and size of capacitors, and larger dimensions cause higher ESL. For example, capacitance of the X-capacitor intended for placement between phases is $2.2\mu\text{F}$ (dimensions $20\times 39.5\times 42$) [50]. Capacitance of the X-capacitor with the same dimensions designed for the phase-to-star connection is 6.8 mF [51]. Nevertheless, after star to delta transformation the resulting equivalent capacitance between phases is quite similar ($2.26\mu\text{F}$ for this particular example). Taking into account tolerance of capacitors, which lies within 20%, the difference is negligible. This means that the resulting equivalent capacitance, which can be placed into some specified volume, only slightly depends on the connection type. The power density is barely affected by a connection type. Price of the X1 category capacitors which can be connected between phases is a factor of 1.35 higher compared to the X2 category designed for the phase-to-star connection.

The direct connection of Y-capacitors between phases and the ground is superior from the technical point of view but leads to higher total costs. Firstly, ESL_{eqv} is lower for the direct connection phase-to-ground, since it is equal to ESL of a capacitor itself. In turn, ESL of the star-to-ground connected Y-capacitors also depends on ESL of X-capacitors used for building the star point. Secondly, Y-capacitors that are directly connected to the ground take an active part in filtering DM disturbances. When the star-to-ground connection is utilized the equivalent Y-capacitance affecting CM disturbance is lower than the values of a physical Y-capacitor, due to its serial connection with star-forming X-capacitors. On the other side the star-to-ground connection is beneficial from the power density and cost points of view. Only one Y-capacitor is used for the star point-to-ground connection so that it decreases a number of utilized components. For the direct phase-to-ground connection one capacitor per phase is needed. Therefore, the phase-to-ground connection might be a factor of 1.36 more expensive than an alternative solution. It is also quite important that the star-connected Y-capacitors have a lower level of leakage current.

It is worth mentioning that for the balanced power grid voltage between an artificial star point and the ground should not exceed a few volts. Only under failure conditions (which is unlikely) voltage across a star-connected Y-capacitor can reach 230 V. It means that a capacitor with lower nominal voltage (less expensive) can theoretically be used. Since a Y-capacitor is connected in parallel with X-capacitors, the probability of a simultaneous failure of two capacitors placed between a phase and the ground is decreased, so that the risk of a short circuit to the ground is reduced. These two assumptions lead to a design trick, which can sometimes be found in EMI filters presented on the market. In order to save money an X2 category capacitor (less expensive than Y category) is placed between an artificial star point and the ground, omitting safety requirements despite the electrical shock hazard. Employment of X2 category capacitors instead of Y1 or Y2 categories can lead to a short circuit between mains and the ground.

The star-to-ground connection is more complicated from the filter design point of view, as changing of values X- and Y-capacitors influences in both CM and DM IL. Nevertheless, the considerably lower total costs of this connection type make it more attractive for practical applications. Higher power density promotes this connection type as well.

In order to investigate possible capacitor connection types two experimental filter topologies are built up in the laboratory (Figure 5.1). The first one is based on the direct connection of Y-capacitors

between phase and the ground and the direct connection of X-capacitors between phases (filter A). The second topology consists of Y- and X-capacitors connected to the star point (filter B). CMCs employed in both filters are the same. Values of components are selected in order to get similar IL suitable for fair comparison. All parameters of these two prototypes are listed in Table I.1. From the prices of components summarized in the table, it is seen that the filter A is a factor of 1.34 more expensive than the filter B. Moreover, the filter B occupies insignificantly smaller volume (only a factor of 0.94 smaller).

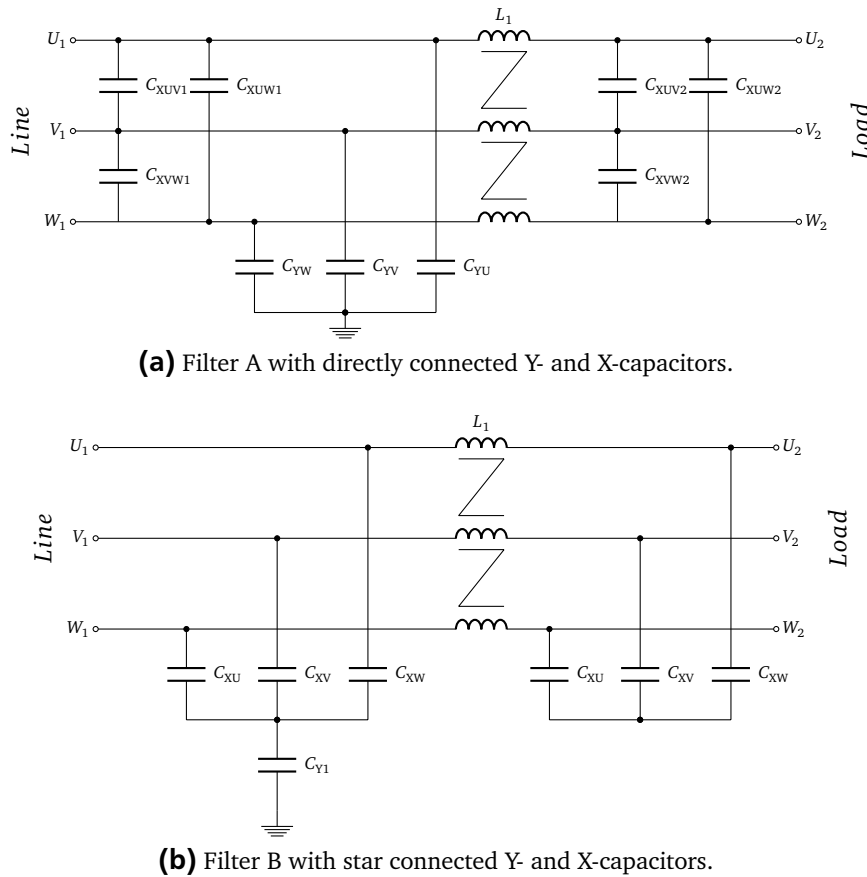
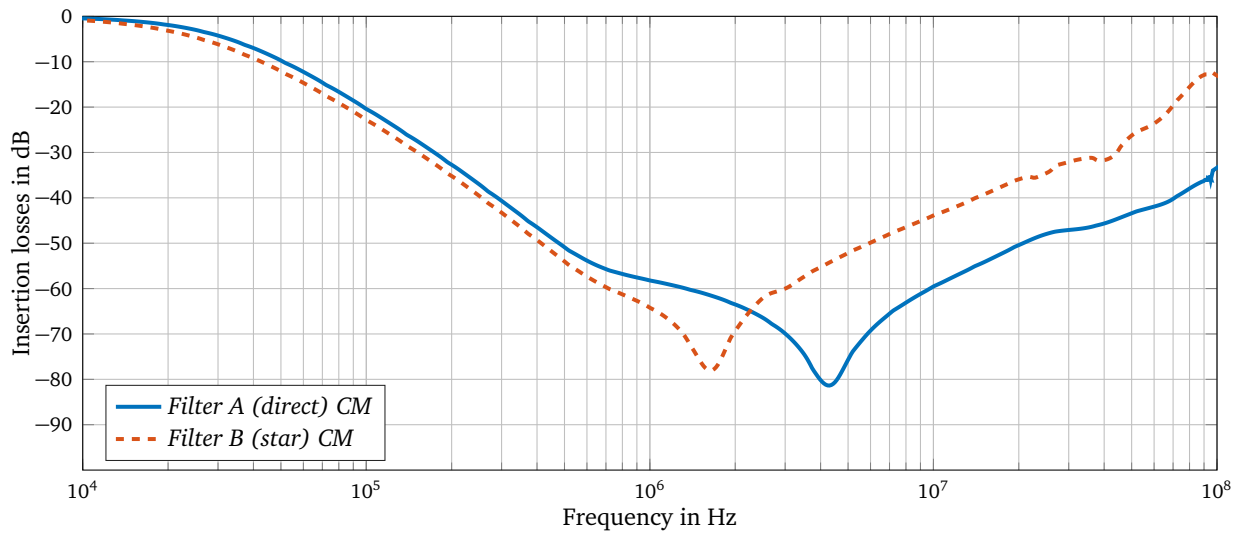


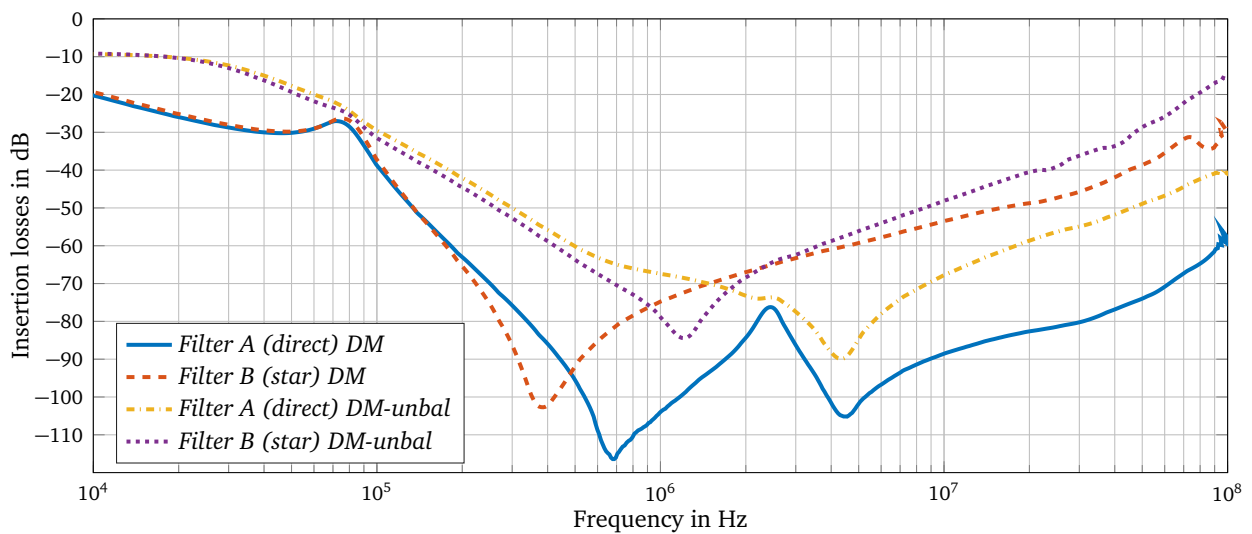
Figure 5.1.: Equivalent circuits of filters with different capacitor connections.

All previously made theoretical assumptions concerning capacitors connections are confirmed with measurements. Firstly, for the filter B a resonance peak caused by ESL of capacitors appears at the lower frequency (1.6 MHz for CM IL and 1.2 MHz for unbalanced DM IL) than for the filter A (4.2 MHz for CM IL and 4.3 MHz for unbalanced DM IL). This phenomenon is caused by a serial connection of ESLs in the filter B. Secondly, components of the filter A occupy more space, due to two additional Y-capacitors. This leads to lower power density, despite of the fact, that the useful capacity per volume is the same for both filters if the star-to-delta or delta-to-star transform is conducted. Nevertheless, the filter A with the direct connection of capacitors exhibits significantly better IL, due to much lower ESL. The difference between CM IL makes more than 15 dB within the frequency range 3 – 100 MHz and up to 30 dB in the frequency range 3–100 MHz for DM IL. Since Y-capacitors exhibit an impact on DM IL too, the second resonance is observed on 4.4 MHz. This resonance appears at the much higher frequency than the resonance of X-capacitors, leading to better IL of the filter A.

It is clearly seen that selection of the correct capacitor connection type is crucially important. Proper choice of a capacitor's connection type makes it possible to optimize a filter design either for lowest cost or maximum performance. None of the ESL compensation techniques, analysed in Section 4.1.2, give such a significant improvement as an optimization of a capacitor connection type. However, use of the various improvement methods in conjunction gives the most optimal results. Therefore, methods for filter improvement have to be selected in accordance with requirements to a particular system.



(a) Common mode.



(b) Differential mode balanced and unbalanced.

Figure 5.2.: Comparison of measured IL exhibited by the filter A with the direct capacitor connection and the filter B with the star point connected capacitors (measured).

5.1.1 Multistage or Ladder Filters

Multistage filters have to be used when the specified IL (especially at low frequencies) cannot be achieved with any of the single-stage filters. Multistage filters introduce an additional degree of freedom for designers. For example, employment of supplementary stages with the direct X- and Y-capacitor connections

improves both high and low frequency IL. As it was discussed in Section 3.1, the maximum possible slope which can be achieved with one stage (Π, Γ or T) filter is 60 dB/decade, which is rather modest. In order to show some benefits of multistage filters, four filter topologies such as $\Gamma, \Pi, CLCL$ and $CLCLC$ filter topologies are studied. Lets assume that a specified CM IL on 200 kHz is -80 dB. Initially the total capacitance ($6.6 \mu\text{F}$) and inductance (1.7 mH) are equally distributed among presented stages. Then for the simplest Γ -topology an inductor must be $1.7 \mu\text{H}$ and Y-capacitors are $2.2 \mu\text{F}$ per phase. The same IL can be achieved with the other L-C combinations, but components with chosen values are typically used in the conventional three-phase EMI filters. Mathematical models of filters are simplified, so that only self-parasitics are taken into account. DM IL are not considered for this study but the principle remains similar.

As demonstrated in Figure 5.3 the required damping -80 dB on 200 kHz is achieved, but some disadvantages of the Γ -topology are clearly seen. Firstly, used components have quite high values. This leads to shifting of the SRF to the lower frequency range and as a consequence degradation of the high frequency IL due to parasitics. Secondly, in the low frequency range (up to 100 kHz) IL reach -60 dB, so that low frequency disturbances with high energy can cause saturation of magnetic components. Lastly, Y-capacitors introduce some leakage current, which is proportional to capacitor value (3.7). Hence, utilization of such filters for application assisted with residual-current device (RCD) is not possible because of unintended tripping of RCD [20, 31].

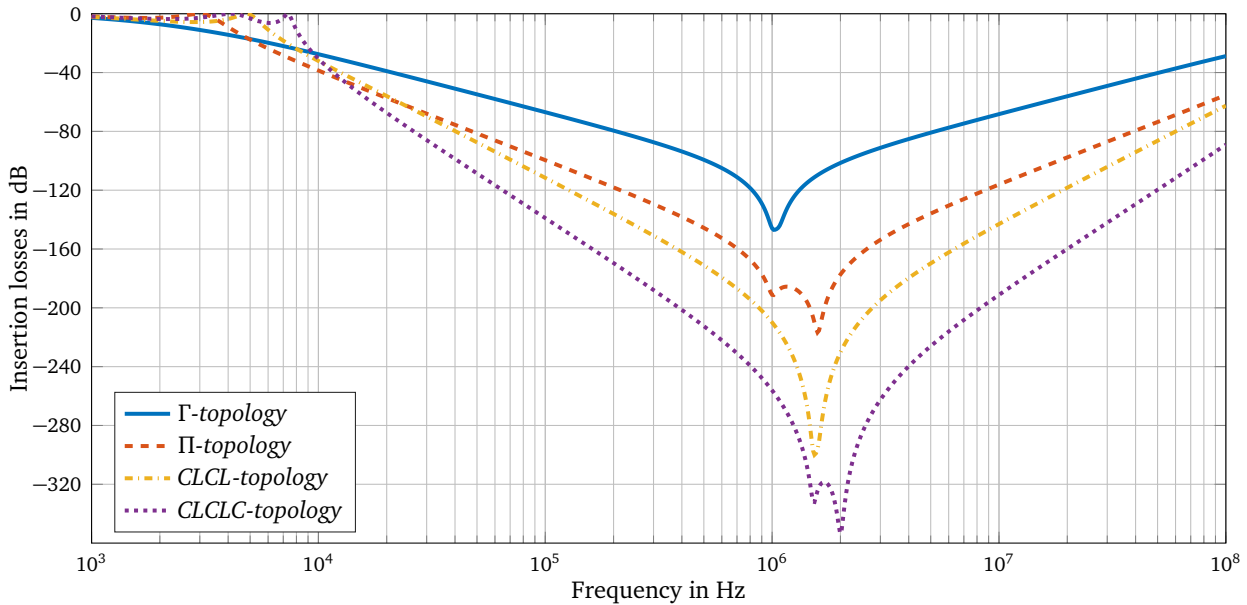


Figure 5.3.: Simulated IL of EMI filters with a different number of stages.

The required IL can be easily achieved with a Π -topology (Figure 5.3). The total values of the employed components are close to the Γ topology ($L = 1.7 \text{ mH} - C = 1.0 \mu\text{F} \times 6$), the deviation is caused by the standard nomenclature of capacitors. For the Π -topology based filter IL are considerably improved in the entire frequency range of interest. Obviously, a higher number of components is the main disadvantage of this filter. This might also negatively affect the power density. Moreover, a low frequency resonance might cause some problems with saturation as well. With one more inductor added to the Π -topology a IL slope becomes 80 dB/decade. Two inductors with 0.74 mH are utilized for a $CLCL$ -

topology. However, employment of the second inductor is rather contradictory. On the one hand, use of two inductors has negative influence on the power density. This is because of quadratic dependency between inductance and the number of turns. On the other hand, it introduces some flexibility, since different magnetic materials can be used. Furthermore, the second inductor improves saturation capabilities of the filter, since it increases impedance of the CM path and consequently less CM current flows through the filter. Comparable with the Π -topology, IL of a $CLCL$ -topology is further improved in the entire frequency range of interest. For a $CLCLC$ -topology an IL slope decreases 100 dB/decade, which explains the maximum of -380 dB. Nine 0.63 mF capacitors are used for this topology. Results of IL simulations for all considered topologies are shown in Figure 5.3.

Because of the superior IL of multistage filters, achieved results are quite challenging to validate with measurements. The noise floor of the used measuring equipment is reached after -120 dB. Nevertheless, initial IL slopes of filters give an opportunity to approximate IL behaviour below -120 dB. In general a tendency in measurements repeats results obtained in simulations. Deviation between results obtained from simulations and measurements at the high frequency is mainly explained by permeability degradation effects. Measured IL of the filters representing four previously analysed topologies are shown in Figure 5.4.

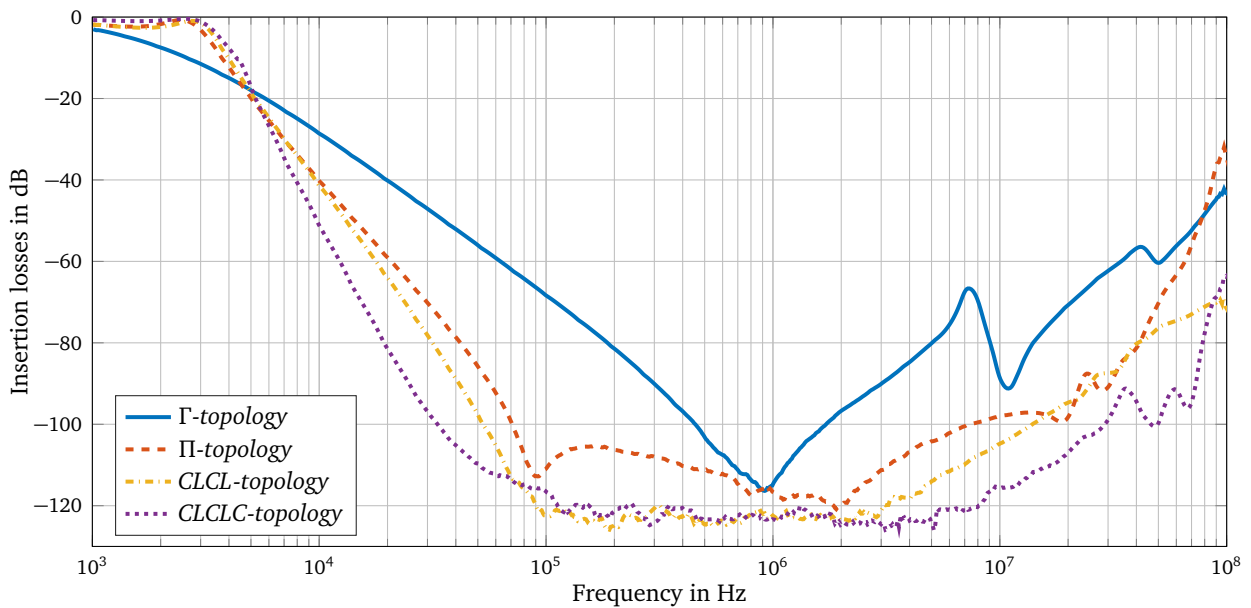


Figure 5.4.: Measured IL of EMI filters with different topologies.

Studies demonstrate that IL of multistage filters significantly exceed IL specified as the aim for this study, despite the same total value of the employed capacity and inductance for all filters. Therefore, the total values of capacity and inductance can be reduced, so that smaller components are used for achievement of the specified IL. Supplementary stages can be utilized if enhancement of some particular filter characteristics (leakage current, power density, costs etc.) is required. For example when IL of the Γ -topology satisfies the initial requirements, with $L = 1.7$ mH, $C = 2.2 \mu\text{F} \times 3$, the Π -topology based filter demonstrates similar results with only $L = 0.57$ mH and $C = 0.2$ mF $\times 6$, which is superior with regard to capacity against the ground. As a result, leakage current of the system is significantly reduced. With employment of a $CLCLC$ -topology the capacity against the ground can be further reduced till

0.033 μF x 9, resulting in the total capacity of only 0.3 μF , but the second inductor with 0.57 mH has to be used. Consideration of prices and power density in the holistic topologies analysis emphasizes future perspective on multistage filters. Technical data about components used for filter design in this chapter is summarised in Appendix I. Information about components used in analysed multistage filters including prices and volume is summarized in Table I.2. The Γ -topology is taken as a reference for power density and cost calculation (factor 1). For a conducted study the Π -topology exhibits the minimal price (only a factor of 0.47 from the reference) and the minimal volume which is occupied by components (a factor of 0.64 from the reference). It was not expected that the $CLCLC$ -topology would surpass the reference in terms of costs (by a factor of 0.603) and also power density (by a factor of 0.88). The results obtained suggest that multistage EMI filters might have good prospects, especially for low leakage current applications. This is because they can significantly reduce the size of needed Y-capacitors. Comparison between simulated IL of Γ -, Π - and $CLCLC$ -topologies optimized in order to reduce leakage current is presented in Figure 5.5.

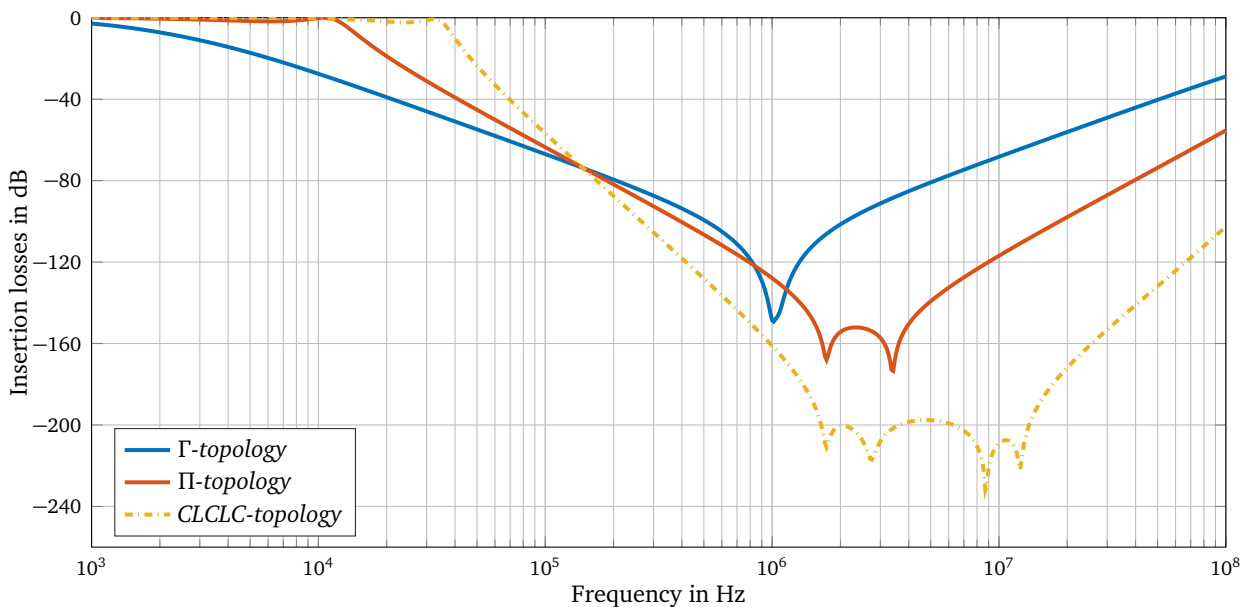


Figure 5.5.: Simulation of Γ -, Π - and $CLCLC$ -topologies optimized in order to get the minimal leakage current.

Besides reduction of the Y-capacitance by a factor of twenty compared to the Γ -topology, the $CLCLC$ filter exhibits superior high frequency performance. Therefore, no measures for the high frequency IL improvement are required. Unfortunately, a higher number of components leads to a more complex layout which, can cause some problems with inter-component couplings. In order to avoid those troubles during the filter design, the recommendations listed in Section 4.2 should be followed. Prototype measurements confirm that IL of the $CLCLC$ -topology are comparable with the Γ -topology IL at the low frequency and surpass the Γ -topology IL at the high frequency (up to 50 dB).

In summary, when compared with the Γ -topology based filter, the $CLCLC$ -topology shows better high frequency characteristics and much lower leakage current, due to reduced capacitance. The peak improvement of the simulated IL reaches 60 dB. Moreover $CLCLC$ -topology is superior in terms of the power density and cost. Obviously, the higher number of components is the main disadvantage of this

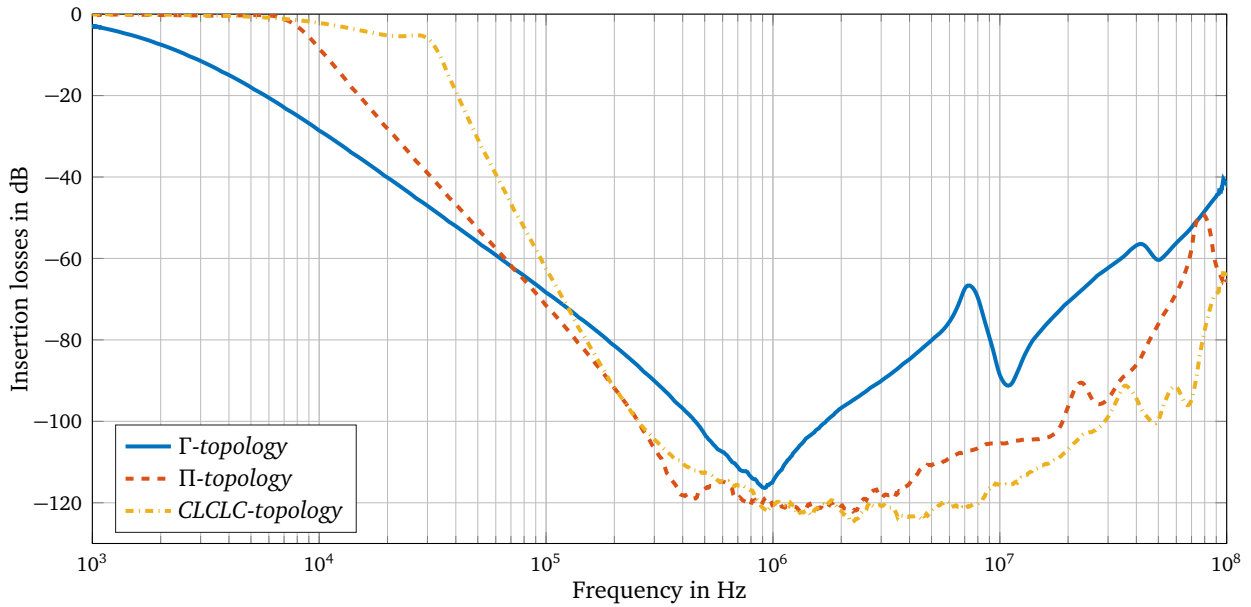


Figure 5.6.: Measurements of Γ -, Π - and $CLCLC$ -topologies optimized in order to get the minimal leakage current.

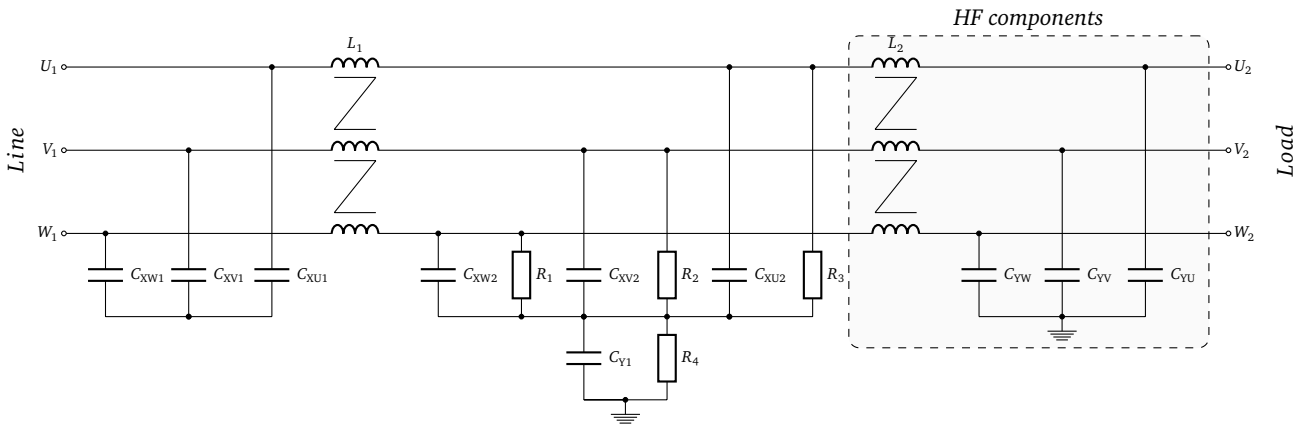
particular filter and multistage filters in general. A resonance at the cut-off frequency might lead to some saturation issues.

5.1.2 Ladder Filters with High Frequency Stages

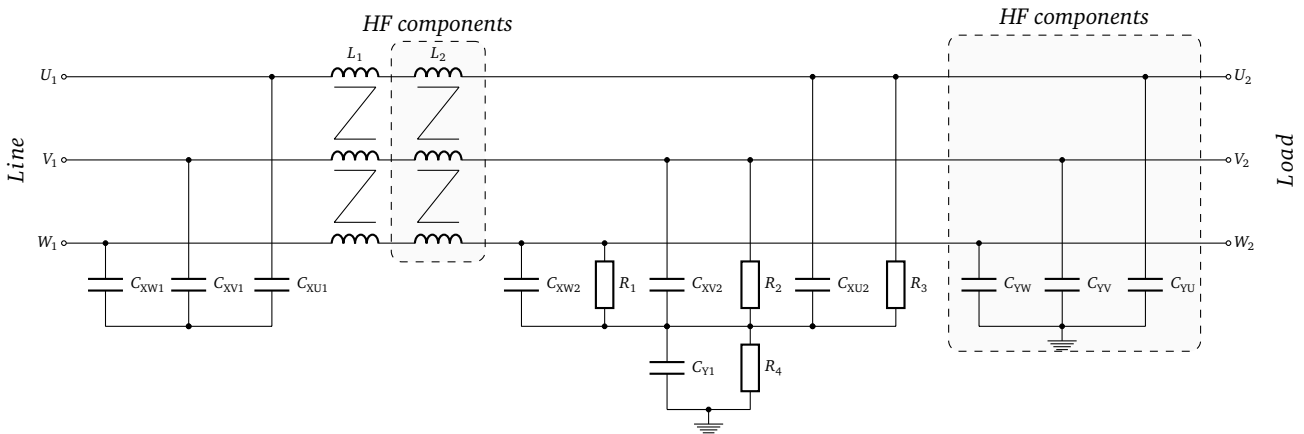
In some cases IL of a single stage filter is completely sufficient for fulfilment of existing limits in the frequency range up to several MHz. But at the higher frequencies, IL degradation caused by self-parasitics and core material properties take place. As a result of this, IL becomes lower and high frequency disturbances can exceed the maximal acceptable level. The most straightforward solution for this issue is to include one more stage and equally split total capacitance and inductance among all stages. This is followed by the proportional increase of the total capacitance and inductance in all stages, until the required IL at the high frequency is achieved. Alternatively, the filter under development can be kept without common changes, although it is supplemented with secondary components, which affect IL only in the high frequency range. Values of these components are an order of magnitude smaller than the main components. Small components establish a secondary stage, which is intended to regulate IL at the high frequency.

There are two possible options of secondary or high frequency components implementation. The first one is a ladder network, when HF components create a full-fledged stage connected to the main filter stage (Figure 5.7a). The second option is realized when the main CMC and the main capacitor's group are assisted with HF components, as depicted in Figure 5.7b. Components L_2 , C_{YU} , C_{YV} and C_{YW} are the HF components, which have a substantial impact on IL only in the MHz range. Employment of the first option with a ladder connection is more efficient but amplifies a resonance at the cut-off frequency. The second option does not have this issue but improvement is considerably smaller. From a construction point of view, it is easier to assist an existing group of capacitors with additional HF components than to form a new stage. For example a PCB based EMI filter can be supplemented with these components

by soldering of them from the other side of the PCB, as components with small dimensions barely affect the power density and costs. Both these HF component-employing options are advantageous compared with the other previously presented methods intended to improve solely HF IL.



(a) Ladder network based realization.

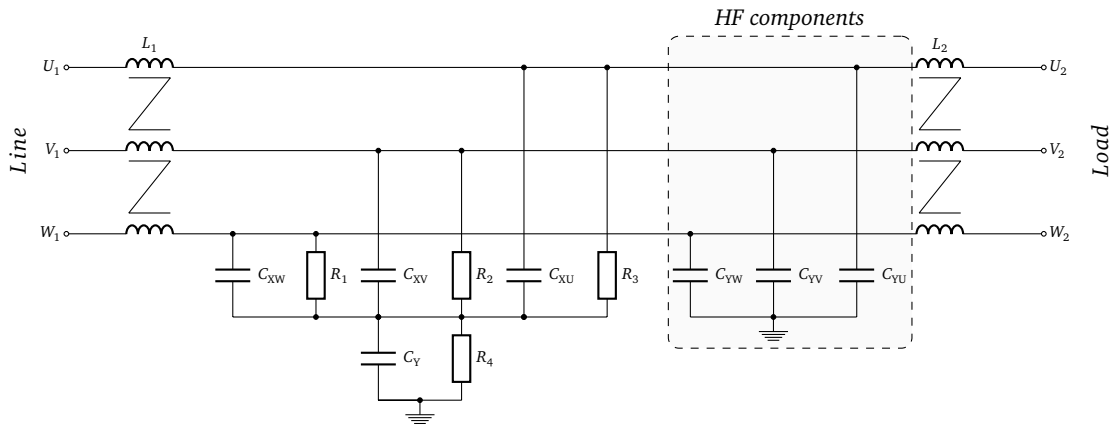


(b) The main stage assisted with high frequency components.

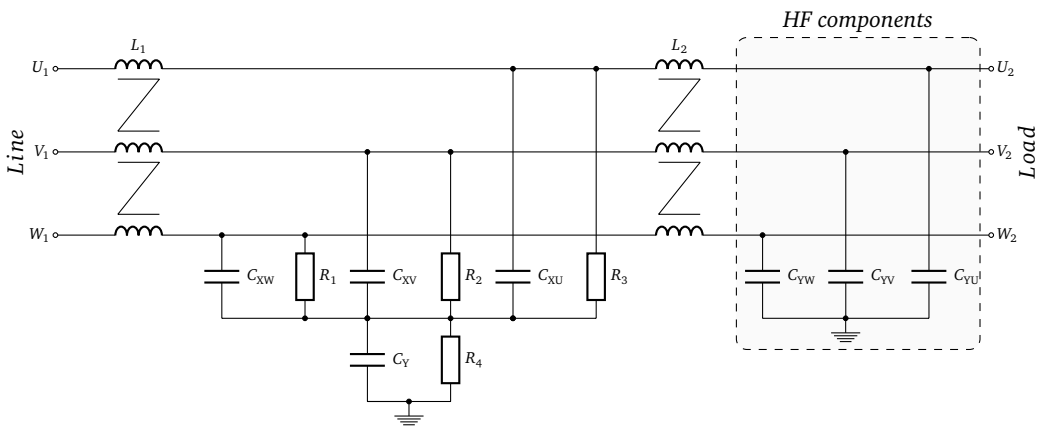
Figure 5.7.: Various ways for high frequency components implementation.

To study the behaviour of EMI filters assisted with high frequency stages several prototypes are built. Firstly, a T -topology based filter is analysed. The reference filter is assisted with a group of 2.2 nF phase-to-ground connected Y-capacitors. During the first experiment the main capacitor group of the T -filter is combined with the HF capacitors forming a $LCCL$ -topology (Figure 5.8a). For the second experiment HF capacitors are connected in series with the main T -stage forming a $LCLC$ -topology (Figure 5.8b). Exhibited CM and DM IL are shown in Figure 5.9. Improvement of CM IL is decent and exceeds 30 dB between ≈ 2 MHz and 70 MHz for the first option. Results exhibited by the second option are more modest and do not exceed 25 dB. Moreover, CM IL deterioration in the range 6 MHz to 10 MHz is observed.

Several experiments are conducted with a Π -topology based filter as well. One of the main capacitor groups is assisted with the HF capacitors, forming a $CLCC$ -topology (Figure 5.10a). This arrangement allows to avoiding use of the second CMC. Deterioration of IL due to a resonance between the HF capacitors stage and a CMC is observed in CM IL (Figure 5.11, $CLCC$). This issue can be solved via connection of damping resistors in serials with the HF capacitors group as it is demonstrated in Figure 5.10b. It allows suppression of this resonance, so that negative effects are diminished (Figure 5.11,



(a) LCCL-topology.



(b) LCLC-topology.

Figure 5.8.: T-topology based filters with different arrangement of HF components.

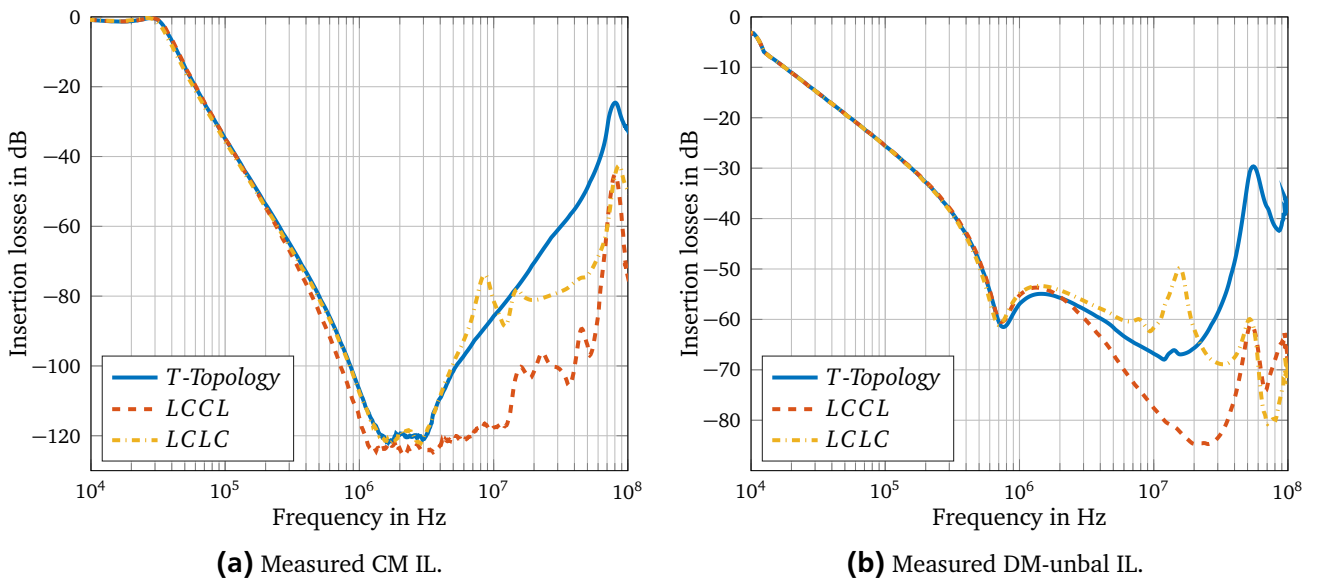


Figure 5.9.: Comparison of two methods of high frequency capacitors implementation with T-topology.

CLCC + R). In this case CM IL improvement reaches 30 dB and DM IL 20 dB. Taking into account the

insignificant increase of costs and occupied volume, these improvement measures exhibit decent results for both T - and Π -topologies.

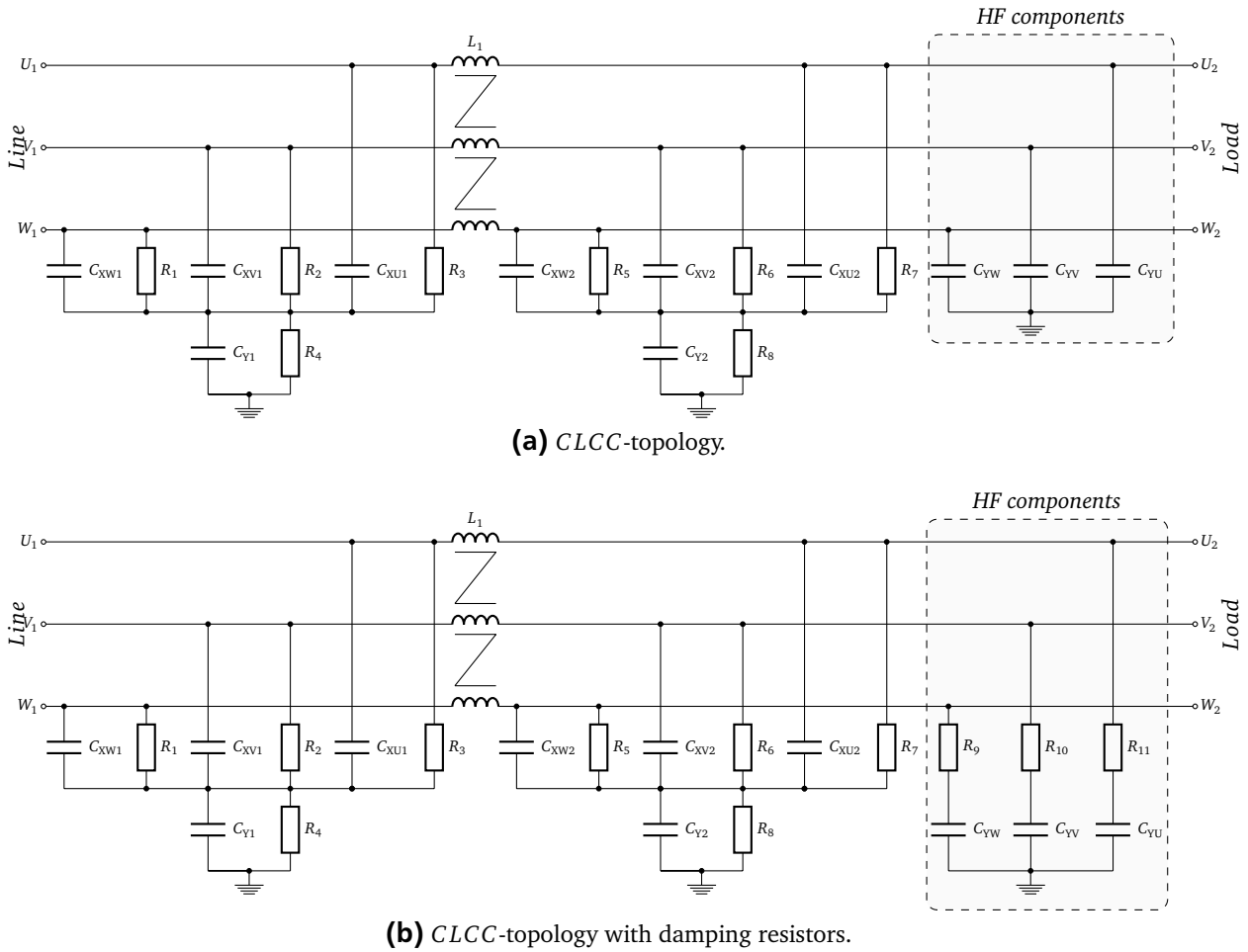


Figure 5.10.: Comparison of two methods of high frequency capacitors implementation with Π -topology.

When a complete HF stage consisting of capacitors and inductors is connected in series with the main stage, a natural resonance of this stage is introduced. The resonance causes degradation of IL. In order to avoid negative influence from the resonance, it can be adjusted to the SRF of one of the filter components. Provided that those two resonances are adjusted to the same frequency they compensate each other. High frequency performance of the secondary stage under this scenario slightly diminishes, but considerably smaller HF components can be used. Improvement of more than 50 dB, compared to the reference filter topology, is still exhibited. For implementation of this method, SRFs of the EMI filter must be precisely predicted. The diagrams in Figure 5.12a show IL of the filter with the natural resonance of the HF stage, which is adjusted to the SRF of a CMC and with no resonances matching. Natural damping, represented by core material, mitigates the resonance of the HF stage. This effect becomes more feasible for all typical CMC core materials (MnZn ferrites, nanocrystalline, amorphous alloys) starting from 0.5 MHz. This damping is a result of the imaginary part of permeability. Therefore, a resonance of the high frequency stage can be shifted to the frequency higher than 0.7 MHz, so that it is mitigated by natural core damping (Figure 5.12b). In reality high frequency IL of the filter with an adjusted resonance are improved compared with the filter with not adjusted resonance.

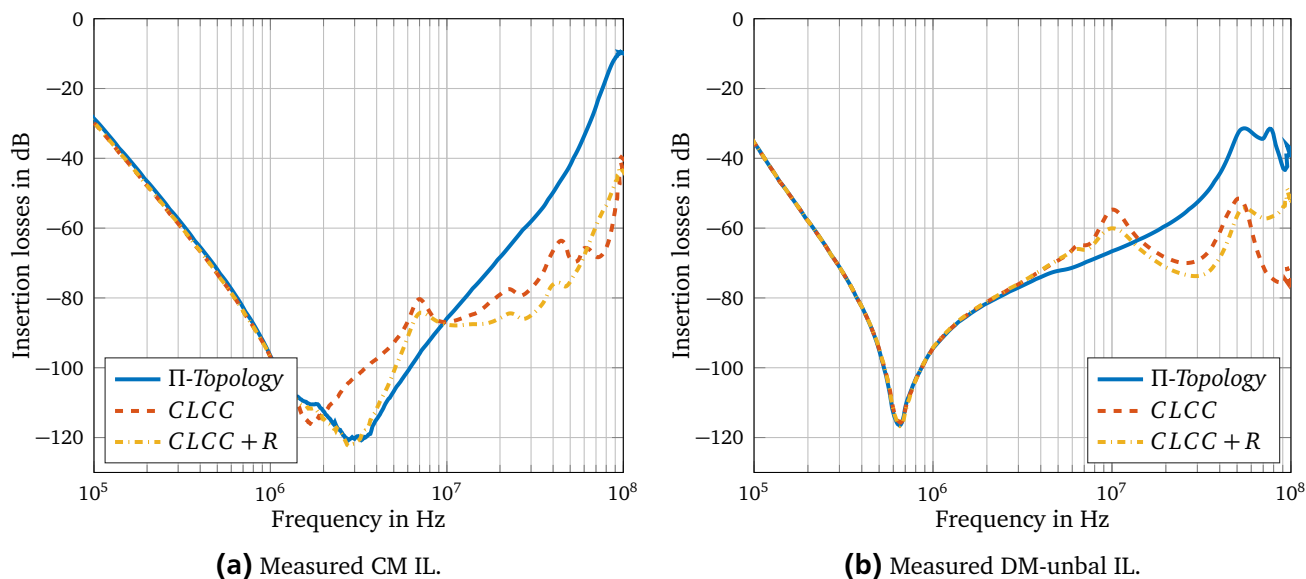
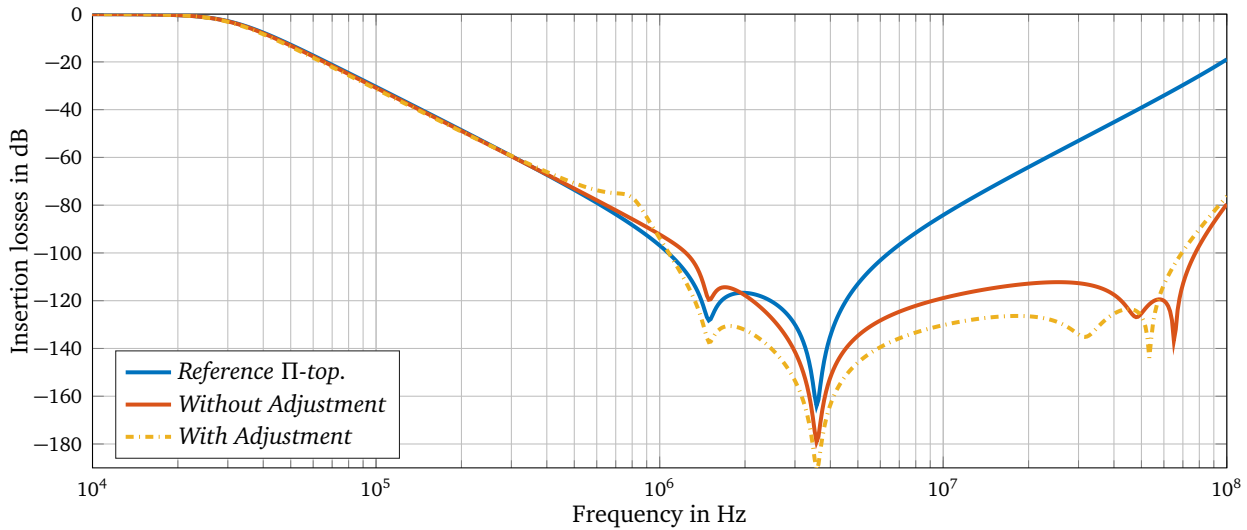


Figure 5.11.: Comparison of Π -topology based filter with and without resonance damping.

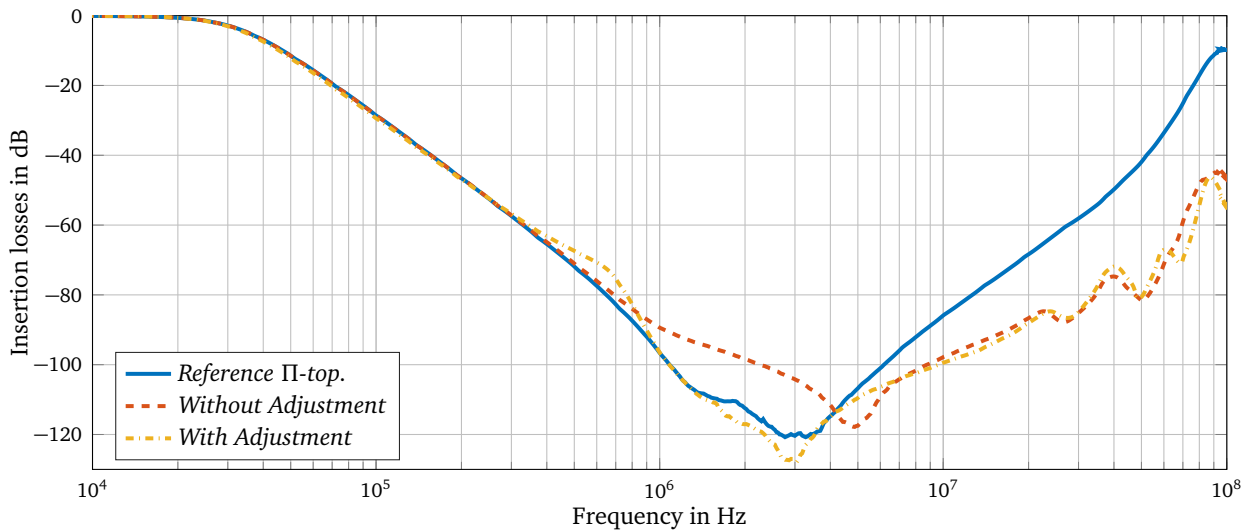
One more important issue which has to be addressed concerns a connection type of HF capacitors. Since employment of directly connected X- and Y-capacitor demonstrates low ESL, this capacitor's connection type should be the best option for IL improvement. It is clear that the main disadvantage is that three components are required for this connection. Necessary values of capacitors for forming of the HF stage are in the range of several nanofarad, so that they can be found as an SMD type. Because of their construction SMD capacitors have lower ESL compared to through-hole analogues. The price of SMD capacitors is also quite low. For example the typical price of a 1 nF Y-type capacitor is 0.4 Euro which is around 10% of the price of main Y-capacitors. NiZn ferrites are recommended for inductors employed in the HF stages. Because NiZn ferrites have relatively stable permeability up to 70 MHz [224]. Capacitors used in the HF stage occupy considerably less space than inductors. Hence, the maximum power density is achieved with this combination: when inductance is minimised and capacitance is maximized (such tiny capacitors have negligible impact on leakage current).

If power density is used as the main criteria in the filter design process, either the Π -stage which includes two star-connected capacitors groups or the T -stage with star-connected capacitors is the best option. The power density of a 10 A EMI filter without improvement based on Π -topology is 925 W/cm^3 and based on T -topology is 755 W/cm^3 . Approximated prices of filter components are 14.10 and 11.55 Euro respectively. These types of topologies have several benefits compared to Γ -type or multistage filters. However, HF IL of those two topologies remains quite poor. This disadvantage can be eliminated with the proposed high frequency stage method. The resulting equivalent circuit of the enhanced Π - and T -topologies based filters are depicted in Figure 5.13b and Figure 5.13a respectively. High frequency IL of the resulting EMI filters can be adopted via appropriate selection of HF stage components.

IL of the T -topology based filter with no improvement measured, with HF capacitors group (Figure 5.8b) and assisted with a HF CL -stage (Figure 5.13a) are demonstrated in Figure 5.14. CM IL of the improved T -filter stay below -100 dB in the range from the SRF and up to 50 MHz and can be qualified as a perfect result. Considerable improvement of DM IL is also achieved after several MHz. Resulting IL of the Π -topology based filter, the same filter with an additional HF capacitors group C_{YU}, C_{YV}, C_{YW}



(a) Simulated CM IL.



(b) Measured CM IL.

Figure 5.12.: CM IL of a Π -filter with the natural resonance of the HF stage adjusted to the SRF and without adjustment.

(Figure 5.10b) and assisted with a HF LC -stage (Figure 5.13b) are shown in Figure 5.15. CM IL are improved in the entire high frequency range 5 MHz–100 MHz. Improvement is stable and reaches 30 dB. Positive effects on DM IL are insignificant, improvement starts only after 20 MHz. Since DM capacitors do not have any limitations of capacitance in contrast with Y-capacitors (leakage current), additional X-capacitors can be easily used for DM improvement. Furthermore, filters with improved high frequency IL have insignificant cost and volume increases. Price of the necessary components for a T -topology based filter are only a factor of 1.26 and volume is a factor of 1.17 higher compared to the filter with no HF IL improvement. For a Π -topology based filter the costs and volume are a factor of 1.21 and a factor of 1.2 higher. All technical parameters of filter prototypes together with prices and volumes are summarized in Table I.3.

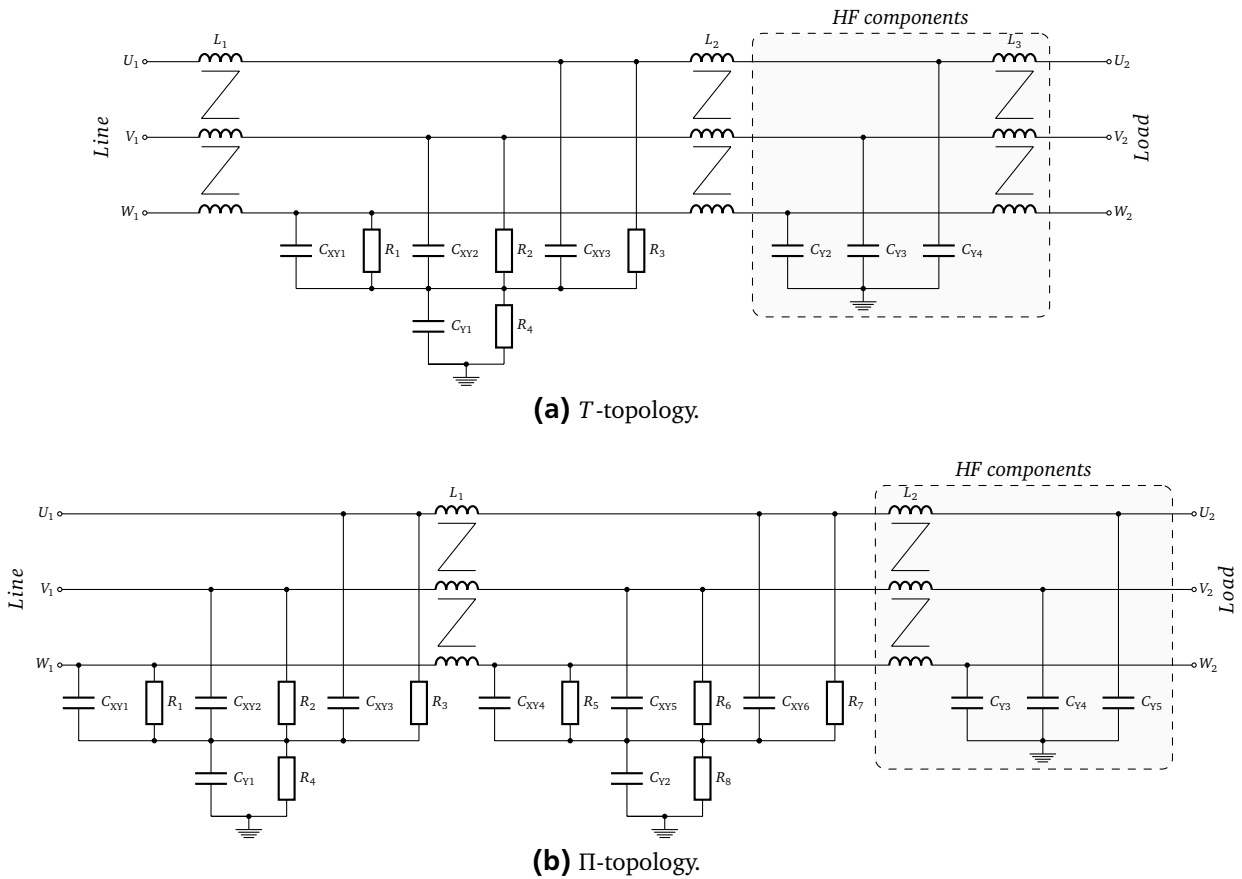
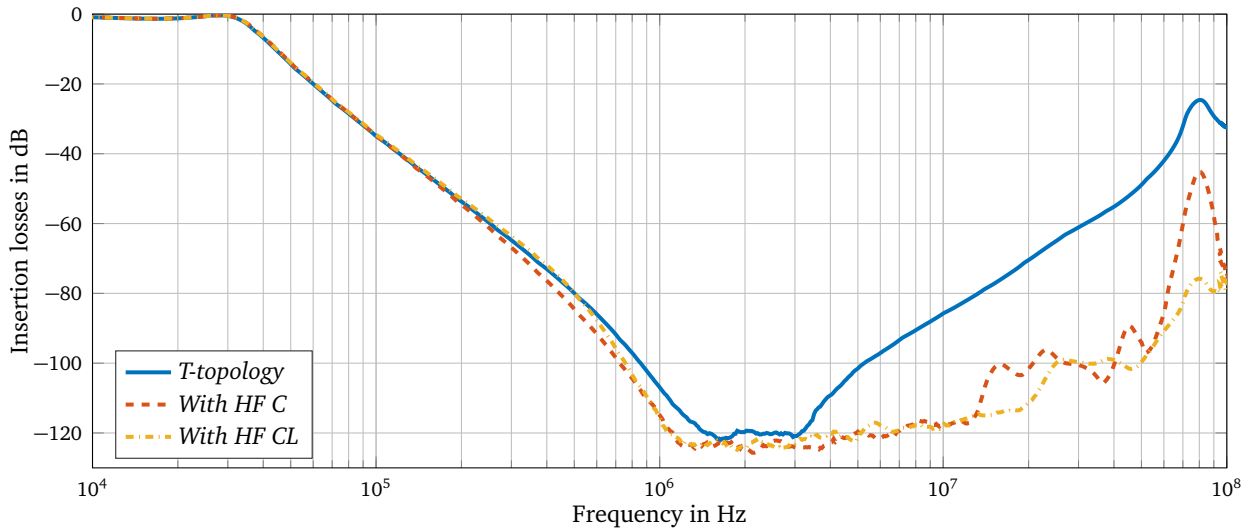


Figure 5.13.: Equivalent circuits of Π - and T -topologies, assisted with high frequency stages.

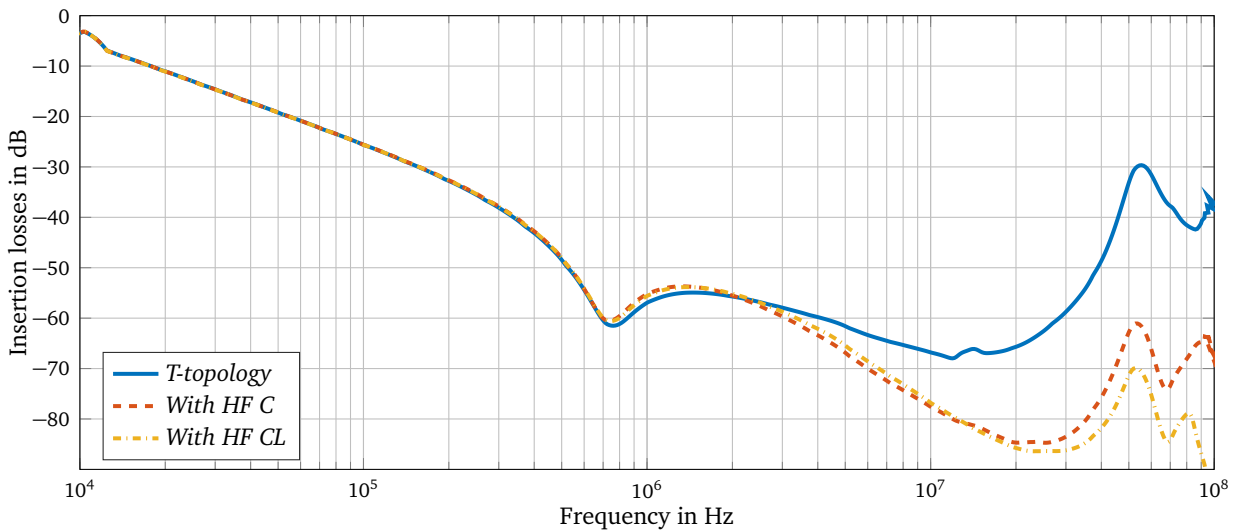
5.2 Impact of Magnetic Material on EMI Filter Performance

Employment of high frequency stages offers great opportunity for high frequency IL improvement, although without considerable influence in the low frequency range (up to 1 MHz). Low frequency IL are mainly affected by the filter topology (Γ , Π , $CLCL$, etc.) and a total amount of used capacitance and inductance. The main stage(s) defines the initial slope of IL, and a CMC plays the most important role in it. Correct combination of the core material, core dimensions and the number of turns allows designing a CMC which provides necessary low frequency impedance for following EMI filter design.

Ferrites and nanocrystallines are the two most suitable materials for CMC design. However, the properties of different material sorts differ significantly. For example ferrites can be optimized in order to get a material with good high frequency permeability, high saturation flux density or high initial permeability. Hence, CMCs based on those cores have rather diverse impedance characteristics. Impedance of CMCs based on different core materials is depicted in Figure 5.16. Inductance of those chokes is strongly nonlinear with frequency. The frequency plot of an ideal inductor in log scale represents a straight line, and for real chokes it deviated from an ideal choke considerably. Nanocrystalline chokes keep inductive properties up to 50 kHz, after this frequency it starts to behave as a hybrid RLC network. Ferrite materials remain purely inductive longer (up to 600 kHz), then a resonance caused by domain wall and gyromagnetic spin motion is observed. This resonance leads to increase of impedance in the range 0.6 MHz–1.4 MHz, followed by impedance degradation. As a result of this degradation (which is



(a) Measured CM IL.



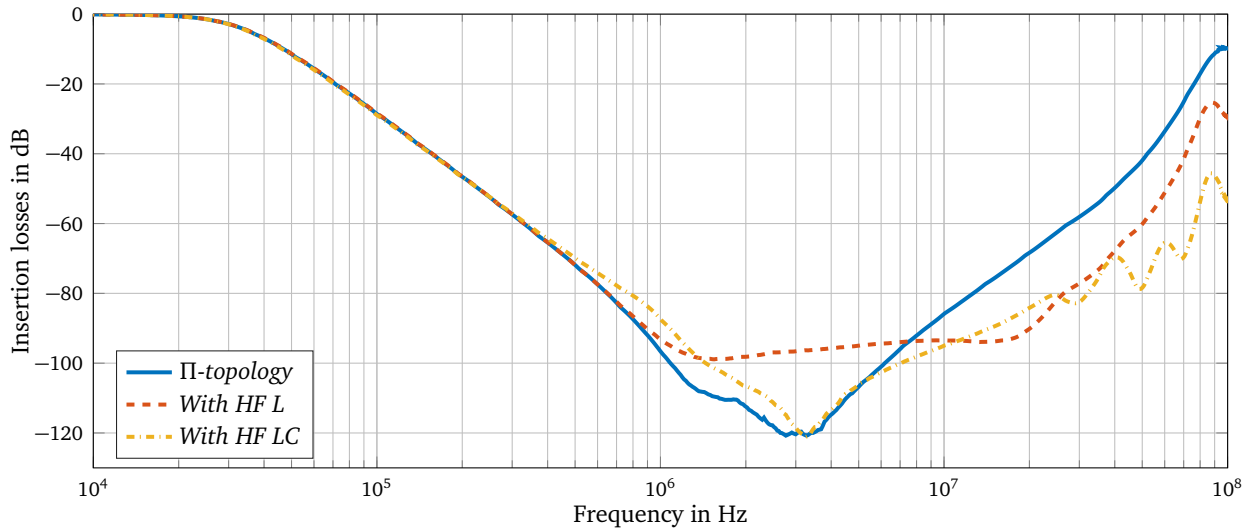
(b) Measured DM IL.

Figure 5.14.: Comparison between IL of the T -filter, T -filter with additional HF capacitors and T -filter supplemented with an LC -stage.

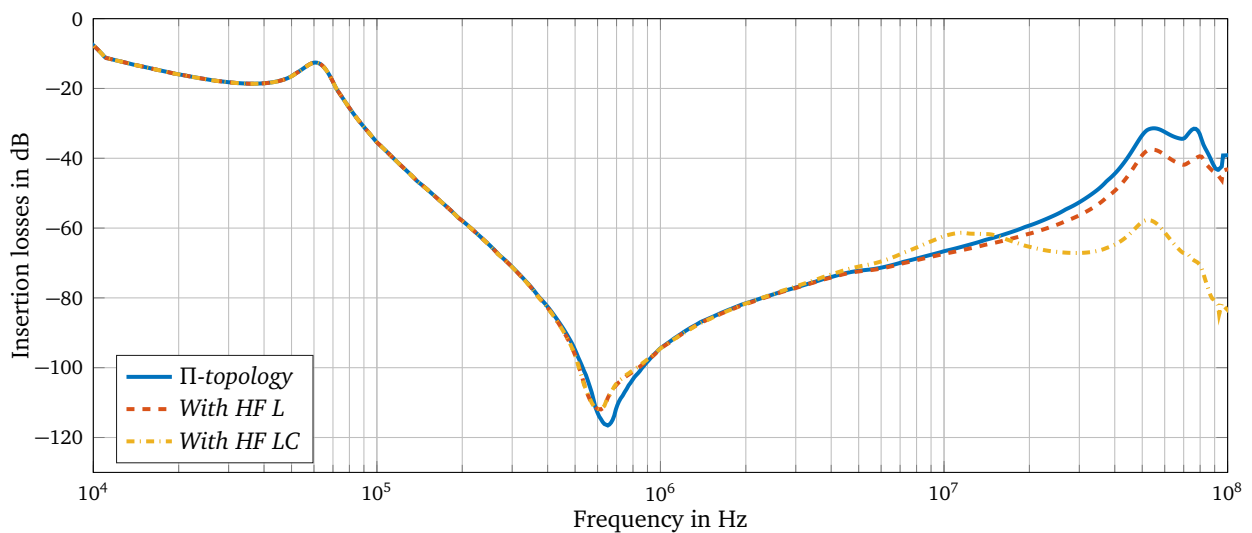
seen in all materials starting from several MHz) other EMI filter components have to provide sufficient impedance.

Figure 5.17 demonstrates effects on IL, when different chokes are installed in the same EMI filter. As a result of the typically higher permeability of nanocrystalline materials, CM IL of a filter with a W424 based CMC are significantly improved (up to 36 dB). Some enhancement (≈ 10 dB) is also observed at the high frequency. In spite of clearly seen CM IL improvement at the filter level, which is introduced by nanocrystalline materials, some critical points of nanocrystalline based CMC utilization must be listed.

Firstly, as a result of high permeability (initial permeability of nanocrystalline W424 is 40 times higher than N87 ferrite) nanocrystalline based cores can withstand much lower current without saturation. Nevertheless, nanocrystalline typically exhibit higher saturation flux density, owing to the fact that nanocrystallines can compete with ferrites. For example the saturation current of a CMC based on W424 with 15 turns is only 0.07 A. At the same time the saturation current of a CMC based on a N87 core of



(a) Measured CM IL.



(b) Measured DM-unbal IL.

Figure 5.15.: Comparison between IL of the Π -filter, Π -filter with additional HF capacitors and Π -filter supplemented with an LC-stage.

the same size and a turn number is 1.36 A. This fact should make ferrites a better option for applications with initially high common current. However, common mode current passing through phase cables is redistributed within a drive system after filter installation. According to Ohm's law, with increasing of CMC impedance less current will pass through it. Topology of the filter makes a big difference in the current distribution process and presence of Y-capacitors before or after a CMC must be considered during core material selection. It means that in order to properly design an EMI filter, its topology must be known before development of a CMC begins. For instance a filter based on a T -topology will have higher saturation demands compared to a CMC located closer to a source of common mode disturbances, as a part of CM current will be terminated to the ground through the Y-capacitor.

Secondly, the large imaginary part of permeability leads to dissipation of the energy, carried by disturbances inside the core. This process can cause overheating of a core, so that neither inductance nor saturation but the maximum heat dissipation defines the size of the core.

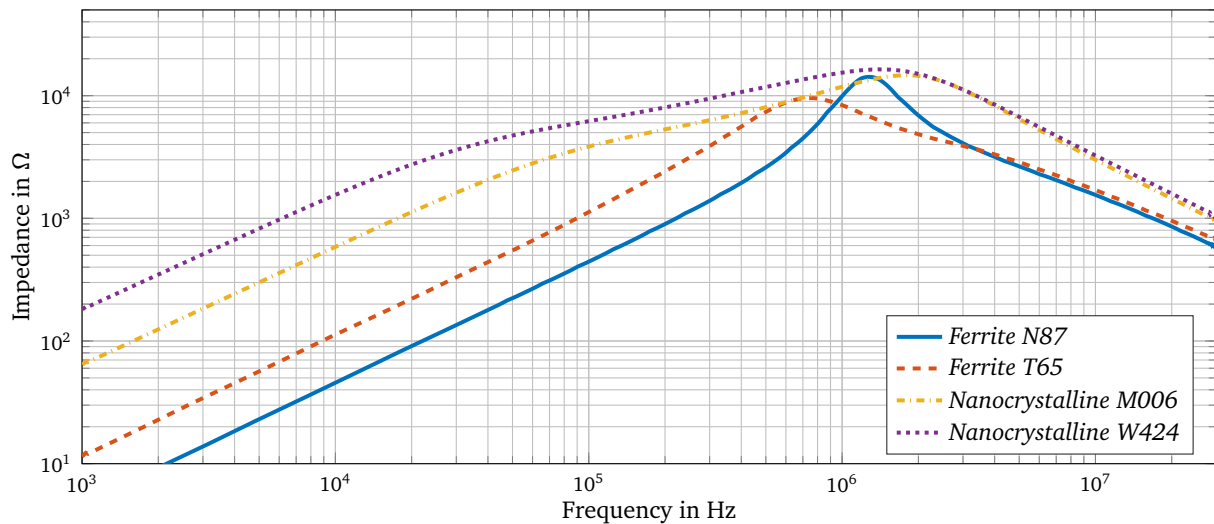


Figure 5.16.: Impedance of CMCs based on different material.

Lastly, stray inductance of nanocrystalline cores is typically smaller. Consequently if the ferrite is substituted with nanocrystalline, resulting DM IL will degrade. In this situation, the size of X-capacitors has to be adapted. Effects of ferrite and nanocrystalline materials on DM IL of the same filter are demonstrated in Figure 5.18. There it is seen that deterioration of DM IL in the complete frequency range of interest is ≈ 5 dB. It confirms a necessity to employ bigger X-capacitors if a CMC with higher permeability is used.

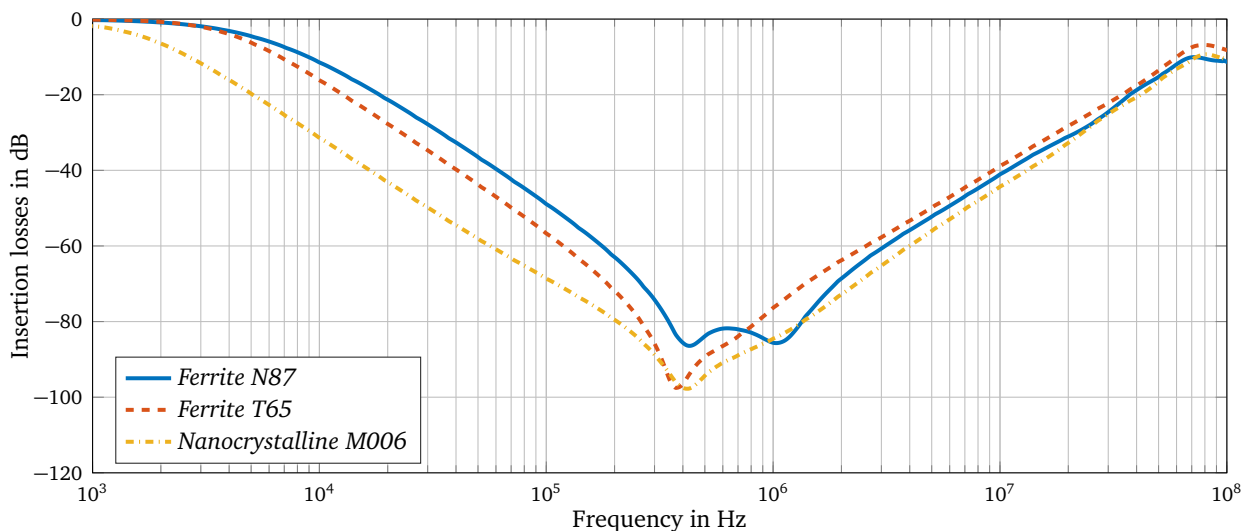


Figure 5.17.: CM IL of an EMI filter with different CMCs.

Some additional experiments involving combination of two different materials for one CMC are carried out in Appendix J. A brief summary from this investigation as follows: general combination of two chokes based on different materials within one filter does not bring any feasible advantages either from performance or from price points of view. Modelling of a hybrid choke with a combined core is quite complicated.

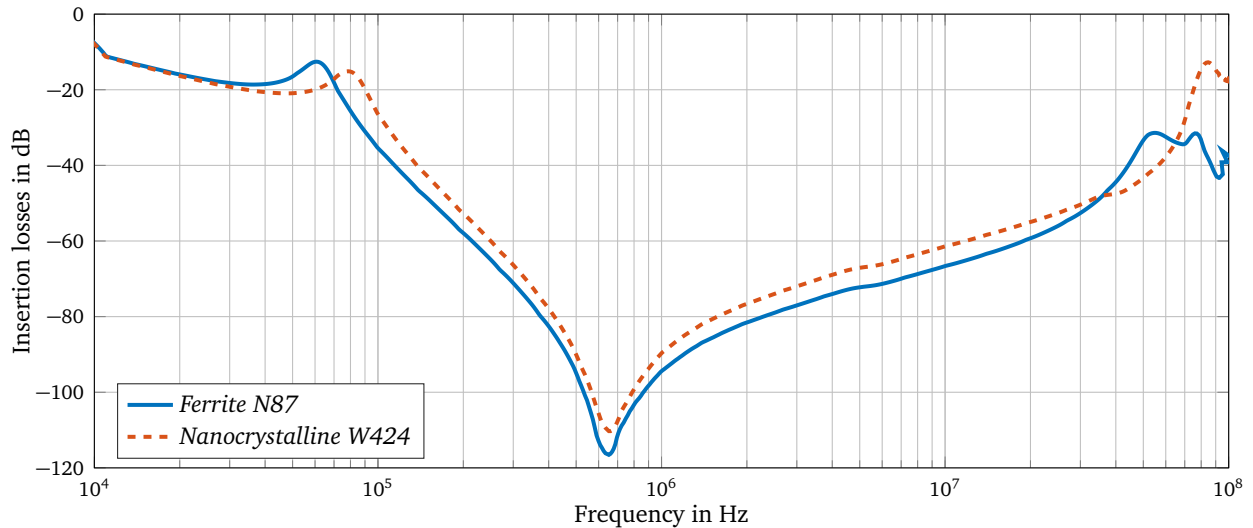


Figure 5.18.: DM IL of an EMI filter with nanocrystalline and ferrite CMCs.

5.3 Summary of EMI Filter Improvement Methods

Several IL improvement methods are presented in Chapter 4 and Chapter 5. In order to compare improvement methods factors such as efficiency, the power density, price and applicability are considered. Multistage filters with equal stages are superior in performance compared to single-stage filters, as is clearly seen from the comparative analysis conducted in Section 5.1.1. Results of the same analysis in terms of the costs and power density are not so unambiguous. However, performance of multistage and Pi-topology filters with equal total component values clearly excel over simple Γ -filters. It must be mentioned that these conclusions are fair only for the topologies when X- and Y-capacitors are connected directly either between phases or the phase and the ground. But the tendency remains similar for other capacitor connection types. The only relevant shortcoming of multistage filters is a higher number of components. This problem leads to a more complicated layout and a higher number of mutual couplings. Employment of parasitics compensation methods in multistage filters complicates the layout even further. However, multistage filters have such superior high frequency IL (at least -100 dB in the range 0.25 MHz–30 MHz) that any additional improvement is unnecessary (Figure 5.5).

The method involving employment of additional HF components and stages is quite simple from an implementation point of view, as used components are an order of magnitude smaller than the main components. Therefore, a HF LC stage can be easily located directly at the input or output of a filter without considerable negative impact on the price and the power density (Table I.3). Results of HF IL improvement for different filters exceed 45 dB for HF IL, as seen in Figure 5.14 and Figure 5.15. With EPC and ESL compensations together, the maximum practically achievable improvement of HF IL is ≈ 25 dB (Figure 4.20). Relatively high development and debugging efforts are needed for achievement of this result, due to a great number of parameters which have to be accounted for.

In contrast with parasitic compensation methods, the HF stages method gives higher improvement and it does not require precise adjustment. Furthermore, positive effects represented by EPC and ESL compensations on CM IL rapidly shrink after 20 MHz. This issue is not present when additional HF stages are included. Impact on the power density and cost is nearly the same for the EPC and ESL

compensation methods and for the HF components method. Γ -topology based filters is the only category where utilization of EPC and ESL compensation might be meaningful from the performance point of view. Utilization of the HF components method is recommended for Π -, T - and $CLCL$ -topologies. With increasing of the number of the main stages HF components does not bring much benefit, since HF IL is already superior.

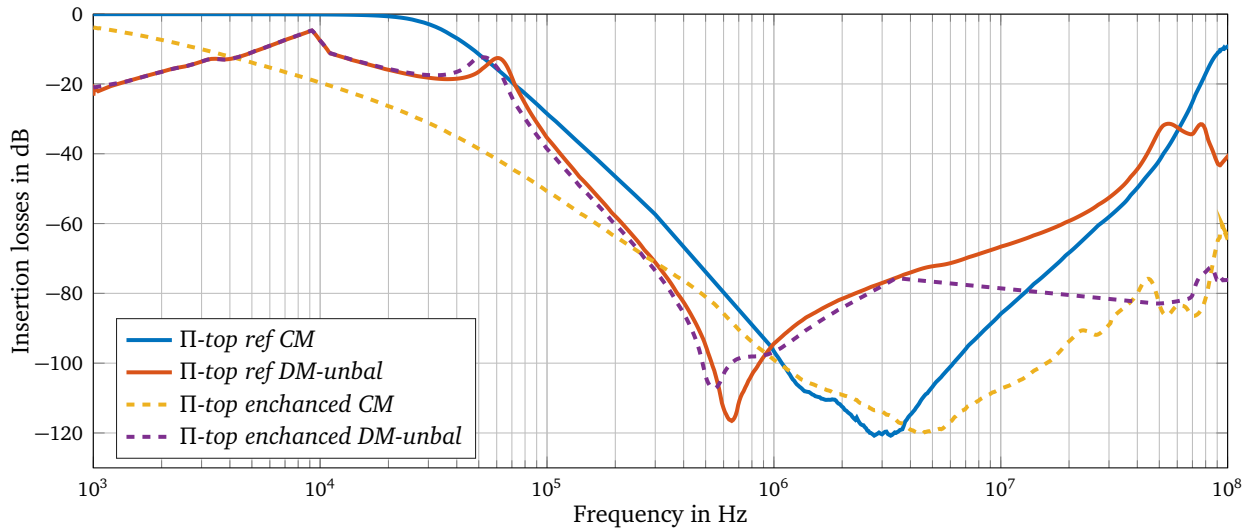
It is worth mentioning that some improvements of high frequency IL can be integrated into a drive system without additional filter components. For example, the layout of a PCB can be explicitly designed in order to increase parasitic capacitance between conductive traces of a filter and the ground: in this way an extra Y-capacitor is implemented. Positive effects presented by this method might be similar to use of high frequency SMD components, discussed above [208]. One more option includes utilization of stray couplings from HF IL improvement, for example use of the stray flux of a CMC in order to compensate ESL of capacitors.

Conventional multistage filters and filters supplemented with HF stages are the most promising solution for high power density applications. On one hand the total number of components increases, but on the other hand, due to enhanced IL the total value of components can be decreased. It opens perfect opportunities for reduction of Y-capacitors, so that leakage current can be optimized. Future developments of EMI filters with low leakage current should be based on multistage topologies. Furthermore, the overall volume and costs required for fulfilment of the technical requirements can be inferior for multistage filters compared to single stage ones. As a result of using smaller components in multistage filters, parasitics become smaller. Hence SRFs of a filter are shifted to the higher frequency range, so that no explicit parasitics compensation measures are required.

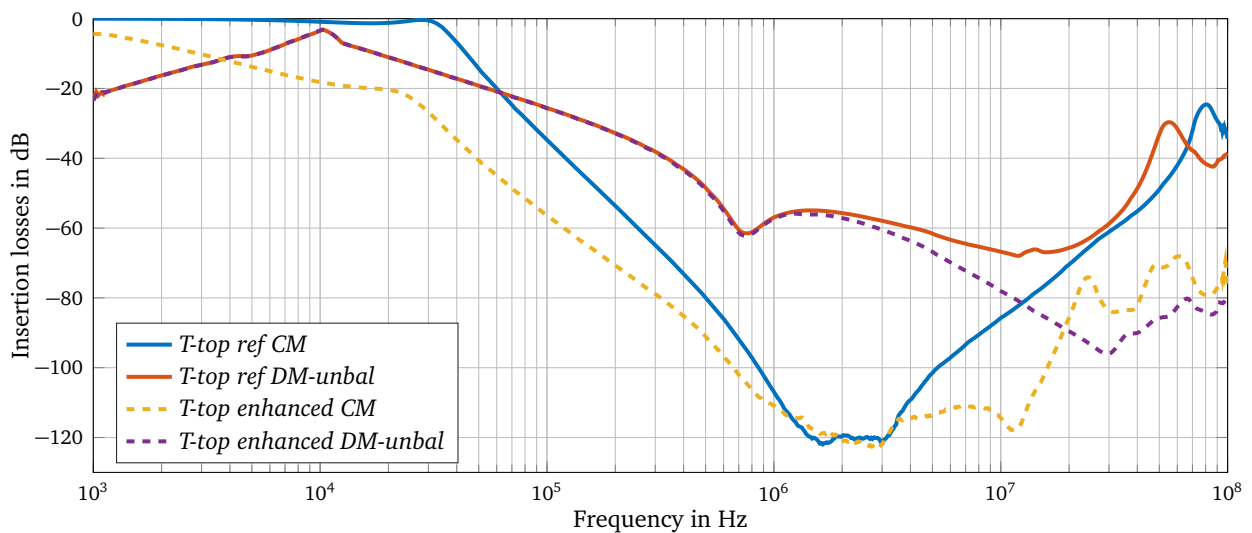
Multistage topologies is a preferable option for both high-performance and low leakage current applications. Depending on the particular design, multistage filters can be either superior or inferior to Π - and T -topologies in terms of the power density and costs (Table I.2). Improvement of high frequency IL can be achieved by means of EPC and ESL compensation (Table 4.1 and Figure 4.20). However, results show that improvement of high frequency IL can be achieved with additional high frequency components or stages. This option allows enhancement of high frequency CM IL up to ≈ 45 dB and DM IL ≈ 30 dB with minimal increase of costs and occupied space (Figure 5.15, Figure 5.14, Table I.3).

The best results can be achieved with a combination of methods. Two filters depicted in Figure 5.13 with already enhanced HF IL are improved further. CMCs which were based on ferrite are substituted with nanocrystalline W424 based chokes with higher permeability. IL of enhanced Π - and T -topologies filter types are compared with IL of conventional Π - and T -filters in Figure 5.19. For both filters CM and DM IL is improved considerably. A summary of filter characteristics can be found in Table 5.2. More detailed data including specification of components which were used are included in Table I.3. The considerably higher costs of enhanced filters are caused by the price of cores.

The number of options for improvement of three-phase EMI filters introduced in Chapter 4 and Chapter 5 is rather large. For simplification of understanding, the improvement process is summarized in a flowchart (Figure E.4). EMI filter mathematical models presented in Chapter 3 should be used in order to perform a model based improvement procedure. According to the flowchart all possible IL enhancement options are separated into two groups: high frequency IL and low frequency IL. Thereafter all previously discussed improvement methods are applied in a sequential order.



(a) IL of a Π -topology based filter.



(b) IL of a T -topology based filter.

Figure 5.19.: IL Comparison of the enhanced EMI filters and state of the art EMI filters with the same topologies.

<i>Filter name</i>	<i>IL</i>	<i>Volume</i>	<i>Price*</i>	<i>Improvement used</i>
Π -topology basic	Figure 5.19a	130 182 mm ³	14.1	none
Π -topology enhanced	Figure 5.19a	157 344 mm ³	32.14	high permeability core & HF stage
T -topology basic	Figure 5.19b	158 841 mm ³	11.55	none
T -topology enhanced	Figure 5.19b	186 003 mm ³	26.55	high permeability core & HF stage

* Prices in Euro per item (by more than 1000 items order)

Table 5.2.: Summary of parameters for basic and enhanced filter topologies.



6 Consideration of EMI Filters Within a Power Electronics System

Analysis of power electronics converters from the EMI point of view has a crucial importance in the EMI filter design process. Ideally a spectrum emitted by a PE converter should be used as input data for EMI filter development. Otherwise, there is no guarantee that a PE converter assisted with a designed EMI filter will comply with standards. Partially "blind" design of EMI combined with an assumption that components of a filter are ideal leads to building of suboptimal EMI filters and unstructured attempts to mitigate disturbances with simple heaping up of components and stages.

The impact of PE converter parameters on a resulting EMI spectrum is discussed in this chapter. Scenarios with utilization of different PWM frequencies, various load characteristics, changed common mode path and other parameters are analysed. Variation of some parameters is more relevant and has considerable influence on the EMI spectrum, and consequently, on the EMI filter design. Therefore, parameters of the PE converters under test are classified in accordance with their influence on the emitted spectrum. One of the main goals is to demonstrate relative changes in the EMI spectrum caused by variation of one or the other system parameter.

Some filter types can guarantee compliance with standards independent of utilized PWM frequency, direction of the power flow, grounding type or even parameters of used semiconductors. Some other filters can be used only under particular conditions and are not effective when the PWM frequency is higher than some particular limit or if CM current is too high. Because of this, selection of a correct filter topology in accordance with the type of final application and system parameters is crucially important. Moreover, arrangement of Y-capacitors directly influences an amplitude of CM current flowing through a CMC. Too high pulses of CM current can either drive a magnetic core of a CMC into saturation or overheat it. Utilization of conventional filters with minor improvement of high frequency IL, as was demonstrated in Chapter 5, extends a number of applications, where relatively simple conventional EMI filters can be successfully used.

6.1 Influence of AIC Parameters on the Emitted EMI Spectrum

In order to investigate different arrangements of a PE converter with EMI filters, a specialized laboratory test bench is built up. A block diagram of the test bench is depicted in Figure 6.1. The setup consists of two AICs, where the first converter is a conventional "active front end" (AFE) converter, and the second one is a self-made AIC with variable parameters. A controllable DC source is connected to the self-made AIC on the load side, which allows a bidirectional power flow. The DC source is isolated from the converter with a specially designed EMI filter. This ensures that the emitted disturbances of the self-made AIC consist of spectral components exclusively emitted by the AIC itself at the respective operating point. The self-made AIC includes a proper line inductor based on a ferrite core with inductance ≈ 6 mH. An EMI filter can be connected on demand between the line inductor and the point of common coupling (PCC). The AFE is also equipped with a line inductor based on a ferrite core on the grid side. There is a possibility to connect an EMI filter on the grid side after the line inductor. For operations in a rectification mode the AFE is loaded by 12 kW resistive load which is directly connected to a DC-link.

During experiments the AFE converter is used only in a power sink mode. Both converters are coupled at the PCC which is connected to mains through a line impedance stabilization network (LISN). In this way the test bench is decoupled from the power grid. A LISN prevents any external influence on the test bench, so that measurements are reproducible. A picture of the test bench is shown in Figure 6.2.

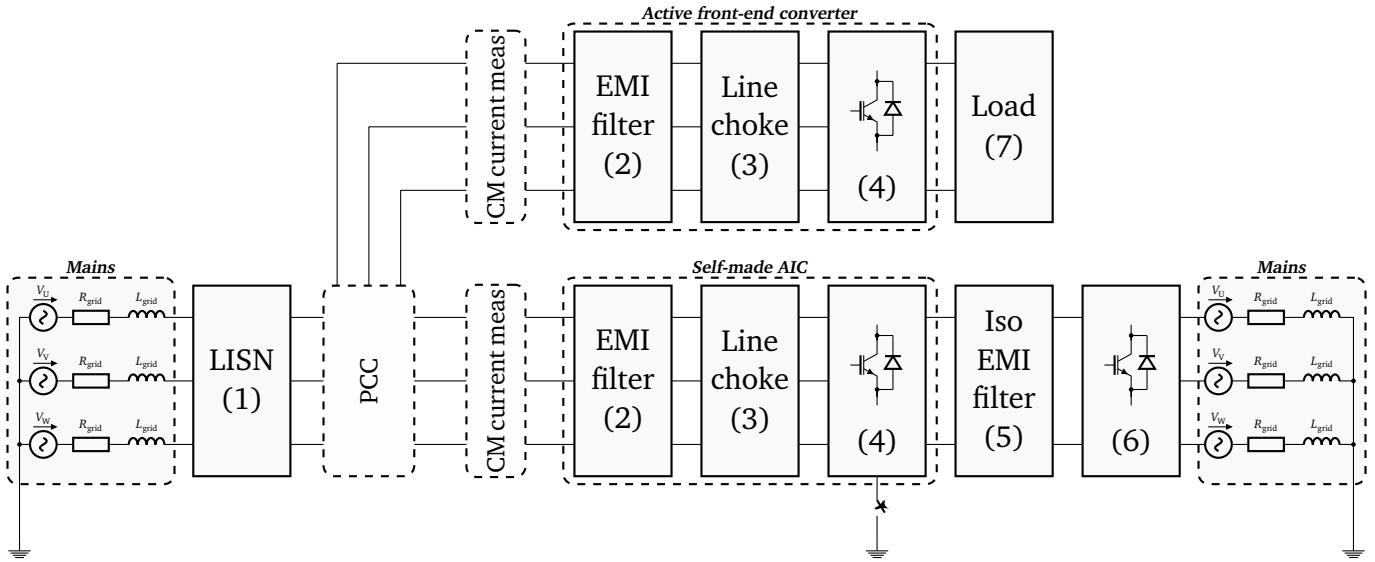


Figure 6.1.: A block diagram of the test bench.



Figure 6.2.: A picture of the test bench.

Necessary measurements are carried out at the specified EMI output of a LISN (voltage signals). CM current is also measured at the different locations as depicted in Figure 6.1. Unfortunately due to limitations of the equipment, evaluation of the whole spectrum cannot be done with one sweep. Spectra are measured in two steps, the low frequency range 2 kHz–500 kHz and the high frequency range 100 kHz–30 MHz. Thereafter these two ranges are concatenated into one diagram using data processing

software. The spectrum analyser used is not capable of conducting measurements in a logarithmic scale, and because of this the number of sampling points is rather low on the border between two measurements.

For the sake of clarity some spectra are plotted in the normal and some in logarithm scale, so that high frequency effects are easier to interpret. Reference measurements of the self-built AIC are conducted under the following conditions: voltage oriented control [197], 10 kHz frequency of sine PWM, no EMI filter installed, I_{rms} is 10 A, V_{DC} is 650 V, feeding into the power grid mode. The AFE converter utilizes hysteresis control with variable PWM frequency and no EMI filter is connected. Reference spectra are shown in Figure 6.3. Although nominal power as well as dimensions of both converters are rather similar, it is seen that emitted EMI spectra differ significantly due to the diversity of previously listed parameters.

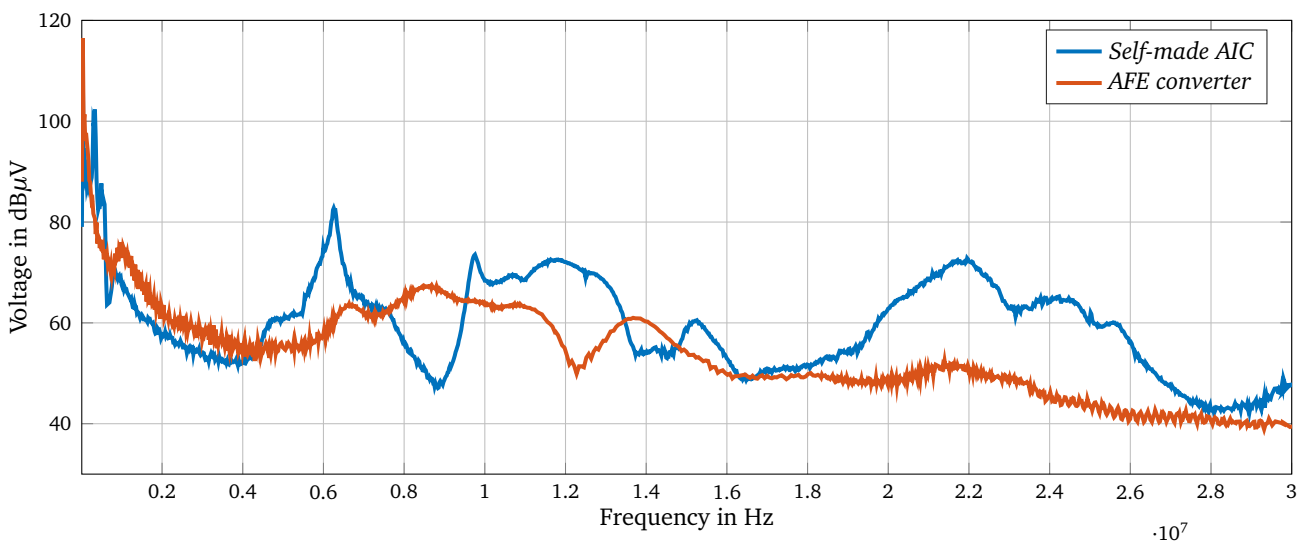


Figure 6.3.: Spectra emitted by the self-made AIC and the AFE with no EMI filter connected.

It must be mentioned that AICs are typically used together with three phase inverters, which drive an electrical motor. Obviously, in this case influence of both an inverter and a motor on the level of emitted electromagnetic disturbances has to be considered. By definition, the set of parameters that affect an emitted EMI spectrum in an inverter is quite similar to that in an AIC. Electromechanical parameters of the motor such as rotational speed, current, voltage, stray capacitance, line inductance etc. demonstrate a certain influence on disturbances as well. For a comprehensive EMI analysis the system consisting of an inverter, a motor and a mechanical load must be studied. Moreover, various operational points of the system must be considered and EMI measurements have to be conducted for diverse motor rotational speed and torque (current) operating points.

6.1.1 PWM Frequency

Several experiments based on the test setup described previously are conducted in order to evaluate and structure effects caused by parameter variation of an AIC. The basic setup for the parameter evaluation does not include any EMI filtration units located between a self-made AIC and the power grid. Disturbances emitted by the self-made AIC are evaluated in terms of voltage and current signals. A sig-

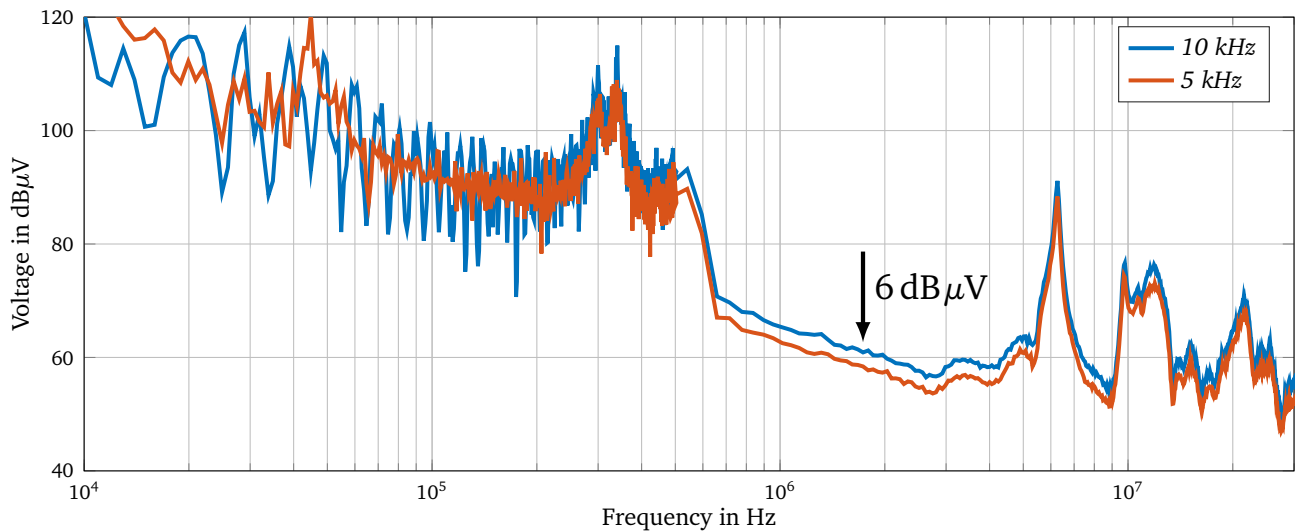
nal output of a LISN is used in order to obtain phase voltage in accordance with CISPR22 [90]. Since common mode current produced by a PE converter presents a particular interest, it is measured using a current probe with a suitable bandwidth. Common mode current is placed at the output of the self-made AIC, as demonstrated in Figure 6.2.

Firstly, effects of a PWM frequency on the emitted EMI spectrum are investigated. Figure 6.4 shows a spectrum of the AIC with default parameters (PWM 10 kHz) and a spectrum of the same AIC with the PWM frequency 5 kHz. It is clearly seen that the resulting level of disturbances drops by $\approx 6 \text{ dB}\mu\text{V}$ in the range from several kilohertz up to couple of megahertz if the PWM frequency is decreased (Figure 6.4a). The mitigation of disturbances by $\approx 6 \text{ dB}\mu\text{V}$ is the same as halving in amplitude, it reflects that in time domain PWM frequency has been changed by a factor of two. It is caused by moving of the first critical frequency of a PE converter toward lower frequency range [183]. Variation of the PWM frequency does not affect the general tendency in the emitted EMI spectrum though. At the same time the total harmonic distribution in the low EMI range (100–300 kHz) is higher for the 10 kHz PWM frequency. It demonstrates a disadvantage of higher switching frequencies from the EMI pollution point of view. Effects observed in the CM current spectrum repeat almost the same behaviour as in the voltage spectrum, with an exception of two resonances at 450 kHz and 550 kHz (Figure 6.4b). These resonances in the voltage spectrum are caused by a line inductor. Since it is based on a ferrite core with relatively poor high frequency properties, permeability of the used core starts to degrade after approximately 550 kHz. The same minimums and maximum are seen in the impedance characteristic of the used line inductor (Figure 6.10). Since a line inductor does not influence a CM current path, no resonances are seen in the measured CM current spectrum.

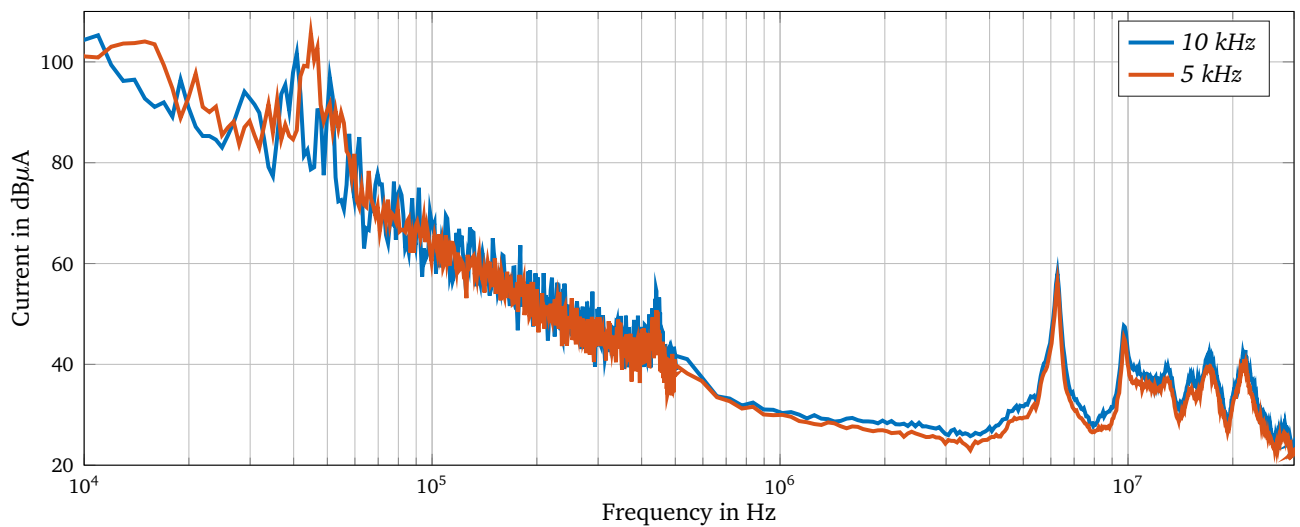
6.1.2 Dead Time

Dead time between switching of the high and low IGBTs is a quite important parameter effecting response of a current controller. However, for a current controller the dead time can be compensated. At the same time negative effects of the dead time on the emitted EMI spectrum are unavoidable. A disturbance level emitted by an AIC with shorter dead time ($1 \mu\text{s}$) is considerably lower than with $2 \mu\text{s}$, which is especially noticeable above 7 MHz (Figure 6.5a). High frequency disturbances are increased by $\approx 10 \text{ dB}\mu\text{V}$, which can cause considerable trouble during EMC tests.

This effect can be explained by two phenomena. Firstly, when the voltage set by an inverter approaches its maximum values, the width of voltage pulses becomes increasingly narrow. After reduction of the pulse width to a dead time, so-called lockout is reached. Consequently the maximum possible amplitude of generated output voltage is lower than a DC-link voltage. This phenomena causes higher current ripple close to amplitude maximums of generated phase currents. As a result voltage disturbances also grow. The second negative effect caused by dead time during every switching event is explained by the presence of a freewheeling diode. During a commutation process the half-bridge output is shortly clamped to an opposite DC-link rail via a freewheeling diode. This condition results in error voltage with an opposite to desirable voltage polarity. Corresponding with increase of dead time, the period when the opposite voltage applies to output of a converter increases, it intensify the high frequency EMI emission. Consequently, reduction of dead time can improve an EMI spectrum in the high frequency range without any changes of hardware [79].



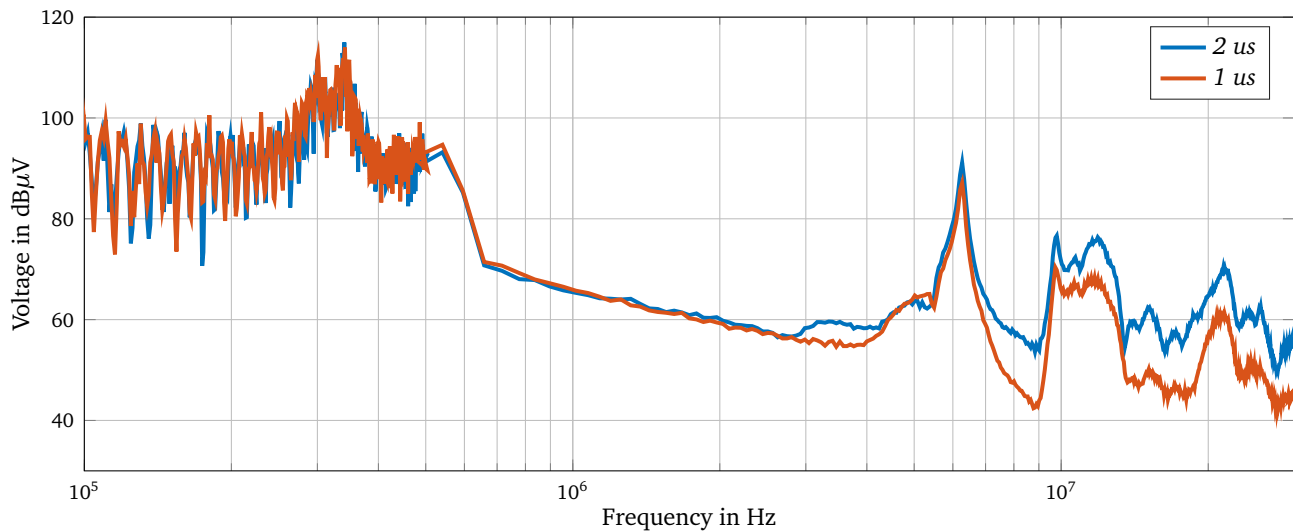
(a) LISN voltage.



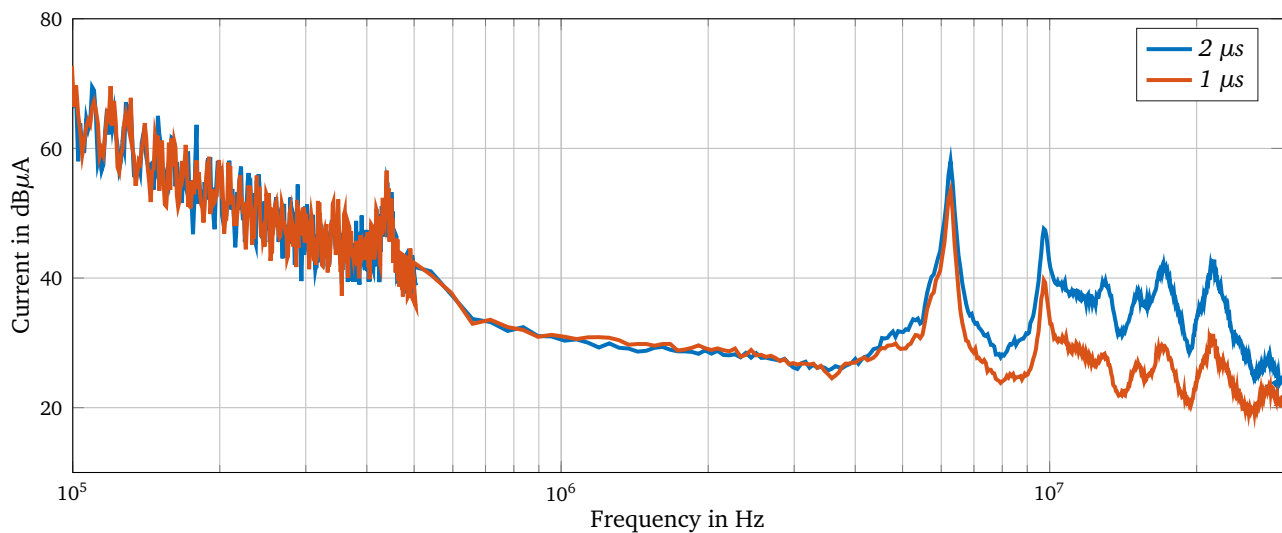
(b) Common mode current.

Figure 6.4.: Spectra of the self-made AIC operating under different PWM frequencies.

As mentioned in Chapter 4 and Chapter 5 design of EMI filters with good high frequency IL is one of the most challenging tasks. When high frequency IL of a particular filter is not sufficient and can be improved with previously described methods, an option with decreasing dead time can be considered. Effects caused by variation of the dead time are also observed in a CM current spectrum (Figure 6.5b). Because the dead time directly influences the switching behaviour of the inverter (which represent a CM current source). With decreased dead time the amplitude of high frequency CM decreases as well. Since CM impedance of the system is not influenced, the shape of the produced CM current spectrum with $2\mu\text{s}$ is similar to the case with $2\mu\text{s}$ dead time. A disturbances level in the low frequency range is barely effected by change of the dead time, therefore it is not shown in the diagrams.



(a) LISN voltage.



(b) Common mode current.

Figure 6.5.: Spectra of the self-made AIC with reference parameters and reduced dead time.

6.1.3 DC Voltage Level

One more experiment is carried out in order to demonstrate the impact of a DC-link voltage variation on emitted disturbances. Theoretically, low DC voltage should descend the whole spectrum, but it is barely seen in the measurements demonstrated in Figure 6.6. There is no observable difference between spectra emitted by the AIC with default parameters and with increased DC voltage up to 750 V. Fluctuation of the DC-link voltage during normal operation does not exceed ± 100 V from the nominal value. It is less than 1 dB in a decibel scale, which is in the same order that the observational error of used equipment. It is worth mentioning that change of a modulation index caused by DC voltage lower than a certain threshold could be a reason of significant changes of the EMI spectrum. It might lead to the incorrect idea, that changing the DC-link voltage level can significantly improve EMI behaviour of a system, although, the main reason is a control strategy, and particularly a modulation index. Changes caused by fluctuation

of DC-link voltage are rather insignificant. As common mode current is only slightly affected by DC link voltage; therefore measurements of a CM current spectrum are not shown.

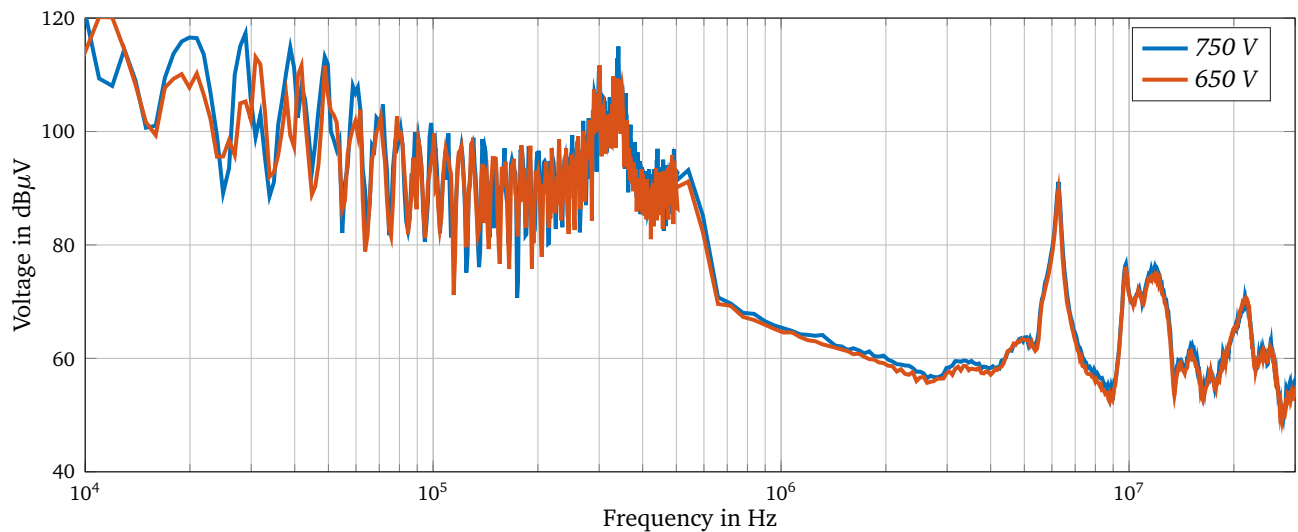


Figure 6.6.: Spectra of the self-made AIC, measured under different DC-link voltages.

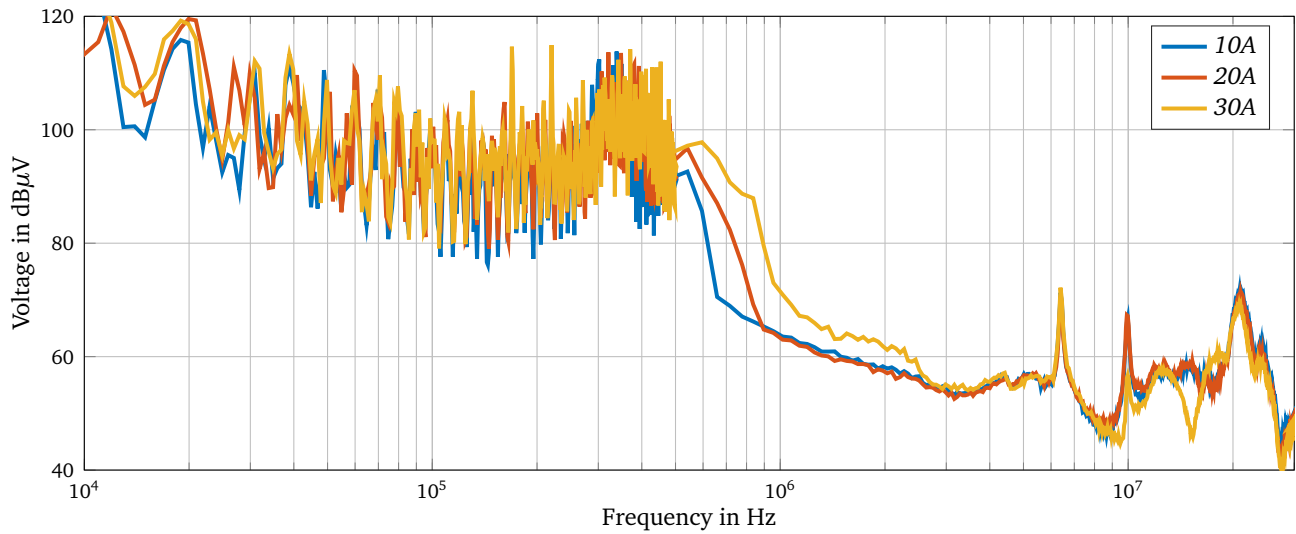
6.1.4 Load Current

Load current effects a disturbances level quite specifically. With increasing of load current high frequency disturbances (above 3 MHz) remain without any significant changes. Furthermore, some unexpected mitigation (rather insignificant) is observed in the range 9 MHz–16 MHz, when higher RMS current (30 A) is fed into the power grid. Reasons of observed spectrum variation cannot be explained with 100% confidence. This effect might be related to variation of some parasitic components due to change of load current. The next probable reason for this phenomena is associated with semiconductor effects e.g. reduction of IGBTs tail current after turning off. Unambiguous conclusions about the reasons for these effects is not possible based on the information received from the experiments.

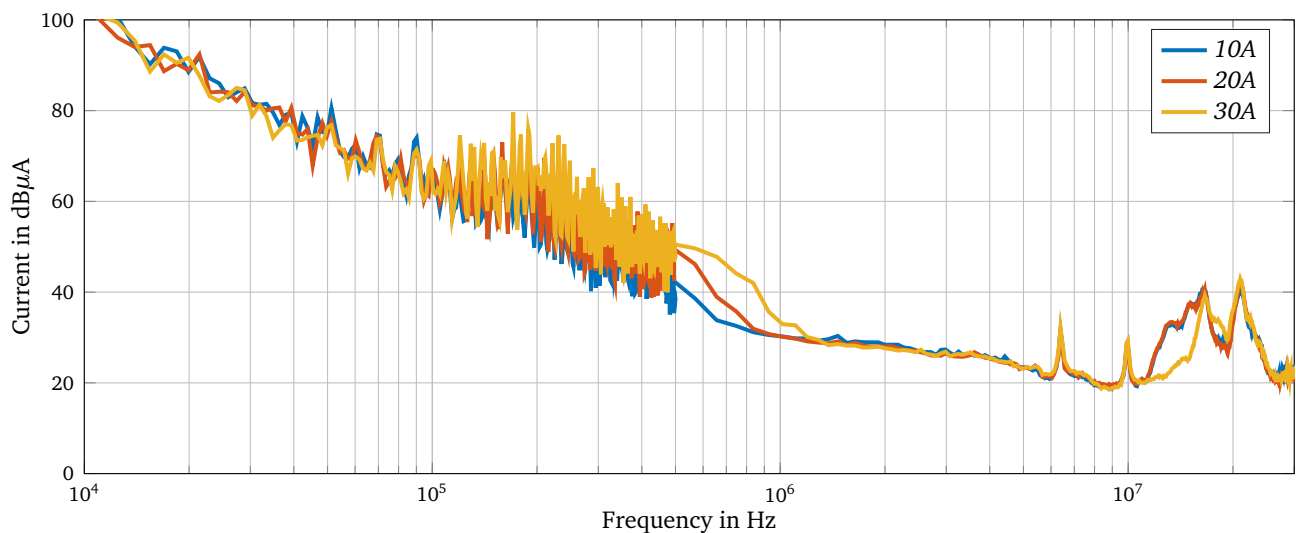
Increasing of the load current causes quite feasible growth of disturbances (up to 15 dBμV) in the specific span between 300 kHz and 2.5 MHz (Figure 6.7a). This span matches with the beginning of the EMI range (150 kHz–30 MHz) and therefore the effects provoked by load current are highly relevant. Unfortunately, specialized techniques for IL improvement of an EMI filter in this range do not currently exist. The only options are rising the number of stages or employing bigger components. Both options negatively affect power density and costs. Experiments show that nominal and overload operation modes of an AIC are the most critical from an EMI point of view and require some particular attention during emission and susceptibility tests. The main conclusion drawn from the experiment with a load current variation is that the worst case scenario in terms of EMC corresponds to a situation when an AIC operates under the maximum load.

Also common mode current increases in the range between 200 kHz and 1.3 MHz under higher load current conditions (Figure 6.7b). In general, a spectrum of common mode current for all three experiments repeats the voltage spectrum depicted in Figure 6.7a. The only exception is two resonances in a voltage spectrum at 450 kHz and 550 kHz caused by DM impedance of a line inductor. It ones again

proves that CM disturbances contribute to the EMI spectrum not only in the high frequency range, but also at lower frequencies [158].



(a) LISN voltage.



(b) Common mode current.

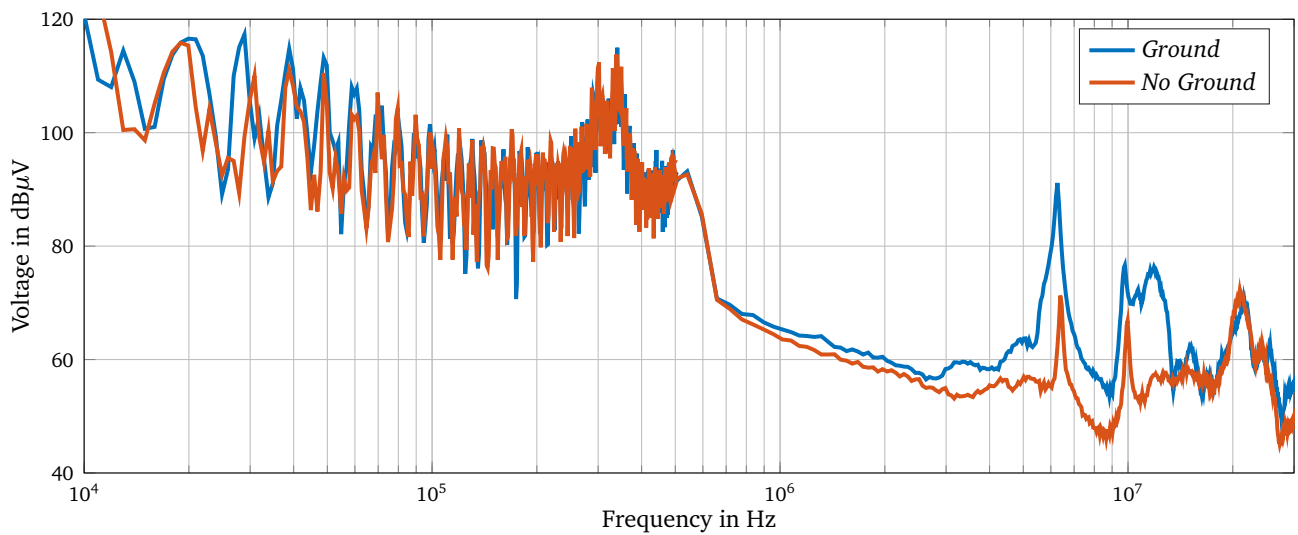
Figure 6.7.: Spectra of the self-made AIC measured under different load conditions.

6.1.5 Connection of Protective Earthing Conductor

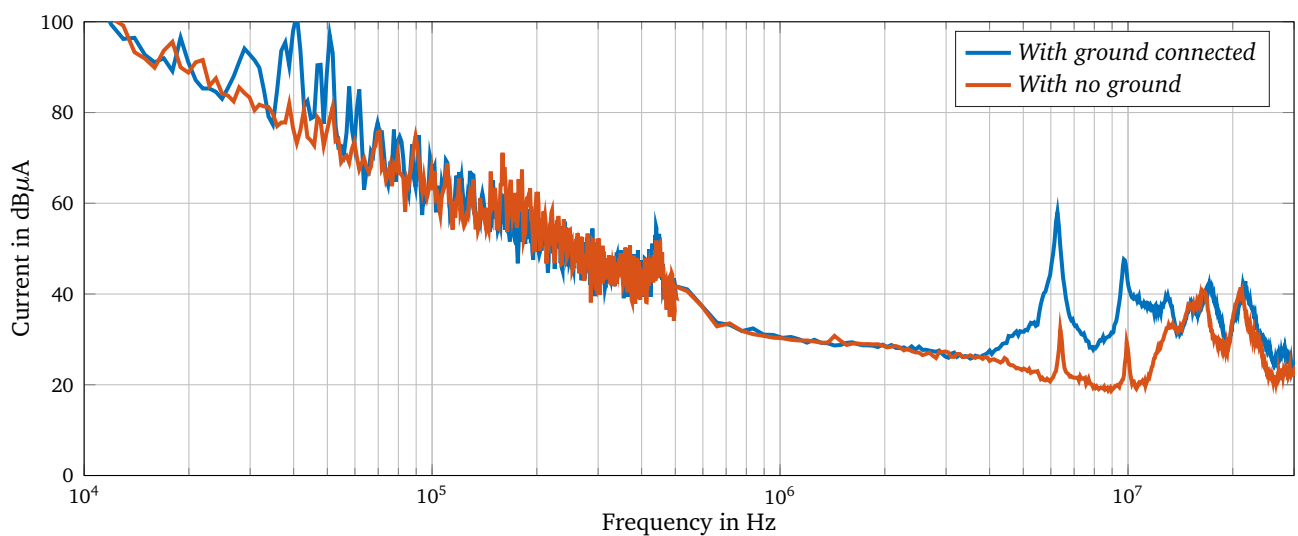
The self-made AIC is designed with a feature which allows complete separating the ground potential of a converter from the global protective earthing. Certainly, this scenario is unrealistic for real application, but it clearly demonstrates the contribution of stray capacitors within a PE system on the emitted EMI spectrum. Starting at 700 kHz the level of disturbances emitted by the AIC with no protective earthing connection diminishes considerably. A resonance peak at the 6.3 MHz is 20 dB μ V lower than the same resonance with a connected protective earthing conductor (Figure 6.8a). This resonance appears between a sum of stray capacitors within a system and stray inductance of the CM path. With no earthing

conductor stray capacity of the AIC is eliminated the resonance is shifted towards higher frequencies and mitigated.

Such improvement is mainly caused by decrease of the CM current flowing into the mains since the current path through the stray capacitors of an AIC is eliminated. However, above 15 MHz only minor changed of the CM current remains if a protective earthing connector is removed. Beginning from ≈ 15 MHz other parasitics within a drive system such as cable and choke stray capacitances, cable stray inductance etc. have the main influence on CM impedance. Contribution of CM disturbances caused by stray capacitance of an AIC into the overall spectrum is easy to assess based on comparison between combined DM and CM voltage spectra (Figure 6.8a) and CM current spectra (Figure 6.8b). CM current generated by AICs stray capacitance has the major contribution in the range starting from ≈ 3 MHz up to 15 MHz.



(a) LISN voltage.



(b) Common mode current.

Figure 6.8.: Spectra of the self-made AIC connected to the global protective earthing conductor and floating.

Though PE converters must be grounded due to the safety restrictions, described above option can theoretically be used for devices placed into non conductive housing. The size of various stray capacitors (Figure 1.9) can be decreased through increasing the distance between conductive and grounded surfaces. In this way a common mode current path can be partially eliminated. It demonstrates one more option to improve EMI behaviour at the system level without employment of EMI filters with higher IL.

As an alternative to manipulation with protective earthing conductor, an additional ground wire for free flow of CM current within a drive system can be implemented. For example three phases on the grid side and three phases on the motor side can be connected to this alternative ground connector via capacitors. This concept supposes short-circuit of the CM disturbances source (semiconductors) inside of the drive system. A general drawing of this concept is depicted in Figure 6.9. It can be assisted with various arrangements of CMC chokes on the load or grid sides. Additional connection of capacitors on the DC side to the alternative ground can also be used.

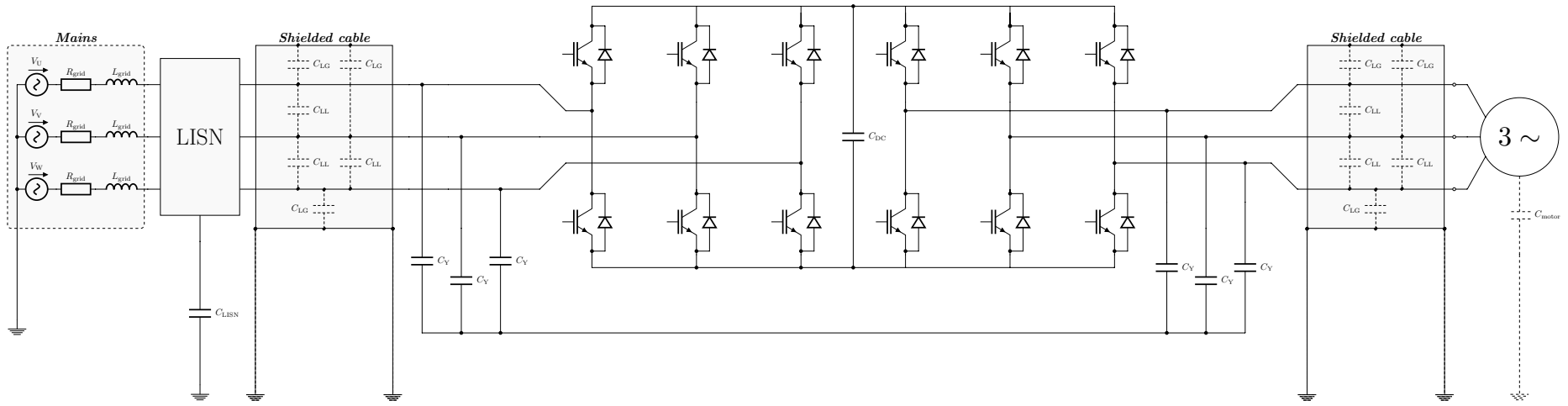


Figure 6.9.: Combined EMI filtering concept on the system level.

6.1.6 Line Inductor

Previously analysed parameters mainly affect CM disturbances. In they turn DM disturbances are mainly defined by impedance of a line inductor. Spectrum emitted by an AIC with no EMI filter connected is defined by a utilized line inductor in the range up to several megahertz. The inductor used in the experiments represents a combination of several compounded chokes connected in series, this allows adjustment of total inductance. Frequency dependent impedance measured for a single line inductor is shown in Figure 6.10. A self-resonance caused by EPC and characteristics of a ferromagnetic core is observed at 700 kHz. In addition, the inductor impedance has noticeable tolerance. In order to achieve specified inductance four series-connected inductors per phase are employed. Due to some deviation from nominal value of the components used, impedance of the serially connected inductors is rather non linear (Figure 6.10).

Impedance of the line inductor is entirely reflected in the AIC spectrum at the low frequency. The minimum of inductor impedance at around 340 kHz (Figure 6.10 red curve) corresponds to the maximum amplitude of disturbances measured at the LISN output, which is shown in Figure 6.8. The peak of impedance at the 700 kHz red curve in (Figure 6.10) corresponds to the minimum in the spectrum at the same frequency (Figure 6.8), showing that low frequency disturbances can be affected by variation of line inductor parameters. Effects caused by stray components of the drive system and semiconductors become dominant starting at ≈ 2 MHz. After several megahertz disturbances are predominately caused by common mode current within a system. A line inductor has no effect on the CM currents by definition.

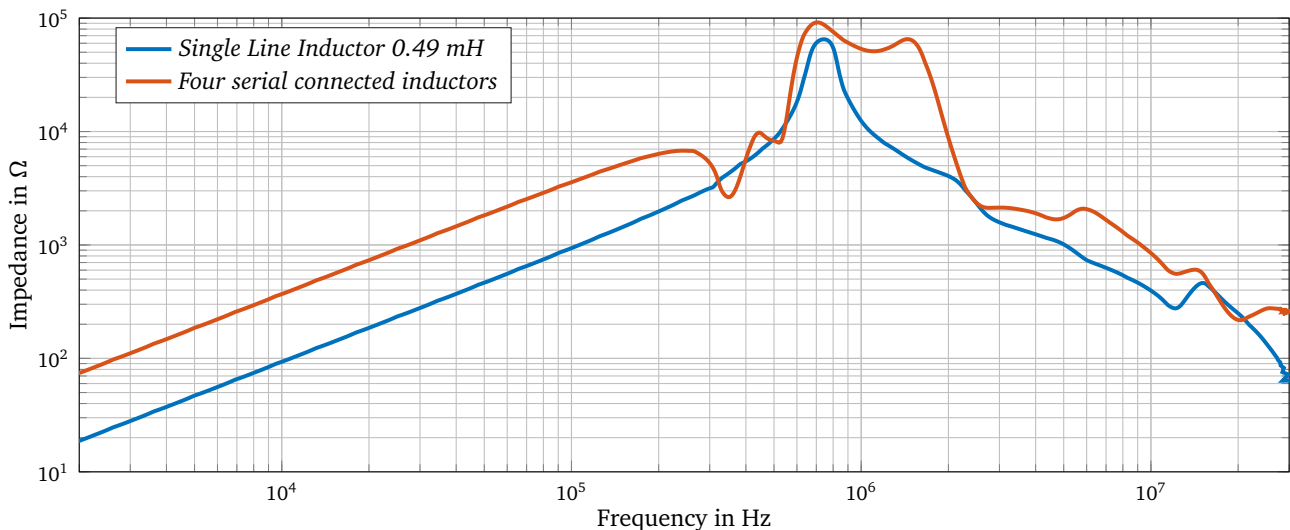


Figure 6.10.: Impedance of a single line inductor and four line inductors in serial.

The experiments conducted in this subchapter with a variation of AIC parameters are summarised in Table 6.1. The effects achieved by variation of those parameters are assessed qualitatively for frequencies, listed in the last column of Table 6.1. Other frequencies not shown in the table are only slightish affected.

<i>Parameter of AIC</i>	<i>Effect on spectrum*</i>	<i>Frequency range affected</i>
PWM frequency	middle ≈ 5 dB, (low 2 dB)	150 kHz - 6 MHz (above 6 MHz)
Dead time	high ≈ 10 dB	above 7 MHz
Variation of DC voltage	very low < 1 dB	whole EMI range
Load current	high ≈ 15 dB	300 kHz - 2.5 MHz
Protective earthing connection	very high 20 dB	above 700 kHz
Line inductor	causes resonances in spectrum	only DM 5 kHz - ≈ 2 MHz

* very low, low, middle, high, very high

Table 6.1.: Summary of analysed AIC parameters influencing the EMI disturbances level.

6.1.7 Damping Capabilities of Grid Side EMI Filters

Previously conducted analysis shows that the most critical frequency ranges which define a topology of an EMI filter are 150 kHz–500 kHz and 3 MHz–8 MHz. The first range defines the size of main passive components. IL of a filter in this range can be easily improved by increasing capacitance and inductance of the main components. Improvement of IL in the second range is more sophisticated since disturbances are mainly caused by CM currents within the whole system. Filters with different arrangements of components affect CM impedance of the system differently. The first element of an EMI filter located after a PE converter contributes to redistribution of CM current extremely. Since the primary path of CM current including Y-capacitors of an EMI filter can either employ a high impedance component or not. It means that from this perspective topologies of EMI filters can be divided into two groups: topologies with a CMC included before a PE converter and with a group of Y-capacitors located before a PE converter.

Three conventional filters representing different topologies are used for determination of the most effective component arrangements. Equivalent circuits of those EMI filters are shown in Appendix K. Filter 1 is based on a Π -topology for both CM and DM filters (Figure K.1). Filter 2 consists of a Γ -topology based CM filter and a $CLCLC$ -topology based DM filter (Figure K.2). Filter 3 represents a T -topology filter for CM and a $CLCL$ -topology for DM disturbances (Figure K.3). The aforementioned filters are assessed in combination with a self-made AIC and a conventional AFE converter in order to evaluate the efficiency of every topology. In addition conventional filters with improved HF properties are tested.

Spectra emitted by the self-made AIC are measured with each filter with default parameters of the AIC (parameters are listed previously). Results of measurements at the LISN output are shown in Figure 6.11 and Figure 6.12. It is clearly seen that both filters (Topology 1 and 2) with Y-capacitors connected directly after an AIC demonstrate rather good results in the range up to 5 MHz. However, the main resonance of the system remains above the limits since CM current continues to flow relative freely through stray capacitances of the system and Y-capacitors. Except for the resonance at 6.3 MHz which definitely exceeds the CISPR22 class "A" limit, the entire spectrum remains below the limit for filters 1 and 2. In order to mitigate this resonance at least a small CMC between an AIC and the Y-capacitors is required.

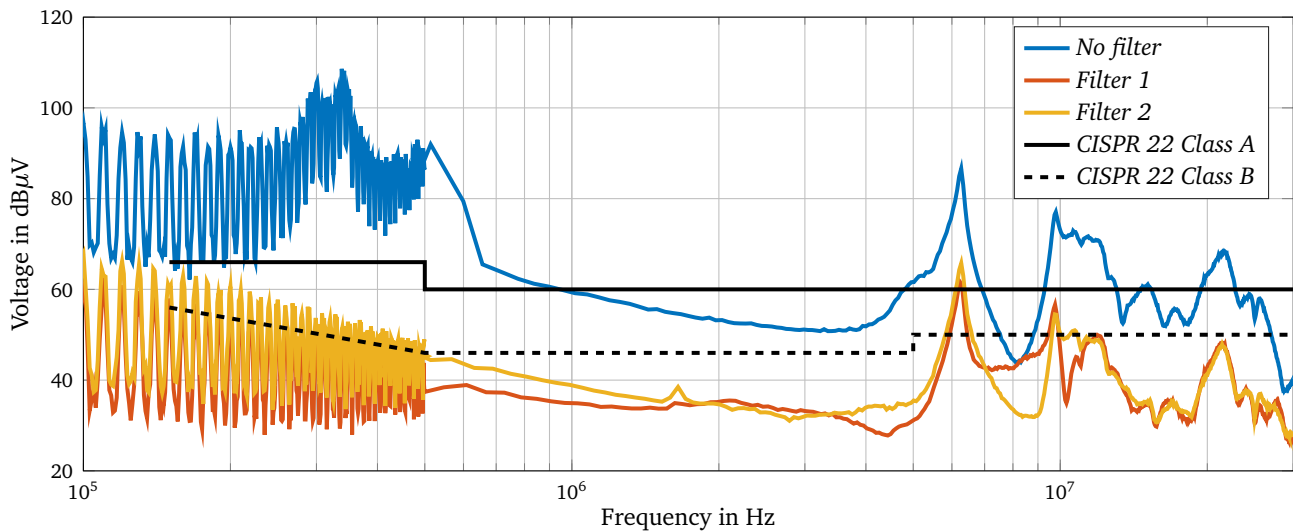


Figure 6.11.: Spectra of a self-made AIC with conventional EMI filters based on Y-capacitors connected directly after AIC and no EMI filter.

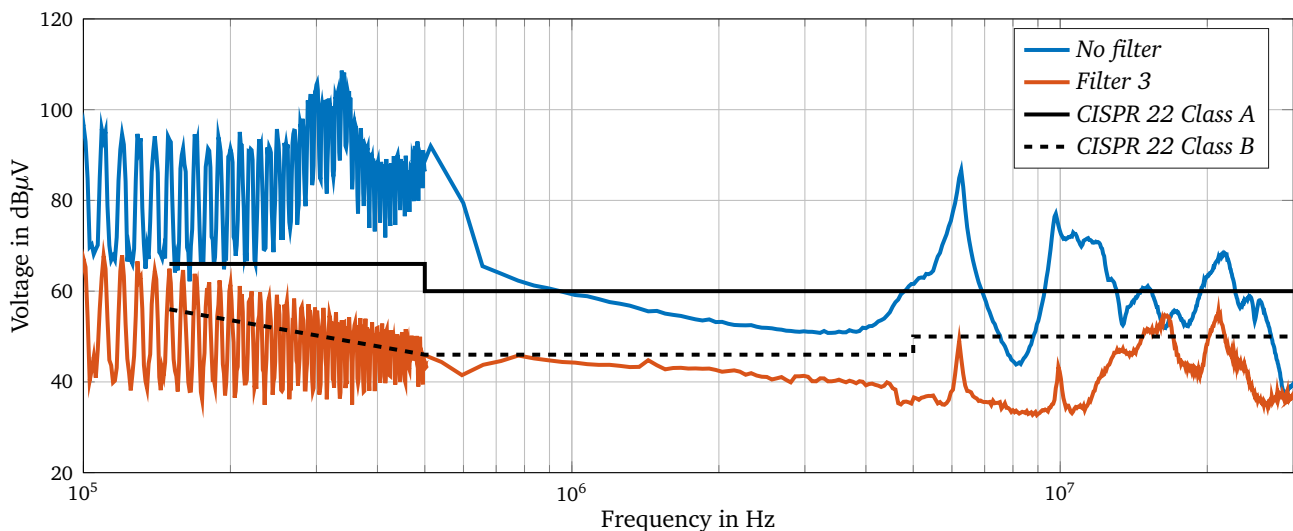


Figure 6.12.: Spectra emitted by a self-made AIC without EMI filter and with a conventional EMI filter including a CMC directly on the input of AIC.

It is important to mention that resonances caused by a line inductor are not observed in a spectrum after the connection of a filter. Therefore an EMI filter defines both DM and CM impedance of the PE converter.

With a filter based on the topology 3, the most critical resonance at 6.3 MHz is almost eliminated by high-impedance components presented on the path of CM current. The self-made AIC assisted with this filter can comply with CISPR22 class "A". Performance of the topology 3 at frequencies above 12 MHz can be further improved utilizing presented in Chapter 5 and Chapter 4 methodologies. However, bigger main components must be used because in the beginning of the EMI range class "B" limits are exceeded.

Performance of the same EMI filters is evaluated together with a conventional AFE. The spectrum of the AFE with no filter connected is evaluated and used as a reference. By default the AFE is equipped with a stock EMI filter with an unknown topology. It includes huge Y-capacitors, so that the leakage

current is extremely high. With the stock EMI filter the AFE converter cannot be used in a combination with an RCD. Nevertheless, a spectrum emitted by the AFE equipped with the standard filter is also used as a reference for further comparisons. Results achieved by the standard filter at 150 kHz are comparable with the other studied filter topologies. IL at this frequency has been used as a design criteria for the stock filter. Therefore a high value of Y-capacitors has been selected. With the stock filter the AFE converter emits disturbances which do not exceed CISPR22 class "A". Although, the class "B" limit is exceeded in the low frequency range and at frequencies close to 4.5 MHz, as demonstrated in Figure 6.13. In frame of the conducted experiments, each of the filters depicted in Appendix K is connected to the AFE converter. Spectra of the AFE converter with different filters employed is depicted in Figure 6.14. Topologies 1 and 3 demonstrate considerably better performance by default, so that for this particular combination no high frequency IL improvement needed. Absence of a sharp resonance in the vicinity of 6.3 MHz (as for the AIC) lowers the requirement for HF IL. As a result, limits of CISPR22 class "A" can be more easily fulfilled. Results obtained with the topology 2 are worse than with a default filter.

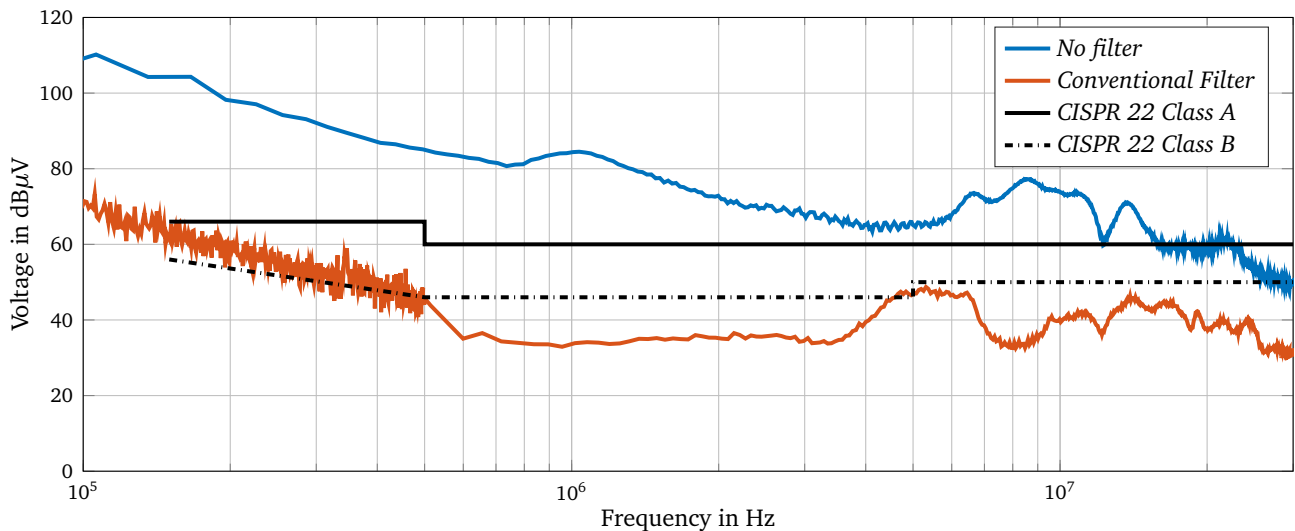


Figure 6.13.: Spectra emitted by a conventional AFE from without EMI filters and with a standard EMI filter.

Conducted experiments show that topology with a CMC included on the way of CM current is more effective for both utilized converters. In order to improve IL of the topology 2 HF capacitors (4.4 nF per phase) are connected (Figure K.4). The main focus is the high frequency IL, since it is aimed to investigate efficiency of the methods discussed in Chapter 5. As Figure 6.15 shows, disturbance emitted in the range 3 MHz–7 MHz with the enhanced filter is 10 dB μ V lower than for a filter without any improvement. Obtained results confirm the effectiveness of previously discussed filter improvement methods on the system level.

It must be mentioned that heating and saturation issues are not considered with a required exactness. The risk of facing these problems is quite high especially if some improvement measures are used.

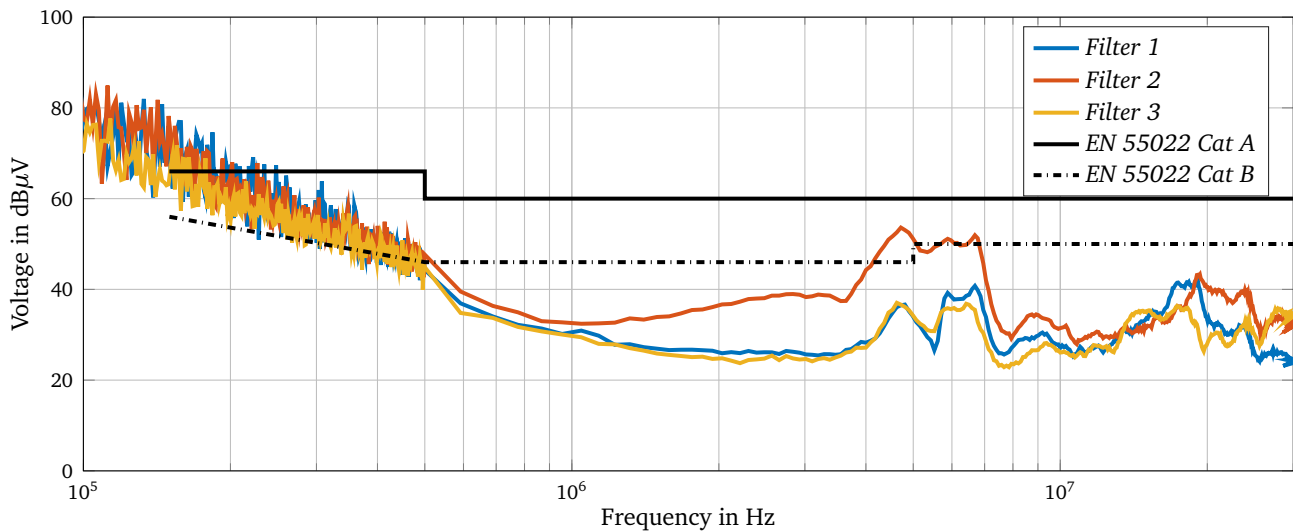


Figure 6.14.: Spectra emitted by a conventional AFE with different EMI filter connected.

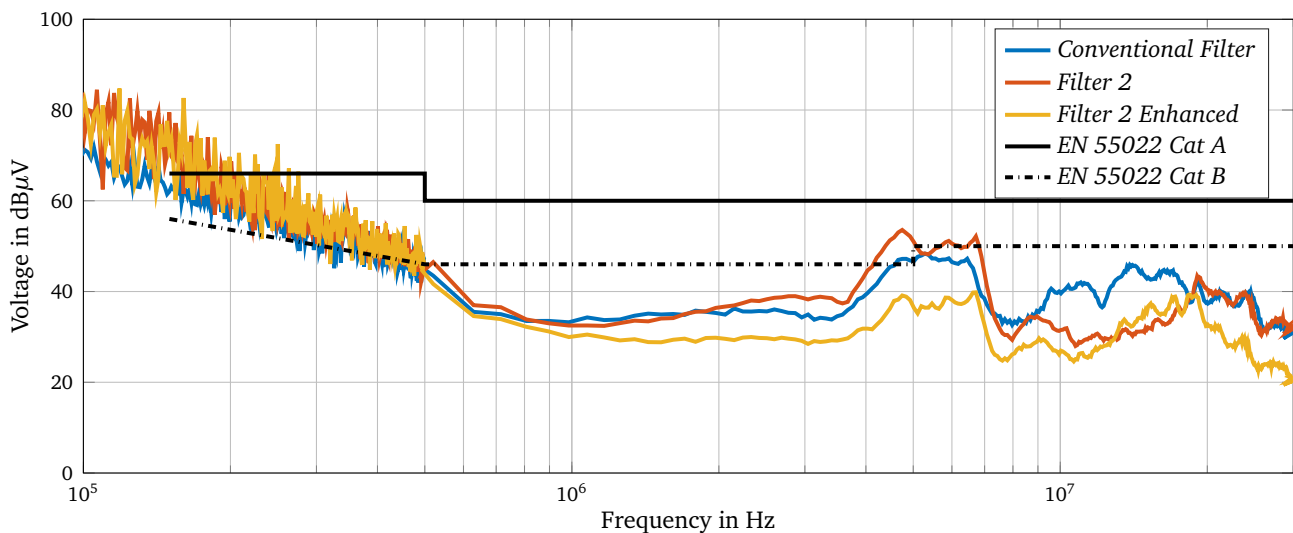


Figure 6.15.: Spectra emitted by a conventional AFE with enhanced EMI filter connected.

6.2 Investigation of the Motor and Inverter Parameters Focused on the EMI

As it has been mentioned previously, physical parameters of the motor and motor side inverter require a separate study. The most important inverter and motor parameters from the EMC point of view are examined. Since a motor side is not the main scope of this thesis, only the most relevant parameters are evaluated. More detailed EMC oriented investigation of the motor side inverter parameters is related to the possible activities which can complement this work.

6.2.1 Motor Stray Capacitance

The most important parameter which influences distribution of CM current within a drive system is motor and cable stray capacitance. It depends on internal construction of the motor, basically on the surface between windings and housing. Three experiments are conducted in order to show the effect on

the EMI spectrum caused by stray capacitance of a motor. A special equivalent load with a possibility to adjust stray capacitance according to real motor values is used. For this test an inverter with a load is connected to a DC power supply. In order to decouple a DC power supply from an inverter a conventional Π -topology based EMI filter is used. Two DC LISNs are used in order to fulfil standard requirements for a measurements setup. The block diagram of the setup used for this experiment is shown in Figure 6.16.

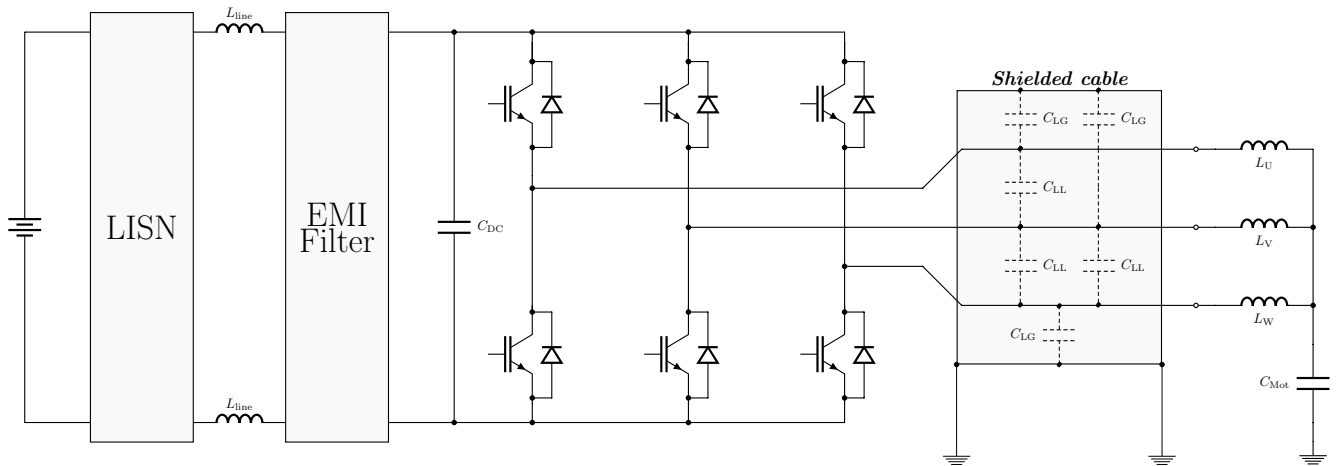


Figure 6.16.: Diagram of the test setup with a motor load.

Emitted disturbances are measured for cases with 16 nF, 24 nF and 32 nF of motor capacitance. All other parameters of the setup remain without changes (the EMI filter stays the same). The results of the measurements carried out at the EMI port of +DC LISN are shown in Figure 6.17. The most critical peak is located in the range between 1.5 MHz and 2.3 MHz (depending on the motor stray capacitance). This resonance is formed by five components, such as stray capacitance of the inverter C_{InvOut} and C_{InvIn} , inductance of the motor cables and windings L_{CabMot} , total stray capacitance on the motor side C_{CabMot} , inductance of the protective ground connectors L_{PE} . An equivalent circuit of equivalent CM paths is depicted in Figure 6.18. With increase of the motor stray capacitance this peak is shifted to the lower frequency and increases in amplitude (Figure 6.17).

It is worth of mentioning that increase of the stray capacitance of a motor cable has similar effects to motor capacitance on the EMC spectrum. It creates one more way for CM current flow on the load side. When considering an equivalent circuit of the drive system, it becomes clear that motor cable stray capacitance is connected in parallel with motor capacitance. Increase of cable capacitance shifts the main system resonance towards lower frequency. It increases proportionally with the length of a cable. Because of this, reason the length of motor cables must be kept as short as possible. In the case when the length of cables is increased after EMC compliance tests, there is a chance that the system might not fulfil the requirements. Therefore, EMC compliance tests have to be repeated with correspondent cables.

6.2.2 PWM Frequency

Similar to experiments carried out with an AIC, a spectra emitted by a motor inverter is measured under diverse PWM frequencies. The PWM frequency is one of the main parameters of a PE converter which influence an EMI spectrum. It might be helpful for designers to know how variation of the PWM

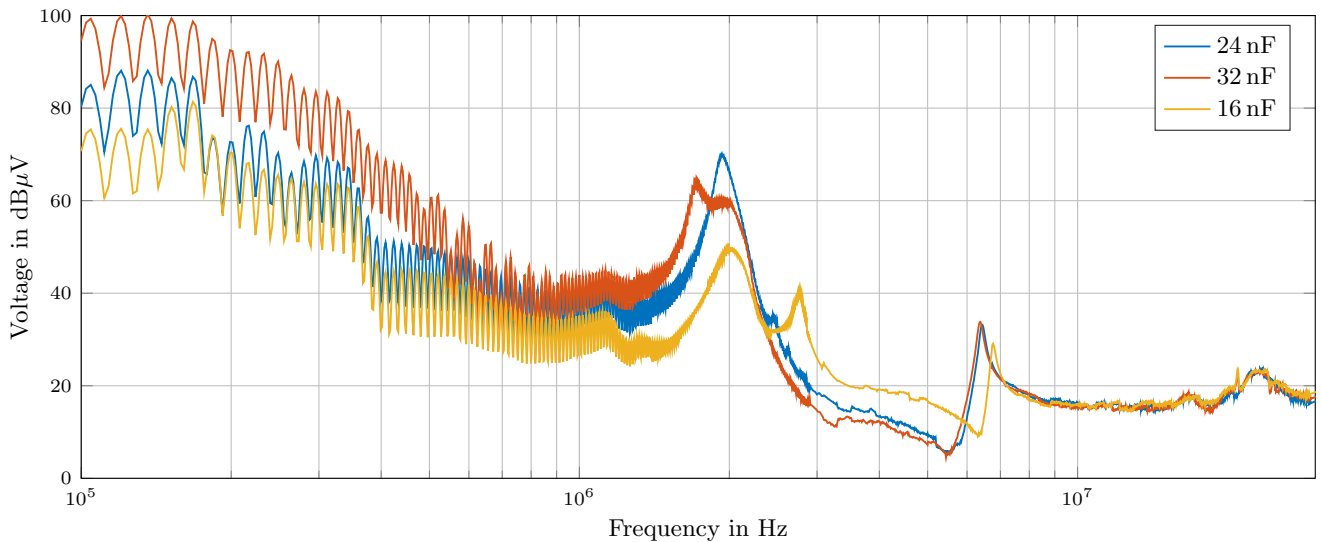


Figure 6.17.: Spectra emitted by an inverter on the DC side with diverse stray capacitance.

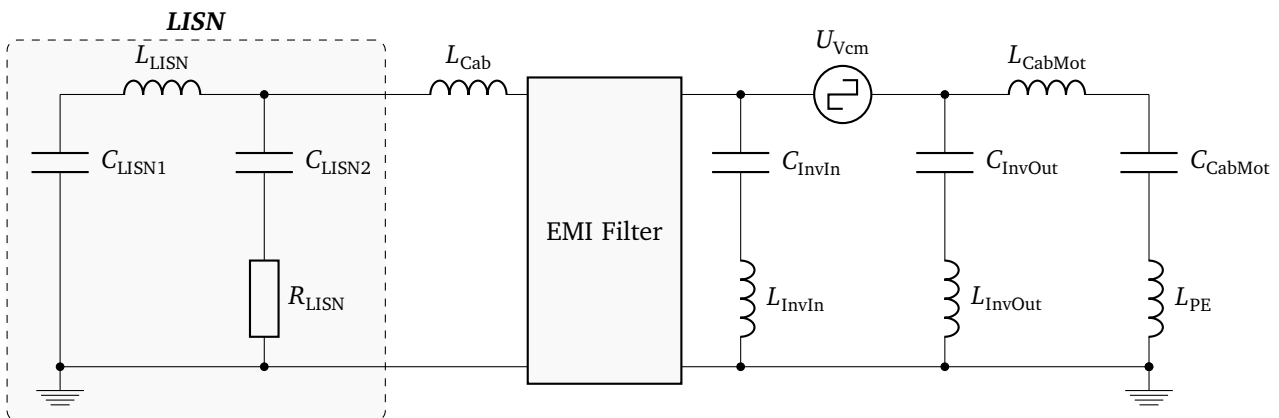


Figure 6.18.: CM equivalent circuit of the test setup with a motor load.

frequency influences a spectrum, so that during the system design procedure the optimal solution for power density can be found. Influence of the PWM frequency on the EMI spectrum emitted by the motor side inverter is depicted in Figure 6.19 for 4 kHz, 10 kHz and 12 kHz. From two conducted experiments (with an AIC and a motor side inverter) it can be concluded that with increase of the PWM frequency by 1 kHz a spectrum is elevated up by roughly by 1 dB μ V. It is independent of a PE converter function (grid side or load side). In consequence, for the critical situations decreasing of the PWM frequency can be used as a measure for improving an EMI spectrum. Obviously, in this case several negative effects on the system level such as a torque ripple or aging of a DC capacitor are observed.

6.2.3 Load Current

In contrast with experiments conducted with the load current of an AIC, the impact of the load current on a motor inverter is opposite. With increase of the load current the emission level of an inverter decreases. This can be explained by variation of a modulation index during operation. The width of voltage impulses changes according to a required amplitude of phase current. During an operation

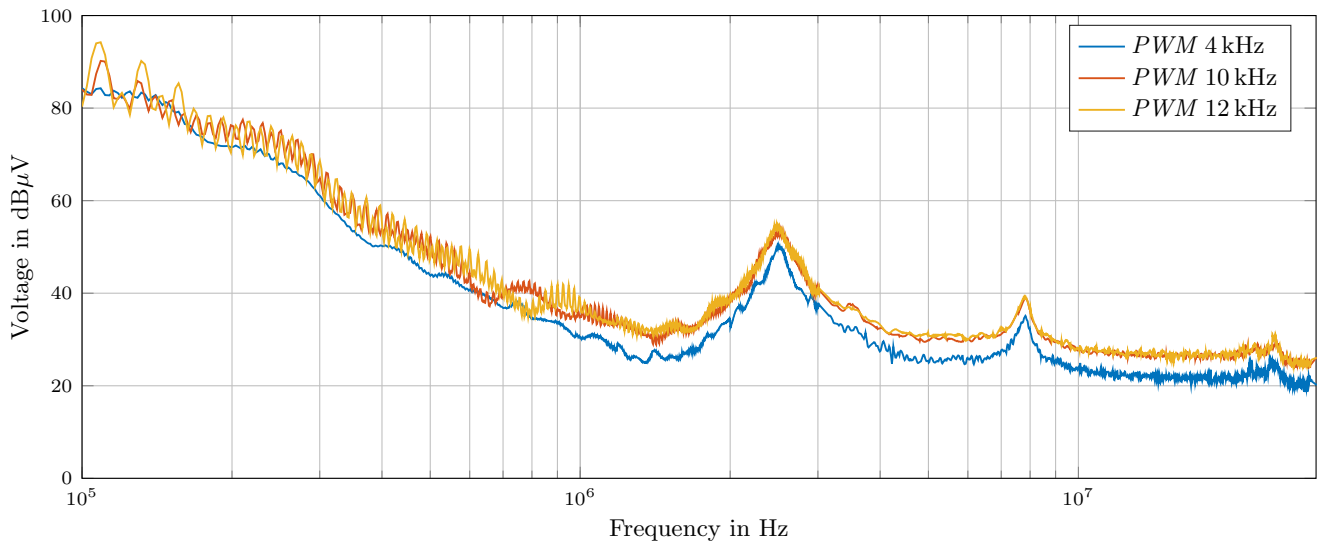


Figure 6.19.: Spectra of an inverter measured under different PWM frequencies.

mode when a current flow to the load is equal to 0 all half bridges switch equally between two zero vectors. With increase of the phase current a portion of the zero vectors diminish. It decreases the number of PWM pulses when the full amplitude of DC-link voltage is applied between a star point of a motor and the ground. Therefore, increasing of the load current leads to reduction of CM current which flows via motor stray capacity at the low frequency. Nevertheless in the frequency range above 4 MHz DM effects caused by switching slopes of semiconductors begin to dominate. This phenomenon causes the resonance at 7.8 MHz when load current 100 A or 200 A is applied.

Results of tests with a motor inverter are shown in Figure 6.20. Measurement with load current 0 A, 100 A and 200 A are conducted. Results confirm previously made assumptions. The worst case scenario corresponds to the standby mode with 0 A current. Because of this reason, assessment of the EMI performance of a motor inverter must be conducted in standby mode, with switching transistors but no current flowing. The difference between 100 A and 200 A scenarios is rather insignificant. It is explained by the fact that the portion of zero vectors decreases relatively quickly with increase of the phase current.

6.2.4 Switching Speed of Semiconductors

In order to show how semiconductors can influence the level of emitted disturbances two types of IGBTs are utilized. The following behaviour is demonstrated by IGBTs during tests. The first IGBT type has the slope of collector current rise during a turn on 8 A/ns and the fall of collector emitter voltage is 4 V/ns. The second type of an IGBT turns on with collector rise current slope 15 A/ns and voltage fall is 5 V/ns.

Typically EMI filters exhibit the highest IL in the range 1–5 MHz. It matches with the frequency where switching time of semiconductors has the maximum impact on the spectrum. In this case disturbances are strongly mitigated by an EMI filter and effects of semiconductors are barely seen, when an EMI filter is connected to the system. Therefore for demonstration of switching time caused effects on the spectrum, measurements are conducted without any EMI filters.

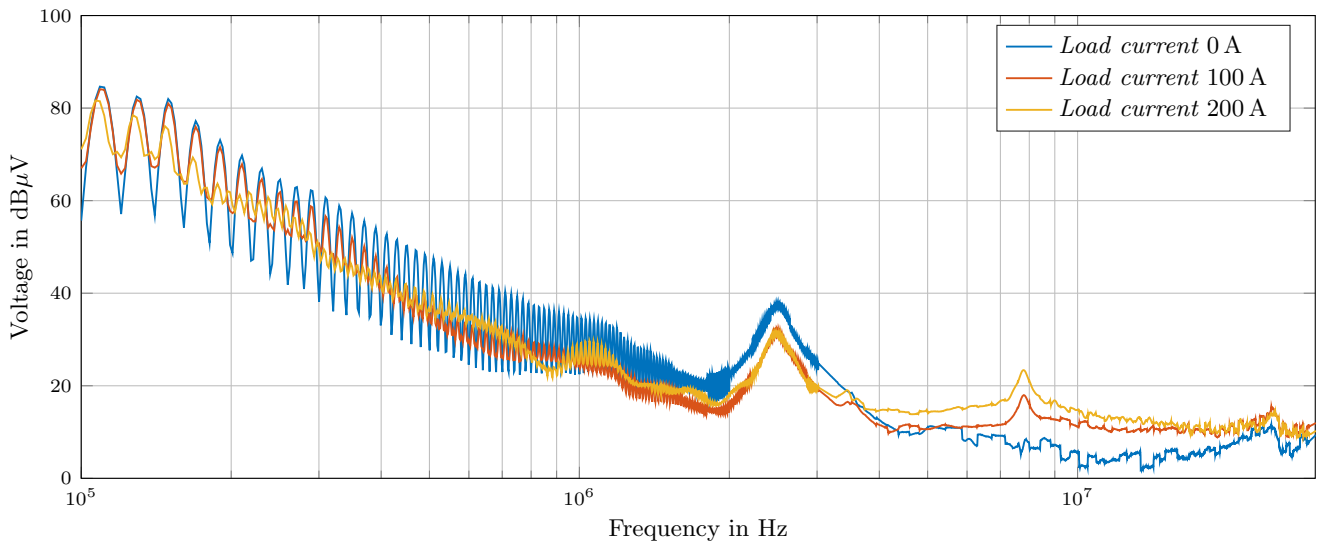


Figure 6.20.: Spectra measured under different load currents.

A relatively modest variation of switching time (For VDC 600 V switching time is 150 ns of the first IGBT type and 120 ns of the second one) has significant influence on the produced disturbances level after 2 MHz. For investigated semiconductors an EMI spectrum is raised by approximately 12 dB μ V in the range 2–8 MHz, if faster switches are used (Figure 6.21). It is quite important to stress that the frequency of the resonances around 5–7 MHz does not change with variation of switching time. This means that by reducing switching speed, the disturbance level in this range can be lowered; but it does not mitigate disturbances at the other frequencies.

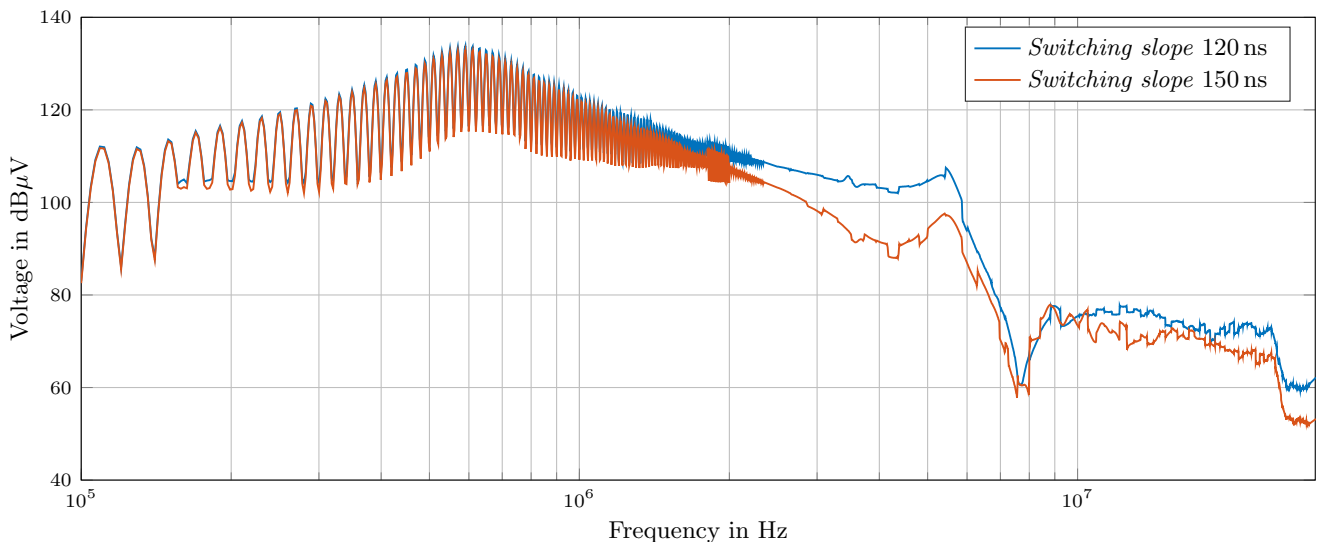


Figure 6.21.: Spectra of an inverter measured for two types of switches with 150 ns and 120 ns switching time.

In contrast to decreasing of the PWM frequency, when power loss of semiconductors are reduced, deceleration of semiconductors has some negative influence on the power loss of semiconductors. However, the EMC oriented system design with consideration of power loss would allow achieving of optimal performance, adjusting both PWM frequency and speed of semiconductor switching. Normally, stray

capacity of a motor as well as nominal current are specified during design of a PE unit and cannot be changed.

In applications where high power density is required, the size of the EMI filter begins to play an even more important role than other components of construction e.g. a heatsink or DC-capacitors. Therefore, in terms of power density a combination of EMC oriented design together with consideration of power losses in semiconductors can be rather beneficial. Development of the mathematical models for such combined EMC and thermal design should allow design of the PE devices with considerably higher power density by variation of PWM frequency and switching speed.

6.2.5 Protective Earthing Conductor Impact

Isolation of the inverter from the ground does not bring any improvement concerning emitted disturbances. This is because CM current, which mainly causes these disturbances, can freely flow through motor stray capacitance. However, CM current can be affected by the connection of a resistor between an inverter and the ground instead of a simple conductor. Unfortunately neither the first nor the second option are applicable because of safety requirements. For some applications where connection of an inverter housing to the protective ground is not prescribed by safety standards, the last option with a resistor can be applied. In this case the main resonance between the motor stray capacitance and a LISN can be reduced by $\approx 15 \text{ dB}\mu\text{V}$. Results of measurements with an inverter connected to the protective earthing, disconnected with the protective earthing and with a series resistor are demonstrated in Figure 6.22.

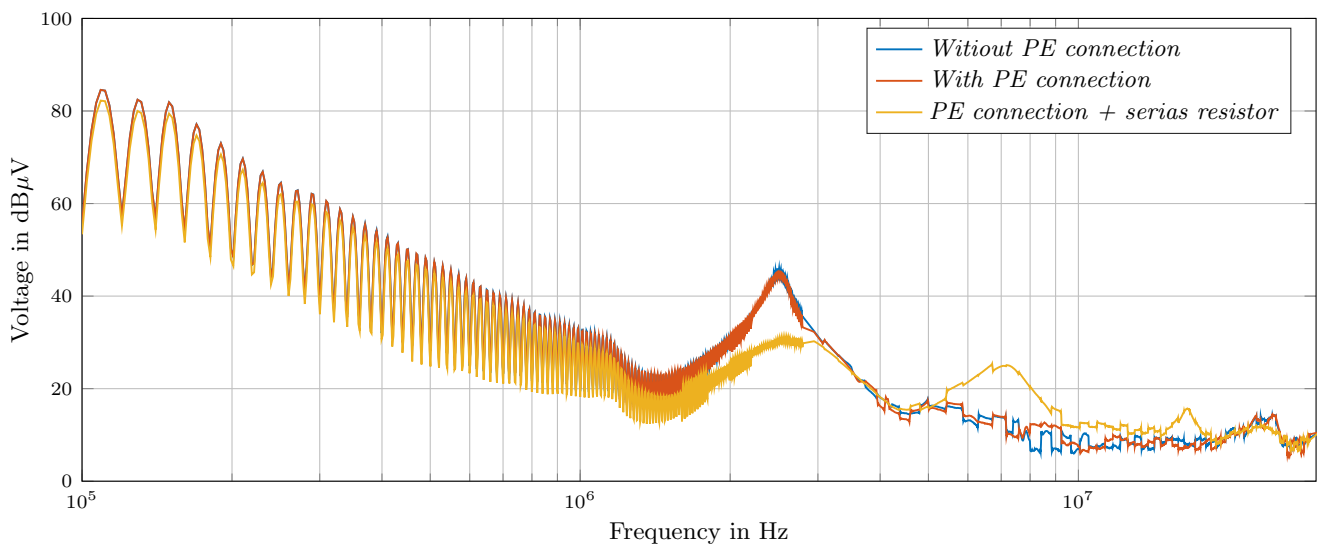


Figure 6.22.: Impact of the protective ground connection on EMI spectrum emitted by an inverter.

The experiments conducted in this subchapter with included quantitative assessment of effects caused by inverter parameters are summarised in Table 6.2. Conducted studies of diverse parameters of PE converters demonstrate additional ways to influence an EMI level emitted by a PE device. For more detailed investigation of the most important parameters in frame of the complete drive system (rectifier, inverter, motor and load) a specialized EMC oriented test bench is needed. Investigation of the complete drive system represents a particular interest for figuring out paths for CM current within a drive system.

Building this kind of a test bench up is quite complicated and exceeds the scope of this thesis. It would be one of the activities that could supplement current work.

<i>Parameter of inverter</i>	<i>Effect on spectrum*</i>	<i>Frequency range affected</i>
Motor stray capacitance	very high 30 dB	100 kHz - 5 MHz
PWM frequency	high ≈ 7 dB, (low 4 dB)	600 kHz - 16 MHz (above 16 MHz)
Load current	high ≈ 10 dB	350 kHz - 4 MHz
Switching speed of semiconductors	very high ≈ 12 dB	2 MHz - 8 MHz
Protective earthing connection	high ≈ 15 dB	1.5 MHz - 5 MHz (depends on the main resonance frequency)

very low, low, middle, high, very high

Table 6.2.: Summary of analysed motor inverter parameters influencing an EMI disturbances level.

6.2.6 Damping Capabilities of DC Side EMI Filters

Selection of a CM EMI filter topology is mainly influenced by the total stray capacitance of the motor, inverter and cable. As it is demonstrated in Figure 6.17 the total stray capacitance causes a resonance in the range between 1.5 MHz and 2.3 MHz. This resonance is used as one of the main filter design criteria. Nevertheless, not all EMI filter topologies can be used for mitigation of this resonance. Common mode current paths which are affected by installation of an EMI filter must be analysed in order to understand reasons for the diverse effects of EMI filter topologies.

Most importantly, the positioning of Y-capacitors directly influences saturation and heating effects of a CMC, since Y-capacitors redistribute CM current within a drive system. If a CMC is placed between stray capacitors on the load side and the first group of Y-capacitors (for example *T*- or *LCLCL*-topologies) high impedance along the CM current path is introduced. As a result the main resonance is well mitigated. The side effect of this arrangement is that the CMC has to sustain the maximum CM current in the drive system. In this case dimensions of the CMC are the largest compared with other arrangements under similar system conditions. Otherwise, Y-capacitors of an EMI filter can be located straight after a PE converter (for example Π - or *LCLC*-topologies). Then a CM path is closed via stray capacitance on the load side and Y-capacitors of an EMI filter, without any additional high impedance components in between. Obviously, under these terms the main resonance is barely mitigated, although an EMI filter is installed. Undoubtedly, CM current load of a CMC is lower for this components arrangement.

Figure 6.23 demonstrates effects of three EMI filter topologies where the first stage of Y-capacitors is located directly after a PE converter. For all used EMI filters Y-capacitance is equally distributed between two capacitor groups. Beside this, topology 1 includes only one CMC with 0.5 mH, topology 2 includes two CMCs; the main CMC is 0.36 mH and an axillary CMC is 0.06 mH. Topology 3 includes the main CMC 0.21 mH and axillary CMC 0.15 mH. Any of the investigated filters cannot really mitigate the main resonance properly. Consequently filter topologies including a group of Y-capacitors next to a

PE converter are not effective for damping of the main system resonance, since they do not affect a CM current path through the total motor-converter-cable capacitance.

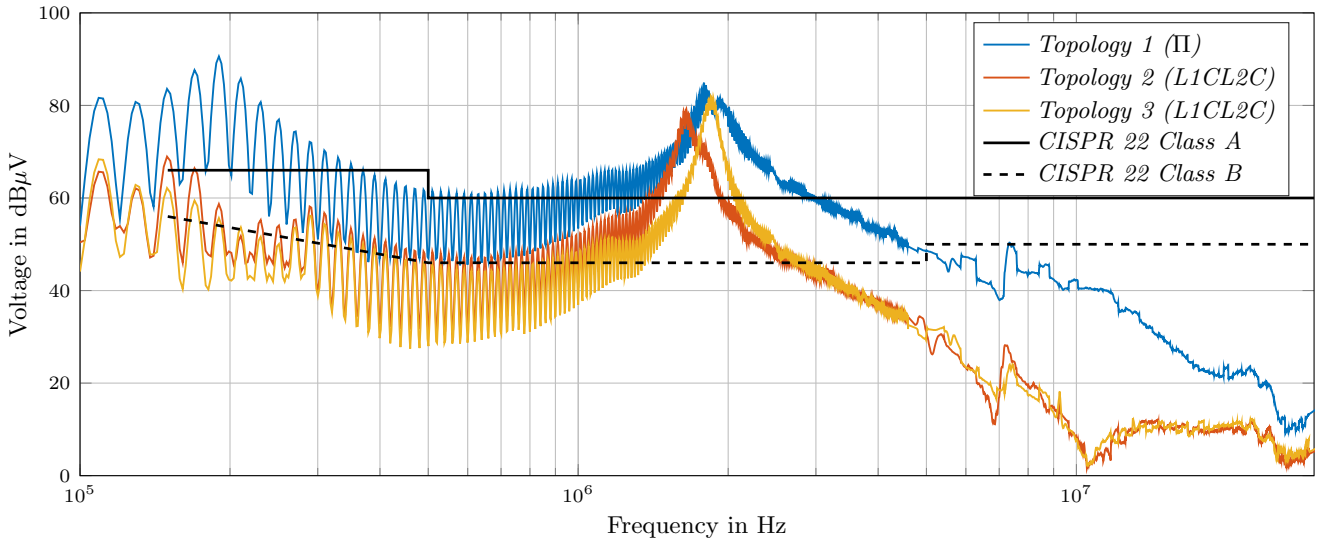


Figure 6.23.: Spectra emitted by an inverter on the DC side with EMI filters based on different topologies including Y-capacitors connected directly after the converter.

Filter topologies with a CMC located on the path of CM current through the total stray capacitance of the load side represent a decent alternative. It can be explicitly seen that results achieved with this type of EMI filter are considerably improved. The main resonance is mitigated by at least 20 dB in comparison with the filters based on a direct connection of Y-capacitors after a PE converter (Figure 6.24). Filters with the following component arrangements are used for these experiments. Filter 4 represents a $L1C1L2C1L1$ -topology with L1 0.06 mH and L2 0.36 mH. Filter 5 is based on $L1C1L2C1$ -topology includes two CMCs: L1 0.15 mH L2 0.36 mH. Filter 6 is based on a $L1C1L2C1L3$ -topology with L1 0.04 mH, L2 0.21 mH and L3 0.06 mH.

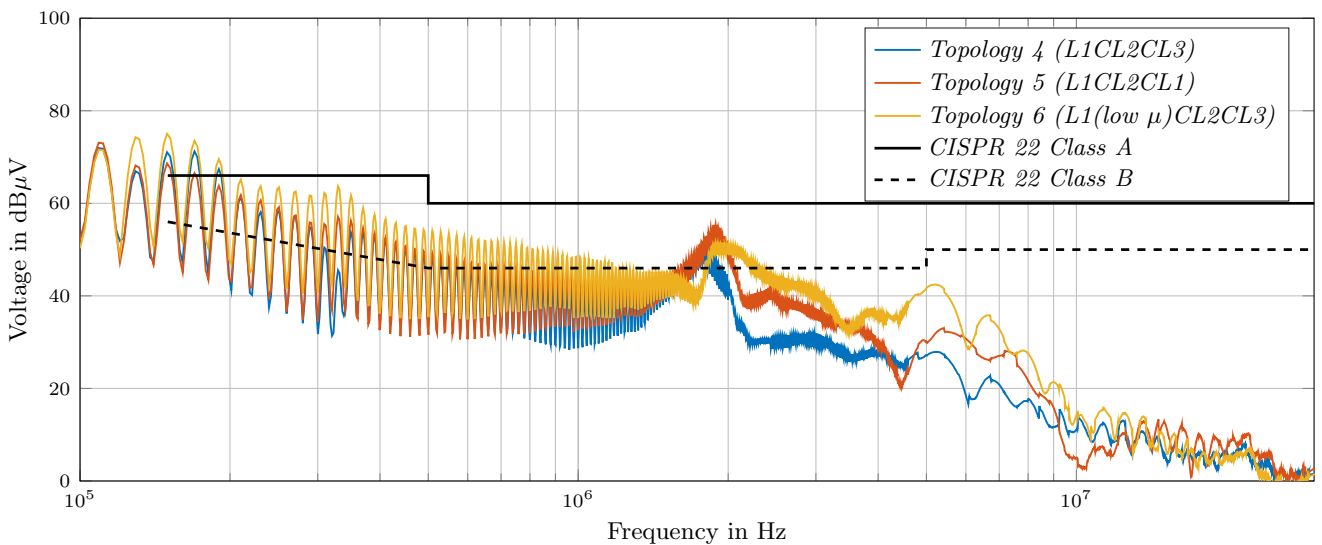


Figure 6.24.: Spectra emitted by an inverter on the DC side with EMI filters based on different topologies including CMC on the CM main current path.

As it was expected, after continuous operation temperature of CMCs in the first stage of filters 4 and 5 is considerably higher than the main CMC. It is explained by Kirchhoff's law, applied to a CM equivalent path. The CMC located in the first stage of a filter has the sum of CM current flowing via the main CMC and current flowing via the first group of Y-capacitors. Because of this, filters 4 and 5 are overheated above 120°C during operation, which is not acceptable for the majority of industrial applications. Moreover, higher current means higher probability of saturation.

Although all investigated filter topologies with a CMC lactated on the main path of CM current mitigate the main resonance quite well, only the filter 6 is not overheated. Because the first CMC (L1) is substituted with a CMC based on material with relatively low permeability. So that hysteresis and eddy current losses in a core caused by CM current are reduced. It once again confirms the importance of core material selection, as suitable materials do not have to have the highest possible permeability. Eventually filter 6 is the only filter which was capable of fulfilling standard limits without overheating. It must be mentioned that heating and saturation issues are not considered during those studies with a required exactness.

As has been shown, practically every parameter of a PE converter (either on the grid or motor side) to a varying degree influences an EMI spectrum. Connection to protective earthing and variation of switching speed for semiconductors demonstrate the most significant effects on disturbances produced by both AICs and motor side inverters. However, disconnecting of a converter from protective earthing cannot be used in real applications due to safety issues. Motor and cable stray capacitance is the most important in terms of parasitic parameters of a drive system. Tuning of those parameters can be used in order to decrease the level of emitted disturbances and minimization of EMI filters. Dead time, load current and PWM frequency demonstrate certain impacts on the emitted disturbances spectrum, but effects are rather intermediate. A filter topology and particularly location of Y-capacitors relative to a PE converter is the most important during filter topology selection. Arrangement of Y-capacitors plays a vital role in redistribution of CM current on the system level. Y-capacitors arrangement must be carefully analysed during consideration of thermal and saturation effects.

7 Conclusions

7.1 Summary

This thesis deals with the comprehensive study of issues related to EMI filter design and optimization. Analysis of the main subject was conducted according to the principle "from simple to complex". The state of the technology and the main direction of research were outlined in Chapter 1. Soft magnetic materials are treated as the basic building block for EMI filters. Applicability of diverse soft magnetic materials in EMI filters is analysed. Advantages and disadvantages of different types of soft magnetic materials were addressed and classified. This knowledge is extended to the components level in Chapter 2.

It continues with modelling of an EMI filter as a component that is isolated from the PE system under $50\ \Omega$ impedance conditions (Chapter 3). Thereafter, various methods of filter improvement (Chapter 4) and several novel advanced topologies (Chapter 5) were proposed. Achieved results were compared to conventional filter topologies. Lastly, in Chapter 6 different parameters of a PE converter were analysed from the EMC point of view. Behaviour of diverse topologies of EMI filters connected to a PE converter was studied. Four major objectives which were determined in the beginning of the work were highlighted:

1. Comprehensively study three-phase EMI filters; collect and structure existing in literature knowledge about this subject; create methods and models permitting accurate anticipation of IL without indispensable filter prototyping.
2. Develop new methods of EMI filter improvement and adopt existing methods to three-phase EMI filters. Determine possible limits of improvement methods and create recommendations which method should be employed for which application.
3. Define the degrees of freedom for IL improvement introduced by multistage or ladder EMI filters. Investigate technical characteristics of different filter topologies. Conduct a comparative analysis of various filter types not only from a performance point of view but also considering price, power density and realization complexity.
4. The final objective is to demonstrate how variation of PE system parameters influences the emitted EMI spectrum. Moreover, to show impact of PE system parameters on EMI filter design and investigate how filters with different topologies can cope with such changes.

7.2 General Conclusions

Diverse simulation approaches were used for profound understanding of the physical processes inherent in EMI filters. Mathematical models of an EMI filter based on the network theory, S-functions and differential equations were developed and described in detail. Presented models allow achievement of a very good agreement between simulation and measurements. Different exactness level of proposed mathematical models allow selection of a suitable method depending on the time available for modelling. Moreover, proposed mathematical models can be extended and adapted in accordance with a

filter topology, used passive components and utilized soft magnetic material. Modelling methods based on developed mathematical models support design of EMI filters with any complexity. All filter design algorithms are summarised in flow charts for ease of understanding.

Design of EMI filters for abstract load and source impedances remains the most well-know topic for discussion. Impact of the load and source impedance variation on the EMI filter IL is studied. It was demonstrated that the worst case scenario load and source impedance combination, which is described in CISPR17/EN55017 [92], does not represent the real worst case IL for all filter topologies. Model based investigation of Γ -, Π - and T -topologies under different load and source impedances were carried out. Active (resistive) as well as reactive (capacitive and inductive) impedances were used for IL assessment. The worst case impedance combinations (when a concrete filter type is the less effective) for every particular topology were found.

It was shown that analytical simulation methods can deliver quite plausible results in a short time frame and with modest development effort. At the same time they are simple to utilize and do not need high computational power. SPICE based filter design exhibits very precise results but it is rather time consuming and requires a deep understanding of physical processes within an EMI filter. Several different tools have to be utilized for this design method, therefore some data can be lost during migration between these tools. Combined FEM simulation can be recommended in the case when a 3D model of a filter is already available. Then, IL of a filter with consideration of all parasitics can be obtained rather quickly after some 3D model adjustments.

Different filter improvement methods were developed. Typically utilization of such improvement methods leads to increasing of the filter's complexity and complicates the design process. For this reason their applicability was examined individually for each particular case. Importance of the parasitics management is highlighted in Chapter 4. Parasitics cancellation techniques that already exist were reviewed and developed further. Due to the reasons discussed in Chapter 4, some conventional compensation techniques cannot be implemented in three-phase filters. For some methods an even number of capacitors of one type per stage is required, but this is usually not the case for three-phase filters. Also it is not possible to implement ESL compensation for Y-capacitors connected to the star point since there is no constant current flow through a coupled inductor. The other compensation techniques were successfully adopted from single-phase filters. A novel method involving utilization of an additional winding of a CMC connected to a Y-capacitor was developed. Although methods dealing with parasitics compensation are quite effective, filters with compensated parasitics are inferior to multistage EMI filters in terms of power density and costs. A comprehensive analysis of different improvement methods was conducted in Chapter 4 and Chapter 5. Parasitics compensation methods are quite beneficial if IL improvement at the particular frequency for an existing EMI filter is required. Multistage concepts have advantages in the case when IL must be improved in the whole conductive EMI frequency range (150 kHz - 30 MHz). Mutual couplings in three-phase EMI filters do not play such important roles as for single-phase filters.

Multistage filters with enhanced topologies were proposed in Chapter 5. Critical comparison of conventional and proposed filter topologies considering power density and costs was carried out. Obtained results demonstrate a considerable advantage of enhanced topologies over conventional ones. Among investigated filter topologies the best results were achieved with $CLCLC$ -filters. Some presented enhanced topologies allow to decrease of the total amount of installed Y-capacitance. Utilizing those topologies, leakage current can be significantly reduced. It is especially important for applications where

a PE converter must be equipped with residual current devices. Use of some other enhanced topologies leads to certain cost and size reductions comparable with conventional EMI filters.

Higher power density can be achieved with utilization of multistage filters. Required IL can be obtained by means of a steeper fall of IL curve (dB/decade) or via shifting of the cut-off frequency towards a lower frequency range. The first method requires implementation of additional stages, but used components are smaller, so that higher power density is ensured. The second option, with simple increase of passive components, is relatively straightforward and ineffective. In general, ubiquitous employment of multistage filters is unavoidable in the near future. This is mainly because of their superior performance and higher power density on the one hand, and quite modest costs comparable with conventional EMI filters on the other hand.

Finally, an analysis diapason was enlarged from the device (EMI filter itself) to the PE system level. EMI filters were analysed together with power electronic converters. Effects caused by variation of converter parameters on the emitted spectrum of disturbances were assessed from a relevance point of view. A discussion about converter parameter influence on EMI filter design and/or selection was carried out. It was determined that essentially all investigated parameters of a PE converter except DC voltage fluctuation have feasible impact on the EMI spectrum. The most significant way that EMI can be affected is by variation of semiconductor speed, PWM frequency, optimizing motor stray capacitance or manipulation with a protective earthing conductor. Initial EMC oriented analysis of a PE system can significantly simplify tasks during EMI filter development. It allows optimization of costs and power density of the PE converter together with a filter.

EMI filters for an assumed PE converter have to be designed (or selected) according to two main boundary conditions. Firstly, low frequency disturbances (150 kHz - 500 kHz) define general demands to filter IL and IL slope. In its turn, IL in this range plays the major role in filter topology selection and defines overall dimensions of filter components. Secondly, an EMI filter has to mitigate the main system resonance which is typically located (depending on the system parameters) in the range between 1 MHz and 10 MHz. This requirement cannot be fulfilled with bigger filter components due to a concomitant increase of parasitic values; instead, more sophisticated filter topologies must be used. Filter topologies which include a high impedance component on the path of CM current right after the converter demonstrate better results compared to topologies with a direct Y-capacitor connection at the input of the converter. This is true for both three-phase AC EMI filters and for DC EMI filters. Otherwise the auxiliary CMC tends to be overheated or saturated due to higher CM current flowing through it. Mitigation of the main system resonance can be achieved with alternative filtering concepts, e.g. when input and output of a PE converter are connected through decoupling capacitors to an additional conductor. This influences a CM current path within a drive system. As a general rule any changes of CM current paths quite significantly influence the emitted EMI spectrum.

It was shown that some filter topologies are more sustainable and can keep an emission level below the limits, independent on the PE converter type or its parameters. In order to get an optimal filter, it has to be designed for a particular PE converter at the early development stage. In this case a required level of EMI emission can be achieved with the smallest and cheapest EMI filter. Contradictorily, more universal filters require more space and usually have higher costs.

7.3 Future Research

The most important step related to continuation of this work is investigation of PE converter arrangements and contemplation of interaction between these converters. This is the next step in accordance with the strategy chosen in this thesis: from materials and components towards a system containing several PE devices.

Investigation of the complete drive system (rectifier, inverter, cable and load) represents a particular interest for dissemination of CM current within a drive system. Deeper understanding of CM paths enables implementation of EMI filtering concepts on the system level. For example, a filter which couples inputs and outputs of a PE converter. Impact of the drive system parameters on the emitted spectrum can be studied further with the following focal points: control methods, modulation techniques and mechanical EMC measures on the motor side (slot shielding, grounding of a rotor, etc.). Study of the power grid impedance with a focus on electromagnetic disturbances represents one more possible field for future work. The most interesting point is the effect of grid impedance on IL of EMI filters.

All developed filter mathematical models can be further developed or supplemented with the following points:

- Parasitics compensation methods presented in this work can be concatenated with developed mathematical models;
- It is possible to include mathematical models of filters to system simulation and evaluate developed EMI filters together with a PE converter;
- New features such as consideration of power loss and/or saturation effects can be implemented
- Ageing of capacitors or other filter components can be considered. The effects the component's aging on IL can be studied.

Proposed topologies of EMI filters can be applied to different types of PE converters, in order to assess their advantages and disadvantages for diverse applications. In this case the impact of multistage or high performance EMI filters on the system costs and power density can also be evaluated in frames of the whole system.

Based on existing trends in power electronics and the current situation in the standardization field, electromagnetic emission in the frequency range between 9 kHz and 150 kHz must be limited in the near future. Therefore, detailed study of EMI filter properties in this frequency range and development of topologies which cover this additional range are important.

The last proposed topic suitable for further research are filter topologies with a scope on low leakage currents. Nowadays there is certain demand for this type of EMI filters, but all activities so far lacked some consistency. Some straightforward attempts to design an EMI filter with low leakage current were until now based on reducing Y-capacitors with simultaneous increasing of CM inductance.

A Model Based Selection of Soft Magnetic Materials

Great diversity of materials makes selection of a proper material for one or the other filter quite challenging. For a proper selection of core material several relevant parameters must be considered. The main technical demand of magnetic material can be simplified to a compromise between specified inductance (impedance) and maximum saturation current. However, frequency dependent properties of a material are also quite important, so that initial permeability cannot be used for adequate selection of material. Ideally, for acceleration of core selection there should be a figure of merit, which describes "performance" of a particular material. This would allow relatively fast comparison between available materials, and minimize development time.

The simplest possible way to evaluate and compare frequency dependent permeability of different materials is to integrate this parameter over a frequency range of interest. However, this approach will decrease importance of the low frequency range, which is critical for inductance calculation. Therefore, it is proposed to use integration of permeability via logarithmically scaled frequency. Log-scale is used in this case as a weight factor (A.1). The final permeability coefficient k_1 can be found as a frequency range from 1 Hz up to 100 MHz as (A.2).

$$\tilde{f} = T^{-1}(f) = 10^{\mu(f)}, \quad (\text{A.1})$$

where T^{-1} is a transformation from normal frequency f (linear scale) to weighted frequency \tilde{f} (logarithmic scale).

$$k_1 = \int_{f_1}^{f_2} 10^{\mu(f)} df - (\mu_i/10 \cdot \Delta f). \quad (\text{A.2})$$

Where k_1 is a coefficient, describing permeability dependency via frequency as a single number, μ_i is initial permeability. A second component $(\mu_i/10 \cdot \Delta f)$ is used in order to get rid of a minimal permeability level, which is not relevant to CMC impedance comparison. After substitution of normal frequency in (A.2) with the weighted factor (A.1) k_1 becomes weighted logarithmically (A.3)

$$k_1 = \int_{\tilde{f}_1}^{\tilde{f}_2} 10^{\mu(\tilde{f})} d\tilde{f} - (\mu_i/10 \cdot \Delta \tilde{f}). \quad (\text{A.3})$$

k_1 is a figure of merit, which describes efficiency of the material with applied weight factor. This process is represented graphically in Figure A.1. In Figure A.1a dependency of permeability from frequency with a normal frequency scale is shown. The area filled with dark blue between a permeability curve and the origin represents the coefficient k_1 . After scaling with a weight function this area becomes bigger, as the

more relevant frequency range is located in vicinity with the origin Figure A.1b. In order to compare possible losses of different materials the same simplification to the figure of merit can be applied to an imaginary permeability part.

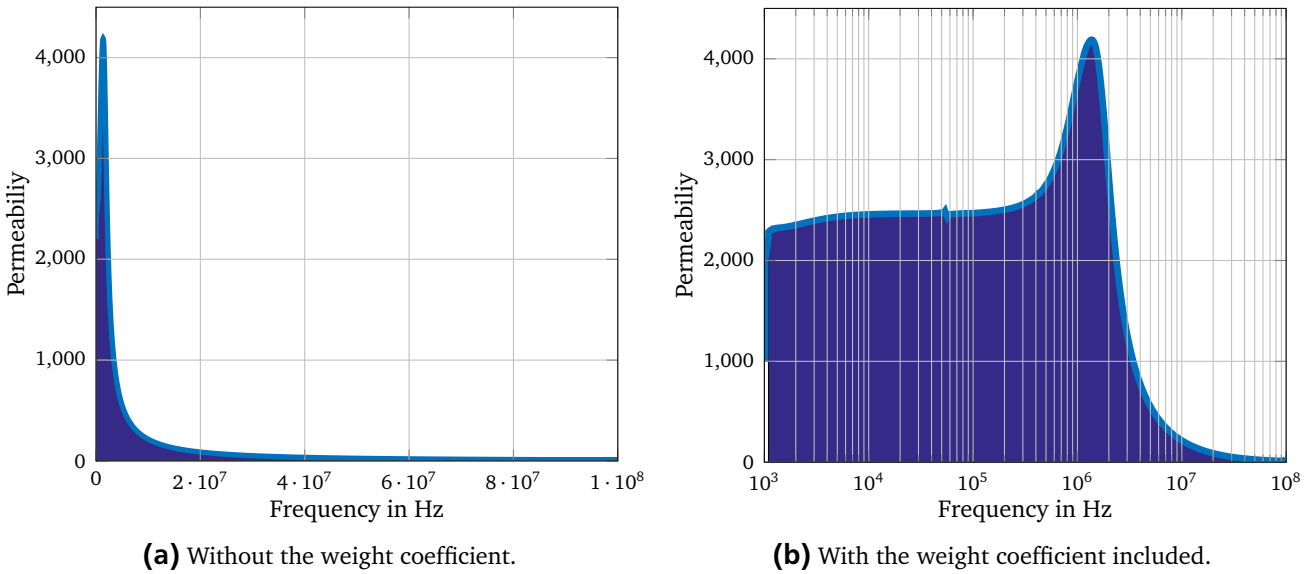


Figure A.1.: Graphical explanation of k_1 , dark blue area represents a merit figure for frequency dependent permeability.

Thereafter, in order to get weighted permeability a cubic root of k_2 must be taken. Then the coefficient k_2 (A.4) will determinate the performance of a material with included saturation flux density B_{sat} independent on a core size and a number of turns [67, 84].

$$k_2 = B_{sat} / \sqrt[3]{k_1} \tag{A.4}$$

The performance coefficient k_2 is evaluated for 5 different cores in accordance with the proposed method. Results are presented in Table A.1. It is seen that nanocrystalline material M006 has the highest score. It basically means that this material has the best performance among analysed materials. However, a core material has other critical parameters which are not considered with k_2 but must be taken into account. Those are: costs, temperature stability and power losses. Costs of ferrite are typically lower than nanocrystallines (Table A.1). Since a CMC based on a core with higher permeability exhibits higher impedance, lower impedance of a capacitors group is required. Some costs can be saved by utilization of smaller capacitors, so that the total filter price would remain approximately in the same order.

A proposed principle of material selection based on the figure of merit has several limitations. It is assumed that the frequency range of interest does not exceed 100 MHz and permeability of the evaluated material above 100 MHz should not exceed a level of 10% from initial permeability. Relevance of the proposed method is proved only for materials suitable for CMC design by definition. High permeability materials such as pure iron or sendust are not considered due to poor high frequency properties.

Material type	Mark	B_{sat}	μ_i	k_2	Price*
Nanocrystalline	W424 VAC [206]	1.2 T	89000	0.0162	17.17
Nanocrystalline	M006 Magnetec [134]	1.1 T	29500	0.0187	15.00
Ferrite (MnZn)	N87 Epcos [46]	0.49 T	2200	0.0167	2.24
Ferrite (MnZn)	T65 Epcos [47]	0.46 T	5200	0.0125	2.24
Ferrite (NiZn)	K8 Epcos [45]	0.34 T	860	0.0158	2.24

* Prices in Euro per item (by more than 1000 items order)

Table A.1.: Parameters of different core materials used for tests.



B Comparison of Soft Magnetic Materials

This table compares main properties of different soft magnetic materials. The highest permeability can be achieved with the nanocrystalline 74%. This material also exhibits good saturation flux density and can be used up to 30 MHz. MnZn ferrite and amorphous Co-based material have the most stable permeability at the high frequency up to 100 MHz. Therefore they are recommended to utilize in the high-frequency filter components described in Chapter 5.

Material type	Material parameters					
	Composition	Permeability	Saturation B_s , T	Power losses, W/kg	Max oper. temp., °C	Max operation f, MHz
MnZn ferrite	$MnZnFe_2O_4$	2000-12000	0.4	17	120	10
NiZn ferrite	$NiZnFe_2O_4$	100-500	0.35	9	120	100
Amorphous Co-based	$Co_{73}(SiB)_{27}$	80000-150000	0.8	5	80-74	100
Amorphous Fe-based	$Fe_{76}(SiB)_{24}$	8000-20000	1.7	18	150	20
Nanocrystalline 74%	$Fe_{73.5}Cu_1Nb_3Si_{13.5}B_9$	20000-150000	1.2	4	180	30
Nanocrystalline 83%	$Fe_{83}Cu_1P_4Si_4B_8$	5000-30000	1.94	8	200	20

Table B.1.: Parameters of available on the market soft magnetic materials.



C Measurement Setup for IL Characterisation

IL measurements of diverse filters in this work were conducted with a setup that is described in this section. The measurement setup used includes a DUT which is placed in a shielded box. N-type connectors are used to provide a clean signal propagation toward the shielded box. The box is connected to a VNA Keysight E5061B [108] with a high frequency coaxial cable. The setup is demonstrated in Figure C.1.

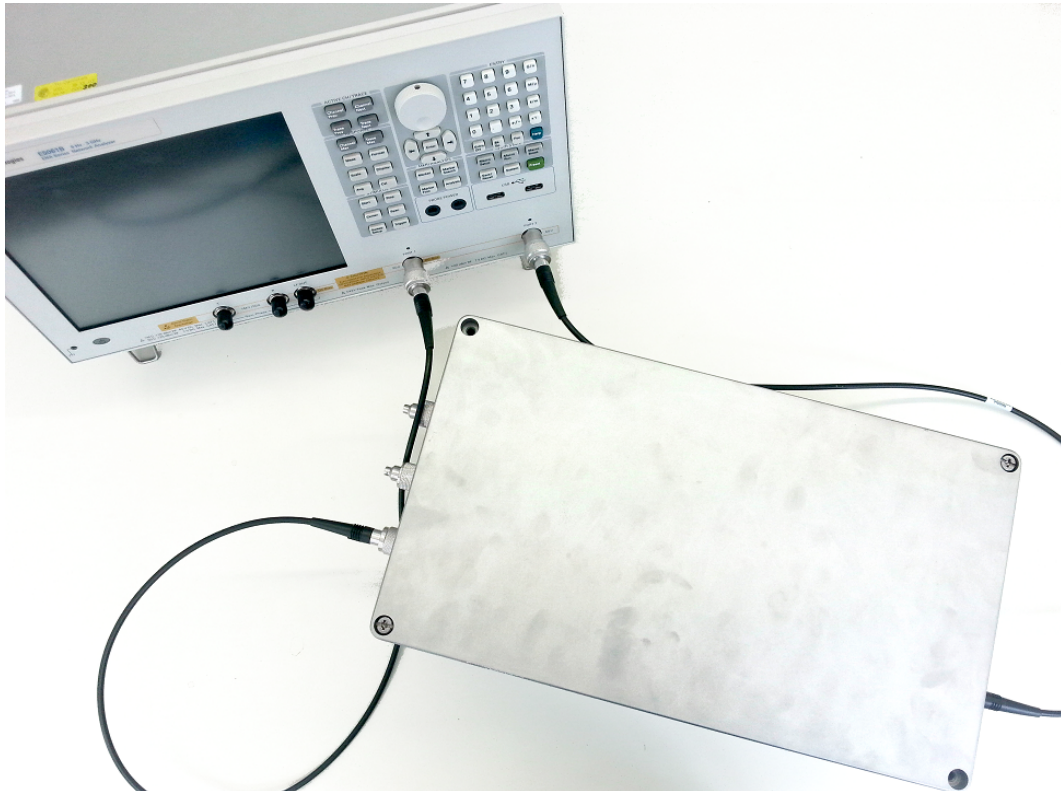


Figure C.1.: Measurement setup of insertion loss.

An accuracy of the used network analyser in the frequency range 1 kHz–1300 MHz is 10 %, related to the dB scale. The most common sources of errors in vector network analysers are listed below.

- Phase Noise;
- Absolute Power Accuracy;
- Displayed Average Noise Level;
- Third Order Intercept;
- Dynamic Range.

They are influenced by the quality of the instrument and accessories. In Figure C.2 the noise floor from the S_{12} measurements of the network analyser is plotted. Coaxial cables used in the setup measurement Radiall RG214 [164], which are connected through with a special N-Type adapter [107]. Insertion loss of utilized coaxial cables in the frequency range of interest can be disregarded. The minimal boundary for the measurements is -120 dB and values below this threshold cannot be measured with a given tolerance. This fact must be considered during validation of the filter models.

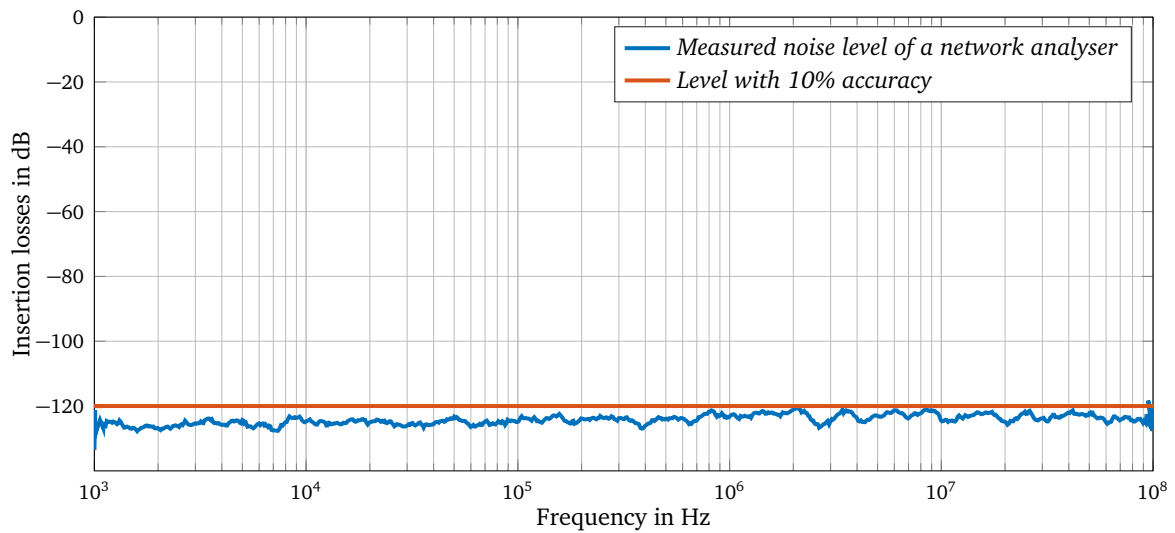


Figure C.2.: Noise floor of the used network analyser.

The shielded box is made of aluminium and the lid adjoins the box with overlapping. This eliminates any interaction of the DUT with the surroundings. Also, the shielded box provides excellent ground connection. Two decoupling PCBs are placed inside of the box. These boards are used for measurement of different IL modes. Depending on the terminal used to the decoupling PCB common, differential or differential unbalanced IL can be evaluated. Internal construction of the shielded box is shown in Figure C.3.

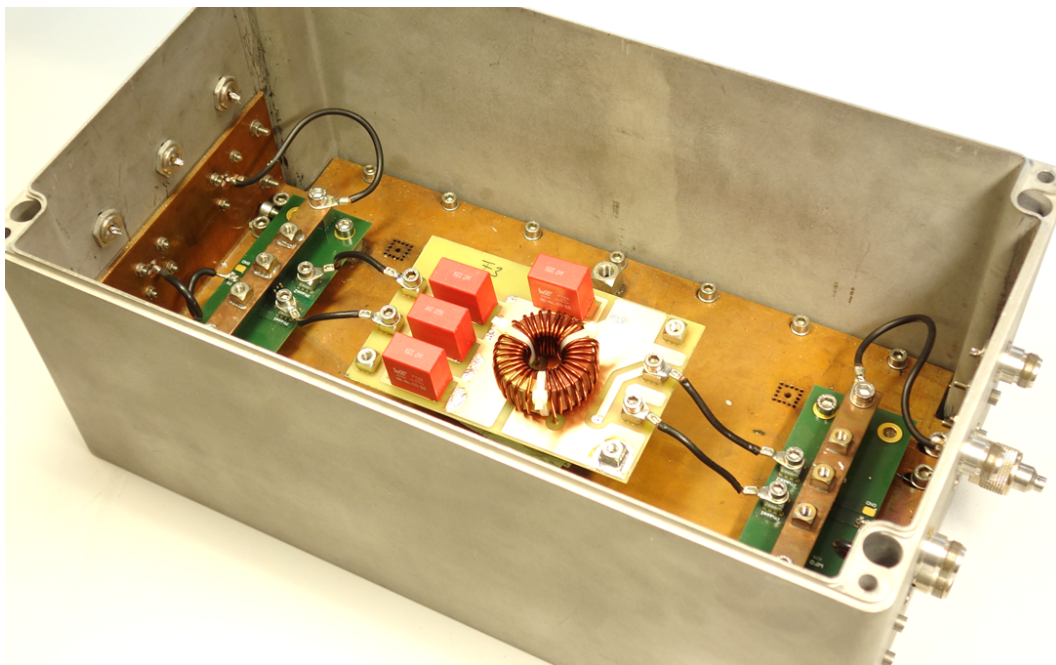


Figure C.3.: Internal construction of the shielded box.

D Laboratory Measurement of Power Grid Impedance

Practical measurements of the grid impedance in the range up to 2 kHz show quite similar behaviour with the assumption made in aforementioned norms with the dominated inductive component [171]. Some sources show that grid impedance becomes capacitive after 8 kHz [39]. Estimation of the low voltage power grid impedance made in Darmstadt (Germany) demonstrated the inductive-resistive character of the low voltage power grid up to 50 kHz (Figure D.1). For frequencies above 60 kHz the power grid becomes unstable and impedance deviates from an RL model. This is mainly caused by mutual couplings within a power cable as well as by distributed stray parameters of cable lines. General information concerning grid impedance in the conductive EMI range is not available in open sources. It might be caused by high time and effort expenses, required for such measurements. Moreover, grid impedance is not stable in time. Depending on the current power grid configuration the impedance can vary dynamically and such measurements would have too high uncertainties. However, for the purpose of EMI filter design it is essential to measure a spectrum produced by a PE converter, rather than to estimate grid and source impedances.

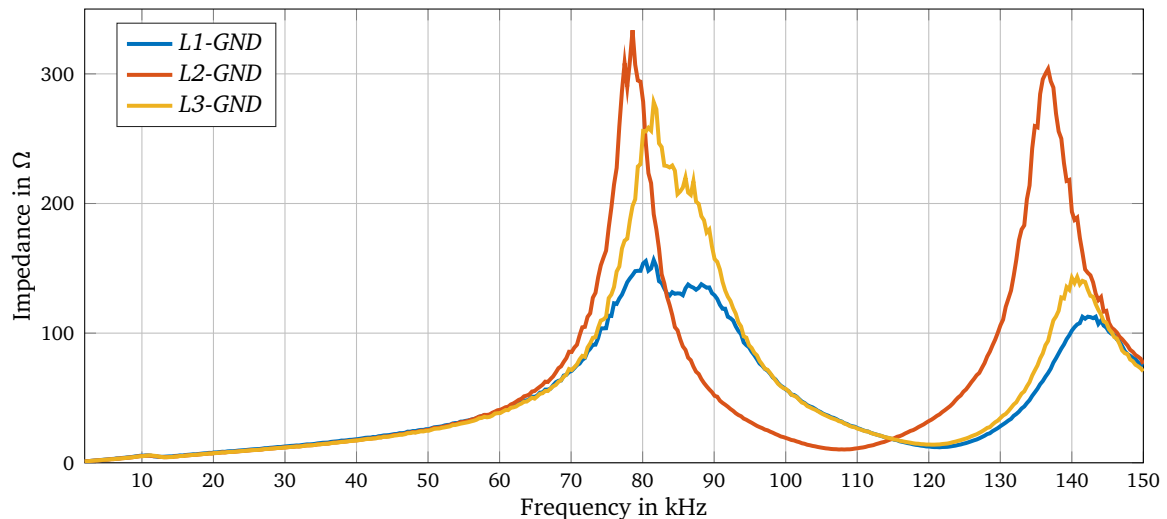


Figure D.1.: Measured DM impedance of the power grid measured in Darmstadt(Germany).

DM impedance exhibited by the three-phase AICs changes in accordance with conductive or non conductive states of semiconductors. During a conductive period a DC-link capacitor is connected between phases. A non-conductive period is represented by a high voltage across closed semiconductors, so that very high ohmic resistance is seen from the grid side. It is only true if a secondary side of a PE converter is treated as an ideal voltage source. Without this simplification impedance seen from the grid side depends on the state of the load-side inverter and the load itself. The high frequency characteristics (ESL and ESR) of a DC-link capacitor must be considered for correct impedance estimation. Basically, impedance of a PE converter can be approximated proportionally to the duration of switching states. CM and DM impedances of a typical AIC in the frequency range up to 1 MHz are depicted in Figure D.2. In this particular case impedances are measured for a complete drive system including an AIC, a line choke, an EMI filter and a load.

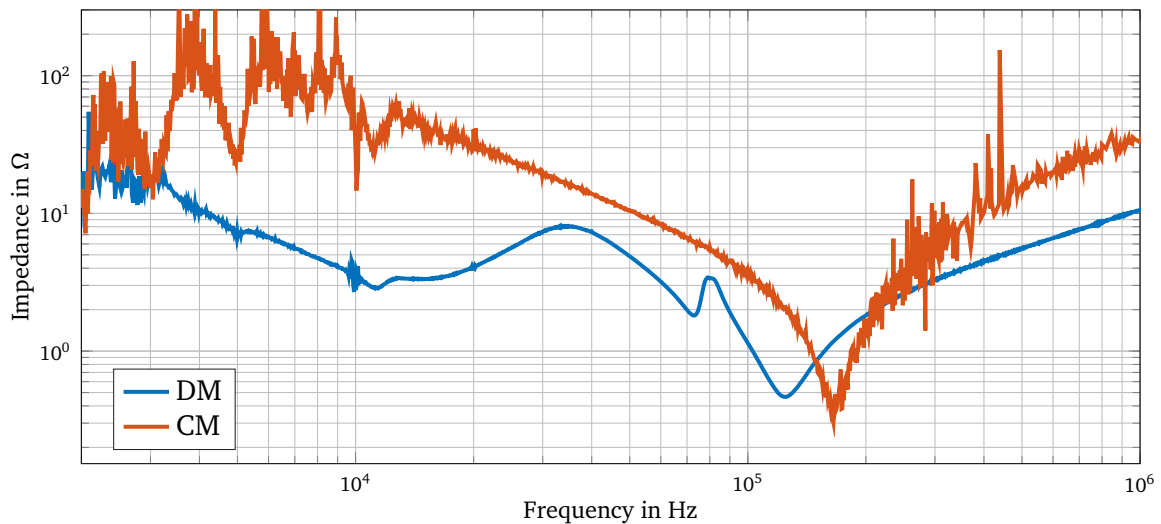


Figure D.2.: Measured DM and CM impedances of the active infeed converter with a line choke and an EMI filter

The grid impedance changes if other PE converters are connected to the same point of common coupling. Due to this dynamic change it is important to measure the grid impedance seen by a particular consumer when it is active. For this purpose so called "in-situ" measurements can be applied [6, 42]. According to available data, which were obtained from the in-situ measurements, it can be concluded that DM impedance of a load is on average larger than impedance of a source by a factor of five [77, 198]. This assumption is valid for frequencies up to 150 kHz.

Estimation of CM impedance of a drive system is rather simple and can be obtained via measurement of component impedances by combining them into a single ladder structure [28, 43, 60]. In this case no in-situ measurements during operation are required. Impedance of the common mode current path is predominantly defined by stray capacitors of a PE converter against the ground. Typical values of stray capacitors lie in the range up to a few picofarads [18]: it depends predominately on mechanical construction of a PE converter. Based on this information a precise mathematical model for CM impedance can be developed and used for EMI filter design. CM impedance of the grid side is determined by grid cable parameters (ESL, ESR, capacity to the ground, etc.) and power transformer characteristics. It is essential that semiconductors switching in a PE converter can be simplified to an ideal source of CM interferences. An equivalent circuit for a drive system with the stray capacitors is depicted in Figure 1.12. Ultimately it can be summarized that the CM load impedance seen by a filter can be assumed to be capacitive and CM line impedance should be predominantly determined by the cable parameters, so that it can be represented as a long line.

E Modelling and Design Methods for EMI Filters Flowcharts

Flowcharts for the filter design methods developed in Chapter 3 filter design methods are summarized in this appendix. The EMI filter development and improvement process including Chapter 3 and Chapter 5 is depicted in Figure E.4.

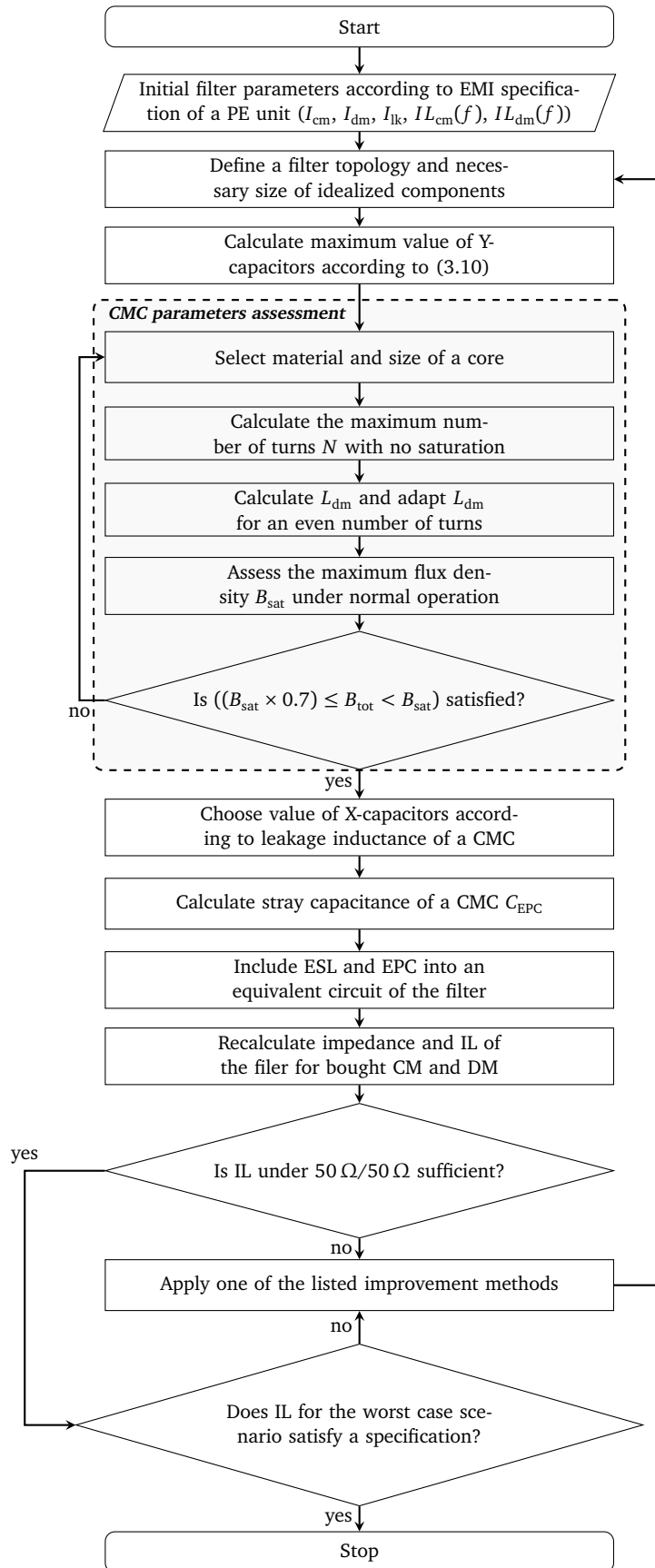


Figure E.1.: Design of EMI filter based on simplified analytical model.

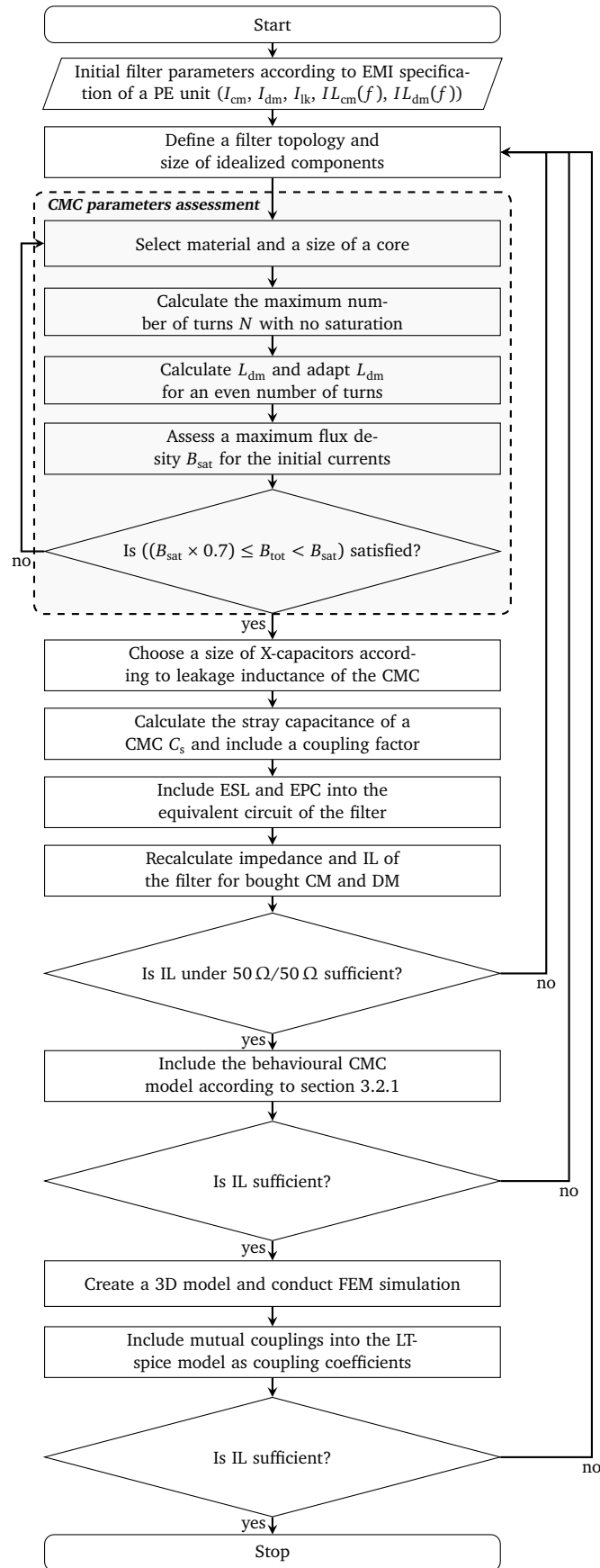


Figure E.2.: Design of an EMI filter based on LTSpice non-ideal model.

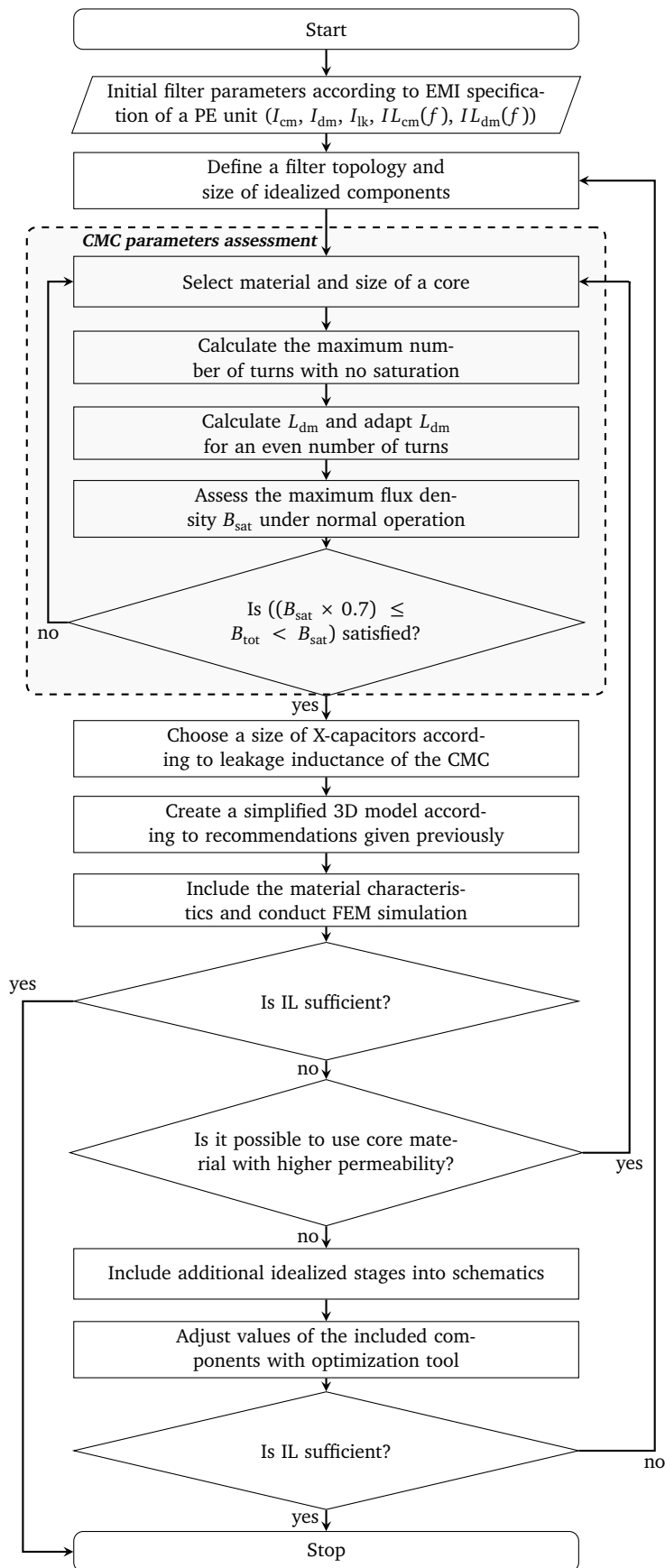


Figure E.3.: Design flow of EMI filter based on FEM

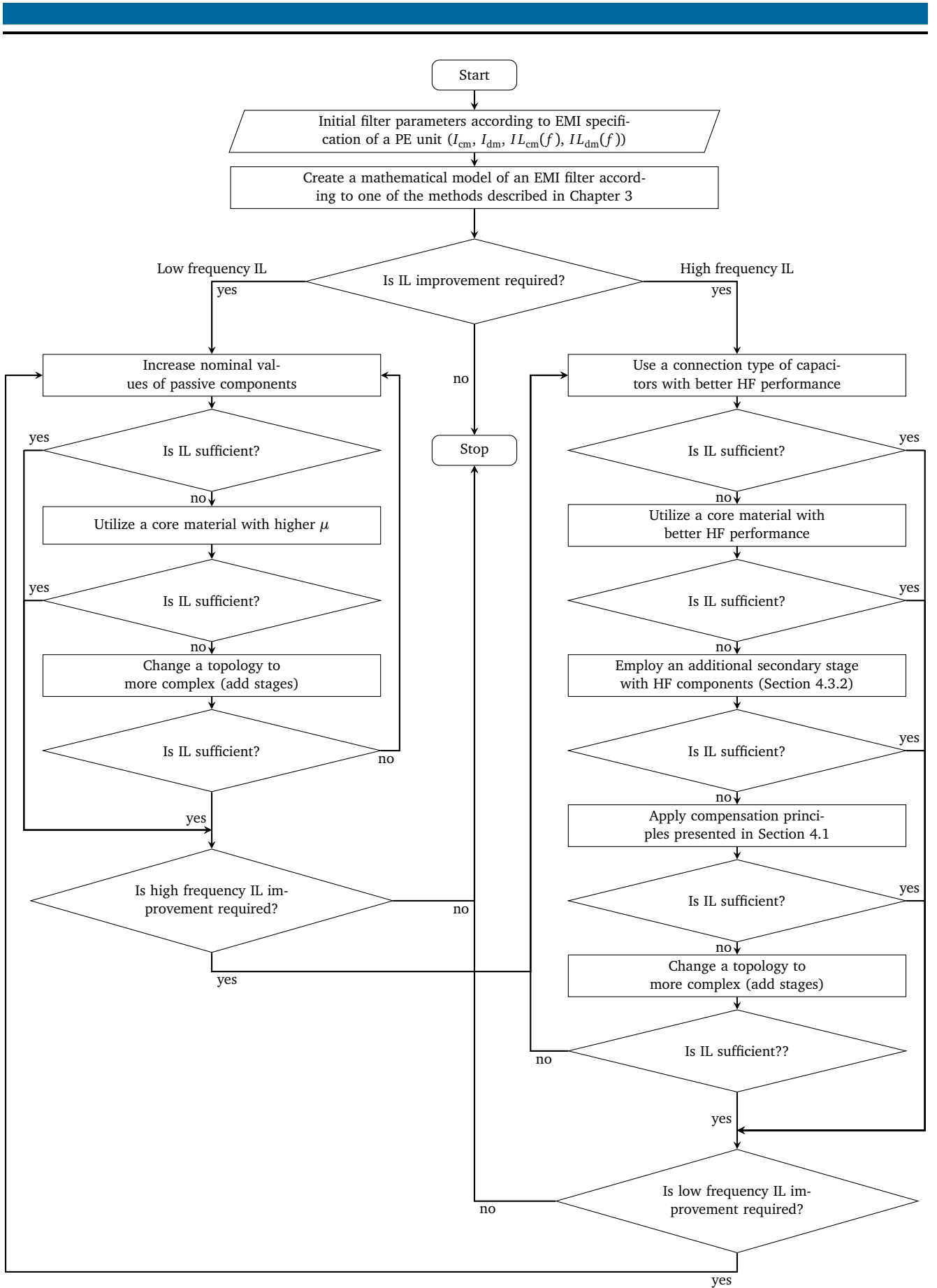


Figure E.4.: Flowchart summarizing proposed EMI filter improvement methods



F Test Bench for Characterisation of Magnetic Materials Under Saturation Conditions

The test bench for characterisation of soft magnetic materials is shown in Figure F.1. It includes the core under test (CUT), previously soldered on a special PCB, representation one turn choke. A core under test is connected to the network analyzer with two high-frequency cables. The saturation network includes a DC source which is capable to provide 30 A. The power resistor R_{load} is used as a load for the DC source. A cable which supplies saturation current is stretched through a toroidal choke so that permeability can be measured independently from the network with high current. In order to avoid an undesirable impact from the current source on the measured characteristics the core under test is decoupled with two inductors L_{dec1} and L_{dec2} . Important to notice, that those decoupling inductors must be based on magnetic material, maintaining their properties up to 100 MHz.

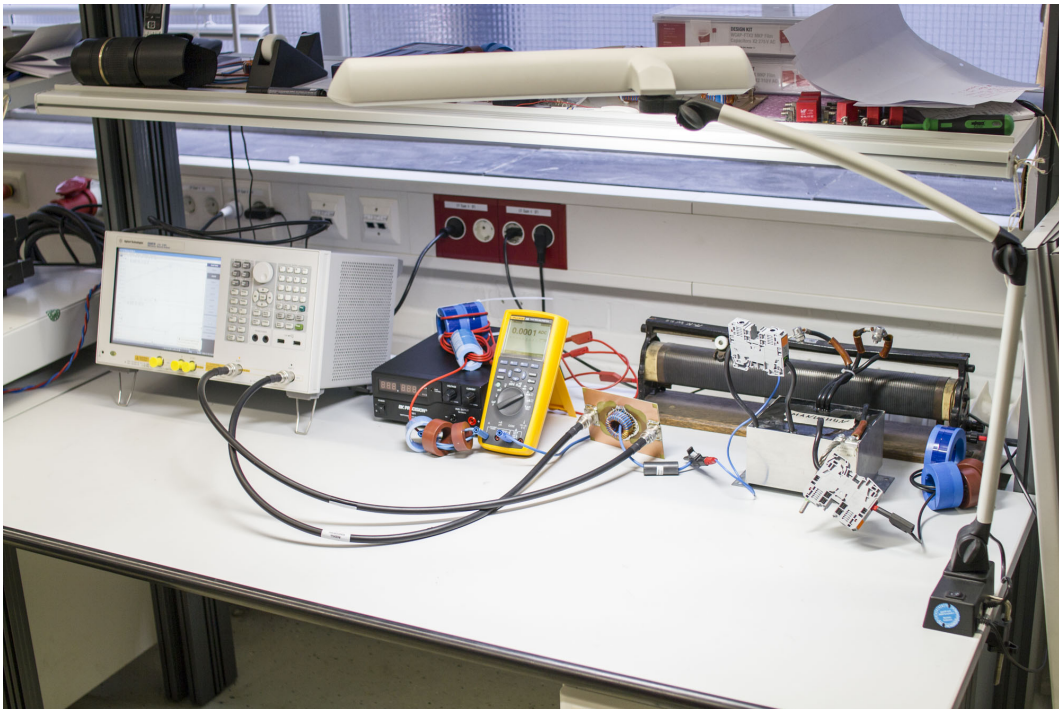


Figure F.1.: Test bench used for measurements of permeability under saturation.

The saturation current must be applied and removed slowly, because the fast current slopes can affect measurements and damage measuring equipment. An equivalent circuit of the test bench used for core materials characterisation is depicted in Figure F.2.

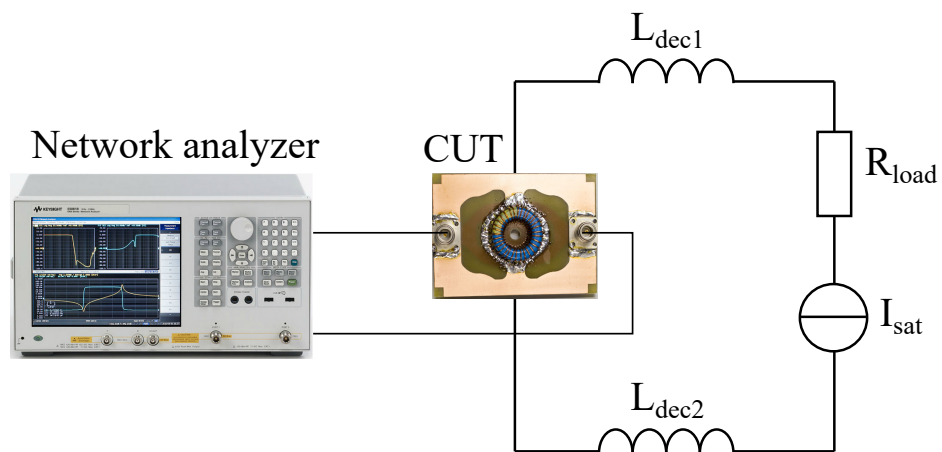


Figure F.2.: Structural diagram of the measurement setup of characterisation of permeability under saturation.

G Table of Mutual Couplings

Tables with mutual coupling between components of an EMI filter discussed and modelled in Chapter 3.2.2. Figure 3.23 and Figure 3.23 demonstrate the model that is used for obtaining of mutual coupling tables.

Inductance

Inductances in mH	Coil 1	Coil 2	Coil 3	X Capacitor 1	X Capacitor 2	X Capacitor 3	Y Capacitor 1	Y Capacitor 2	Y Capacitor 3	Y Capacitor 4
Coil 1	2,31E-03	2,27E-03	2,27E-03	-6,92E-07	-9,86E-07	-6,62E-07	-2,34E-07	-3,34E-07	-2,64E-07	-2,06E-07
Coil 2	2,27E-03	2,31E-03	2,27E-03	3,04E-07	5,63E-07	6,77E-07	2,25E-07	1,72E-07	1,41E-08	6,31E-07
Coil 3	2,27E-03	2,27E-03	2,31E-03	3,46E-07	3,30E-07	2,30E-09	7,96E-09	1,35E-07	2,33E-07	-4,83E-07
X Capacitor 1	-6,92E-07	3,04E-07	3,46E-07	9,08E-06	1,28E-06	2,29E-07	-8,92E-09	-1,11E-08	-9,56E-09	-2,58E-09
X Capacitor 2	-9,86E-07	5,63E-07	3,30E-07	1,28E-06	8,58E-06	1,02E-06	-1,05E-08	-1,54E-08	-1,57E-08	5,73E-09
X Capacitor 3	-6,62E-07	6,77E-07	2,30E-09	2,29E-07	1,02E-06	8,65E-06	-1,33E-08	-2,29E-08	-2,62E-08	1,98E-08
Y Capacitor 1	-2,34E-07	2,25E-07	7,96E-09	-8,92E-09	-1,05E-08	-1,33E-08	8,83E-06	1,16E-06	2,53E-07	2,44E-07
Y Capacitor 2	-3,34E-07	1,72E-07	1,35E-07	-1,11E-08	-1,54E-08	-2,29E-08	1,16E-06	8,74E-06	1,21E-06	4,61E-07
Y Capacitor 3	-2,64E-07	1,41E-08	2,33E-07	-9,56E-09	-1,57E-08	-2,62E-08	2,53E-07	1,21E-06	8,85E-06	-2,88E-07
Y Capacitor 4	-2,06E-07	6,31E-07	-4,83E-07	-2,58E-09	5,73E-09	1,98E-08	2,44E-07	4,61E-07	-2,88E-07	8,81E-06

Inductive Coupling Coefficient

	Coil 1	Coil 2	Coil 3	X Capacitor 1	X Capacitor 2	X Capacitor 3	Y Capacitor 1	Y Capacitor 2	Y Capacitor 3	Y Capacitor 4
Coil 1		0,98622	0,98612	-0,0047818	-0,0070128	-0,0046841	-0,0016426	-0,002352	-0,0018499	-0,0014478
Coil 2	0,98622		0,9863	0,0020989	0,0040018	0,0047901	0,001574	0,0012126	0,000098527	0,004431
Coil 3	0,98612	0,9863		0,0023917	0,0023455	0,00001625	0,000055802	0,00094981	0,001631	-0,0033927
X Capacitor 1	-0,0047818	0,0020989	0,0023917		0,14456	0,025865	-0,00099605	-0,0012419	-0,001067	-0,0002891
X Capacitor 2	-0,0070128	0,0040018	0,0023455	0,14456		0,11881	-0,001208	-0,001782	-0,0018019	0,00065971
X Capacitor 3	-0,0046841	0,0047901	0,00001625	0,025865	0,11881		-0,0015254	-0,0026337	-0,0029918	0,0022717
Y Capacitor 1	-0,0016426	0,001574	0,000055802	-0,00099605	-0,001208	-0,0015254		0,13149	0,028665	0,027625
Y Capacitor 2	-0,002352	0,0012126	0,00094981	-0,0012419	-0,001782	-0,0026337	0,13149		0,13706	0,052576
Y Capacitor 3	-0,0018499	9,8527E-05	0,001631	-0,001067	-0,0018019	-0,0029918	0,028665	0,13706		-0,032584
Y Capacitor 4	-0,0014478	0,004431	-0,0033927	-0,0002891	0,00065971	0,0022717	0,027625	0,052576	-0,032584	

Figure G.1.: Inductance and inductive coupling coefficients.

Capacitance

Capacitances in pF	X Capacitor 1	X Capacitor 2	X Capacitor 3	Y Capacitor 1	Y Capacitor 2	Y Capacitor 3	Y Capacitor 4	Coil 1	Coil 2	Coil 3	Ground
X Capacitor 1		-2,21E+00	-2,57E-03	-6,09E-06	-6,09E-06	-6,09E-06	-6,09E-06	-7,21E-02	-5,25E-03	-8,59E-05	-3,49E+04
X Capacitor 2	-2,21E+00		-1,33E+00	-7,75E-07	-7,75E-07	-7,75E-07	-7,75E-07	-1,23E-01	-8,61E-04	-1,36E-03	-2,77E+04
X Capacitor 3	-2,57E-03	-1,33E+00		-7,01E-08	-7,01E-08	-7,01E-08	-7,01E-08	-1,19E-01	-7,99E-05	-2,52E-02	-3,45E+04
Y Capacitor 1	-6,09E-06	-7,75E-07	-7,01E-08		-1,63E+00	-6,64E-03	-4,83E-02	-4,75E-05	-1,09E-02	-3,24E-04	-3,38E+04
Y Capacitor 2	-1,14E-06	-1,47E-07	-5,86E-08	-1,63E+00		-1,63E+00	-7,31E-01	-9,49E-06	-3,94E-03	-2,38E-04	-2,42E+04
Y Capacitor 3	-5,24E-09	-8,29E-08	-3,71E-06	-6,64E-03	-1,63E+00		-4,13E-01	-3,05E-06	-2,79E-05	-5,31E-04	-3,17E+04
Y Capacitor 4	-7,45E-06	-4,16E-06	-1,36E-04	-4,83E-02	-7,31E-01	-4,13E-01		-2,15E-04	-1,45E-01	-1,52E-01	-2,57E+04
Coil 1	-7,21E-02	-1,23E-01	-1,19E-01	-4,75E-05	-9,49E-06	-3,05E-06	-2,15E-04		-2,11E+00	-2,17E+00	-2,11E+04
Coil 2	-5,25E-03	-8,61E-04	-7,99E-05	-1,09E-02	-3,94E-03	-2,79E-05	-1,45E-01	-2,11E+00		-2,15E+00	-2,25E+04
Coil 3	-8,59E-05	-1,36E-03	-2,52E-02	-3,24E-04	-2,38E-04	-5,31E-04	-1,52E-01	-2,17E+00	-2,15E+00		-2,24E+04
Ground	-3,49E+00	-2,77E+00	-3,45E+00	-3,38E+00	-2,42E+00	-3,17E+00	-2,57E+00	-2,11E+00	-2,25E+00	-2,24E+00	

Capacitive Coupling Coefficient

	X Capacitor 1	X Capacitor 2	X Capacitor 3	Y Capacitor 1	Y Capacitor 2	Y Capacitor 3	Y Capacitor 4	Coil 1	Coil 2	Coil 3	Ground
X Capacitor 1		-3,63E-01	-4,82E-04	-1,12E-06	-1,87E-07	-9,53E-10	-1,54E-06	-1,16E-02	-8,45E-04	-1,37E-05	-2,75E-01
X Capacitor 2	-3,63E-01		-2,36E-01	-1,36E-07	-2,29E-08	-1,43E-08	-8,13E-07	-1,87E-02	-1,31E-04	-2,06E-04	-2,07E-01
X Capacitor 3	-4,82E-04	-2,36E-01		-1,40E-08	-1,04E-08	-7,31E-07	-3,05E-05	-2,06E-02	-1,39E-05	-4,38E-03	-2,95E-01
Y Capacitor 1	-1,12E-06	-1,36E-07	-1,40E-08		-2,86E-01	-1,29E-03	-1,06E-02	-8,14E-06	-1,88E-03	-5,53E-05	-2,84E-01
Y Capacitor 2	-1,87E-07	-2,29E-08	-1,04E-08	-2,86E-01		-2,81E-01	-1,43E-01	-1,45E-06	-6,02E-04	-3,61E-05	-1,81E-01
Y Capacitor 3	-9,53E-10	-1,43E-08	-7,31E-07	-1,29E-03	-2,81E-01		-8,97E-02	-5,15E-07	-4,72E-06	-8,95E-05	-2,63E-01
Y Capacitor 4	-1,54E-06	-8,13E-07	-3,05E-05	-1,06E-02	-1,43E-01	-8,97E-02		-4,13E-05	-2,79E-02	-2,90E-02	-2,42E-01
Coil 1	-1,16E-02	-1,87E-02	-2,06E-02	-8,14E-06	-1,45E-06	-5,15E-07	-4,13E-05		-3,15E-01	-3,23E-01	-1,54E-01
Coil 2	-8,45E-04	-1,31E-04	-1,39E-05	-1,88E-03	-6,02E-04	-4,72E-06	-2,79E-02	-3,15E-01		-3,20E-01	-1,65E-01
Coil 3	-1,37E-05	-2,06E-04	-4,38E-03	-5,53E-05	-3,61E-05	-8,95E-05	-2,90E-02	-3,23E-01	-3,20E-01		-1,63E-01
Ground	-2,75E-01	-2,07E-01	-2,95E-01	-2,84E-01	-1,81E-01	-2,63E-01	-2,42E-01	-1,54E-01	-1,65E-01	-1,63E-01	

Figure G.2.: Capacitance and capacitive coupling coefficients.



H Comparison of Parasitics Compensation Methods

Comp. method	Extra components and materials	Implementation efforts	Degradation reasons	Possible improvement	Price
EPC comp. with extra winding.	<ul style="list-style-type: none"> • A wire for an additional winding with a factor 10 smaller diameter as a phase wire. • A compensation capacitor (10-500 μF) and a resistor (1-100 Ω). 	<ul style="list-style-type: none"> • Space for an extra winding is required (approx. 5% from the core size). • Spacing between an extra winding and phase windings must be kept sufficient for nominal voltage. • Low inductance ground connection is required. 	<ul style="list-style-type: none"> • Permeability degradation and secondary parasitics of compensation components. • The maximum frequency of compensation reaches 14 MHz. 	<ul style="list-style-type: none"> • A practically achieved improvement for CM IL is 20 dB. • Some degradation due to extra resonances can be observed. 	<ul style="list-style-type: none"> • 3% from a total components price. • 100 V nominal voltage of compensation components. • no changes in PCB size.
EPC comp. with a center tapped capacitor	<ul style="list-style-type: none"> • A compensation capacitor (10-500 μF) and a resistor (1-100 Ω). • Nominal voltage of used components must be equal to the phase voltage. 	<ul style="list-style-type: none"> • Specific PCB design with perfect grounding for a compensation network is needed. • The middle point of a winding must be identified very exact. 	<ul style="list-style-type: none"> • Permeability degradation and secondary parasitics of compensation components. • The maximum frequency of compensation reaches 30 MHz. 	<ul style="list-style-type: none"> • A practically achieved improvement for CM IL is 20 dB. 	<ul style="list-style-type: none"> • 6% from a total components price. • 250 V nominal voltage of compensation components. • no changes in PCB size.
ESL comp. based on crossed over capacitors	<ul style="list-style-type: none"> • An initial number of X-capacitors must be doubled. • Every group of X-capacitors must contain 2 special compensation inductors. 	<ul style="list-style-type: none"> • PCB must be entirely redesigned. • Compensation inductors is recommended to fix with a compound. 	<ul style="list-style-type: none"> • Non ideal properties of capacitors (dielectric loss, ESR, etc). • Mutual coupling of a coupled inductor degrade on the high frequency. 	<ul style="list-style-type: none"> • A practically achieved improvement for DM IL is 8 dB. 	<ul style="list-style-type: none"> • 36% from a total components price. • Size of a filter is increased significantly (factor 1.6).
ESL comp. based on a coupled inductor	<ul style="list-style-type: none"> • Only PCB must be redesigned. 	<ul style="list-style-type: none"> • Could should be designed very accurate. • Use of FEM tools is recommended. 	<ul style="list-style-type: none"> • Non ideal properties of capacitors (dielectric loss, ESR, etc). • Mutual coupling of a coupled inductor degrade on the high frequency. 	<ul style="list-style-type: none"> • Improvement for DM IL is up to 25 dB. 	<ul style="list-style-type: none"> • 8% from components price. • Size of PCB might increase.

Table H.1.: Summary of analysed self-parasitics compensation techniques.

I Parameters of Passive Components Used for Filter Prototypes in Chapter 5

Filter	Filter A (Figure 5.1a)				Filter B (Figure 5.1b)			
IL diagram	Figure 5.2a				Figure 5.2b			
Parameters	Name	Value	Price*	Size	Name	Value	Price*	Size
Y-capacitors	B32023B3 Y2 x3	0.1 uF	0.69	10.5 x 16.5 x 26.5	B32023A3 Y2	0.39 uF	1.51	14.5 x 29.5 x 26.5
X-capacitors	B32916A5 X1 x6	2.2 uF	4.6	20 x 39.5 x 42	B32926H3 X2 x3	6.8 uF	3.43	20 x 39.5 x 42
XY- capacitors	-	-	-	-	B32926H3 X2 x3	6.8 uF	3.43	20 x 39.5 x 42
Common mode choke	5 turns choke	196 uH	-	-	5 turns choke	196 uH	-	-
CMC core	EPCOS T65 [47]	-	2.24	40 x 24 x 16	EPCOS T65 [47]	-	2.24	40 x 24 x 16
Total	-	-	29.6	212 853 mm ³	-	-	22.1	199 091 mm ³

* Prices in Euro per item (by more than 1000 items order)

Table I.1.: Parameters of the filters under test (different capacitor connection types).

Parameters of the analysed in Chapter 5 EMI filters based on Γ -, Π - and *CLCLC*-topologies are summarised in Table I.2. Prices and volume are also included as an evaluation criteria.

Filter Topology	Γ				Π				<i>CLCLC</i>			
IL diagram	Simulation Figure 5.4, Measurements Figure 5.5											
Parameters	Name	Value	Price*	Size	Name	Value	Price*	Size	Name	Value	Price*	Size
Y-capacitors	B32916A5 X1 530V x3	2.2 uF	4.6	20.0 x 39.5 x 42.0	B32023A3 Y2 x6	0.22 uF	0.805	12.0 x 22.0 x 26.0	B32022A3 Y2 x9	0.033 uF	0.447	8.0 x 14.0 x 18.0
Common mode choke	16 turns choke	1.7 mH	-	62 500 mm ³ ***	13 turns choke	0.53 mH	-	62 500 mm ³ ***	13 turns choke x2	0.54 mH	-	62 500 mm ³ ***
CMC core	EPCOS T65 [47]	-	2.24	40 x 24 x 16	EPCOS N87 [46]	-	2.24	40 x 24 x 16	EPCOS N87 [46] x2	-	2.24	40 x 24 x 16
Total	-	-	16.8 **	162 040 mm ³	-	-	7.83 **	103 684 mm ³	-	-	10.023 **	143 144 mm ³

* Prices in Euro per item (by more than 1000 items order)

** CMC with wire is accounted with 3 euro

*** Volume of the CMC with windings

Table I.2.: Parameters of the filters under test.

Table I.3 demonstrates comparison of EMI filter with utilisation of high-frequency components with conventional one-stage filters. Prices and volumes of all used components are included without additional PCBs, wiring, filter housing, etc.

Topology	Π with HF CL stage				T with HF CL stage			
	Parameters	Name	Value	Price*	Size	Name	Value	Price*
Y-capacitors	B32023B3104 Y2 x2	0.1 uF	0.84	10.5 x 16.5 x 26.5	B32023B3104 Y2 x1	0.1 uF	0.84	10.5 x 16.5 x 26.5
XY-capacitors	WE 890324026034 x6	2.2 uF	1.57	26.0 x 25.0 x 15.0	WE 890324026034 x3	2.2 uF	1.57	26.0 x 25.0 x 15.0
Common mode choke	13 turns choke	0.54 mH	-	62 500 mm ^{3***}	13 turns choke x2	0.54 mH	-	62 500 mm ^{3***}
CMC core	EPCOS N87 [46]	-	2.24	40 x 24 x 16	EPCOS N87 [46]	-	2.24	40 x 24 x 16
Total without improvement	-	-	14.1**	130 182 mm ³	-	-	11.55**	158 841 mm ³
HF capacitors	WE 885352213015 Y2/X1 [225] x3	2.2 nF	0.68	6 x 3 x 3	WE 885352213015 Y2/X1 [225] x3	2.2 nF	0.68	6 x 3 x 3
HF CMC	WE 74270032 [224]	5 uH	0.63	26 x 26 x 29	WE 74270032 [224]	5 uH	0.63	26 x 26 x 29
Total with improvement	-	-	17.14**	157 344 mm ³	-	-	14.59**	186 003 mm ³

* Prices in Euro per item (by more than 1000 items order)

** CMC with wire is accounted with 3 euro

*** Volume of the CMC with windings

Table I.3.: Parameters of filters with and without high frequency components based improvement applied.

J Hybrid Chokes

Diverse parameters of different materials brought designers to an idea to combine benefits exhibited by different materials in one CMC. A stack of two or more cores creates a base of such hybrid CMC. The main benefit of the hybrid choke is the following: saturation is automatically prevented, in the situation when the resonance on the cut-off frequency is hit by specific disturbances (harmonics or PWM multiples). Since an EMI filter represent a second- or higher-order passive circuit, a resonance close to its cut-off frequency is essential. It may happen that an EMI filter amplifies interferences which match its cut-off frequency, leading to CMC saturation. A CMC based on two different core materials with diverse permeability can solve this issue. When some disturbances match with the resonance frequency, a core with higher permeability saturates and the cut-off frequency shifts to the higher frequency. As a result, complete saturation of a CMC is prevented. Detailed description of this principle can be found in [125]. A hybrid CMC based on the N87 ferrite and nanocrystalline W424 is depicted in Figure J.1. Moreover an effective frequency range of CMC can be extended with materials combination.

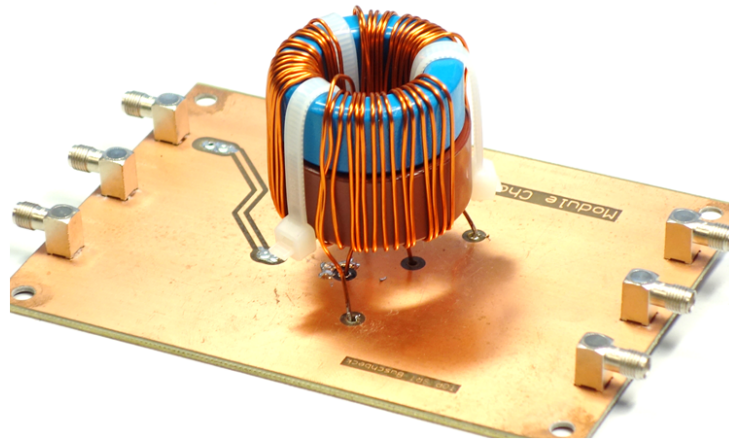


Figure J.1.: Hybrid choke.

A specific form-factor of two stacked chokes makes this option interesting for 3-D packaging applications, which allow an improvement of power density up to 66 %. [101]. The idea of hybrid choke can be combined with a so-called integrated CMC [25,172]. When one core with low permeability is used for DM inductance embodiment and a second core is based on a high permeability material, some benefits in terms of the power density can be obtained. The optimized structure of an inductor with integrated DM and CM chokes have already been presented in [150]. Necessary CM and DM impedances can be adjusted with the size of an air gap. Alternatively it can be done with material with lower permeability, which is placed into this air gap. CM impedance of such construction can be improved with employment of an external toroid based on nanocrystalline material with internal partitions of powder material. This solution will allow increasing the power density further.

Some shortcomings of a hybrid CMC have to be mentioned. Most importantly a hybrid CMC is more complicated in all relationships when compared with classical CMCs. Firstly, practical employment of hybrid CMCs might face some problems related to production, due to different manufacturing pro-

cesses of ferrites and nanocrystallines. Secondly, thermal design of a hybrid CMC is more challenging. Nanocrystalline and ferrite materials have different power losses and Curie temperature, so that losses in one core might cause overheating of a partner core. Lastly, mathematical modelling of a hybrid CMC impedance is more complicated and requires more time for development of suitable models. It especially affects mathematical modelling of saturation effects as well as a model based design process. The last reason can turn design of EMI filters based on hybrid CMCs into a trial and error process.

As an alternative to hybrid chokes with two cores stacked together (Figure J.1), a series connection of two CMCs based on different materials which form a single inductor can be proposed. IL of this solution is similar to a hybrid CMC based design, as demonstrated in Figure J.2. Although, a series connection of CMCs does eliminate some of the disadvantages of a hybrid choke, such as a difficult production process and mutual overheating. Furthermore, EPC of this option would be lower. Flexibility which is shown by two separated chokes is higher than a hybrid CMC. For example; a number of turns can be adjusted for every CMC separately, cores of different sizes can be independently selected, etc. The price of two series connected CMCs is also comparable with a hybrid choke with two cores.

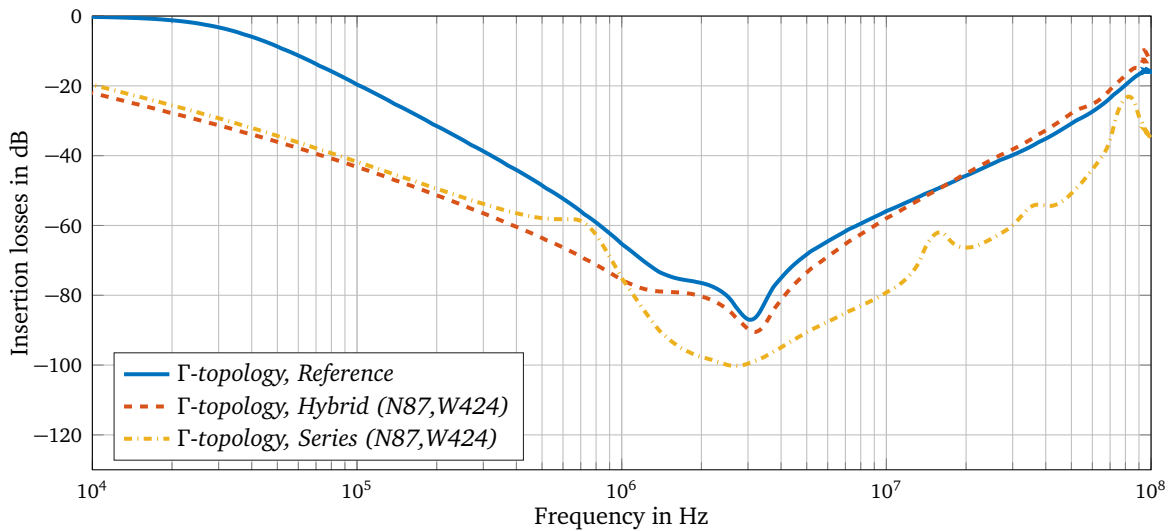


Figure J.2.: Γ -filter with included hybrid choke and Γ -filter with a series connection of two chokes.

Furthermore, if two separated CMCs have already been used in one filter, the structure of the filter can be transformed to a T -topology with two CMCs based on different materials. This variant has the same capabilities, preventing the CMC from saturation. When a T -topology is used, a high permeability material based CMC should be placed at the output and a low permeability CMC at the input [58]. Comparison of IL of a T -filter composing of CMCs based on different materials and a Γ -filter with a hybrid CMC is presented in Figure J.3. Since IL of the T -filter is superior in the whole frequency range either the total inductance or the total capacitance can be reduced. Reduction of inductance is achieved with utilization of a smaller nanocrystalline core W624 for one of the CMCs. The number of turns is also decreased. The price and power density of those three variants are rather similar.

In summary, the application range for any hybrid CMCs is quite limited. An EMI filter based on T -topology with two chokes made of different materials has much better properties in respect to the majority of criteria. Use of CMCs based on different materials in multistage filters gives one more degree

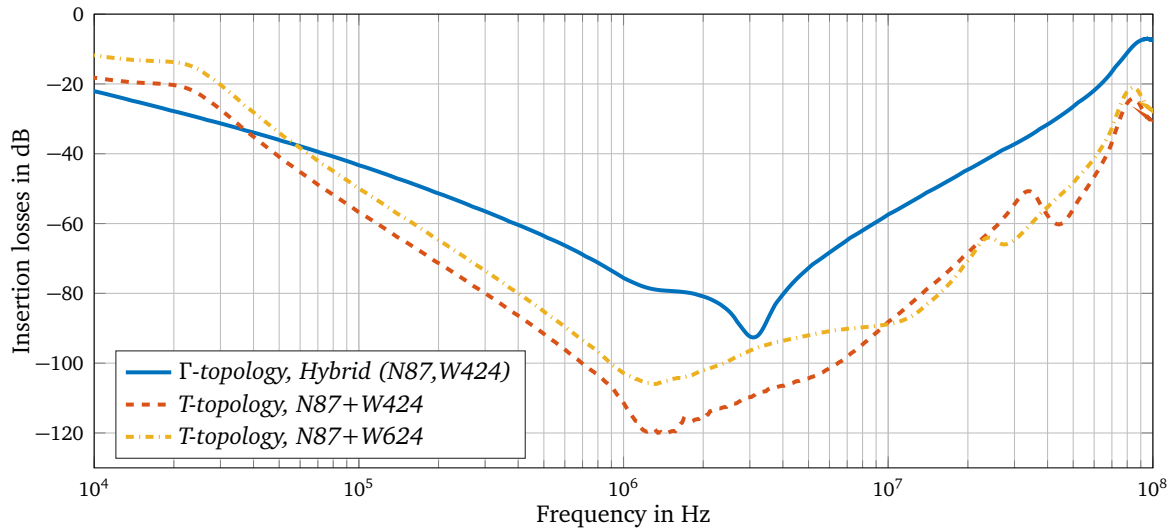


Figure J.3.: Comparison Γ -filter with a hybrid choke, T -filter with the same cores and number of turns, T -filter with a smaller choke.

of freedom in the research development process. Basically, all the advantages demonstrated by a hybrid choke remain, but several shortcomings are eliminated.



K Topologies of Conventional Filters Used for System Level Experiments

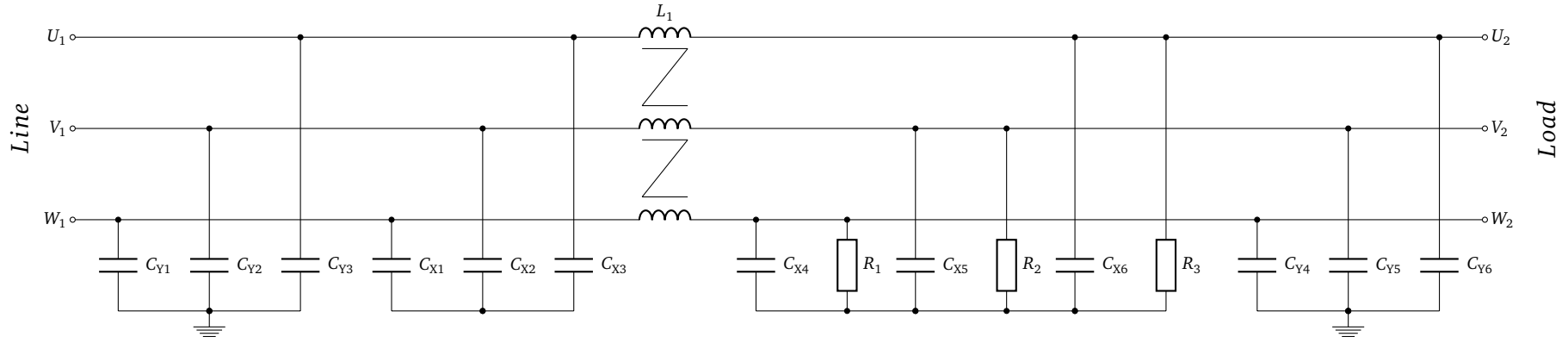


Figure K.1.: Filter 1: Π -topology for both CM and DM.

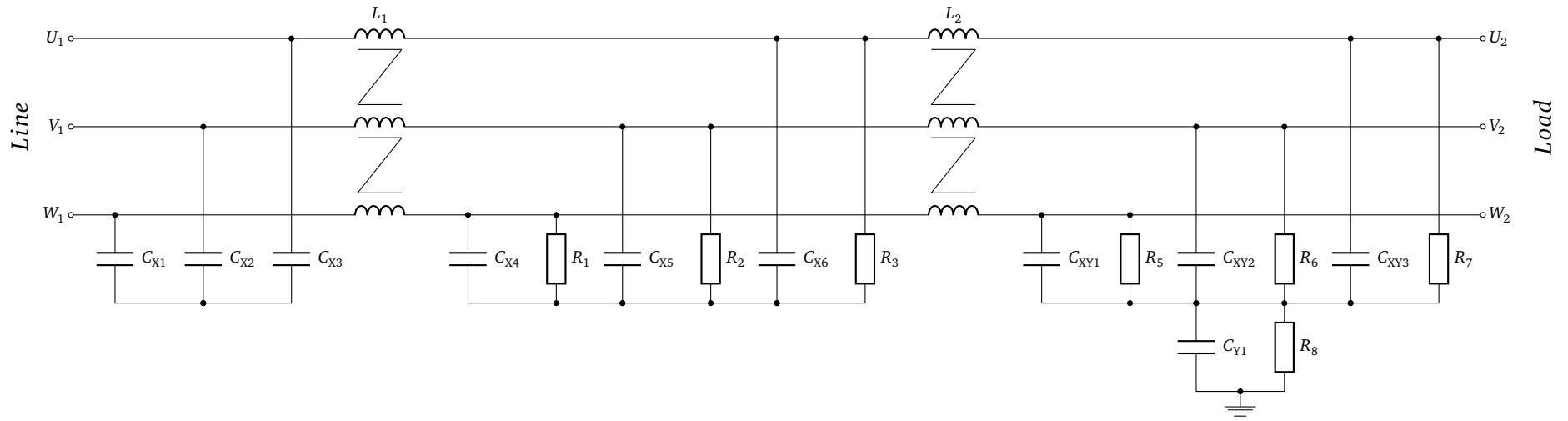


Figure K.2.: Filter 2: Γ -topology for CM and a $CLCLC$ -topology for DM.

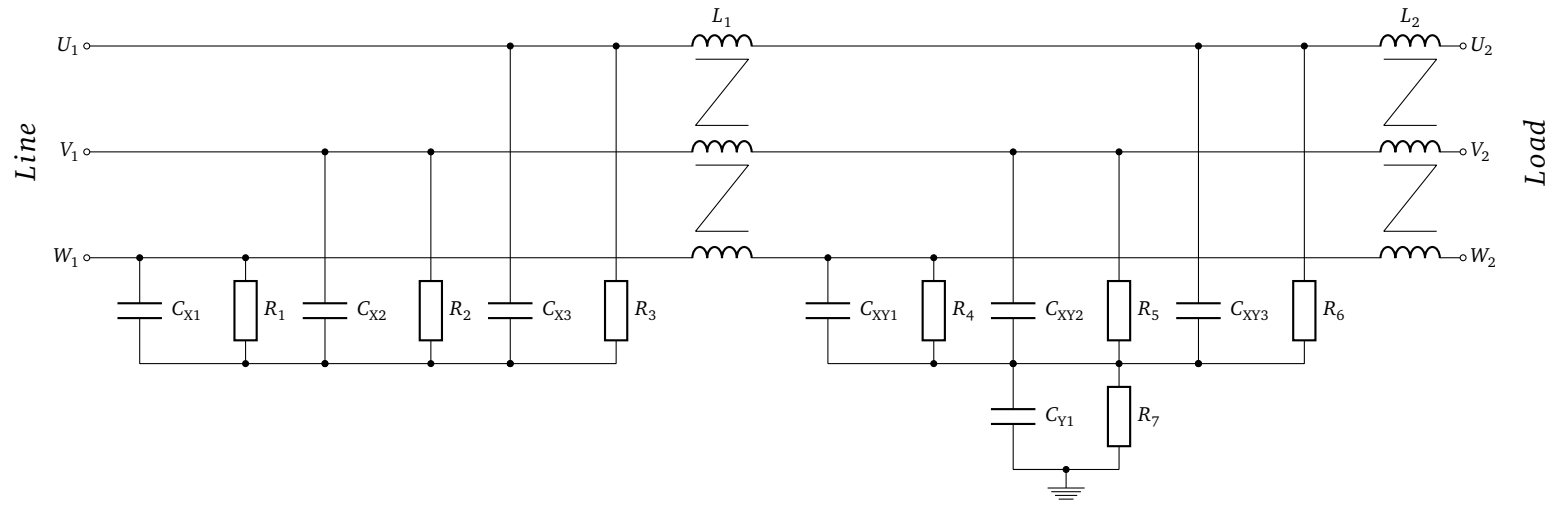


Figure K.3.: Filter 3: *T*-topology for CM and a *CLCL*-topology for DM.

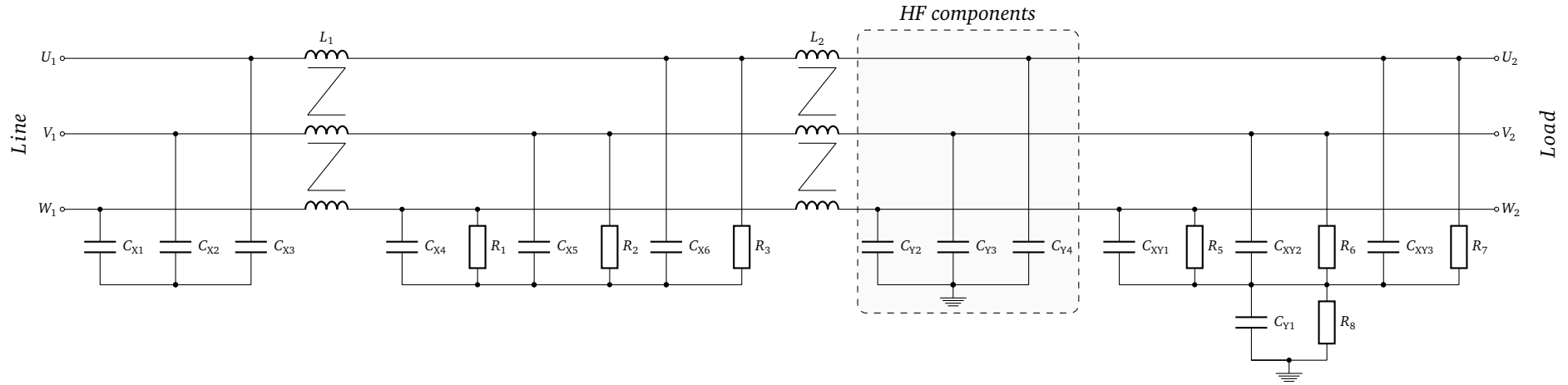


Figure K.4.: Filter 2 improved: T -topology for CM and a $CLCL$ -topology for DM.

Bibliography

- [1] *Energy Efficiency in Electric Motor Systems: Technology, saving potentials and policy options for developing countries*. Vienna, 2012.
- [2] A. ROC'H, D. ZHAO, B. FERREIRA and F.B.J. LEFERINK: *Scale and weight consideration of emi filters*. In *Proceedings ESA Workshop on Aerospace EMC*, pp. 1–5, Los Alamitos, 2009. IEEE EMC Society Press.
- [3] AHMED, M. R., R. TODD and A. J. FORSYTH: *Analysis of SiC MOSFETs under hard and soft-switching*. In *2015 IEEE Energy Conversion Congress and Exposition*, pp. 2231–2238.
- [4] ALBERT-MIQUEL SÁNCHEZ DELGADO: *Electric-Device Characterization for Interference Prediction and Mitigation by an Optimal Filtering Design*. 2009.
- [5] ANNETE MUETZE: *Bearing Currents in Inverter-Fed AC-Motors*. Darmstadt, 2009.
- [6] ANTONIALI, M. and A. M. TONELLO: *Measurement and Characterization of Load Impedances in Home Power Line Grids*. *IEEE Transactions on Instrumentation and Measurement*, 63(3):548–556, 2014.
- [7] ASMANIS, G., A. ASMANIS and D. STEPINS: *Mutual couplings in three phase T-type EMI filters*. In *2012 International Symposium on Electromagnetic Compatibility - EMC EUROPE*, pp. 1–6.
- [8] ASMANIS, G., L. RIBICKIS, D. STEPINS and A. ASMANIS: *Differential mode π -type EMI filter modeling using CST MWS*. In *2015 56th International Scientific Conference on Power and Electrical Engineering of Riga Technical University (RTUCON)*, pp. 1–5.
- [9] ASMANIS, G., D. STEPINS, A. ASMANIS and L. RIBICKIS: *Mutual couplings between EMI filter components*. In *2015 IEEE International Symposium on Electromagnetic Compatibility - EMC 2015*, pp. 908–913.
- [10] AXELROD, A.: *Experimental study of DM-to-CM and vice-versa conversion effects in balanced signal and power line filters*. In *2003 IEEE International Symposium on Electromagnetic Compatibility, 2003. EMC '03*, pp. 599–602 Vol.1.
- [11] AZMI, S. A., K. H. AHMED, S. J. FINNEY and B. W. WILLIAMS: *Comparative analysis between voltage and current source inverters in grid-connected application*. In *IET Conference on Renewable Power Generation (RPG 2011)*, p. 101, 6-8 Sept. 2011.
- [12] BENABOU, A., S. CLÉNET and F. PIRIOU: *Comparison of Preisach and Jiles–Atherton models to take into account hysteresis phenomenon for finite element analysis*. *Journal of Magnetism and Magnetic Materials*, 261(1-2):139–160, 2003.
- [13] BERTOTTI, G.: *Physical interpretation of eddy current losses in ferromagnetic materials. I. Theoretical considerations*. *Journal of Applied Physics*, 57(6):2110, 1985.

-
- [14] BERTOTTI, G., F. FIORILLO and P. MAZZETTI: *Basic principles of magnetization processes and origin of losses in soft magnetic materials*. *Journal of Magnetism and Magnetic Materials*, 112(1-3):146–149, 1992.
- [15] BINDRA, A.: *Wide-Bandgap-Based Power Devices: Reshaping the power electronics landscape*. *IEEE Power Electronics Magazine*, 2(1):42–47, 2015.
- [16] BLAABJERG, F.: *Snubbers in PWM-VSI-inverter*. In *PESC '91 Record 22nd Annual IEEE Power Electronics Specialists Conference*, pp. 104–111, 24-27 June 1991.
- [17] BLAABJERG, F., M. P. KAŻMIERKOWSKI and R. KRISHNAN (eds.): *Control in power electronics: Selected problems*. Academic Press series in engineering. Academic Press, Amsterdam, New York, 2002.
- [18] BOCK, M.: *Analyse von Streugrößen in 2-Level Wechselrichtern*. Bachelorarbeit, TU Darmstadt, Darmstadt, 01.02.2016.
- [19] BOSE, B. K.: *Modern power electronics and AC drives*. Prentice Hall, Upper Saddle River, NJ, 2002.
- [20] BRENNAN, P. V.: *Residual current device with high immunity to nuisance tripping*. *IEE Proceedings G Circuits, Devices and Systems*, 140(2):140, 1993.
- [21] CADIRCI, I., B. SAKA and Y. ERISTIREN: *Practical EMI-filter-design procedure for high-power high-frequency SMPS according to MIL-STD 461*. *IEE Proceedings - Electric Power Applications*, 152(4):775, 2005.
- [22] CAPONET, M. C., F. PROFUMO, R. W. DE DONCKER and A. TENCONI: *Low stray inductance bus bar design and construction for good EMC performance in power electronic circuits*. *IEEE Transactions on Power Electronics*, 17(2):225–231, 2002.
- [23] CHEN, H. and Z. QIAN: *Modeling and Characterization of Parasitic Inductive Coupling Effects on Differential-Mode EMI Performance of a Boost Converter*. *IEEE Transactions on Electromagnetic Compatibility*, 53(4):1072–1080, 2011.
- [24] CHEN, H., Z. QIAN, Z. ZENG and C. WOLF: *Modeling of Parasitic Inductive Couplings in a Pi-Shaped Common Mode EMI Filter*. *IEEE Transactions on Electromagnetic Compatibility*, 50(1):71–79, 2008.
- [25] CHU, Y., S. WANG, N. ZHANG and D. FU: *A Common Mode Inductor With External Magnetic Field Immunity, Low-Magnetic Field Emission, and High-Differential Mode Inductance*. *IEEE Transactions on Power Electronics*, 30(12):6684–6694, 2015.
- [26] COEY, J. M. D.: *Magnetism and magnetic materials*. Cambridge Univ. Press, Cambridge, Repr ed., 2013.
- [27] COSTA, F., E. LABOURE and B. REVOL: *Electromagnetic compatibility in power electronics*. ISTE. Wiley-ISTE, London, 1. Aufl. ed., 2014.
- [28] COSTA, F., C. VOLLAIRE and R. MEURET: *Modeling of Conducted Common Mode Perturbations in Variable-Speed Drive Systems*. *IEEE Transactions on Electromagnetic Compatibility*, 47(4):1012–1021, 2005.

-
- [29] CREE: *Design Considerations for Designing with Cree SiC Modules: Part 1. Understanding the Effects of Parasitic Inductance*. 2012.
- [30] CREE: *Design Considerations for Designing with Cree SiC Modules: Part 2. Techniques for Minimizing Parasitic Inductance*. 2013.
- [31] CZAPŃ, S.: *The impact of higher-order harmonics on tripping of residual current devices*. In *2008 13th International Power Electronics and Motion Control Conference (EPE/PEMC 2008)*, pp. 2059–2065.
- [32] DALESSANDRO, L., F. DA SILVEIRA CAVALCANTE and J. W. KOLAR: *Self-Capacitance of High-Voltage Transformers*. *IEEE Transactions on Power Electronics*, 22(5):2081–2092, 2007.
- [33] DE-OLIVEIRA, T., J.-L. SCHANEN, J.-M. GUICHON and L. GERBAUD: *Optimal Stray Magnetic Couplings for EMC Filters*. *IEEE Transactions on Industry Applications*, 49(4):1619–1627, 2013.
- [34] DELLA TORRE, F., S. LEVA and A. P. MORANDO: *A Physical Decomposition of Three-Phase Variables into Common and Differential Mode Quantities*. In *2007 18th International Zurich Symposium on Electromagnetic Compatibility*, pp. 127–130.
- [35] DEMIRDELEN, T., M. INCI, K. C. BAYINDIR and M. TUMAY: *Review of hybrid active power filter topologies and controllers*. In *2013 IV International Conference on Power Engineering, Energy and Electrical Drives (POWERENG)*, pp. 587–592.
- [36] DENG, J. and K. Y. SEE: *In-Circuit Characterization of Common-Mode Chokes*. *IEEE Transactions on Electromagnetic Compatibility*, 49(2):451–454, 2007.
- [37] DI PIAZZA, M. C., M. LUNA, A. RAGUSA and G. VITALE: *An improved common mode active filter for EMI reduction in vehicular motor drives*. In *2011 IEEE Vehicle Power and Propulsion Conference (VPPC)*, pp. 1–8.
- [38] DIMIAN, M. and P. ANDREI: *Noise-Driven Phenomena in Hysteretic Systems*, vol. 218. Springer New York, New York, NY, 2014.
- [39] DO, T. T., M. JORDAN, H. LANGKOWSKI and D. SCHULZ: *Novel grid impedance measurement setups in electrical power systems*. In *2016 IEEE International Workshop on Applied Measurements for Power Systems (AMPS)*, pp. 1–6.
- [40] DONGBING ZHANG, D. Y. CHEN and D. SABLE: *A new method to characterize EMI filters*. 1998.
- [41] DR. PETER FRIEDRICHS, INFINEON TECHNOLOGIES: *ECPE Position Paper: Next Generation Power Electronics based on Wide Bandgap Devices Challenges and Opportunities for Europe*. 2015.
- [42] DRINOVSKY, J., J. SVACINA, M. ZAMAZAL, T. URBANEC and J. LACIK: *Variable Impedance in Measuring EMI Filter's Insertion Loss*. In *2005 Asia-Pacific Conference on Communications*, pp. 24–27, 03-05 Oct. 2005.
- [43] DROZHZHIN, D., G. GRIEPENTROG, A. SAUER, R. DE MAGLIE and A. ENGLER: *Suppression of conducted, high frequency signals in aerospace DC/AC converters designed with SiC MOSFETs*. In *2016 18th European Conference on Power Electronics and Applications (EPE'16 ECCE Europe)*, pp. 1–10.

-
- [44] ELECTRONICON: *PK16TM and E61 HIGH DENSITY DC FILM CAPACITORS: DC KONDENSATOREN MIT HOHER ENERGIEDICHTE*. 2016.
- [45] EPCOS AG: *Ferrites and accessories: SIFERRIT material K8*. 2006.
- [46] EPCOS AG: *Ferrites and accessories: SIFERRIT material N87*. 2006.
- [47] EPCOS AG: *Ferrites and accessories: SIFERRIT material T65*. 2006.
- [48] EPCOS AG: *Ferrites and accessories: es and accessories Toroids R 41.8 × 26.2 × 12.5*. 2014.
- [49] EPCOS AG: *Film Capacitors: EMI Suppression Capacitors (MKP)*. 2014.
- [50] EPCOS AG: *Film Capacitors: EMI Suppression Capacitors (MKP)*. 2016.
- [51] EPCOS AG: *Film Capacitors: EMI Suppression Capacitors (MKP)*. 2016.
- [52] ERICKSON, R. W.: *Optimal single resistors damping of input filters*. In *APEC '99. Fourteenth Annual Applied Power Electronics Conference and Exposition. 1999 Conference Proceedings (Cat. No.99CH36285)*, pp. 1073–1079 vol.2.
- [53] ERICKSON, R. W. and D. MAKSIMOVIĆ: *Fundamentals of Power Electronics*. Kluwer Academic Publishers, Boston, MA, Second Edition ed., 2004.
- [54] ESKANDARI-TORBATI, H. and D. ARAB KHABURI: *Direct Power Control of three phase PWM rectifier using Model Predictive Control and SVM switching*. In *2013 4th Power Electronics, Drive Systems & Technologies Conference (PEDSTC)*, pp. 193–198.
- [55] ESTERLY, S. and R. GELMAN: *2013 Renewable Energy Data Book (Book). Energy Efficiency & Renewable Energy (EERE)*. NREL, Washington, DC, 2014.
- [56] FAN, Z., Y. ZHI, B. ZHU, G. YAN and Y. SHI: *Research of bearing voltage and bearing current in induction motor drive system*. In *2016 Asia-Pacific International Symposium on Electromagnetic Compatibility (APEMC)*, pp. 1195–1198.
- [57] FENG, S., W. SANDER and T. WILSON: *Small-capacitance nondissipative ripple filters for DC supplies*. *IEEE Transactions on Magnetics*, 6(1):137–142, 1970.
- [58] G. I. ROZMAN: *Input EMI filter for motor drive including an active rectifier*, 2015.
- [59] GOLDMAN, A.: *Modern Ferrite Technology*. Springer, Dordrecht, 2006.
- [60] GUBIA, E., P. SANCHIS, A. URSUA, J. LOPEZ and L. MARROYO: *Frequency Domain Model of Conducted EMI in Electrical Drives*. *IEEE Power Electronics Letters*, 3(2):45–49, 2005.
- [61] GUNDARS ASMANIS: *Measurement and modeling of EMI filter high frequency parasitic parameters*. Riga, 2014.
- [62] GUO, T., D. Y. CHEN and F. C. LEE: *Separation of the common-mode- and differential-mode-conducted EMI noise*. *IEEE Transactions on Power Electronics*, 11(3):480–488, 1996.

-
- [63] HABIGER, E.: *Elektromagnetische Verträglichkeit: Grundzüge ihrer Sicherstellung in der Geräte- und Anlagentechnik*. Hüthig, Heidelberg, 1992.
- [64] HARTMANN, M., H. ERTL and J. W. KOLAR: *EMI Filter Design for a 1 MHz, 10 kW Three-Phase Level PWM Rectifier*. Vol. 26, pp. 1192–1204.
- [65] HARTMANN, M., H. ERTL and J. W. KOLAR: *EMI filter design for high switching frequency three-phase level PWM rectifier systems*. In *2010 IEEE Applied Power Electronics Conference and Exposition - APEC 2010*, pp. 986–993.
- [66] HELDWEIN, M. L.: *EMC filtering of three-phase PWM converters: Three-phase line filter concepts and design for modern power electronics*. Südwestdeutscher Verlag für Hochschulschriften, Saarbrücken, 2009.
- [67] HELDWEIN, M. L., L. DALESSANDRO and J. W. KOLAR: *The Three-Phase Common-Mode Inductor: Modeling and Design Issues*. *IEEE Transactions on Industrial Electronics*, 58(8):3264–3274, 2011.
- [68] HELDWEIN, M. L. and J. W. KOLAR: *Winding Capacitance Cancellation for Three-Phase EMC Input Filters*. *IEEE Transactions on Power Electronics*, 23(4):2062–2074, 2008.
- [69] HELDWEIN, M. L. and J. W. KOLAR: *Impact of EMC Filters on the Power Density of Modern Three-Phase PWM Converters*. *IEEE Transactions on Power Electronics*, 24(6):1577–1588, 2009.
- [70] HELDWEIN, M. L., T. NUSSBAUMER, F. BECK and J. W. KOLAR: *Novel three-phase CM/DM conducted emissions separator*. In *APEC 2005. Twentieth Annual IEEE Applied Power Electronics Conference and Exposition*, pp. 797–802, 6-10 March 2005.
- [71] HELDWEIN, M. L., T. NUSSBAUMER and J. W. KOLAR: *Differential mode EMC input filter design for three-phase AC-DC-AC sparse matrix PWM converters*. In *PESCO4*, pp. 284–291, Piscataway, N.J., 2004. IEEE.
- [72] HERMAN, H.: *Treatise on Materials Science and Technology: Ultrarapid Quenching of Liquid Alloys*. Elsevier Science, Oxford, 1981.
- [73] HERZER, G.: *Grain structure and magnetism of nanocrystalline ferromagnets*. *IEEE Transactions on Magnetics*, 25(5):3327–3329, 1989.
- [74] HILZINGER, R. and W. RODEWALD: *Magnetic materials: Fundamentals, products, properties, and applications*. Erlangen, 2013.
- [75] HOENE, E., A. LISSNER and S. GUTTOWSKI: *Prediction of EMI behaviour in terms of passive component placement*. In *Electromagnetic Compatibility, 2007. EMC Zurich 2007. 18th International Zurich Symposium on*, pp. 49–52, 2007.
- [76] HOENE, E., A. LISSNER, S. WEBER, S. GUTTOWSKI, W. JOHN and H. REICHL: *Simulating Electromagnetic Interactions in High Power Density Converters*. In *IEEE 36th Conference on Power Electronics Specialists, 2005*, pp. 1665–1670, June 12, 2005.

-
- [77] HOFFMANN, N. and F. W. FUCHS: *Minimal Invasive Equivalent Grid Impedance Estimation in Inductive–Resistive Power Networks Using Extended Kalman Filter*. IEEE Transactions on Power Electronics, 29(2):631–641, 2014.
- [78] HOFMANN, W. and J. ZITZELSBERGER: *PWM-control methods for common mode voltage minimization - a survey*. In *International Symposium on Power Electronics, Electrical Drives, Automation and Motion, 2006. SPEEDAM 2006*, pp. 1162–1167, May, 23rd - 26th, 2006.
- [79] HOLMES, D. G. and T. A. LIPO: *Pulse width modulation for power converters: Principles and practice*. IEEE Press series on power engineering. Wiley-Interscience IEEE Press, Hoboken, New Jersey and Piscataway, New Jersey, 2003.
- [80] HOU, C.-C., C.-C. SHIH, P.-T. CHENGT and A. M. HAVA: *Common-mode voltage reduction modulation techniques for three-phase grid connected converters*. In *2010 International Power Electronics Conference (IPEC - Sapporo)*, pp. 1125–1131.
- [81] HUANG, H.-F., L.-Y. DENG, B.-J. HU and G. WEI: *Techniques for Improving the High-Frequency Performance of the Planar CM EMI Filter*. IEEE Transactions on Electromagnetic Compatibility, 55(5):901–908, 2013.
- [82] HURLEY, W. G. and W. H. WÖLFLE: *Transformers and inductors for power electronics: Theory, design and applications*. Wiley, Chichester, Reprint. with corr ed., 2014.
- [83] I. N. MANUSHYN: *Model-based design of EMI filters for power electronics converters with cst studio suite*. Component and Technologies, 2018(1):118–126.
- [84] I. N. MANUSHYN, G. J. GRIEPENTROG: *Assessment and classification of the soft magnetic material cores for emi filter application*. In *Energy Science Technology Karlsruhe 2015*.
- [85] I. N. MANUSHYN, G. J. GRIEPENTROG: *Finite element method based electromagnetic modeling of three-phase EMI filters*. In *2016 IEEE 2nd Annual Southern Power Electronics Conference (SPEC)*, pp. 1–6.
- [86] I. N. MANUSHYN, L. M. KOLEFF, G. J. GRIEPENTROG: *Holistic approach to three-phase EMI filter improvement*. In *PEMD 2016 Glasgow*, pp. 1–6.
- [87] I. N. MANUSHYN, L. M. KOLEFF, G. J. GRIEPENTROG: *Non-ideal model of the common mode choke for EMI filters*. In *2017 IEEE Applied Power Electronics Conference and Exposition (APEC)*, pp. 938–944.
- [88] INTERNATIONAL ELECTROTECHNICAL COMMISSION: *Electromagnetic compatibility (EMC) - Part 1-4: General - Historical rationale for the limitation of power-frequency conducted harmonic current emissions from equipment, in the frequency range up to 2 kHz*, 2005.
- [89] INTERNATIONAL ELECTROTECHNICAL COMMISSION: *Electromagnetic compatibility (EMC) - Part 3-3: Limits - Limitation of voltage changes, voltage fluctuations and flicker in public low-voltage supply systems, for equipment with rated current ≤ 16 A per phase and not subject to conditional connection*, 2008.

-
- [90] INTERNATIONAL ELECTROTECHNICAL COMMISSION: *Information technology equipment - Radio disturbance characteristics - Limits and methods of measurement*, 2008.
- [91] INTERNATIONAL ELECTROTECHNICAL COMMISSION: *Electromagnetic compatibility (EMC) - Part 3-2: Limits - Limits for harmonic current emissions (equipment input current ≤ 16 A per phase)*, 2011.
- [92] INTERNATIONAL ELECTROTECHNICAL COMMISSION: *Methods of measurement of the suppression characteristics of passive EMC filtering devices*, 2011.
- [93] INTERNATIONAL ELECTROTECHNICAL COMMISSION: *Information technology equipment – Safety – Part 1: General requirements*, 2012.
- [94] INTERNATIONAL ELECTROTECHNICAL COMMISSION: *Electromagnetic compatibility (EMC) - Part 4-6: Testing and measurement techniques - Immunity to conducted disturbances, induced by radio-frequency fields*, 2013.
- [95] INTERNATIONAL ELECTROTECHNICAL COMMISSION: *Specification for radio disturbance and immunity measuring apparatus and methods - Part 1-2: Radio disturbance and immunity measuring apparatus - Coupling devices for conducted disturbance measurements*, 2014.
- [96] INTERNATIONAL ELECTROTECHNICAL COMMISSION: *Industrial, scientific and medical equipment - Radio-frequency disturbance characteristics - Limits and methods of measurement*, 2015.
- [97] INTERNATIONAL ELECTROTECHNICAL COMMISSION: *Passive filter units for electromagnetic interference suppression - Part 3: Passive filter units for which safety tests are appropriate*, 2015.
- [98] INTERNATIONAL ELECTROTECHNICAL COMMISSION: *Fixed capacitors for use in electronic equipment - Part 14: Sectional specification - Fixed capacitors for electromagnetic interference suppression and connection to the supply mains*, 2016.
- [99] INTERNATIONAL ELECTROTECHNICAL COMMISSION: *Hand-held motor-operated electric tools - Safety - Part 1: General requirements*, 2016.
- [100] JILES, D. C. and D. L. ATHERTON: *Theory of ferromagnetic hysteresis (invited)*. *Journal of Applied Physics*, 55(6):2115, 1984.
- [101] JONG, E. DE, B. FERREIRA and P. BAUER: *Toward the Next Level of PCB Usage in Power Electronic Converters*. *IEEE Transactions on Power Electronics*, 23(6):3151–3163, 2008.
- [102] K. KOSTOV and J. KYRA: *Common-mode choke coils characterization*. In *Power Electronics and Applications, 2009. EPE '09. 13th European Conference on*, pp. 1–9, 2009.
- [103] KANDA, M., N. OKA and S. NITTA: *Common mode impedance model of power electronic equipment to evaluate noise reduction effect of a line noise filter*. In *2000 International Symposium on Electromagnetic Compatibility (EMC 2000)*, pp. 65–70, 21-25 Aug. 2000.
- [104] KAZIMIERCZUK, M.: *High-Frequency Magnetic Components*. John Wiley & Sons, Ltd, Chichester, UK, 2013.

-
- [105] KAZMIERKOWSKI, M. P. and L. MALESANI: *Current control techniques for three-phase voltage-source PWM converters: A survey*. IEEE Transactions on Industrial Electronics, 45(5):691–703, 1998.
- [106] KEMPSKI, A., R. SMOLENSKI and R. STRZELECKI: *Common mode current paths and their modeling in PWM inverter-fed drives*. In *PESC 2002 - Power Electronics Specialists Conference*, pp. 1551–1556, 23-27 June 2002.
- [107] KEYSIGHT TECHNOLOGIES: *85032F Standard Mechanical Calibration Kit, DC to 9 GHz, Type-N, 50 ohm: 5 Hz to 9 GHz*. 2015.
- [108] KEYSIGHT TECHNOLOGIES: *Network Analyzer E5061B: 5 Hz to 3 GHz*. 2015.
- [109] KLAUS VOGEL, DANIEL DOMES, INFINEON TECHNOLOGIES AG, WARSTEIN, GERMANY.: *IGBT inverter with increased power density by use of a hightemperature-capable and low-inductance design*. PCIM, 24(5), 2012.
- [110] KODALI, V. P.: *Engineering electromagnetic compatibility: Principles, measurements, technologies, and computer models*. Institute of Electrical and Electronics Engineers, New York, 2. ed. ed., 2001.
- [111] KOLAR, J. W., U. DROFENIK, J. BIELA, M. L. HELDWEIN, H. ERTL, T. FRIEDLI and S. D. ROUND: *PWM Converter Power Density Barriers*. In *2007 Power Conversion Conference - Nagoya*, pp. P-9–P-29.
- [112] KOLAR, J. W. and H. ERTL: *Status of the techniques of three-phase rectifier systems with low effects on the mains*. In *21st International Telecommunications Energy Conference. INTELEC '99 (Cat. No.99CH37007)*, p. 279.
- [113] KOLAR, J. W. and T. FRIEDLI: *The essence of three-phase PFC rectifier systems*. In *INTELEC 2011 - 2011 33rd International Telecommunications Energy Conference*, pp. 1–27.
- [114] KOLAR, J. W., F. KRISMER, Y. LOBSIGER, J. MUHLETHALER, T. NUSSBAUMER and J. MINIBOCK: *Extreme efficiency power electronics*. In *Integrated Power Electronics Systems (CIPS), 2012 7th International Conference on*, pp. 1–22, 2012.
- [115] KOSTOV K.: *Design and Characterization of Single-Phase Power Filters*. 2009.
- [116] KOTNY, J.-L., X. MARGUERON and N. IDIR: *High-Frequency Model of the Coupled Inductors Used in EMI Filters*. IEEE Transactions on Power Electronics, 27(6):2805–2812, 2012.
- [117] KOVACEVIC, I., F. KRISMER, S. SCHROTH and J. W. KOLAR: *Practical characterization of EMI filters replacing CISPR 17 approximate worst case measurements*. In *2013 IEEE 14th Workshop on Control and Modeling for Power Electronics (COMPEL)*, pp. 1–10.
- [118] KOVACEVIC, I. F., T. FRIEDLI, A. M. MUESING and J. W. KOLAR: *3-D Electromagnetic Modeling of EMI Input Filters*. IEEE Transactions on Industrial Electronics, 61(1):231–242, 2014.
- [119] KOVACEVIC, I. F., T. FRIEDLI, A. M. MUSING and J. W. KOLAR: *Full PEEC Modeling of EMI Filter Inductors in the Frequency Domain*. IEEE Transactions on Magnetics, 49(10):5248–5256, 2013.

- [120] KOVACEVIC, I. F., A. MUSING and J. W. KOLAR: *PEEC modelling of toroidal magnetic inductor in frequency domain*. In *2010 International Power Electronics Conference (IPEC - Sapporo)*, pp. 3158–3165.
- [121] KOVACIC, M., S. STIPETIC, Z. HANIC and D. ZARKO: *Small-Signal Calculation of Common-Mode Choke Characteristics Using Finite-Element Method*. *IEEE Transactions on Electromagnetic Compatibility*, 57(1):93–101, 2015.
- [122] KUO, F. F.: *Network analysis and synthesis*. Wiley, New York NY u.a., 2. ed. ed., 1966.
- [123] KUT, T., A. LÜCKEN, S. DICKMANN and D. SCHULZ: *Common mode chokes and optimisation aspects*. *Advances in Radio Science*, 12:143–148, 2014.
- [124] KYRÄ, J. J. and K. S. KOSTOV: *Insertion loss in terms of four-port network parameters*. *IET Science, Measurement & Technology*, 3(3):208–216, 2009.
- [125] LAFONTAINE, J.: *Common-mode filtering device and speed variator comprising such a device*, 2011.
- [126] LI, J. and Y. HUANG: *Time-Domain Finite Element Methods for Maxwell's Equations in Metamaterials*, vol. 43. Springer Berlin Heidelberg, Berlin, Heidelberg, 2013.
- [127] LISERRE, M., A. DELL'AQUILA and F. BLAABJERG: *An overview of three-phase voltage source active rectifiers interfacing the utility*. In *2003 IEEE Bologna Power Tech*, pp. 284–291, June 23-26, 2003.
- [128] LISSNER, A., E. HOENE, B. STUBE and S. GUTTOWSKI: *Predicting the influence of placement of passive components on EMI behaviour*. In *Power Electronics and Applications, 2007 European Conference on*, pp. 1–10, 2007.
- [129] LIU, D. H. and J. G. JIANG: *High frequency characteristic analysis of EMI filter in switch mode power supply (SMPS)*. In *PESC 2002 - Power Electronics Specialists Conference*, pp. 2039–2043, 23-27 June 2002.
- [130] LIU DEHONG and JIANG XANGUO: *High frequency model of common mode inductor for EMI analysis based on measurements*. In *Electromagnetic Compatibility, 2002 3rd International Symposium on*, pp. 462–465, 2002.
- [131] LUO, F., D. BOROYEVICH and P. MATTAVELLI: *Improving EMI filter design with in circuit impedance mismatching*. In *2012 IEEE Applied Power Electronics Conference and Exposition - APEC 2012*, pp. 1652–1658.
- [132] LUO, F., D. DONG, D. BOROYEVICH, P. MATTAVELLI and S. WANG: *Improving High-Frequency Performance of an Input Common Mode EMI Filter Using an Impedance-Mismatching Filter*. *IEEE Transactions on Power Electronics*, 29(10):5111–5115, 2014.
- [133] LUSZCZ, J.: *High frequency harmonics emission of modern power electronic AC-DC converters*. In *2013 International Conference on Compatibility and Power Electronics (CPE)*, pp. 269–274.
- [134] MAGNETEC: *Product specification for inductive components: M-006*. 2014.

-
- [135] MASSARINI, A. and M. K. KAZIMIERCZUK: *Self-capacitance of inductors*. IEEE Transactions on Power Electronics, 12(4):671–676, 1997.
- [136] MOHAN, N., T. M. UNDELAND and W. P. ROBBINS: *Power electronics: Converters, applications, and design*. Wiley, Hoboken, NJ, Media enhanced 3. ed., [Nachdr.] ed., ca. 2007.
- [137] MONTROSE, M. I. and E. M. NAKAUCHI: *Testing for EMC compliance: Approaches and techniques*. IEEE Press, Piscataway, NJ, 2004.
- [138] MOONEN, N., F. BUESINK and F. LEFERINK: *Unexpected poor performance of presumed high-quality power line filter, and how it improved*. In *2015 IEEE International Symposium on Electromagnetic Compatibility - EMC 2015*, pp. 382–385.
- [139] MUETZE, A.: *On a New Type of Inverter-Induced Bearing Current in Large Drives with Oil-Lubricated Bearings*. In *2008 IEEE Industry Applications Society Annual Meeting (IAS)*, pp. 1–8.
- [140] MUETZE, A. and E. G. STRANGAS: *On inverter induced bearing currents, bearing maintenance scheduling, and prognosis*. In *2014 XXI International Conference on Electrical Machines (ICEM)*, pp. 1915–1921.
- [141] MUETZE, A. and C. R. SULLIVAN: *Simplified Design of Common-Mode Chokes for Reduction of Motor Ground Currents in Inverter Drives*. IEEE Transactions on Industry Applications, 47(6):2570–2577, 2011.
- [142] MUNIR, H. A., M. JENU and M. ABDULLAH: *Analysis and design of EMI filters to mitigate conducted emissions*. In *2002 Student Conference on Research and Development. SCORED2002.. Global Research and Development in Electrical and Electronics Engineering*, pp. 204–207, 16-17 July 2002.
- [143] MURALIDHARA, B., A. RAMACHANDRAN, R. SRINIVASAN and M. C. REDDY: *Experimental measurement of shaft voltage and bearing current in an inverter fed three phase induction motor drive*. In *2011 3rd International Conference on Electronics Computer Technology (ICECT)*, pp. 37–41.
- [144] MUTOH, N., M. KANESAKI, J. NAKASHIMA and M. OGATA: *A new method to control common mode currents focusing on common mode current paths produced in motor drive systems*. In *Conference Record of the 2003 IEEE Industry Applications Conference. 38th IAS Annual Meeting*, pp. 459–466, 12-16 Oct. 2003.
- [145] NAGEL, A. and R. W. DE DONCKER: *Systematic design of EMI-filters for power converters*. In *World Congress on Industrial Applications of Electrical Energy and 35th IEEE-IAS Annual Meeting*, pp. 2523–2525, 8-12 Oct. 2000.
- [146] NAVE, M. J.: *On Modeling the Common Mode Inductor*. In *IEEE 1991 International Symposium on Electromagnetic Compatibility*, pp. 452–457, 12-16 Aug. 1991.
- [147] NEUGEBAUER, T. C. and D. J. PERREAULT: *Filters With Inductance Cancellation Using Printed Circuit Board Transformers*. IEEE Transactions on Power Electronics, 19(3):591–602, 2004.
- [148] NEUGEBAUER, T. C. and D. J. PERREAULT: *Parasitic capacitance cancellation in filter inductors*. IEEE Transactions on Power Electronics, 21(1):282–288, 2006.

-
- [149] NEUGEBAUER, T. C., J. W. PHINNEY and D. J. PERREAULT: *Filters and components with inductance cancellation*. In *2002 IEEE Industry Applications Society Annual Meeting*, pp. 939–947, 13-18 Oct. 2002.
- [150] NING ZHU, JINSONG KANG, DEWEI XU, BIN WU and YUAN XIAO: *An Integrated AC Choke Design for Common-Mode Current Suppression in Neutral-Connected Power Converter Systems*. *IEEE Transactions on Power Electronics*, 27(3):1228–1236, 2012.
- [151] NITSCH, J., F. GRONWALD and G. WOLLENBERG: *Radiating Nonuniform Transmissionline Systems and the Partial Element Equivalent Circuit Method*. John Wiley & Sons, Ltd, Chichester, UK, 2009.
- [152] NUSSBAUMER, T., M. L. HELDWEIN and J. W. KOLAR: *Common Mode EMC Input Filter Design for a Three-Phase Buck-Type PWM Rectifier System*. In *Twenty-First Annual IEEE Applied Power Electronics Conference and Exposition, 2006. APEC '06*, pp. 1617–1623, March 19, 2006.
- [153] OTT, H. W.: *Electromagnetic compatibility engineering*. John Wiley & Sons, Hoboken, N.J., 2009.
- [154] OTTERSTEN, R.: *On control of back-to-back converters and sensorless induction machine drivers: Univ. Diss.–Göteborg, 2003*, vol. 450 of *Technical report / School of Electrical Engineering, Chalmers University of Technology*. Chalmers Univ. of Technology, Göteborg, 2003.
- [155] OZENBAUGH, R. L. and T. M. PULLEN: *EMI filter design*. Taylor & Francis, Boca Raton, FL, 3rd ed. ed., 2012.
- [156] PASKO, S. and B. GRZESIK: *High frequency model of EMI filter*. *Electronics ETF*, 16(1), 2012.
- [157] PASKO, S. W., M. K. KAZIMIERCZUK and B. GRZESIK: *Self-Capacitance of Coupled Toroidal Inductors for EMI Filters*. *IEEE Transactions on Electromagnetic Compatibility*, 57(2):216–223, 2015.
- [158] PAUL, C. R.: *Introduction to electromagnetic compatibility*. Wiley series in microwave and optical engineering. Wiley, Hoboken, NJ, 2. ed. ed., 2006.
- [159] PÉREZ, A., A.-M. SÁNCHEZ, J.-R. REGUÉ, M. RIBÓ, P. RODRÍGUEZ-CEPEDA and F.-J. PAJARES: *Characterization of Power-Line Filters and Electronic Equipment for Prediction of Conducted Emissions*. *IEEE Transactions on Electromagnetic Compatibility*, 50(3):577–585, 2008.
- [160] PIBOONWATTANAKIT, K. and W. KHAN-NGERN: *Parasitic capacitance cancellation of filter in power supply using mutual capacitance technique*. In *2008 5th International Conference on Electrical Engineering/Electronics, Computer, Telecommunications and Information Technology (ECTI-CON)*, pp. 1025–1028.
- [161] PIERQUET, B. J., T. C. NEUGEBAUER and D. J. PERREAULT: *Inductance Compensation of Multiple Capacitors With Application to Common- and Differential-Mode Filters*. *IEEE Transactions on Power Electronics*, 21(6):1815–1824, 2006.
- [162] PIERQUET, B. J., T. C. NEUGEBAUER and D. J. PERREAULT: *A Fabrication Method for Integrated Filter Elements With Inductance Cancellation*. *IEEE Transactions on Power Electronics*, 24(3):838–848, 2009.

-
- [163] QIAN LIU: *Modular Approach for Characterizing and Modeling Conducted EMI Emissions in Power Converters*. 2005.
- [164] RADIALL: *Cable Assembly: RG214 Coaxial Cable, Connector to Connector N, 50 Ohm, 1m.*. 2007.
- [165] RAGGL, K., T. NUSSBAUMER and J. W. KOLAR: *Model based optimization of EMC input filters*. In *2008 11th Workshop on Control and Modeling for Power Electronics (COMPEL)*, pp. 1–6.
- [166] RAN, L., S. GOKANI, J. CLARE, K. J. BRADLEY and C. CHRISTOPOULOS: *Conducted electromagnetic emissions in induction motor drive systems. I. Time domain analysis and identification of dominant modes*. *IEEE Transactions on Power Electronics*, 13(4):757–767, 1998.
- [167] RASHID, M. H. (ed.): *Power electronics handbook: Devices, circuits, and applications*. Butterworth-Heinemann, Burlington, MA, 3rd ed. ed., 2011.
- [168] REBHOLZ, H. and S. TENBOHLEN: *Prospects and limits of common- and differential-mode separation for the filter development process*. In *2008 International Symposium on Electromagnetic Compatibility - EMC Europe*, pp. 1–6.
- [169] REDDY, S. and B. BASAVARAJA: *Simulation and analysis of common mode voltage, bearing voltage and bearing current in two-level and three-level PWM inverter fed induction motor drive with long cable*. In *2015 International Conference on Power and Advanced Control Engineering (ICPACE)*, pp. 221–226.
- [170] RENGANG CHEN: *Integrated EMI Filters for Switch Mode Power Supplies*. Blacksburg, Virginia, 2004.
- [171] RICCOBONO, A., S. K. A. NAQVI, A. MONTI, T. CALDOGNETTO, J. SIEGERS and E. SANTI: *Online wideband identification of single-phase AC power grid impedances using an existing grid-tied power electronic inverter*. In *2015 IEEE 6th International Symposium on Power Electronics for Distributed Generation Systems (PEDG)*, pp. 1–8.
- [172] RIXIN LAI, Y. MAILLET, F. WANG, SHUO WANG, R. BURGOS and D. BOROYEVICH: *An Integrated EMI Choke for Differential-Mode and Common-Mode Noise Suppression*. *IEEE Transactions on Power Electronics*, 25(3):539–544, 2010.
- [173] ROC'H, A., H. BERGSMA, DONGSHENG ZHAO, B. FERREIRA and F. LEFERINK: *Comparison of evaluated and measured performances of common mode chokes*. In *Electromagnetic Compatibility - EMC Europe, 2008 International Symposium on*, pp. 1–5, 2008.
- [174] RODRIGUEZ, J. R., J. W. DIXON, J. R. ESPINOZA, J. PONTT and P. LEZANA: *PWM regenerative rectifiers: State of the art*. *IEEE Transactions on Industrial Electronics*, 52(1):5–22, 2005.
- [175] RODRÍGUEZ PÉREZ, J. and P. C. ESTAY: *Predictive control of power converters and electrical drives*. IEEE, Chichester, West Sussex, s.l., 2012.
- [176] ROHM SEMICONDUCTOR: *SiC Power Devices and Modules: Application Note*. 2013.
- [177] SÁNCHEZ, A. M., A. PÉREZ, J. R. REGUÉ, M. RIBÓ, P. RODRÍGUEZ-CEPEDA and F. J. PAJARES: *A Modal Model of Common-Mode Chokes for Conducted Interference Prediction*. *IEEE Transactions on Electromagnetic Compatibility*, 52(3):749–752, 2010.

-
- [178] SCHAFFNER GROUP: *Leakage Currents in Power Line Filters*. 2008.
- [179] SCHAFFNER GROUP: *3-Phase Filters FN 3100: EMC/EMI Filter for Regenerative Motor Drives*. 2014.
- [180] SCHAFFNER GROUP: *3-Phase Filters FN 3258: Ultra-compact EMC/RFI Filter for Motor Drives Applications*. 2014.
- [181] SCHLIEWE J., SCHEFLER S. AND WEBER S.: *Simulating Saturation Behavior of Inductive Components*. In *PCIM Europe 2014*, pp. 1–8.
- [182] SCHRÖDER, D.: *Leistungselektronische Bauelemente*. Springer-Verlag Berlin Heidelberg, Berlin, Heidelberg, Zweite Auflage ed., 2006.
- [183] SCHWAB, A. J. and W. KÜRNER: *Elektromagnetische Verträglichkeit*. Springer-Verlag Berlin Heidelberg, Berlin Heidelberg, 5., aktualisierte und ergänzte Auflage ed., 2007.
- [184] SCHWEIZER, M., T. FRIEDLI and J. W. KOLAR: *Comparative Evaluation of Advanced Three-Phase Three-Level Inverter/Converter Topologies Against Two-Level Systems*. *IEEE Transactions on Industrial Electronics*, 60(12):5515–5527, 2013.
- [185] SENINI, S. and P. J. WOLFS: *The coupled inductor filter: Analysis and design for AC systems*. *IEEE Transactions on Industrial Electronics*, 45(4):574–578, 1998.
- [186] SHANCHENG, X. and W. ZHENG GUO: *Characteristic Research of Bearing Currents in Inverter-Motor Drive Systems*. In *2006 5th International Power Electronics and Motion Control Conference (IPEMC 2006)*, pp. 1–4.
- [187] SHARKH, S. M., B. HUSSAIN, G. I. ORFANOUDAKIS and M. A. ABUSARA: *Power electronic converters for microgrids*. Wiley, Singapore, 2014.
- [188] SHEN, W., F. WANG and D. BOROYEVICH: *Conducted EMI characteristic and its implications to filter design in 3-phase diode front-end converters*. In *Conference Record of the 2004 IEEE Industry Applications Conference, 2004. 39th IAS Annual Meeting*, pp. 1840–1846, 3-7 Oct. 2004.
- [189] SHENAI, K.: *Future Prospects of Widebandgap (WBG) Semiconductor Power Switching Devices*. *IEEE Transactions on Electron Devices*, 62(2):248–257, 2015.
- [190] SHUO WANG: *Characterization and Cancellation of High-Frequency Parasitics for EMI Filters and Noise Separators in Power Electronics Applications*. Blacksburg, Virginia, 2005.
- [191] SHUO WANG, F. C. LEE and W. G. ODENDAAL: *Controlling the parasitic parameters to improve EMI filter performance*. In *Nineteenth Annual IEEE Applied Power Electronics Conference and Exposition, 2004. APEC '04*, pp. 503–509, 22-26 Feb. 2004.
- [192] SHUO WANG, F. C. LEE and J. D. VAN WYK: *A Study of Integration of Parasitic Cancellation Techniques for EMI Filter Design With Discrete Components*. *IEEE Transactions on Power Electronics*, 23(6):3094–3102, 2008.

-
- [193] SHUO WANG, W. G. ODENDAAL and F. C. LEE: *Extraction of parasitic parameters of EMI filters using scattering parameters*. In *Industry Applications Conference, 2004. 39th IAS Annual Meeting. Conference Record of the 2004 IEEE*, vol. 4, pp. 2672–2678 vol.4, 2004.
- [194] SINGH, B., B. N. SINGH, A. CHANDRA, K. AL-HADDAD, A. PANDEY and D. P. KOTHARI: *A Review of Three-Phase Improved Power Quality AC–DC Converters*. *IEEE Transactions on Industrial Electronics*, 51(3):641–660, 2004.
- [195] SPECOVIVUS, J.: *Grundkurs Leistungselektronik: Bauelemente, Schaltungen und Systeme*. Springer, Wiesbaden, 6., akt. u. überarb. Aufl. 2013 ed., 2013.
- [196] SWAMY, M. M., K. YAMADA and T. KUME: *Common mode current attenuation techniques for use with PWM drives*. *IEEE Transactions on Power Electronics*, 16(2):248–255, 2001.
- [197] SYLVAIN LECHAT SANJUAN: *Voltage Oriented Control of Three-Phase Boost PWM Converters*. 2010.
- [198] TAN, J., D. ZHAO and B. FERREIRA: *A method for in-situ measurement of grid impedance and load impedance at 2 k–150 kHz*. In *2015 9th International Conference on Power Electronics and ECCE Asia (ICPE 2015-ECCE Asia)*, pp. 443–448.
- [199] TARATEERASETH, V.: *EMI filter design: Part III: Selection of filter topology for optimal performance*. *IEEE Electromagnetic Compatibility Magazine*, 1(2):60–73, 2012.
- [200] TARATEERASETH, V., K. Y. SEE, F. G. CANAVERO and R. W.-Y. CHANG: *Systematic Electromagnetic Interference Filter Design Based on Information From In-Circuit Impedance Measurements*. *IEEE Transactions on Electromagnetic Compatibility*, 52(3):588–598, 2010.
- [201] TAYLOR, L., WENHUA TAN, X. MARGUERON and N. IDIR: *Reducing of parasitic inductive couplings effects in EMI filters*. In *Power Electronics and Applications (EPE), 2013 15th European Conference on*, pp. 1–8, 2013.
- [202] THOMAS, O. DE, M. SYLVAIN, G. JEAN-MICHEL, J.-L. SCHANEN and A. PERREGAUX: *Reduction of conducted EMC using busbar stray elements*. In *2009 Twenty-Fourth Annual IEEE Applied Power Electronics Conference and Exposition (APEC)*, pp. 2028–2033.
- [203] TIHANYI, L.: *EMC in Power Electronics*. Elsevier Science, Oxford, 1995.
- [204] TOURÉ, B., J.-L. SCHANEN, L. GERBAUD, T. MEYNARD, J. ROUDET and R. RUELLAND: *EMC Modeling of Drives for Aircraft Applications: Modeling Process, EMI Filter Optimization, and Technological Choice*. *IEEE Transactions on Power Electronics*, 28(3):1145–1156, 2013.
- [205] TRZYNADLOWSKI, A. M., F. BLAABJERG, J. K. PEDERSEN, R. L. KIRLIN and S. LEGOWSKI: *Random pulse width modulation techniques for converter-fed drive systems-a review*. *IEEE Transactions on Industry Applications*, 30(5):1166–1175, 1994.
- [206] VAC: *Specification for Soft Magnetic Cores: W424*. 2011.
- [207] VAJTAI, R. (ed.): *Springer Handbook of Nanomaterials*. Springer Berlin Heidelberg, Berlin, Heidelberg, s.l., 2013.

-
- [208] VRANKOVIC Z.: *Input EMI filter for motor drive including an active rectifier*, 2015.
- [209] WAIDE, P. and U. BRUNNER: *Energy-Efficiency Policy Opportunities for Electric Motor-Driven Systems*. Paris, 2011.
- [210] WANG, J., S. YU and X. ZHANG: *Effect of key physical structures on the laminated bus bar inductance*. In *2016 IEEE 8th International Power Electronics and Motion Control Conference (IPEMC 2016 - ECCE Asia)*, pp. 3689–3694.
- [211] WANG, S.: *Modeling and Design of EMI Noise Separators for Multiphase Power Electronics Systems*. IEEE Transactions on Power Electronics, 26(11):3163–3173, 2011.
- [212] WANG, S., R. CHEN, J. D. VANWYK, F. C. LEE and W. G. ODENDAAL: *Developing Parasitic Cancellation Technologies to Improve EMI Filter Performance for Switching Mode Power Supplies*. IEEE Transactions on Electromagnetic Compatibility, 47(4):921–929, 2005.
- [213] WANG, S., F. C. LEE, D. Y. CHEN and W. G. ODENDAAL: *Effects of Parasitic Parameters on EMI Filter Performance*. IEEE Transactions on Power Electronics, 19(3):869–877, 2004.
- [214] WANG, S., F. C. LEE and W. G. ODENDAAL: *Characterization and Parasitic Extraction of EMI Filters Using Scattering Parameters*. IEEE Transactions on Power Electronics, 20(2):502–510, 2005.
- [215] WANG, S., F. C. LEE and J. D. VANWYK: *Inductor Winding Capacitance Cancellation Using Mutual Capacitance Concept for Noise Reduction Application*. IEEE Transactions on Electromagnetic Compatibility, 48(2):311–318, 2006.
- [216] WANG, S., J. D. VAN WYK and F. C. LEE: *Effects of Interactions Between Filter Parasitics and Power Interconnects on EMI Filter Performance*. IEEE Transactions on Industrial Electronics, 54(6):3344–3352, 2007.
- [217] WANG, Y., F. CASTLES and P. S. GRANT: *3D Printing of NiZn ferrite/ABS Magnetic Composites for Electromagnetic Devices*. MRS Proceedings, 1788:29–35, 2015.
- [218] WEBER, S., E. HOENE, S. GUTTOWSKI, W. JOHN and H. REICHL: *Predicting Parasitics and Inductive Coupling in EMI-Filters*. In *Twenty-First Annual IEEE Applied Power Electronics Conference and Exposition, 2006. APEC '06*, pp. 1157–1160, March 19, 2006.
- [219] WEBER, S.-P: *Effizienter Entwurf von EMV-Filtern für leistungselektronische Geräte unter Anwendung der Methode der partiellen Elemente*.
- [220] WEIDMANN, H. and W. MCMARTIN: *Two Worst-Case Insertion Loss Test Methods for Passive Power-Line Interference Filters*. IEEE Transactions on Electromagnetic Compatibility, EMC-10(2):257–263, 1968.
- [221] WINTRICH, A., U. NICOLAI, W. TURSKY and T. REIMANN: *Application Manual Power Semiconductors*. ISLE, Ilmenau, 2nd, rev. ed. ed., 2015.
- [222] WU, B.: *High-power converters and AC drives*. John Wiley distributor, Hoboken, N.J and Chichester, 2006.

-
- [223] WU, W., Y. JIANG, Y. LIU, M. HUANG, Y. HE and S.-H. CHUNG: *A new passive filter design method for overvoltage suppression and bearing currents mitigation in a long cable based PWM inverter-fed motor drive system*. In *2016 IEEE 8th International Power Electronics and Motion Control Conference (IPEMC 2016 - ECCE Asia)*, pp. 3103–3110.
- [224] WURTH ELEKTRONIK: *Axial EMI Suppression Ferrite: WE-AEFA 782013125285*. 2014.
- [225] WURTH ELEKTRONIK: *Ceramic Capacitors: WCAP-CSSA X1/Y2*. 2014.
- [226] XIANG LUO, Y. DU, X. H. WANG and M. L. CHEN: *Tripping Characteristics of Residual Current Devices Under Nonsinusoidal Currents*. *IEEE Transactions on Industry Applications*, 47(3):1515–1521, 2011.
- [227] XING, L. and J. SUN: *Optimal Damping of Multistage EMI Filters*. *IEEE Transactions on Power Electronics*, 27(3):1220–1227, 2012.
- [228] YINGHUA, Y., G. HONGLIN, W. XINHUA and T. JINFEI: *Study on Soft Switching Technology to Reduce Electromagnetic Interference of PWM Inverter*. *Energy Procedia*, 17:384–390, 2012.
- [229] YOSHIKAWA, Y., S. OGUMA and K. YAMAUCHI: *New Fe-based soft magnetic alloys composed of ultrafine grain structure*. *Journal of Applied Physics*, 64(10):6044, 1988.
- [230] ZANGUI, S., K. BERGER, C. VOLLAIRE, E. CLAVEL, R. PERRUSSEL and B. VINCENT: *Modeling the near-field coupling of EMC filter components*. In *Electromagnetic Compatibility (EMC), 2010 IEEE International Symposium on*, pp. 825–830, 2010.
- [231] ZEMAN, M., V. BLAHNIK, Z. PEROUTKA and J. MICHALIK: *Optimal control of single-phase voltage source active rectifier with emphasis on the minimal electromagnetic interference*. In *2011 IEEE Ninth International Conference on Power Electronics and Drive Systems (PEDS 2011)*, pp. 745–749.
- [232] ZHAO, D., J. A. FERREIRA, H. POLINDER, A. ROCH and F. LEFERINK: *Noise propagation path identification of variable speed drive in time domain via common mode test mode*. In *2007 European Conference on Power Electronics and Applications*, pp. 1–8.
- [233] ZHE LI, D. POMMERENKE and Y. SHIMOSHIO: *Common-mode and differential-mode analysis of common-mode chokes*. In *International Symposium on Electromagnetic Compatibility*, pp. 384–387, 18-22 Aug. 2003.